SAND--89-2294

DE90 004987

SAND89-2294
Unlimited Release
Printed November 1989

Multi-Dimensional Discrete Ordinates Solutions To Combined Mode Radiation Heat Transfer Problems And Their Application to a Free-Falling Particle, Direct Absorption Solar Receiver

Michael J. Rightley
Solar Thermal Test Facility
Sandia National Laboratories
Albuquerque, NM 87185

ABSTRACT

This is a dissertation that was submitted to the Graduate School of New Mexico State University in partial fulfillment of the requirements for the degree of doctor of philosophy. It reports that radiative transfer in combined mode heat transfer problems was investigated with emphasis on the analysis and characterization of a free-falling particle cloud, direct-absorption solar central receiver. A model was developed to calculate the relevant distributions in the curtain while a concentrated solar beam is impinging on the front face of the medium. The discrete ordinates approximation was applied to allow the spectral equation of transfer to be modeled as a PDE. Model verification tests were conducted to determine the accuracy of the model. One- and two-dimensional results showed that the discrete ordinates model provides satisfactorey estimates of the radiant intensity, the heat flux and the temperature distributions for ordinate sets above S_4 (12-flux approximation) for both the black and gray cases. An experimental program was conducted to measure the unknown thermal and radiative properties of a typical particle curtain and to obtain data on receiver performance for comparison with the model. Indications are that the model performs satisfactorily for the higher order sets and that, when applied to a full-scale receiver, reasonably small errors can be expected.

Abstract

Multi-Dimensional Discrete Ordinates Solutions to Combined Mode Radiation Heat Transfer Problems and Their Application to a Free-Falling Particle, Direct Absorption Solar Receiver

By

Michael J. Rightley

Doctor of Philosophy in Mechanical Engineering

New Mexico State University

Las Cruces, New Mexico, 1989

Dr. L. K. Matthews, Co-Chairman

Dr. G. P. Mulholland, Co-Chairman

Multi-dimensional radiative transfer in combined mode heat transfer problems was investigated with emphasis on the analysis and characterization of a free-falling particle cloud, direct absorption solar central receiver. A model was developed to calculate the relevant distributions in the curtain while a concentrated solar beam is impinging on the front face of the medium. The discrete ordinates approximation was applied to allow the spectral equation of transfer (EOT) to be modeled as a PDE.

Model verification tests were conducted to determine the accuracy of the model. One- and two-dimensional results showed that the discrete ordinates model provides satisfactory estimates of the radiant intensity, the heat flux and the temperature distributions for ordinate sets above S_4 (12-flux approximation) for both the black and gray cases.

An experimental program was conducted to provide data on the performance of the free-falling particle receiver and to compare the results with model predictions. The extinction coefficient and the curtain porosities along with the transmitted fluxes and the exit temperatures were measured.

The boundary condition for the front face of the curtain, which was described in terms of a Fredholm integral problem, was determined through the use of angular heat flux data and parameter estimation techniques. A check of the accuracy of these calculations was performed by integrating the intensity to determine the boundary fluxes. Results showed reasonable flux distributions with a significant improvement from the 12- to the 24-flux model.

Comparisons of the exit temperature and the transmitted flux distributions were made with the model. Results showed satisfactory agreement with errors within 25% being observed at most points.

The results of the temperature predictions also showed reasonable agreement with the measured data. Errors ranged from 8% to 52%. Small temperature increases were thought to be the primary cause of the relatively large errors. This indicates that a larger temperature increase through the receiver would probably result in more accurate readings.

Indications are that the model performs satisfactorily for the higher order sets and that, when applied to a full scale receiver, reasonably small errors can be expected.

Table of Contents

List of Tables

List of Appendix Tables

List of Figures

Nomenclature

a - coefficient of Legendre expansion of scattering phase function

A - coefficients for general solution to Fredholm problem

A, B, C, D - curve fit parameters for velocity data

c - particle clearance

c_p - specific heat

e - emissive power (also error in Chapter 7)

$\hat{e}$ - non-dimensional emissive power for plotting

$\mathcal{F}$ - source function (emission + in-scattering)

h - convection coefficient

I - radiant intensity

$\hat{I}, \hat{G}$ - mean radiant intensity (integration of I over solid angle)

I_b - blackbody emission intensity

$\bar{j}_H$ - Colburn j-factor

$K(x,t)$ - kernel of general Fredholm integral equation

L_x, L_y - curtain dimensions in the x- and y-directions

M - total number of nodes in a given direction

m - mass

$\mathbf{n}$ - normal vector

N_t - number flow rate of particles

$\overline{Nu}$ - Nusselt number

$N_\forall$ - number of particles per unit volume

P - Legendre polynomial

Pr - Prandtl number

$\mathbf{q}, q_i$ - radiative flux vector

$\mathbf{q_{solar}}$ - set of heat flux data as a function of angle

$q^*(y)$ - Gaussian curve fit of front face fluxes angle

$\hat{q}$ - non-dimensional flux for plotting

q''' - internal energy generation term

Q_{conv} - convective loss term

Q - energy (for derivation of the flux vector divergence)

$\mathbf{r}$ - spatial location vector

$\mathbf{r_b}$ - spatial location vector for boundary point

Re - Reynolds number

S - path length

T - temperature

$\hat{T}$ - non-dimensional temperature for plotting

$u(x)$ - general function (used to define Fredholm problem)

v - particle velocity

$\forall$ - volume

w - quadrature weighting function for numerical integration

x, y, z - coordinate axes

X - size parameter, $\frac{\pi d}{\lambda}$

$\hat{y}, \hat{x}$ - non-dimensional distances for plotting

$z(t)$ - general integrand (used to define Fredholm problem)

Greek Symbols

α - absorption coefficient

β - parameter for assumed intensity model

ϵ - emissivity

ε - porosity

γ - finite difference coefficient

$\Gamma_{\chi,\psi}$ - modified sensitivity coefficient of parameter χ on dependent variable ψ.

θ, ϕ - directional angles (altitude and azimuth)

κ - extinction coefficient $\alpha + \sigma_s$

λ - wavelength (also eigenvalue in Chapter 2)

μ - direction cosine, ordinate

ξ - direction cosine, ordinate

η - direction cosine, ordinate (or finite difference coefficient, Chapter 4)

ρ - density and reflectivity

σ_s - scattering coefficient

σ - Stefan-Boltzmann constant

Φ - scattering phase function

$\hat{\Phi}$ - scattering probability (integration of Phi over solid angle)

τ - optical thickness

τ_D - total optical thickness of layer

$\mathbf{\Omega}$ - direction vector

ω_0 - single scattering albedo

ω - uncertainty value

Subscripts and Superscripts

λ - denotes spectral dependence

$1, 2, 3, \ldots$ - denotes a particular direction in the discrete ordinates approximation (i.e. I_1)

c - critical value

$^+, ^-$ - forward or backward hemisphere, respectively

x, y, z - denotes the component in the given cartesion direction

m - refers to the discrete directions in the discrete ordinates approximation

$\vec{}$ - denotes a vectorial quantity

eff - refers to a "bulk" quantity of the curtain (air and particles together)

a, p - denotes air or particle quantity respectively

D - refers to basing on diameter

i, j - refers to a node defined in the finite differencing analysis

w_i - refers to the i^{th} bounding surface

Chapter 1

Introduction

1.1 Mathematical Background

The explosive growth of advanced technology systems utilizing newly designed materials which often must withstand hostile environments (both mechanical and thermal) has created a situation that requires researchers to be better able to predict the response of these systems to external stimuli. In many applications, the expense involved with producing a prototype and testing it to determine it's weaknesses is prohibitive. With the advent of the ultra-high speed computer, it now becomes easier to accurately predict the system response before actually producing working models.

The challenge now becomes to develop more generalized, yet highly accurate, models that will take full advantage of the present and future computational capabilities. However, in the study of participating medium radiative heat transfer, good models already exist that are significantly general and couple easily with the governing equations of other physical processes. These models, if applied to realistic contemporary physical situations, can very quickly utilize the modern computer to it's total capability and are often actually limited by this machine.

The difficulty lies in the form of the general equation of radiative transfer (EOT). The EOT, which describes the intensity field in an absorbing, scattering and emitting medium, is an integro-differential equation. To determine the temperature distribution in the medium for the general case of multi-mode heat transfer, a formulation of energy conservation in the medium will be coupled to the EOT, requiring a simultaneous solution to the entire equation system. A further complication is that the relationship of the heat flux (which appears in the energy equation) to the intensity distribution (which is the dependent variable in the EOT) is also integral in nature.

Further, for many problems in the study of radiation, solutions may be functions of more than one spatial dimension and the wavelength of the radiation itself. These effects can significantly increase the difficulty encountered in

attempting to obtain a solution to the EOT.[1]

In the midst of these complexities, it becomes apparent that 1.) obtaining exact solutions for realistic problems will be prohibitively difficult, 2.) an approximating model of the intensity field in the medium is needed and 3.) this model should be very general and should couple easily with the governing equations of other physical processes to obtain all the pertinent heat transfer quantities.

1.2 Solar Receiver Applications

One important physical situation that requires solution of an equation system like that just described can be found in the field of large scale solar energy utilization. Researchers in this field have applied the sun's energy on a large scale in an effort to produce large amounts of energy at low expense and with little or no waste products. In order to obtain these large amounts of solar energy, some type of concentrating system is required. There are three main types of concentrators now being studied. A large mirrored dish, in the shape of a parabola, has been used to concentrate the rays of the sun to a small area. An energy conversion system is then placed at the focal plane which converts thermal energy into some other mode (often electrical or mechanical). This type of system can also be used in conjunction with a flat mirror (called a "heliostat") to simply produce a high flux, non-moving heat source at a stated test area. This system is known as a "solar furnace." The second type, known as a trough receiver, concentrates the sun's rays down to a line that runs along the length of the trough. One very useful application of this type of solar receiver is to pump some type of liquid through a pipe that runs along this line to heat the liquid.

[1] Allowing for more than one spatial direction has the effect of transforming the ordinary derivatives in the EOT into partial derivatives. Also, the addition of spectral dependency requires another integration and more computer memory to obtain the total radiant heat flux.

The third, and certainly the largest, of the receivers is known as the solar tower concept. This type of system utilizes an array of flat mirrors arranged around an elevated tower. Each mirror is oriented so that it's unit normal vector bisects the angle defined by a line coming from the sun, reflecting off the mirror and striking the target on the tower. The device used at this point to capture the incoming solar rays is called the receiver. In this way, the image of the sun appears on the receiver after having been reflected from the heliostat. As the number of heliostats increases, more and more solar concentration is achieved and the receiver is now being irradiated by a large amount of solar energy. Figure 1.1 shows the basic orientation of the heliostats and the tower in order to produce very high heat flux levels on the receiver target. Obviously, the design of the heliostats and the receiver and the layout and geographical orientation of the field play a significant part in the overall efficiency of such a system.

In an effort to increase the generation efficiency of alternative energy forms from solar tower systems, researchers have begun to explore the concept of direct absorption receivers (DAR). A direct absorption receiver, which eliminates the fluid conduit normally used in liquid-in-tube receivers, will theoretically yield greater efficiencies due to the fact that the energy that is lost due to tube heating can now be absorbed by the working medium. Also, the medium itself can serve as the energy storage material thus eliminating the need to use heat exchangers.

One potential candidate for use as the active medium in a DAR is a small solid particle that is a good absorber of solar radiation. The design of the receiver to introduce these particles to the active area of the target bears obvious importance. Several studies have been undertaken to investigate three primary solid particle receiver designs: 1) the fluidized bed concept, 2) the entrained flow receiver, and 3) the free-falling particle cloud. Both the fluidized bed and the entrained flow concepts require a forced flow of gas to operate. The free-

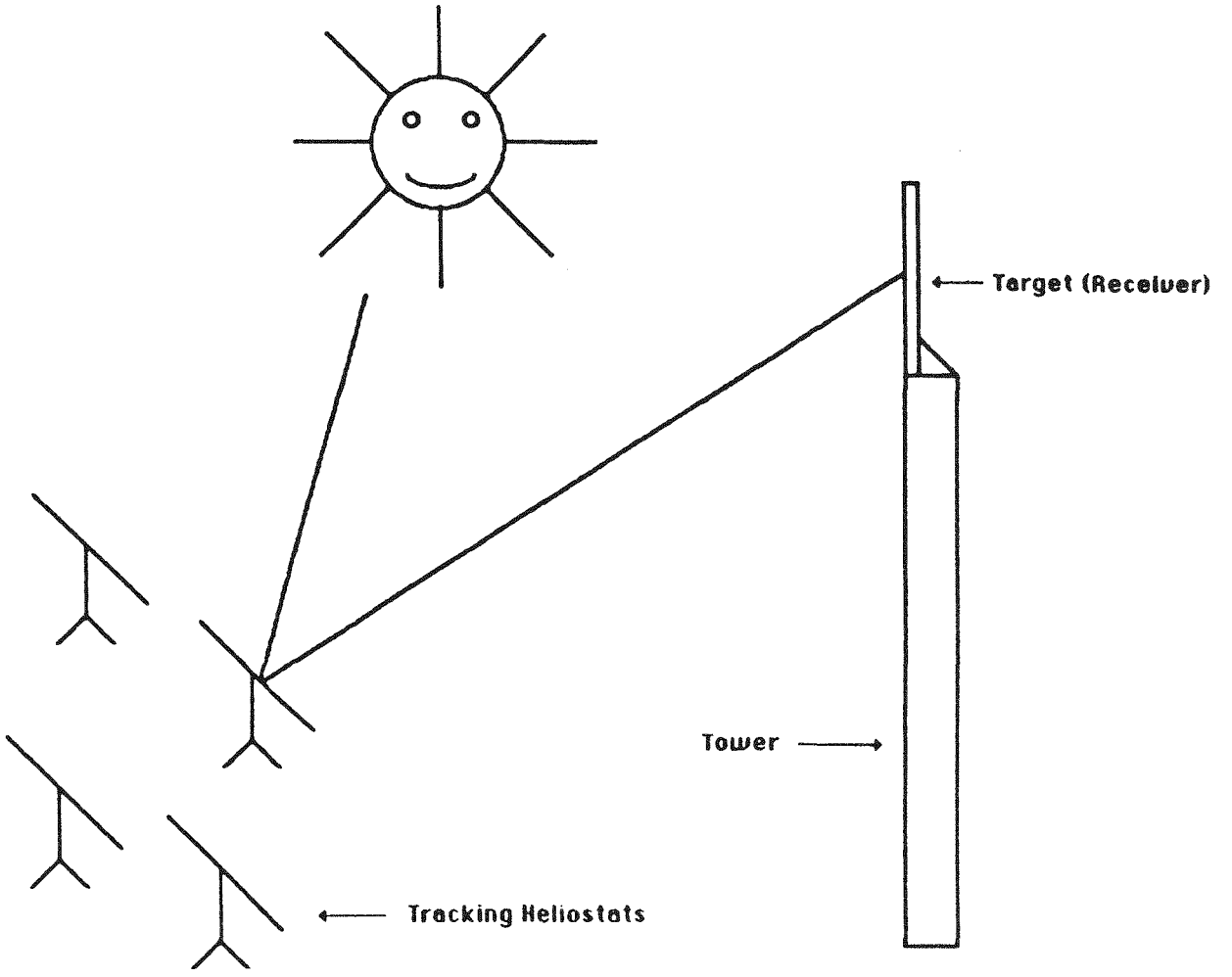

Figure 1.1: Solar Central Receiver Concept

falling particle flow, however, does not require any forced gas flow and, hence, a more simplistic design approach can be used. Also, due to other inherent design characteristics, the free-falling flow should be able to achieve higher overall efficiencies than the other designs.

Researchers at Sandia National Laboratories[17] have investigated the feasibility of the free-falling direct absorption concept. Studies have been undertaken to determine optimal design factors such as particle material selection and receiver cavity configuration. However, to produce an optimum receiver design with suitable particles, the complete heat transfer characteristics of the particle cloud, including all losses and the effects of the receiver walls, must be investigated.

The present study investigated the application of the discrete ordinates approximation of the intensity field to the free-falling particle receiver design. Due to the significant temperature increase of the particles in the receiver, the intensity field in the "curtain," as it is called, is certainly multi-dimensional in nature. Also, since the driving mechanism for the energy transfer in the problem is the solar beam, the spectral effects of the problem must be addressed. For this study, a 2-dimensional spectral formulation of the EOT is solved using the discrete ordinates approximation. The energy equation is formulated to allow for convective heat loss from the particles as they fall through the receiver cavity and solutions for the heat flux transmitted through the curtain and the exit temperature of the particles are compared to experimental data that are obtained at the NMSU Solar Furnace facility.

1.3 Scope

As has been stated previously, the active medium in a direct absorption solar receiver will heat up significantly in the cavity. This large temperature increase will cause the emission by the particles to become a significant part of the overall intensity field in the curtain. For this reason, an accurate analysis of

the heat transfer processes occurring in the medium must be multi-dimensional in nature. Also, the highly directional nature of the incoming solar beam and it's lack of uniformity add to the departure from uni-dimensionality for the curtain.

The present study attempts to model the intensity field in a free-falling particle curtain as it passes through a concentrating solar beam. Also, since any analysis of a DAR must include the most important variable, the exit temperature of the active medium, a formulation of the energy equation is also used to determine the exit temperature of the particles.

A 2-dimensional formulation of the EOT is an integro-partial differential equation. To model the equation with sufficient ease, an approximation of the intensity field is made that allows the integral in the equation of transfer to be replaced with an expression that is easier to handle in a PDE. This allows the application of standard PDE solution techniques to obtain the intensity field. Also, as has been mentioned, sufficient generality is desired in the model to allow for it's application to several different problems and to allow for the relative comparison of the magnitudes of each of the physical processes occurring (i.e., absorption, out-scattering, emission and in-scattering).

The discrete ordinates approximation, developed by Chandrasekhar[20] to analyze stellar atmospheres, is a model that satisfies the criteria discussed above and has the added benefit of algorithmic simplicity. The model is explained in detail in Chapter 3 and various problem solutions are presented in Chapters 4, 5 and 7.

Since emission becomes important in the intensity field for hot particles, a formulation of the EOT will require simultaneous solution of a formulation of energy conservation in the medium to accurately model the system and to obtain temperature predictions. The energy equation for this type of system requires a specific form for the radiant heat flux vector; this vector represents the amount of heat flux contributed to the total heat flux due to the radiative

intensity field. This quantity is calculated by integrating the intensity field over direction (solid angle) and, for this case, over wavelength, making the solution significantly more complex.

The relationship of the radiant heat flux to the intensity distribution (integral) also produces a difficulty in formulating the front surface boundary condition for the curtain (i.e., the side of the curtain that faces the solar beam). To come up with the front surface intensity distribution, measurements of the heat flux are made (since measurements of the intensity are not possible). The boundary condition then must relate the measured fluxes (which is the integrated intensity) to the corresponding intensity (the integrand). The problem, an "ill-posed" problem, is known as the Fredholm integral equation and must be addressed to obtain a solution for a solar receiver.

Once the overall model has been developed, some model verification work is presented in Chapters 4 (1-dimensional) and 5 (2-dimensional). Then, the model is compared to some experimental data measured at a solar furnace (since no solutions exist for this particular problem). The experimentation, explained in Chapter 6, was broken down into secondary and primary phases. The secondary phase involved measuring a radiative parameter, the extinction coefficient, needed in the solution and the porosities of the air and the particles in the curtain. The primary phase of the testing was to obtain back surface heat flux values and average exit temperatures for the particle curtain for various particle flow rates. Results of the experimentation are presented in Chapter 7.

It is anticipated that the results of this study can aid researchers in determining the optimal design configuration for a direct absorption solar receiver. The development of appropriate (and accurate) multi-dimensional models for this problem will allow greater efficiencies to be achieved and possibly help to make solar receivers an integral part of our global energy supply.

Chapter 2

Literature Review

2.1 Scope

A review of the literature that is pertinent to this problem is presented. Section 2.2 presents results from studies that investigated the overall system design for the direct absorption solar receiver system. Three main designs have been primarily considered for this type of application. A brief description of the basic design is presented along with their inherent advantages and disadvantages and the results of some research work that has been conducted in the area.

Since the solid particle direct absorption idea is still in a research phase (particularly in the free-falling particle design,) there are currently no particles available that have been specifically designed for this type of system. Consequently, some investigation has been conducted in order to assess the suitablility of certain types of commercially available particles to be used as the active medium in the receiver. The results of some of these tests are presented in the third Section.

The importance of a full understanding of the heat transfer processes occurring in such a receiver is obvious. Consequently, extensive analytical work has been performed to model the system. One of the crucial aspects to any model of a direct absorption solar receiver is the treatment of the radiative transport involved. As has been discussed, this requires a solution of the EOT formulated for multi-dimensional analyses. Some work has been performed to characterize the radiative transport in the DAR curtain and this work is discussed. However, a significant body of research exists for modelling the EOT in both single and multiple dimensions. The fourth Section presents results of research into suitable radiative modelling techniques for the prescribed receiver geometry and reports on several promising intensity modelling theories.

The last Section discusses the scattering aspects of the particles involved. Categorizations of the type of scattering occurring as well as some results of investigations into determining the scattering behavior of particles in this application are presented. Some applicable theoretical techniques as well as some

experimental methods to determine the scattering phase function are reported.

2.2 Receiver Design Configurations

In the fluidized bed direct absorption receiver concept, a bed of small diameter absorbing particles is "fluidized" by forcing gas flow upward through a containment vessel. The gas flow causes random particle motion to occur with a net particle velocity of zero. This motion is achieved when the particle weight is equalized by the drag force induced on the particle by the gas flow. In solar applications, the walls of the containment vessel are made of a solar-transparent material to allow concentrated solar radiation to enter the vessel. The heat flux will be absorbed by the particles resulting in a temperature increase in the particle/gas mixture. To achieve optimal performance, minimal attenuation of the incident beam by the walls is desired as is maximum absorption of the heat flux by the particles. Degradation of the efficiency from convective losses and particle emission must also be minimized. As with all direct absorption, solid particle designs, particle material selection is very important in obtaining maximum system efficiency.

Fluidized bed research is being pursued at the Laboratiore d'Energétique Solaire in France. Papers by Flamant[1], Flamant and Olalde[2], and Flamant, Olalde, and Gauthier[3] have discussed the results of experimental tests and some theoretical analysis on the subject. Their experiments involved exposing refractory particles with diameters in the range $250 - 700\ \mu m$ to fluxes of $2200\ kW/m^2$ through transparent quartz tubes. They discovered that a proportional correlation existed between the gas flow rate and the receiver efficiency, defined as the ratio of the increase of the gas internal energy to the incident solar energy. Maximum efficiency, around 70%, was achieved using SiC particles. Lower efficiencies were obtained with lower gas flow rates using lighter ZrO_2 particles. Also, temperature measurements indicated that the fluidized bed was nearly isothermal which is considered desirable to minimize particle

emission losses. However, it should be noted that the maximum efficiency for this receiver configuration was estimated to be 83% and the differences were attributed to large thermal emission loss due to the open experimental design that was used.

The theoretical results are presented in [1]. The model that was used is an extension of theoretical work performed by Kubelka and Munk[4], Chen and Churchill[5], and Hamaker[6]. The author used a Schuster-Schwarzschild (2-flux) approximation[7] for the radiant transport through the bed. Equations for the forward and backward components of the radiative flux were written as first-order ordinary differential equations. A second-order energy balance was formulated to yield an ODE for the particle temperatures and a first order balance, based on the bed porosity and the characteristic length of the particles, was used for the gas temperature distributions. The set of ODE's were solved using a Runge-Kutta technique.

Satisfactory agreement between experimental data and the theoretical results for flux and temperature distributions as well as estimations of the mean penetration distance was achieved for gas flow rates near the minimum fluidization condition. Differences were attributed to a lack of spectral considerations in the development of the radiative model and to local variations in the bed porosity near the surface.

Fluidized bed research has also been pursued at the Georgia Tech Research Institute (GTRI)[8],[9]. The test bed, which was larger than the French facility, used fused silica walls as the transmitting medium. Satisfactory fluidization was not achieved due to a limitation on the available air velocities and to the relatively large particles used in the study (1000 μm to 3000 μm.) Consequently, measured efficiencies were in the 30% to 40% range. It was noted in the course of the experimentation that the fused silica bed walls were discolored when the bed was operated with non-oxide particles such as SiC and copper. This discoloration certainly degrades the optical performance of the silica walls but

the actual amount of degradation on a spectral basis is unclear.

If the gas velocity is increased beyond the fluidization condition, the particles will now move upward in the same direction as the gas flow. This type of system is known as an entrained flow receiver. GTRI has also investigated this type of receiver design[10],[11]. Inert particles in the size range $60 - 90\ \mu m$ were used as well as $40\ \mu m$ carbon particles. Approximately 50% of the inert particles were actually entrained which is contrary to some predictions made using the Stoke's theory.

Unsatisfactory efficiencies were attributed to low flow opacities due to the small particle loadings which could be realistically entrained. Also, the same wall discoloration was noted in these experiments. However, due to the relatively large effect of convection on the heat transfer from the gas to the particles, the wall discoloration was not observed to have significant effect on the overall energy transfer to the particles.

Entrained flow receiver work also has been pursued at Lawrence Berkeley Laboratory (LBL)[12]-[16]. Carbon particles of $0.1\ \mu m$ diameter were generated by pyrolysis of acetylene in Argon upstream of the receiver. The particles were then mixed with air and exposed to radiant heating through quartz tubes. Note that the carbon particles were completely consumed in the process and that the amount of carbon necessary to produce an equivalent amount of heat was small compared to direct carbon combustion. No efficiencies were measured but theoretical calculations estimated values in the range $85 - 90\%$ for the given design.

The last of the direct absorption systems investigated is the free-falling flow concept. In this design, particles are quickly heated as they fall under the force of gravity through an area of concentrated solar flux. Some obvious advantages to this design are; 1) the elimination of the need for a transparent window through which the radiation must pass, 2) minimal hydrodynamically imposed constraints on the particle size compared to the entrained flow and

fluidized bed concepts, and 3) the overall design is less complicated and the hardware needs will be relatively less severe.

A significant amount of investigation into the feasibility of a free-falling receiver has been carried out by Sandia National Laboratories. A feasibility study by Hruby[17] summarizes the major points involved with the Sandia research. Investigations of the receiver design, which necessitates a full understanding of the thermal and hydrodynamic behavior of the particle curtain, and the selection of the particle material were reported in the paper.

Radiant heat tests were conducted by exposing SiC and silica sand particles to infrared lamps through a fused silica plate wall. The particle temperatures and velocities were measured using thermocouples and laser doppler velocimetry (LDV), respectively. SiC particles exposed to 500 kW/m^2 of incident flux were heated to a maximum temperature of 1300 K. However, based on particle heating, this represents a thermal efficiency of only 25%. It was suggested that improvements in cavity design could increase the efficiency by reducing emission losses.

The results of the velocity measurement indicated that thermal coupling exists between the particle momentum and the thermal characteristics of the flow. This was determined after a one-dimensional formulation of the momentum equations for the gas and for the particles significantly underestimated the terminal velocity of the particles measured using LDV for the case of no incident flux. The reason for this underestimation is based on the air entrainment that is occurring inside the curtain. This entrainment will cause a smaller relative velocity between the air and the particles which will result in a lower coefficient of drag. Also, horizontal particle velocities will occur near the bottom of the flow where the entrainment is most severe and, because of this, the curtain will "spread." Consequently, a two-dimensional formulation of the momentum equations was solved using a model of dilute gas-particle flows (i.e., one in which particle-particle interactions are negligible) developed by Crowe[18].

The model, known as PSI-Cell (for particle source in cell) utilized a two-fluid or trajectory approach which tracks the particles through the fluid where they act as sources of momentum and energy to the gas. The disadvantage of this model is that excessive computational time is required if many particles are to be tracked. However, when this model was compared to velocity measurements taken with the particles exposed to the flux, the model consistently overestimated the particle velocity. This error was associated with buoyancy effects caused by increased gas temperatures. The gas, which is warmed primarily by convection with the hot particles, will now move at a higher relative interstitial velocity than with no incident flux and the corresponding drag coefficient will increase. Accurate estimations of the particle velocity were eventually achieved by adjusting the drag coefficient used in the two-dimensional model upwards to match the data. However, drag coefficient adjustment was not attempted on the one-dimensional model.

The thermal analysis of the receiver system was accomplished by formulating the energy equations for the gas phase and the particle phase separately. These equations, which were coupled through convection to each other and through the velocity terms to the momentum equations, were coupled to the equation of radiative transfer by including a radiative source term in the particle energy expression. The equation of transfer (EOT) was formulated in one-dimension for any given elevation in the flow[19]. Measurements of the extinction coefficient, the single scattering albedo, and the scattering phase function were made which ultimately yielded the absorption and scattering coefficients to use in the EOT. The phase measurements were used to determine the coefficients of a Legendre polynomial expansion of the phase function. The EOT was solved using the method of discrete ordinates[20] and parametric evaluations were conducted with the model[19]. The evaluations indicated that, by decreasing the particle cloud optical density or the particle bulk absorptivity, a reduction in the overall absorption of the incident energy will be observed

but the spatial distribution of the particle heating will be more uniform. Also, increasing the back wall reflectivity will result in a more uniform curtain heating, increased overall energy absorption by the particles, and a higher thermal efficiency. It should be noted that a uniform distribution of heat in the cloud is not necessarily beneficial since considerable particle mixing will occur.

2.3 Particle Material Considerations

Of critical importance to the direct absorption concept is the material selection for the active medium. Intuitively, the particle characteristics will have a direct bearing on the efficiency of the receiver. Also, as was discussed above, a poor particle selection can have adverse effects on the long term system performance for the entrained flow and fluidized bed design configurations. This was indicated in the discoloration of the transparent window reported in the fluidized bed and the entrained flow research from GTRI[8]-[11]. Another drawback of the forced gas flow receivers is the limitation placed on the particle size in order to achieve fluidization or upward entrainment. The free-falling design, however, eliminates these two fundamental constraints on the allowable particle sizes and materials. A suitable particle type for the free-falling receiver must display the following characteristics:

a.) a low propensity towards agglomeration in high temperature, high heat flux environments,

b.) a large resistance to the inherent thermal and mechanical fatigue associated with the receiver design,

c.) a large absorptivity in the solar spectral range,

d.) commercial availability, and

e.) low cost.

The results of material evaluations for the free-falling receiver design are

presented in the feasibility study by Hruby[17]. Initially, Sandia considered the traditional ceramic materials such as alumina, silica, silicon carbide, and zircon as candidate materials.

To evaluate the suitability of any particular material, particles were tested for agglomeration behavior[21], thermal and mechanical fracture characteristics, bulk absorptivity, and optical properties such as the scattering phase function, the extinction coefficient, and the single scattering albedo[22],[23]. The optical property measurements were conducted at Battelle Pacific Northwest Laboratories.

Of the standard ceramic materials tested, none displayed both high solar absorptivity and good non-agglomeration characteristics in the high heat flux environments and the use of a more robust new particle type was indicated.

A class of alumina-, silica-, or zircon-based particles called proppants were discovered to have the desired characteristics for the free-falling receiver design. The particles are used extensively in the oil drilling industry and the market for these particles is competitive with several companies producing different versions. This will have the beneficial effect of making the particles easily obtainable and relatively inexpensive. Table 2.1 lists some of the particles and their solar absorptivities. The table was taken from Hruby[17].

Out of the above list of candidate particles, two were chosen for further investigation because of their favorable agglomeration characteristics and relatively high solar absorptivities. The two particles and their respective compositions are shown below.

Norton Master Beads^{tm} -86% alumina
-2 – 4% silica
-6 – 8% iron oxide
-4 – 5% titania

Table 2.1: Some Common Proppant Materials

Brand Name	Description	Solar Absorptivity
National Refractories KF95 Grain 14×35	Spherical sintered bauxite	0.519
Dresser Industries Proflow	Spherical nebulized low density mullite	0.659
Norton/Alcoa Master Beads 1708	Spherical sintered bauxite	0.896
Norton/Alcoa Master Beads 1711	Spherical sintered mullite/bauxite	0.917
Norton Research Master Beads	Spherical fused bauxite	0.942
Coors Ceramics Micro Media Type M	Spherical sintered mullite	0.556
Carborundum Corporation Carbo Prop	Spherical sintered mullite	0.931
Carborundum Corporation Sintered Bauxite	Spherical sintered bauxite	0.931
SEPR Zirprop	Spherical fused zirconia	0.740

SEPR Zirprop^{tm} -40% zircon

-46% silica

-7% alumina

-6% titania

Results, obtained with the same tests and property measurements as were outlined for the traditional ceramic materials, indicated that the two proppant particles were more suitable for the direct absorption receiver than the standard ceramics. The Master Beads^{tm} showed no signs of agglomeration up to temperatures of $1100°C$ at ambient pressures[24]. Also, measurements of bulk absortivity as a function of wavelength showed the Master Beads^{tm} to have a fairly flat absorptivity curve over the solar spectrum with a minimum value of about 87% at 2300 nm[25],[26]. An investigation of the thermal fatigue characteristics showed no reduction in compressive strength after more than 100 solar cycles were applied. The Zirprop^{tm} particles, having an as-received value of the solar absorptivity significantly less than the Master Beads^{tm}, displayed more satisfying agglomeration trends. No agglomeration was noticed up to $1200°C$ with applied pressures. However, it was noticed that the Zirprop^{tm} particles absorptivity decreased sharply to about 30% at $1000°C$ after being heat treated in an oven. This suggests using some kind of doping material for future solar applications.

2.4 Radiative Modelling Techniques

Since the particle curtain is an active absorbing, scattering, and emitting medium, a thermal analysis of the system will necessarily involve a solution of the equation of radiative transfer (EOT) which is given below in a general vectorial form for energy passing in the direction Ω.

$$(\Omega \bullet \nabla)\, I_\lambda(\mathbf{r},\Omega) = -(\alpha_\lambda + \sigma_{s\lambda})\, I_\lambda(\mathbf{r},\Omega) + \alpha_\lambda\, I_b(\mathbf{r}) + \frac{\sigma_{s\lambda}}{4\pi} \int_{\Omega'=4\pi} I_\lambda(\mathbf{r},\Omega')\Phi(\Omega' \rightarrow \Omega) d\Omega' \tag{2.1}$$

Extensive literature exists concerning the solution of the EOT. Most solutions involve the application of a model for the radiative intensity field and, consequently, there are many models used to obtain a solution. Some of the models considered applicable to this particular problem are outlined below for both the one- and two-dimensional cases.

2.4.1 One-Dimensional Methods

Possibly the simplest and one of the most common solution models being used is the Two-Flux model which is also known as the Schuster-Schwarzchild approximation[7]. This model is based on the assumption that the intensity field in the medium is semi-isotropic and has been developed for the cases of an absorbing-emitting medium[6], an absorbing-emitting medium with isotropic scattering[27]-[29], and for anisotropic scattering[30],[31].

Brewster and Tien[32] attempted to assess the predictive capabilities of the two-flux method when applied to a slab of anisotropically scattering particles exposed to diffuse incident radiation. The results were compared to a discrete ordinates solution[20] with no empirical or adjustable constants used in the model approximation. Findings indicate that only acute anisotropy in the scattering phase function is responsible for causing significant inaccuracies in the two-flux model. Recent studies have indicated that both acute anisotropy and large optical thicknesses caused the errors[33],[34].

Incropera and Houf[35] solved the problem of radiative transfer through an aqueous suspension using the three-flux method. The three-flux method was chosen since it has been determined that the two-flux method is incapable of accounting for the interface reflection and refraction effects[36],[37] that are significant at air/water interfaces and because of the strongly anisotropic scattering characteristics of aqueous suspensions. The three-flux method assumes a semi-isotropic intensity field with constant intensity values over three regions instead of two as in the two-flux model. Figure 2.1 illustrates the intensity fields

for the two methods mentioned.

Note that the angle separating the two regions in the lower hemisphere in the Figure is the critical angle associated with the air/water interface refraction.

Results from the three-flux model were compared to the method of discrete ordinates and to radiative flux measurements obtained from a dense algal suspension. Good agreement was noticed. This agreement was considerably better than that obtained by applying two-flux models to aqueous suspension problems[33],[38],[39]. The three-flux method is generally considered more accurate for problems where the scattering is predominantly forward which is characteristic of the solid particles being considered for use in the central receiver designs.

The method of discrete ordinates was applied to the problem of radiative transfer in a solar absorbing particle flow that was investigated by Houf and Greif[19]. The results were used to assess the influence of the radiative parameters appearing in the EOT formulation and were not compared to any experimental data. The model calculated the radiative heat flux and the volumetric absorption within the particle curtain. It also predicted the fraction of the incident solar radiation that was absorbed by the particle curtain, the fraction absorbed by the rear wall of the receiver and the combined reflection effects from the rear wall and the particles. The radiative parameters considered are the single scattering albedo, the rear wall reflectivity, the total optical thickness, the angular scattering distribution, and the angular distribution of the incident solar radiation.

The results showed that absorption uniformity can be increased by decreasing the optical thickness. However, this causes the overall absorption of radiation by the particle curtain to decrease. The same effects occur if the albedo is increased. Increasing the rear wall reflectivity had the desired effect, that of increasing the uniformity of the absorption as well as increasing overall absorption by the curtain. It was also shown that particles displaying dominant

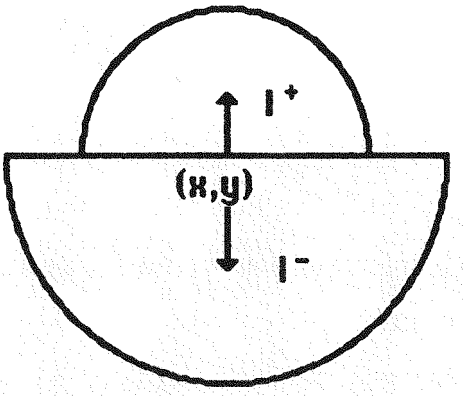

Two Flux

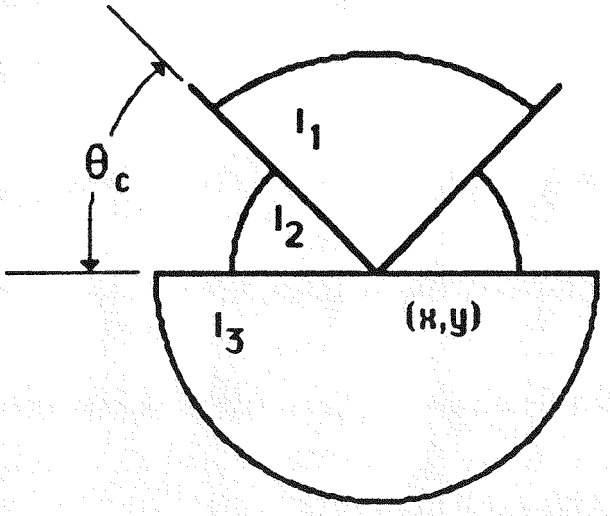

Three Flux

Figure 2.1: Intensity Fields for the Two- and Three-Flux Methods

forward scattering characteristics, such as the Al_2O_3 particles used in the study, exhibited an overall better total energy absorption than other less forward oriented particles, a point which supports the choice of Master Beads^{tm} for the direct absorption receivers.

2.4.2 Multi-Dimensional Methods

While there is a considerable amount of literature dedicated to the solution of the EOT for the absorbing particle problem, all of these papers assumed that the radiative field was one-dimensional in nature. For the free-falling particle design already discussed, there will be a large temperature increase in the vertical direction as the particles fall from the storage hopper through the incident solar beam. This large temperature increase (on the order of several hundred degrees K) implies that the radiative field may be better described by a multi-dimensional formulation of the equation of transfer.

Many models have been developed to solve the multi-dimensional formulation of the EOT. These models have been developed either to specifically address a certain class of problems or in an effort to re-formulate the EOT for all cases into an equation system that is more compatible with a numerical solution technique. The latter approach is the one applied in the present study due to 1.) the lack of specialized models for the DAR, 2.) the need for algorithmic simplicity and computational efficiency and 3.) a generality constraint set by the need to easily couple the governing equation for the intensity field to other equations (usually partial differential equations) describing important physical processes in the DAR. Some of these will be presented below.

A two-dimensional formulation of the EOT was developed by Breig and Crosbie[40] for a finite non-scattering medium subjected to cosine varying radiation, by Crosbie and Linsenbardt[41] for an isotropically scattering semi-infinite medium, by Crosbie and Dougherty[42] for isotropic scattering in a cylindrical medium, and by Crosbie and Koewing[43] for an anisotropically scattering finite

planar medium. All of the above formulations involved calculating the source function integral, the flux, and the intensity at the medium boundaries only. A survey of some recent two-dimensional radiation literature can be found in Crosbie and Linsenbardt[41].

In [41], the classical solution to the EOT for isotropic scattering in a homogeneous, non-emitting medium with an index of refration of unity was formulated to calculate the radiative flux in a semi-infinite medium as a function of two spatial directions. (A similar approach was taken in [40] – [43].) Four different types of incident radiation were considered: cosine varying, semi-infinite strip, step at the origin, and a finite strip. Mathematical expressions for each of these are presented in tabular form as well as the expressions that are developed for the dimensionless source function and the radiative flux inside the medium resulting from the given boundary conditions. Eventually, the intensity inside the medium is expressed in terms of generalized transmission and reflection functions and is likewise tabulated for the different boundary conditions.

Ambarzumian's method[44] is then used to evaluate the source function at the boundary without knowing it at every interior point in the medium. This is accomplished by formulating the problem for the dimensionless collimated source function as an integro-differential equation with an appropriate boundary condition. The boundary condition then is shown to be analagous to the one-dimensional H-function of Chandrasekhar[20] which can be expressed in exponential integral form. Laplace transforms are then taken and the result is a solvable integral equation for the source function at the boundary which is eventually used to determine the fluxes at the boundary.

A numerical procedure is outlined for evaluating the resulting equations. The results are presented for each of the incident radiation cases in a parametric sense for different values of albedo. Although no comparisons with experimental work are presented, a comparison to an appproximation of the non-dimensional source function at the boundary developed by Jefferies[45] shows reasonable

aggreement with differences attributed to "unrealistic discontinuities in some of Jefferies results."

Bellman, Kalaba, and Ueno[46] consider a semi-infinite non-homogeneous, anisotropically scattering, non-emitting medium and use the method of invariant imbedding to solve the radiative transfer problem. A development of the invariant imbedding technique can be found in Bellman and Kalaba[47],[48]. The method involves adding a flat layer of infinitely small thickness to the boundary surface. This thin layer has a single scattering albedo different from that of the medium of interest. This has the effect of changing the reflecting power of the original medium. In considering the contributions of the new layer to the change in the medium, the functional equations governing the radiative processes in the medium are developed. In this way, the original radiative transport problem is imbedded in a new problem that defines the transport through the new medium. No results, along with any corresponding comparisons, are presented.

A vertical two-stream approximation developed by Harshvardhan, Weinman, and Davies[49] was used to solve the three dimensional equation of transfer for radiation in cuboidal clouds. The two-stream approximation separates the intensity in the medium into a forward and backward hemisphere where the intensities, I^+ and I^-, are identified with $\mu = \pm\sqrt{\frac{1}{3}}$ where μ is the direction cosine, $cos\theta$, with θ measured from the vertical axis in the cloud (z-axis). Note that $\pm\sqrt{\frac{1}{3}}$ are the first order gaussian quadrature points. This choice allows the θ integral, rewritten in terms of μ, to be evaluated using first order gaussian quadrature. The equation of transfer is then recast in these terms and the scattering phase function is expanded in a series consisting of zero and first order Legendre functions. Next, the forward and backward intensities are also expanded in a series of Legendre functions in terms of the x and y direction intensity components as well as the forward and backward components of the

z direction intensity. Several variable substitutions are made until, eventually, the three dimensional EOT is expressed as a standard elliptical equation of the form

$$\nabla^2 I = \lambda^2 (I - B_0) \tag{2.2}$$

where

$$\lambda = \sqrt{3(1-\omega)(1-\omega g)} \tag{2.3}$$

$$I = \frac{1}{2}(I_z^+ + I_z^-) \tag{2.4}$$

and B_0 is the Planck blackbody distribution (assumed constant throughout the cloud.) In Eq. (5) above, ω is the single scattering albedo and g is an asymmetry parameter introduced in the Legendre expansion of the phase function. The fluxes on the cloud faces are then expressed as functions of I and gradients of I and the net radiant flux vector becomes a simple expression in terms of the albedo, I, and B_0.

An exact solution to the two-stream development was obtained using finite Fourier transforms. Results from the two-stream approximation were then compared to a direct Monte Carlo simulation that was developed for cloud applications by Davies[50] and Weinman and Davies[51]. The two-stream approximation was seen to predict the flux on the cloud faces to within about 5% of the Monte Carlo results.

As was mentioned in the cuboidal cloud paper discussed above, Monte Carlo methods have been used to confirm the validity of newly developed theories. They have also been applied to simulate the transfer processes occurring in direct absorption solar receivers. Yang, Howell, and Klein[52] used a Monte Carlo simulation to predict radiative transfer through a randomly packed bed of spherical particles of uniform diameters. Emission was neglected and the container was assumed evacuated. The two-flux approximation was used as the theoretical basis for the Monte Carlo simulation that predicted the effective

scattering and absorption coefficients. The random particle packing was modeled by a numerical simulation of rigid spheres slowly settling into a packing assemblage. Some comparisons with existing experimental data and with exact solutions for the limiting case of cubic packing show reasonable aggreement. However, the Monte Carlo method is not expected to be easily applied to free-falling or entrained flow particle systems where the particle motion complicates the simulation technique.

As was previously mentioned, the method of discrete ordinates has been used to solve the equation of transfer for many different participating media. A one-dimensional solution for a direct absorption, solid particle solar receiver was presented in [19]. This method has been expanded to the multi-dimensional case for rectangular enclosures by Fiveland[53]. The EOT was formulated for a gray absorbing, emitting, and isotropically scattering medium. Derivations of the discrete ordinates equations are given in Chandrasekhar[20]. Basically, the method involves breaking up the radiative field into a discrete set of ordinate directions where the intensity is assumed constant in each. Hence, the discrete ordinate method is just an extension of the two-, three-, and six-flux methods that are common in the literature. Figure 2.2 illustrates the concept. The EOT can then be written for each direction with the in-scattering integrals evaluated through the use of a quadrature technique and summed over each ordinate direction. The two-dimensional transfer equation for ordinate direction m in cartesian coordinates for a gray medium then becomes (the wavelength subscript has been dropped for convenience but the quantities are monochromatic)

$$\mu_m \frac{\partial I_m}{\partial x} + \xi_m \frac{\partial I_m}{\partial y} = -\kappa I_m + \alpha I_b + \frac{\sigma_s}{4\pi} \sum_{m'} w_{m'} \Phi_{m' \to m} I_{m'} \qquad (2.5)$$

where μ and ξ are the ordinates (i.e., the direction cosines) and κ and α are the extinction and absorption coefficients, respectively. The $w_{m'}$ is the quadrature weighting function which is determined by the choice of quadrature method

used. The in-scattering term represents energy coming into the m direction from each of the other ordinate directions. The above equation, written for each ordinate direction represents m coupled partial differential equations for the intensities, I_m. The radiant heat flux at a point, which is physically related to the intensity field through an integral over all solid angles, then becomes a weighted sum of the intensities from each ordinate direction multiplied by the ordinate direction

$$\mathbf{q}(\mathbf{r}) = \int_{\Omega=4\pi} I(\mathbf{r},\Omega)\Omega d\Omega = \sum_i w_i \Omega_i I(\mathbf{r},\Omega_i) \tag{2.6}$$

where Ω represents the ordinate direction.

The solution to the discrete ordinate set of equations requires an iterative numerical procedure characterized by initially assuming the boundaries are black and the in-scattering source terms are zero (i.e., for the first iteration through the expression to determine a "first guess" at the intensity field). Then, after calculation of the initial iteration of the radiant intensity distribution in the medium, the non-zero values of the source terms and the boundary emissivity are used and the process is repeated until satisfactory convergence of the nodal intensity values is observed.

The results of the method are compared with exact solutions, Hottel's zone results, P3 differential approximations[54], and an approximation developed by Modest[55] in Fiveland's study. In general, the discrete ordinates method predicts heat fluxes that are closer to the exact solution than the P3 approximation and the zone method if the method is applied as a 12-flux approximation at least. The author evaluated results for 4-, 12-, and 24-flux approximations in his study. Other researchers have also verified the accuracy of the discrete ordinates method (Truelove[58]).

It is clear that the discrete ordinates method is a valuable tool in the solution of the direct absorption solar receiver problem. It's simple concept

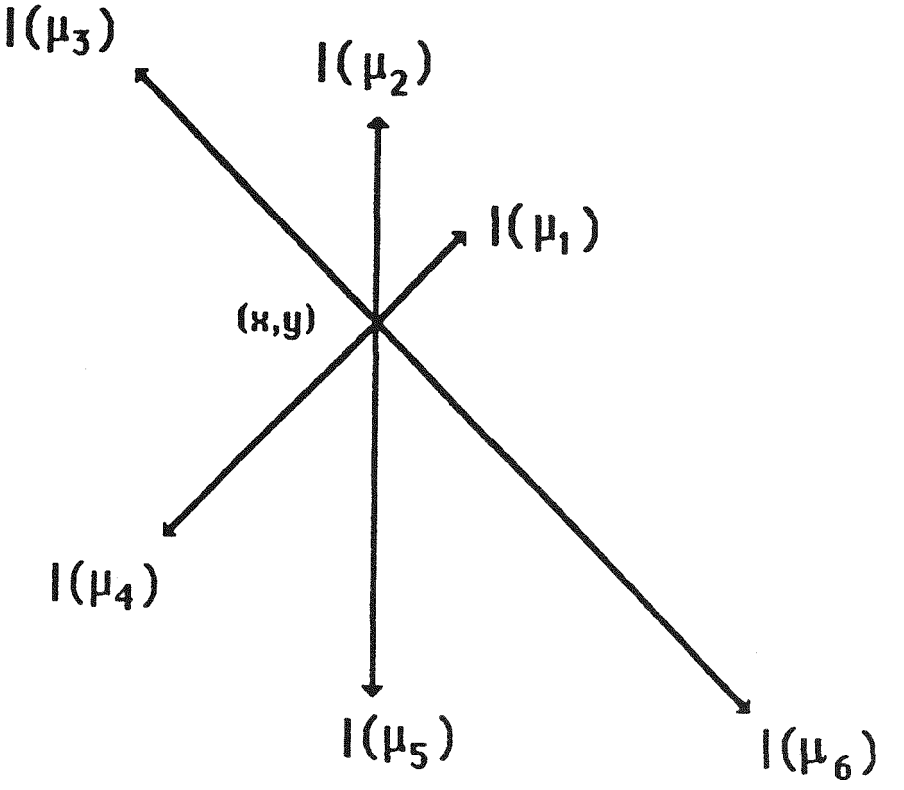

Figure 2.2: Discrete Ordinates Approximation of the Intensity

translates into a generalized approximation of the EOT that is accurate (the accuracy increases if higher order ordinate sets are used) and algorithmically simple. Also, since the method approximates the general continuous equation of transfer with a discrete set of partial differential equations (in multi-dimensional cases) each with a simple numerical quadrature summation term, the coupling between this equation system and other physical process equations is considered straightforward.

A description of a method to derive the values for the ordinate sets and an explanation of some of the inherent errors associated with the technique are presented in Carlson and Lathrop[59]. The errors originate due to the assumption of constant intensities over a defined solid angle. At the boundary of one of these regions, there will essentially be a step change in the intensity value. If the line between an emitting element in the medium and an absorbing element lies along this boundary, then the absorbing element cannot "see" the emitter. Consequently, the total energy that is absorbed by this element will be in error for all emitters that lie along the boundaries of one of the ordinate directions. This type of error has been called "ray effects" by the authors and is discussed in their study.

2.5 Particle Scattering Characteristics

Some literature was reviewed in an effort to establish some of the scattering characteristics involved with the free-falling direct absorption particles. It is apparent, due to the anticipated particle curtain thickness and the distances between free-falling particles, that only single elastic scattering need be considered.

The parameter of interest in scattering theory is the scattering phase function. The phase function, usually denoted by the symbol Φ, represents the probability density with which energy is scattered into the direction of interest from all of the other directions. The function appears in the in-scattering

integral in the EOT and the entire term represents an increase in the intensity field in the direction Ω due to scattering from all other directions. There are basically two ways in which the scattering phase function is determined for a certain medium. A theoretical approach may be employed. The general scattering theory is known as the Mie scattering theory. In the limit as the scattering cross-sections (basically the effective area of the particle that can scatter energy) become either very large or very small, simpler theories known as the geometric and Rayleigh theories (respectivley) may be applied. The second approach for determining of the phase function is to fit experimental data taken from the medium to a function that is well suited to modelling spherically varying quantities, the Legendre polynomial. The data are generally obtained by measuring the energy that is scattered into a given direction from a collimated source entering the medium from a known direction.

A paper by Cartigny[56] on dependent scattering of spherical particles dealt with scattering categorizations with respect to three characteristic lengths; the wavelength of the radiation, λ, the particle diameter, d, and the clearance between particles, c. Recall that the range of particle diameters being considered in this study is $100 - 1000\ \mu m$. As is described in Cartigny and in Seigel and Howell[7], the type of scattering is determined by the magnitude of the size parameter, X, where $X = \frac{\pi d}{\lambda}$. The three types of scattering theory that were mentioned above are defined by this size parameter; the respective ranges of applicability, based on this parameter, are shown below.

$$X << 1 \implies Rayleigh$$

$$X \approx 1 \implies Mie$$

$$X >> 1 \implies geometric$$

Note that Mie scattering theory is actually a general theory that is capable of determing the scattering characteristics of a particle of any diameter. Because of this more wide ranging applicability, the theory is consequently much

more complicated to apply than the Rayleigh and geometric theories which are considered limiting cases for large or small particles. For the Norton Master Beads^{tm}, with a diameter of about 600 μm exposed to solar radiation, the size parameter ranges from 942 to 6280 which clearly indicates geometric scattering. However, in an attempt to insure accuracy, it is anticipated that both the geometric and the Mie theories will be applied to predict the scattering characteristics.

Brewster and Tien[57] discuss the separation of particle scattering into dependent and independent regimes based on the size parameter, the dimensionless clearance, $\frac{c}{\lambda}$, and the particle volume fraction. Their results, in the form of a plot of the various scattering regimes as functions of the clearance and size parameter, is reproduced in Figure 2.3. Their findings clearly indicate that, regardless of the volume fraction or the clearance to wavelength ratio, the scattering from particles with large size parameter values will be independent in nature.

Researchers at Sandia[22] have made measurements of the phase function and fit them to Legendre polynomials to obtain a usable form for the solution of the EOT. The results displayed the expected behavior for absorbing particles in the geometric regime, namely, linear anisotropic scattering. This type of particle scatters strongly in the forward direction and is approximately isotropic in all others. A sketch of the linear anisotropic scattering phase function is shown in Figure 2.4.

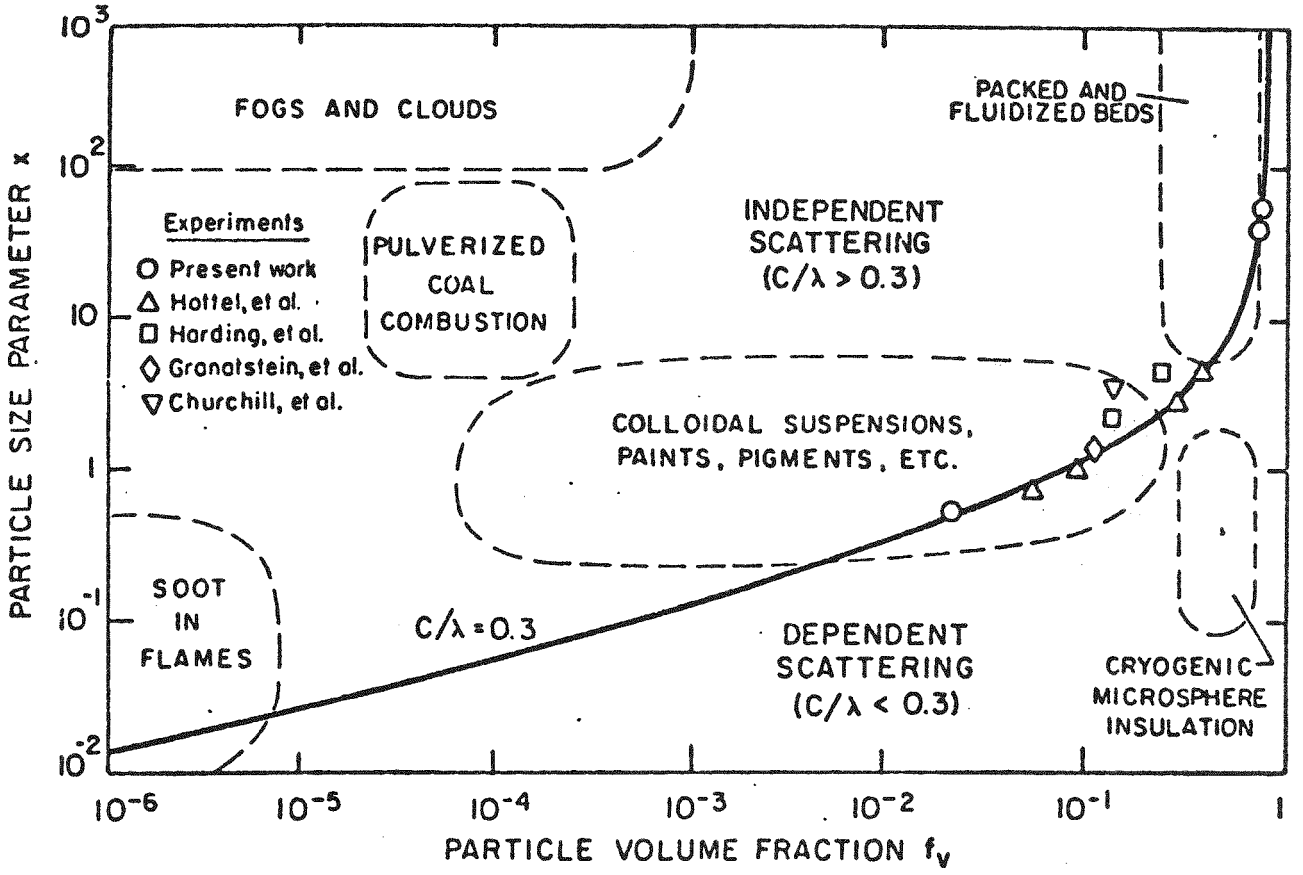

Figure 2.3: Brewster-Tien Scattering Characterization

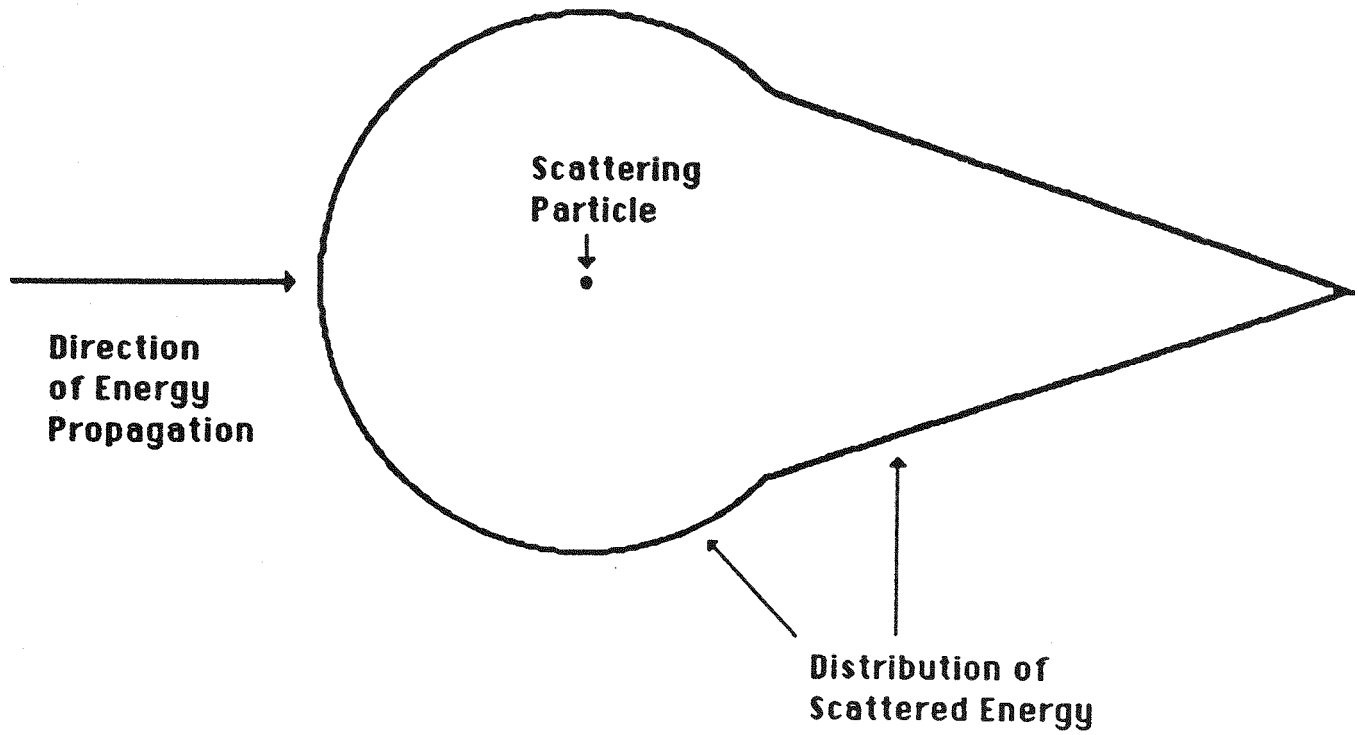

Figure 2.3: Linear Anisotropic Scattering

Chapter 3

Theory

3.1 Introduction

A derivation and explanation of the discrete ordinates approximation for the equation of radiative transfer (EOT) is included in this Chapter. The EOT and a formulation of the conservation of energy equation are presented in general form for problems in Cartesian coordinates. Also, general forms of the pertinent boundary conditions for the governing equation system are presented. Details of the specific derivations of the method to one-, two- and three-dimensional problems with media in both radiative equilibrium and combined mode situations will be presented separately in subsequent Chapters. This Chapter is intended to introduce the reader to the multi-dimensional equation of transfer and the discrete ordinates approximation.

3.2 General Formulation of the Equation of Radiative Transfer

The equation of transfer is developed by considering the net change in the spectral radiant intensity in the direction $\mathbf{\Omega}$ as it passes through a region of an absorbing-emitting-scattering medium (Figure 3.1). If the local absorption and scattering coefficients are written as $\alpha_\lambda(T,p)$ and $\sigma_{s\lambda}(T,p)$ and if local thermodynamic equilibrium (LTE) is assumed, then the general form of the EOT for energy passing through a distance dS at a point $\mathbf{r}$ is

$$\frac{dI_\lambda}{dS}(\mathbf{r},\mathbf{\Omega}) = -[\alpha_\lambda(T,p)+\sigma_{s\lambda}(T,p)]I_\lambda(\mathbf{r},\mathbf{\Omega}) + \alpha_\lambda(T,p)I_{\lambda,b}(\mathbf{r}) + \frac{\sigma_{s\lambda}}{4\pi}\int_{\Omega_i=4\pi} I_\lambda(\mathbf{r},\mathbf{\Omega}_i)\Phi(\lambda,\mathbf{\Omega},\mathbf{\Omega}_i)d\mathbf{\Omega}_i \tag{3.1}$$

Physically, the above expression equates the spatial changes in the spectral radiant intensity as it passes through the infinitesimal volume element to (1) the decrease in the intensity due to absorption and out-scattering, (2) the increase in intensity due to the volumetric emission from the medium $\left(\alpha_\lambda(T,p)I_{\lambda,b}(\mathbf{r})\right)$ and (3) the increase in intensity due to in-scattering (the integral term in Eq.

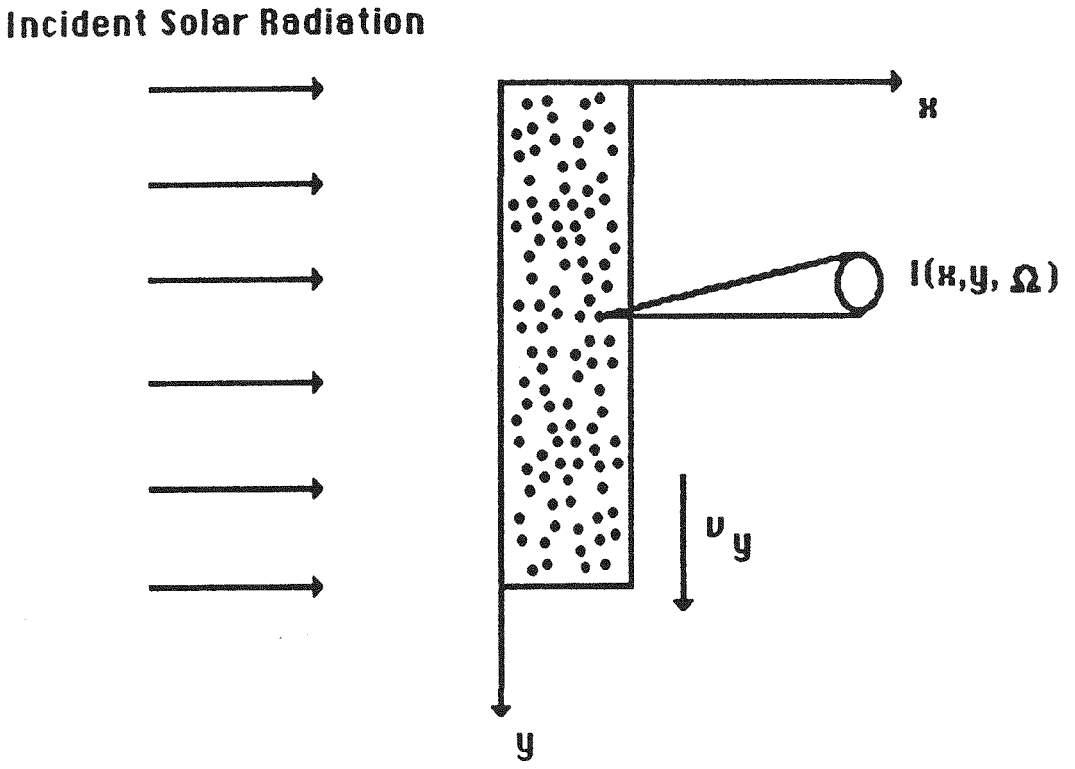

Figure 3.1 Geometry for Derivation of the EOT

3.1). The scattering phase function, $\Phi(\lambda, \mathbf{\Omega}, \mathbf{\Omega_i})$, is a normalized quantity representing the ratio of the intensity that is scattered in a particular direction, Ω_i, to the intensity that would be scattered into that direction if the scattering were isotropic (i.e directionally uniform). Since Φ is actually a distribution function, then it must be true that

$$\frac{1}{4\pi}\int_{\Omega_i=4\pi}\Phi(\lambda,\Omega,\Omega_i)d\Omega_i = 1 \tag{3.2}$$

The in-scattering integral represents the spectral radiant intensity that is scattered into the $\mathbf{\Omega}$ direction from all other directions.

Due to the complexity of the general form of the EOT, and to the physical conditions present for typical engineering applications of radiative transfer problems, Eq. 3.1 can be simplified to a more reasonable form for comparison to other known solutions of the radiation problem. This may be accomplished by considering a gray medium (i.e independent of wavelength) in which the radiative properties are independent of direction (i.e., diffuse). For this case

$$\alpha_\lambda(T,p) = \alpha \tag{3.3}$$

$$\sigma_{s\lambda}(T,p) = \sigma_s \tag{3.4}$$

The general form of the equation of transfer becomes, for the gray, diffuse properties case

$$\begin{aligned}\frac{dI}{dS}(\mathbf{r},\mathbf{\Omega}) = &-[\alpha+\sigma_s]I(\mathbf{r},\mathbf{\Omega}) + \alpha I_b(\mathbf{r}) \\ &+\frac{\sigma_s}{4\pi}\int_{\Omega_i=4\pi} I(\mathbf{r},\mathbf{\Omega_i})\Phi(\mathbf{\Omega},\mathbf{\Omega_i})d\mathbf{\Omega_i}\end{aligned} \tag{3.5}$$

Eq. 3.5 is often rewritten by defining the extinction coefficient (κ), the optical thickness ($\vec{\tau}$) and the single scattering albedo (ω_0) as

$$\kappa = \alpha + \sigma_s \tag{3.6}$$

$$\vec{\tau} = \int_0^S \kappa(S^*)dS^* = (\alpha + \sigma_s)\mathbf{r} \tag{3.7}$$

$$\omega_0 = \frac{\sigma_s}{\kappa} = \frac{\sigma_s}{\sigma_s + \alpha} \tag{3.8}$$

where the quantities in Eqs. 3.6, 3.7, and 3.8 are written for a gray medium with uniform (i.e., invariant along the path), diffuse properties. Substituting these quantities into the diffuse, gray form of the EOT (Eq. 3.5), we obtain

$$\begin{aligned}\frac{dI}{d\vec{\tau}}(\vec{\tau},\Omega) = &- I(\vec{\tau},\Omega) + (1-\omega_0)I_b(\vec{\tau}) \\ &+ \frac{\omega_0}{4\pi}\int_{\Omega_i=4\pi} I(\vec{\tau},\Omega_i)\Phi(\mathbf{\Omega},\mathbf{\Omega_i})d\mathbf{\Omega_i}\end{aligned} \tag{3.9}$$

Often, the expression is simplified further by defining the *source function* as

$$\mathcal{F}(\vec{\tau},\Omega) = (1-\omega_0)I_b(\vec{\tau}) + \frac{\omega_0}{4\pi}\int_{\Omega_i=4\pi} I(\vec{\tau},\Omega_i)\Phi(\mathbf{\Omega},\mathbf{\Omega_i})d\mathbf{\Omega_i} \tag{3.10}$$

which yields

$$\frac{dI}{d\vec{\tau}}(\vec{\tau},\Omega) + I(\vec{\tau},\Omega) = \mathcal{F}(\vec{\tau},\Omega) \tag{3.11}$$

The equation of transfer, in any of the forms above, can be written for Cartesian coordinates in three dimensions by transforming the spatial derivative into it's three components

$$\frac{d}{d\vec{\tau}} = \frac{\partial}{\partial x}\frac{dx}{d\vec{\tau}} + \frac{\partial}{\partial y}\frac{dy}{d\vec{\tau}} + \frac{\partial}{\partial z}\frac{dz}{d\vec{\tau}} \tag{3.12}$$

The direction cosines between the $\vec{\tau}$ direction and the three coordinate axes can be defined as $\mu = dx/d\vec{\tau} = cos\theta$, $\xi = dy/d\vec{\tau} = sin\theta cos\phi$ and $\eta = dz/d\vec{\tau} = sin\theta sin\phi$ where θ, ϕ are defined in Figure 3.2. The EOT can then be written for both the spectral, diffuse and the gray, diffuse cases, respectively, as

$$\mu\frac{\partial I_\lambda}{\partial x}(\vec{\tau},\Omega) + \xi\frac{\partial I_\lambda}{\partial y}(\vec{\tau},\Omega) + \eta\frac{\partial I_\lambda}{\partial z}(\vec{\tau},\Omega) = -I_\lambda(\vec{\tau},\Omega) + \underset{\lambda}{\mathcal{F}}(\vec{\tau},\Omega) \tag{3.13}$$

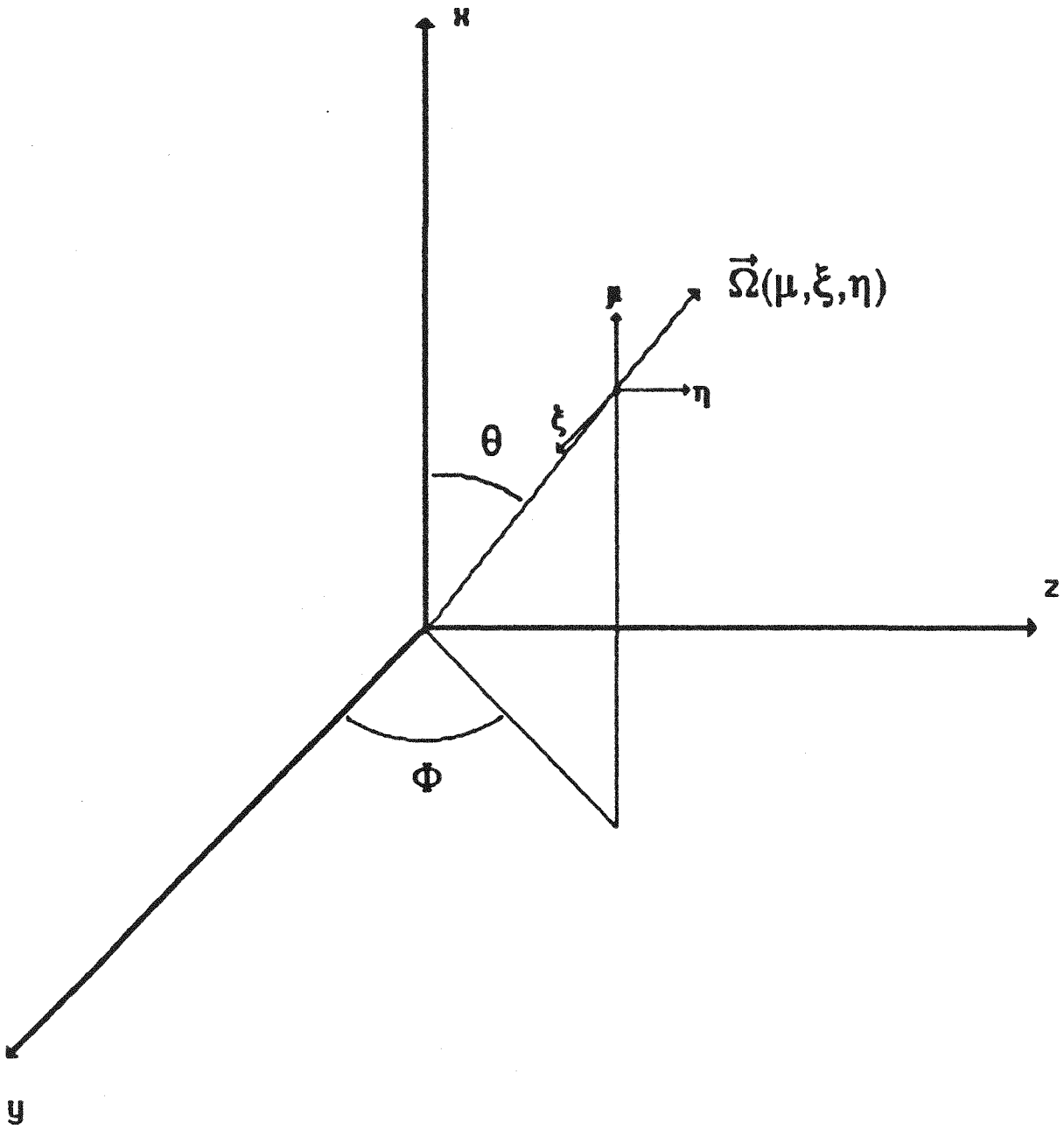

Figure 3.2 Direction Cosines of the Vector Ω in Cartesian Coordinates

and

$$\mu\frac{\partial I}{\partial x}(\vec{r},\Omega)+\xi\frac{\partial I}{\partial y}(\vec{r},\Omega)+\eta\frac{\partial I}{\partial z}(\vec{r},\Omega)=-I(\vec{r},\Omega)+\mathcal{F}(\vec{r},\Omega) \tag{3.14}$$

where the direction vector, $\mathbf{\Omega}$, can be written as

$$\mathbf{\Omega}=\mathbf{\Omega}(\mu,\xi,\eta) \tag{3.15}$$

This leads to the following general vectorial formulation of the equation of radiative transfer

$$(\nabla\cdot\Omega)I_\lambda(\vec{r},\Omega)=-I_\lambda(\vec{r},\Omega)+\underset{\lambda}{\mathcal{F}}(\vec{r},\Omega) \tag{3.16}$$

The spectral heat flux in the x direction at a point, $\vec{r}$, in the medium is then determined by integrating the radiant intensity over the direction cosines that correspond to the x direction

$$q_{r_x}(\vec{r},\lambda)=\int_{\mu=4\pi}I_\lambda(\vec{r},\Omega)\mu d\mu \tag{3.17}$$

The spectral radiative heat flux vector then becomes

$$\mathbf{q_r}(\lambda)=q_{r_x}(\vec{r},\lambda)\hat{i}+q_{r_y}(\vec{r},\lambda)\hat{j}+q_{r_z}(\vec{r},\lambda)\hat{k} \tag{3.18}$$

And the total heat flux is obtained by integrating the spectral vector over all wavelengths

$$\mathbf{q_r}=\int_{\lambda=0}^{\infty}\mathbf{q_r}(\lambda)d\lambda \tag{3.19}$$

3.3 The Method of Discrete Ordinates

As was discussed earlier, a solution of the general formulation of the EOT is difficult for all but the simplest radiative situations in which the solutions

are not physically realistic. The development of an approximate method of solution for the governing equation and the associated boundary conditions has been a critical aspect of the study of radiation heat transfer. In the past, researchers have approached this problem from two general directions. In both cases, approximations to the field variable distribution (i.e., the radiant intensity field, $I_\lambda(\vec{r}, \Omega)$, in the EOT, or the neutron density field in the identical neutron transport equation (NTE) used in the field of reactor physics) have produced meaningful results that exhibited satisfactory accuracy when compared to exact solutions of limiting case problems. The first approach involves obtaining a highly accurate approximation to the pertinent field variable distribution through whatever methods exist. This type of solution has the advantage of high accuracy but suffers from it's lack of generality. It may only be applied to the specific problem at hand and quickly loses accuracy and physical significance when applied outside it's intended domain.

A second approach to the problem involves the development of an all-purpose technique that can be applied to any situation in which the pertinent equation applies. This approach has the advantage that it represents a general approximation of the governing equation system itself rather than describing the behavior of the field variable in a specific situation. It's disadvantage rests in the fact that, since it was developed to be applicable to all problems, it produces estimates of the distributions that are less accurate than a specific, high accuracy solution would yield. However, this second approach will have sufficient generality to provide information about the relationships among different classes of problems that are all governed by the same equation system (eg., scattering dominated versus absorption dominated media). This added benefit illustrates this approach's superior ability to describe the physical characteristics of any applicable problem.

The development of the discrete ordinates method was carried out along the lines of the second method described above. It is a general approximation

of the pertinent physical quantities that is applicable to any situation that can be described by the distribution of that variable.

The main underlying assumption upon which the discrete ordinates method was constructed was first discussed by Schuster in 1905[60] and Schwarzschild in 1906[61] in a model of the intensity distribution that bears both of their names. They broke the intensity field at any point in a participating medium into constant, but not necessarily equal, streams; one value over the forward hemisphere, I_λ^+, and one over the back hemisphere, I_λ^-.

The EOT can be written for the constant intensity in the forward and backward directions and the resulting form then integrated over θ for each hemisphere to yield two, coupled partial differential equations of the form

$$-\frac{1}{2}\frac{dI_\lambda^+(\tau)}{d\tau} = I_\lambda^+(\tau) - \frac{1}{2}[I_\lambda^+(\tau) + I_\lambda^-(\tau)] - I_{\lambda,b}(\tau) \tag{3.20}$$

and

$$-\frac{1}{2}\frac{dI_\lambda^-(\tau)}{d\tau} = I_\lambda^-(\tau) - \frac{1}{2}[I_\lambda^+(\tau) + I_\lambda^-(\tau)] - I_{\lambda,b}(\tau) \tag{3.21}$$

The first term on the right hand side of Eqs. 3.20 and 3.21 represents the extinction, the second term represents the already integrated value of the in-scattering and the last term is the emission from the medium.

The extension of the Schuster-Schwarzschild (2 flux) approximation to the general discrete ordinates method was considered by Chandrasekhar[20]. To adequately describe the radiation transport in a medium that scatters anisotropically, the intensity field must be broken up into more than two discrete directions. Consequently, the discrete ordinates method breaks the intensity field down into N discrete streams. The directions for each stream are determined by dividing the unit sphere into equal segments and are defined as the direction cosines of each direction projected onto the coordinate axes. The three dimensional, spectral equation of transfer can then be written for the intensity

in each of the discrete directions with the in-scattering integral now replaced by a numerical quadrature technique where the quadrature points correspond to the ordinates. The equation becomes

$$\mu_m \frac{\partial I_{m,\lambda}}{\partial x} + \xi_m \frac{\partial I_{m,\lambda}}{\partial y} + \eta_m \frac{\partial I_{m,\lambda}}{\partial z} = -I_{m,\lambda} + (1-\omega_0) I_{m,\lambda,b} + \frac{\omega_0}{4\pi} \sum_{i=1}^{N} w_i \Phi_{i \to m} I_{i,\lambda} \tag{3.22}$$

Equation 3.22 represents $\frac{n(n+2)}{2}$ coupled, first-order ordinary differential equations, where n is the number of independent ordinate values chosen. Due to symmetry over the unit sphere, only 2 ordinate values for each spatial direction are required to provide a 4 flux approximation of the intensity field.

Applying the definition of the spectral radiative flux vector, Eq. 3.17, to the discrete intensities in Eq. 3.22 yields

$$q_r(x,y,z,\lambda) = \int_{\Omega=4\pi} \Omega I_\lambda(x,y,z,\Omega) d\Omega = \sum_{i=1}^{N} w_i \Omega_i I_{i,\lambda} \tag{3.23}$$

The total integrated flux must be calculated using Eq. 3.19 before it's divergence is calculated for use in the conservation of energy expression.

3.3.1 Ordinate Points and Weights

Since the discrete ordinates method was developed to allow the solution of the general transport equation, any and all physical conditions and symmetries that are exhibited by the particular distribution function (i.e., intensity or neutron diffusion) must be preserved in the approximation. To ensure this preservation, careful attention must be paid when selecting the angular quadrature points and weights for the model.

The choice of the components of the direction vector, Ω, (i.e., μ_i, ξ_i, η_i) is made by dividing the unit sphere into equal surface areas. The weights

associated with these ordinate points are then determined such that they sum to unity provided the surface area on the unit sphere is stated in units of 4π steradians. Also, to be mathematically consistent (Carlson and Lathrop[59]), the relationships between the weights and the ordinates must satisfy at least one of the following relationships:[1]

$$\sum_{i=1}^{N} \mu_i w_i = 0 \tag{3.24a}$$

$$\sum_{i=1}^{N} \xi_i w_i = 0 \tag{3.24b}$$

$$\sum_{i=1}^{N} \eta_i w_i = 0 \tag{3.24c}$$

The choice of the ordinates and weights actually is a discretization of the direction domain similar to the spatial discretization that will be performed on the medium to allow the calculation of the intensity field. As such, the direction "mesh" as defined by the ordinates (μ, ξ, η) must be computationally invariant regardless of the spatial mesh chosen and should preserve the physical properties of the in-scattering term (i.e., equal probabilities that scattering will take place from the direction $\mathbf{r}$ into the direction $\mathbf{r}'$ and vice-versa).

Likewise, symmetry considerations also impose conditions on the choice of the weights. As is true with the ordinates, the weights must also be invariant under geometric transformation. Because of this constraint, it can be shown that there are $\frac{n}{2} - 1$ independent point weights for values of n in the range $2 \leq n \leq 12$. Negative weights occur for values on n greater than 22. However,

[1] For the present study, a set of ordinates was chosen from a paper by Lee[62] that, in order to allow all of the weights to be positive, only satisfied the sum-to-zero relationship for the μ and ξ directions.

since unrealistic results can be obtained when applying the discrete ordinates method with negative weights and comparisons have shown that excessively higher order ordinate sets (above S_6) do not significantly increase the model accuracy while requiring excessive CPU time, ordinate sets above 24-fluxes are not considered.

For the current project, the ordinates and weights that were used are given in Tables 3.1, 3.2, and 3.3. As was previously mentioned, these values were taken from Lee[62].

Table 3.1

Ordinates and Weights for the S_2 Approximation (taken from Lee[62])

Direction Number	Ordinates			Weight*
	(μ_i)	(ξ_i)	(η_i)	(w_i)
1	-.57735026	-.57735026	0.57735026	1
2	0.57735026	-.57735026	0.57735026	1
3	-.57735026	0.57735026	0.57735026	1
4	0.57735026	0.57735026	0.57735026	1

* Weights should be multiplied by π.

3.3.2 Scattering Phase Function

Knowledge of the scattering behavior of the medium is required to solve the EOT using the discrete ordinates formulation. Since the discrete ordinates method is a general approximation of the intensity or neutron distributions, a general formulation for the scattering phase function that also satisfies the physical constraints of the medium is needed. The phase function represents the normalized probability density function that describes the scattering from

Table 3.2

Ordinates and Weights for the S_4 Approximation (taken from Lee[62])

Direction Number	Ordinates			Weight*
	(μ_i)	(ξ_i)	(η_i)	(w_i)
1	-.333333333	-.881981710	0.333333333	1/3
2	0.333333333	-.881981710	0.333333333	1/3
3	-.881981710	-.333333333	0.333333333	1/3
4	-.333333333	-.333333333	0.881981710	1/3
5	0.333333333	-.333333333	0.881981710	1/3
6	0.881981710	-.333333333	0.333333333	1/3
7	-.881981710	0.333333333	0.333333333	1/3
8	-.333333333	0.333333333	0.881981710	1/3
9	0.333333333	0.333333333	0.881981710	1/3
10	0.881981710	0.333333333	0.333333333	1/3
11	-.333333333	0.881981710	0.333333333	1/3
12	0.333333333	0.881981710	0.333333333	1/3

* Weights should be multiplied by π.

one direction, Ω' into the direction in which the equation of transfer is currently being solved, Ω. The common means for describing the scattering phase function is in terms of an infinite series of Legendre polynomials written for each of the directions as

$$\Phi(\Omega', \Omega) = 1 + \sum_{j=1}^{\infty} a_j P_j(\Omega') P_j(\Omega) \tag{3.25}$$

where $P_j(\Omega')$ and $P_j(\Omega)$ are the Legendre polynomials of order j in the two directions of interest.

For practical reasons, the series of Eq. 3.25 is truncated after a certain number of terms has been calculated. Increased accuracy is obtained for series with more terms at the expense of computational efficiency and increased

Table 3.3

Ordinates and Weights for the S_6 Approximation (taken from Lee[62])

Direction Number	Ordinates			Weight*
	(μ_i)	(ξ_i)	(η_i)	(w_i)
1	-.25819889	-.93094934	0.25819889	0.16086125
2	0.25819889	-.93094934	0.25819889	0.16086125
3	-.68313005	-.68313005	0.25819889	0.17247209
4	-.25819889	-.68313005	0.68313005	0.17247209
5	0.25819889	-.68313005	0.68313005	0.17247209
6	0.68313005	-.68313005	0.25819889	0.17247209
7	-.93094934	-.25819889	0.25819889	0.16086125
8	-.68313005	-.25819889	0.68313005	0.17247204
9	-.25819889	-.25819889	0.93094934	0.16086125
10	.25819889	-.25819889	0.93094934	0.16086125
11	0.68313005	-.25819889	0.68313005	0.17247204
12	0.93094934	-.25819889	0.25819889	0.16086125
13	-.93094934	0.25819889	0.25819889	0.16086125
14	-.68313005	0.25819889	0.68313005	0.17247204
15	-.25819889	0.25819889	0.93094934	0.16086125
16	0.25819889	0.25819889	0.93094934	0.16086125
17	0.68313005	0.25819889	0.68313005	0.17247204
18	0.93094934	0.25819889	0.25819889	0.16086125
19	-.68313005	0.68313005	0.25819889	0.17247204
20	-.25819889	0.68313005	0.68313005	0.17247204
21	0.25819889	0.68313005	0.68313005	0.17247204
22	0.68313005	0.68313005	0.25819889	0.17247204
23	0.25819889	0.93094934	0.25819889	0.16086125
24	-.25819889	0.93094934	0.25819889	0.16086125

* Weights should be multiplied by π.

difficulty for determining the coefficients, a_j. Usually, lack of data on the distribution of scattered energy limits the number of terms allowed.

The coefficients in Eq. 3.25 can be determined either by experimentation or

through theoretical considerations. Measurements of the energy that a medium scatters into certain directions can be made for many directions. The resulting data can be curve fit using Eq. 3.25 as the model. The number of parameters in the model (i.e., the a_j's) will then be determined through statistical constraints regarding the accuracy of the model and the data. Physically, the number of parameters must always be less than the number of data points which places significant limitations on the series expansion.

Theoretically, the scattered energy in the medium can be determined using Mie scattering theory which is based on the size parameter defined as $x = \frac{\pi d}{\lambda}$ where d is the diameter of the scattering particle and λ is the wavelength of the incident energy. This method is usually prohibitively difficult for most practical engineering applications (although easier approximations can be made for cases when the size parameter is relatively large or small). While the final step will still involve fitting the Legendre function to results of the scattering theory, the series can usually be taken out to many more terms than the experimental system will allow.

For isotropic scattering (i.e., directionally uniform), no terms from the infinite series are used and the phase function becomes

$$\Phi(\Omega', \Omega) = 1 \tag{3.26}$$

Many cases involving linear anisotropic scattering can be closely approximated by considering the zeroth and first order Legendre functions. So, for azimuthally symmetric media, the relationship can be written

$$P(\theta', \theta) = 1 + cos(\theta')cos(\theta) \tag{3.27}$$

In terms of the scattering phase function as given in Eq. 3.25, Φ can be written

$$\Phi(\Omega', \Omega) = 1 + a_1(\mu'\mu + \xi'\xi + \eta'\eta) \tag{3.28}$$

In this form, a_1 represents an asymmetry factor with a range of $-1 \leq a_1 \leq 1$ where values of -1, 0 and 1 denote backward, isotropic and forward scattering

respectively. Equation 3.28, while being a one parameter model, has been modified to a two parameter model of the form

$$\Phi(\Omega', \Omega) = a_0 + a_1(\mu'\mu + \xi'\xi + \eta'\eta) \tag{3.29}$$

to allow for calculation of a higher accuracy function for Φ.

To be used in the discrete ordinates formulation, Eq. 3.28 (or 3.29) is simply written in terms of the scattering from one ordinate direction to the direction that is being considered in the given ODE (i.e., $\Phi_{m' \to m}$).

3.4 Energy Conservation

A general statement of energy conservation in the medium allowing for fluid motion, convective losses and internal energy generation can be written

$$\rho c_p \frac{DT}{Dt}(x, y, z, t) = -[\nabla \cdot \mathbf{q_r}(x, y, z, t)] + q''' + Q_{conv} \tag{3.30}$$

where q''' is the volumetric internal generation term. For the free-falling particle problem and any radiative situations that will be used for model verification in this work, steady-state conditions may be assumed (i.e., the free-falling particle problem is reduced to a "steady-state, steady flow" problem). Eq. 3.30 becomes

$$\rho_{eff} c_{p_{eff}} \left(v_x \frac{\partial T}{\partial x} + v_y \frac{\partial T}{\partial y} + v_z \frac{\partial T}{\partial z} \right) = -[\nabla \cdot \mathbf{q_r}(x, y, z)] + q''' + Q_{conv} \tag{3.31}$$

The radiative flux vector can be determined using Eq. 3.23 and it's gradient calculated numerically. However, a more accurate representation of the flux vector gradient may be developed by determining the net radiative energy that is supplied to a volume element of the medium. This is accomplished by algebraically combining the absorbed, scattered and emitted energy in a volume element of the medium. For the non-scattering case ($\sigma_s = 0$), the absorbed

energy can be determined by considering the amount of the incident intensity, $I_\lambda(x,y,z,\Omega)$, that arrives within the solid angle $d\Omega$ as

$$d^4Q_a(x,y,z,\lambda) = \alpha_\lambda I_\lambda(x,y,z,\Omega)d\forall d\Omega d\lambda \tag{3.32}$$

By integrating over solid angle and wavelength, the above expression can be written in terms of the zeroth moment of intensity, $\hat{I}$, as

$$d^2Q_a = 4\pi d\forall \int_{\lambda=0}^{\infty} \alpha_\lambda \hat{I}_\lambda(x,y,z) \tag{3.33}$$

where the zeroth moment is defined as

$$\hat{I}_\lambda(x,y,z) \equiv \frac{1}{4\pi}\int_{\Omega=0}^{4\pi} I_\lambda(x,y,z,\Omega)d\Omega \tag{3.34}$$

Likewise, the energy that is emitted from the volume element can be written as

$$d^2Q_e = 4d\forall \int_{\lambda=0}^{\infty} \alpha_\lambda e_{\lambda,b}(T)d\lambda \tag{3.35}$$

Combining the emission and the absorption yields an expression for the flux vector gradient for non-scattering media of

$$[\nabla \cdot \mathbf{q_r}(x,y,z)] = 4\int_{\lambda=0}^{\infty} \alpha_\lambda[e_{\lambda,b}(T) - \pi\hat{I}_\lambda(x,y,z)]d\lambda \tag{3.36}$$

Similar arguments lead to the expression for $\nabla \cdot \mathbf{q_r}$ for a general absorbing, emitting and anisotropically scattering medium. The result is

$$\begin{aligned}[\nabla \cdot \mathbf{q_r}(x,y,z)] =& 4\int_{\lambda=0}^{\infty}\Big\{\alpha_\lambda[e_{\lambda,b}(T) - \pi\hat{I}_\lambda(x,y,z)] + \\ & \frac{\sigma_s}{4}\int_{\Omega_i=4\pi} I_\lambda(x,y,z,\Omega_i)\hat{\Phi}(\Omega_i)d\Omega_i\Big\}d\lambda\end{aligned} \tag{3.37}$$

where

$$\hat{\Phi}(\Omega_i) = \frac{1}{4\pi} \int_{\Omega=4\pi} \Phi(\Omega, \Omega_i) d\Omega \tag{3.38}$$

For the purposes of comparison, the energy equation will be written in three forms (to allow for three different energy situations); 1) radiative equilibrium, 2) uniform internal energy generation with no covective losses and 3) fluid motion and convective losses with negligible internal generation. For the free-falling particle problem, the curtain is considered the medium. So, the conduction loss term, which would be driven by the temperature non-uniformity of the particles and the intervening air, may be assumed negligible. Also, the particle motion is primarily in the vertical direction (y-direction) with negligible curtain "spreading" (i.e., relatively small velocities through the thickness, x-direction, or width, z-direction, of the curtain) and, due to insulation and the fact that the surface area of the z boundaries is usually much smaller than the other bounding surfaces, the intensity distribution is assumed uniform in the z direction.

For an enclosure with a quiescent medium, the energy balance can be written either as a situation of radiative equilibrium or with uniform internal generation assuming that the conductive transfer through the medium is negligible compared to the other energy transport mechanisms). The three resulting forms of the energy conservation equation which will be considered are the following:

$$\nabla \cdot \mathbf{q_r}(x, y, z) = 0 \tag{3.39}$$

$$\nabla \cdot \mathbf{q_r}(x, y, z) = q''' \tag{3.40}$$

$$\rho_{eff} c_{p_{eff}} \left(v_y \frac{\partial T}{\partial y} \right) = -[\nabla \cdot \mathbf{q_r}(x, y, z)] + Q_{conv} \tag{3.41}$$

for radiative equilibrium, internal generation and radiation with convection and fluid motion, respectively. The formulation of the convective loss term is discussed in Section 3.7 of this Chapter. The effective density and the effective

specific heat are defined in terms of the porosities as

$$\rho_{eff} = \varepsilon_a \rho_a + \varepsilon_p \rho_p \tag{3.42}$$

and

$$c_{p_{eff}} = \varepsilon_a c_{p_a} + \varepsilon_p c_{p_p} \tag{3.43}$$

The values of the air porosity, ε_a, (i.e., the volume of air in a volume of curtain) and the particle porosity, ε_p, $(1 - \varepsilon_a)$ will be determined experimentally.

3.5 Formulation of Boundary Conditions

The boundary conditions that are used to solve the equation system defined by the coupling of the EOT and a formulation of energy conservation are presented here in general form and then in discrete ordinates form. Boundary conditions for both the free-falling particle flow and the benchmark cases of rectangular walled enclosures are both developed.

The boundary conditions for the walled enclosure radiative problem can be developed by balancing the intensities at each boundary. The boundary intensity will be a function of the emission of energy from the wall (isotropic) and the reflection of incoming energy from the wall to the medium if the walls have emissivities that are less than unity (non-black). Figure 3.3 illustrates the intensity components at the boundary.

If the walls are assumed to reflect and emit diffusely, than the general form of the radiative boundary condition can be stated as

$$I_\lambda(\mathbf{r_b}, \mathbf{\Omega}|_{\mathbf{n}\cdot\mathbf{\Omega}>0}) = \epsilon_w I_{\lambda,b}(\mathbf{r_b}) + \frac{\rho_w}{4\pi} \int_{\mathbf{n}\cdot\mathbf{\Omega}'<0} |\mathbf{n}\cdot\mathbf{\Omega}'| I(\mathbf{r_b}, \mathbf{\Omega}') d\Omega' \tag{3.44}$$

where $\mathbf{n}$ is the unit normal vector of the bounding surface and $\mathbf{r_b}$ represents the position vector along the boundary. Notice that the reflection term is written with the integral over only the incoming solid angles. The integrated value

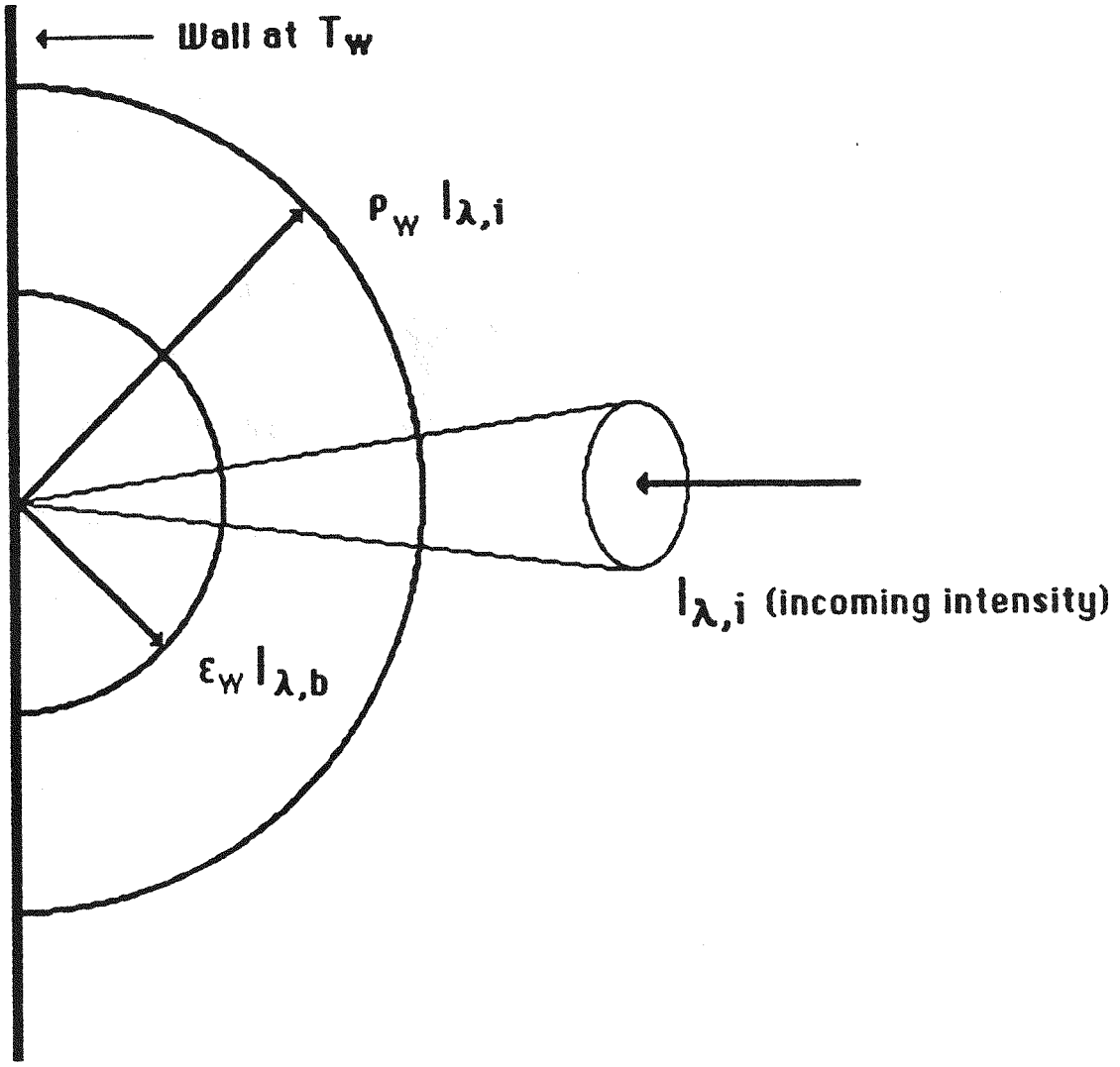

Figure 3.3 Intensity Balance at the Wall

is actually the incoming heat flux, the intensity is determined by dividing the quantity by the solid angle of a hemisphere (π).

Eq. 3.44 is written for every solid bounding surface. In the case of the free-falling particle flow, the front face of the particle curtain has no solid boundary. Rather, concentrated solar energy is directed into the curtain at that point. For this case, the intensity at the boundary is only a function of the energy delivered to the curtain from the incident flux (doesn't depend on the conditions at a solid wall). The formulation of this boundary condition in a manner that makes it conducive to easy solutions given experimental data presents certain mathematical difficulties. The problem posed by the solar central receiver merits special attention due to it's uniqueness and is discussed in Section 3.6 of this Chapter.

In order to demonstrate the validity of the model, comparisons with existing solutions are made. These comparisons were comprised of some exact solutions of certain limiting case problems and some numerical solutions whose accuracy has already been demonstrated. For all of these problems, the boundaries were formulated as solid walls. So, a general discrete ordinates formulation of the wall boundary condition must be developed. The expression is obtained by writing the continuous boundary expression (Eq. 3.44) for each discrete direction that has ordinate values corresponding to a positive surface (i.e., $\mathbf{n} \cdot \mathbf{\Omega}(\mu, \xi, \eta) > 0$) and once again replacing the integral in the expression by a numerical quadrature routine. For a general two-dimensional enclosure with the walls numbered as shown in Figure 3.4, the boundary conditions in discrete ordinates form are

$$I_m(0,y) = \epsilon_{w1} I_b(0,y) + \frac{\rho_{w1}}{\pi} \sum_{\substack{i \\ \mu_i<0}}^{N} w_i |\mu_i| I_i(0,y) \quad ; \mu_m > 0 \qquad (3.45a)$$

$$I_m(L_x,y) = \epsilon_{w3} I_b(L_x,y) + \frac{\rho_{w3}}{\pi} \sum_{\substack{i \\ \mu_i>0}}^{N} w_i |\mu_i| I_i(L_x,y) \quad ; \mu_m < 0 \qquad (3.45b)$$

$$I_m(x,0) = \epsilon_{w4} I_b(x,0) + \frac{\rho_{w4}}{\pi} \sum_{\substack{i \\ \xi_i<0}}^{N} w_i |\xi_i| I_i(x,0) \quad ;\xi_m > 0 \tag{3.45c}$$

$$I_m(x,L_y) = \epsilon_{w2} I_b(x;L_y) + \frac{\rho_{w2}}{\pi} \sum_{\substack{i \\ \epsilon_i>0}}^{N} w_i |\xi_i| I_i(x,L_y) \quad ;\xi_m < 0 \tag{3.45d}$$

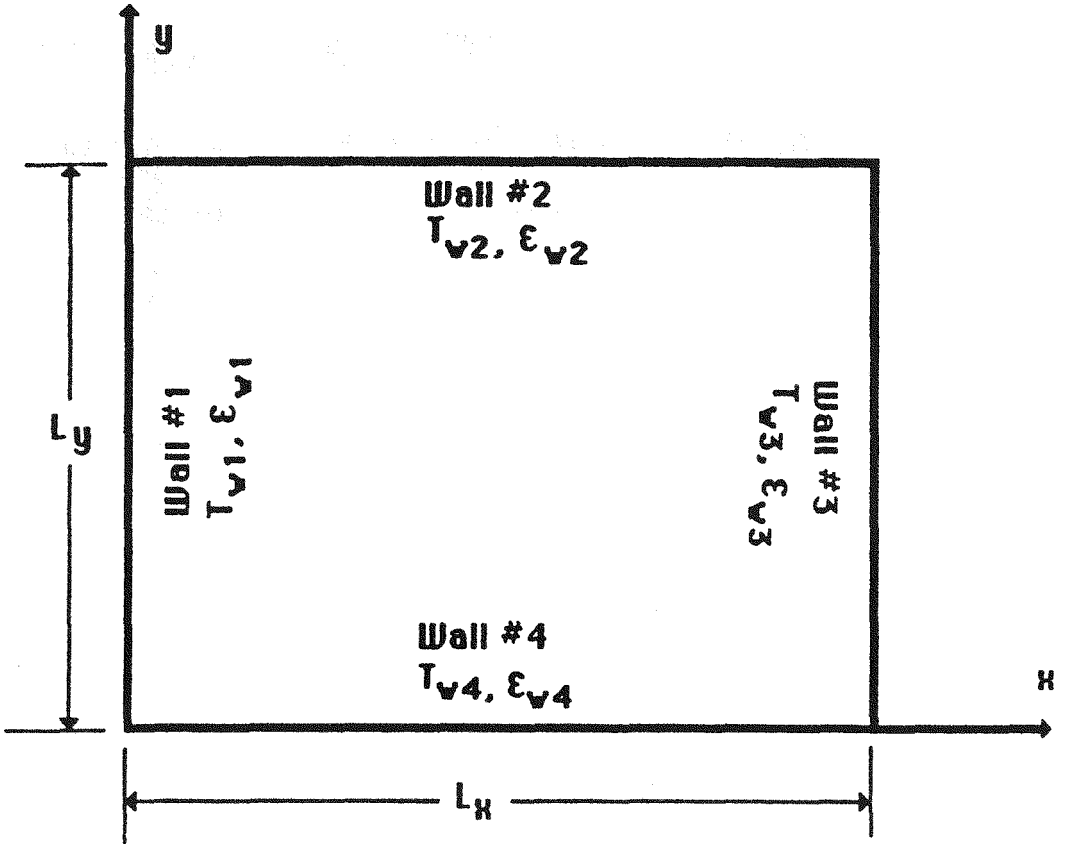

Figure 3.4 Two-Dimensional Walled Enclosure

The boundary conditions for the steady-state form of the energy equation depend on which of the combined mode forms the model is being applied to. For the radiative equilibrium and internal generation problems, the model will be compared to existing solutions in which the temperature at each wall is known (usually one wall is "hot", $T > 0$ and all of the others are "cold", $T = 0$ for the equilibrium case and both walls cold for the generation case) and is

assumed uniform. So, the energy boundary conditions for this case are simply stated uniform temperatures on each wall. For the free-falling particle flow through the solar receiver, the energy equation requires only a statement of the medium inlet temperature at the top of the receiver. Since this temperature is known (usually ambient), the boundary condition for this case is also a simple statement of a known, uniform temperature.

3.6 Front Face Boundary Condition Formulation

To develop a statement of the boundary condition at the front face of the solar receiver (i.e., the $x = 0, y$ face of the free-falling particle curtain), a discussion of the physical system is warranted. The boundary condition can then only be formulated in terms of measurable quantities that accurately describe this physical interpretation.

In modern solar central receivers, a field of sun-tracking mirrors (heliostats) are mounted independently and aligned such that the direction of their unit normal vectors subtends the angle defined by the sun and the receiver target at the heliostat. Each heliostat, which is comprised of several slighty curved facets, is also partially parabolized to more efficiently focus the solar energy to the target. In this way, the reflection of the sun from each heliostat is directed to the receiver target point in as small a focal "spot" as possible. High flux concentrations are produced when many heliostats operate simultaneously. More uniform flux distributions occur if each heliostat tracks the motion of the sun independently of the others.

Because of the motion of the sun and the position of the heliostats in the field, the incident flux on the target exhibits significant angular variations. To determine the boundary *intensity* on a curtain of particles whose front face is the receiver target point for a given heliostat field and time of day, measurements (or computer estimations) of the *flux* as a function of the solid angle at the target point are made (i.e., $q_{i,\lambda}(x, y, z, \Delta\phi, \Delta\theta)$). The incremental components

of the solid angle for each data point (ϕ being the altitudinal angle and θ being the azimuthal angle) that define the field of view of the flux measuring device are $\Delta\phi = \phi_2 - \phi_1$ and $\Delta\theta = \theta_2 - \theta_1$. With this flux data, the corresponding intensity must be determined through the relationship between the flux and the intensity which has the form

$$q_{i,\lambda}(\mathbf{r_b}, \Delta\theta, \Delta\phi) = \int_{\phi_1}^{\phi_2} \int_{\theta_1}^{\theta_2} I_\lambda(\mathbf{r_b}, \theta', \phi') cos\theta' sin\theta' d\theta' d\phi' \tag{3.46}$$

Notice that the problem is a formulation of the classic Fredholm integral equation of the first kind in which it is desired to determine the integrand ($I_\lambda(\mathbf{r_b}, \mathbf{\Omega})$) from knowledge of the integrated result ($q_{i,\lambda}(\mathbf{r_b}, \Delta\theta, \Delta\phi)$). This problem is one of a class of problems known as "ill-posed" problems and is treated in Tikhonov and Arsenin[63].

The problem can be further characterized as an inverse problem as defined by Markovsky[64] in which the output and the operator of a given equation are considered known and it is desired to determine the input. In general form, the Fredholm integral can be written

$$u(x) = \int_a^b K(x,t) z(t) dt; \qquad c \leq x \leq d \tag{3.47}$$

where $K(x,t)$ is the kernel of the equation. The unknown function, $z(t)$, is determined through direct knowledge of the measured function, $u(x)$, and the kernel operator. The problem is ill-posed due to the fact that, for a given measured function, $u(x)$, an infinite set of possible integrands, $z(t)$, can be developed that will reproduce the measurements (or estimations) accurately. This non-uniqueness causes the problem to become unstable and warrants careful attention.

Since the problem is not unique, Eq. 3.47 is typically solved by assuming a functional form of the solution, $z(t)$, with a corresponding set of unknown

parameters, and then determining the parameter values that best "fit" the measured function. Usually, the assumed form of the integrand is expanded with the kernel in an infinite series with the coefficients representing the unknown parameters in the form

$$u_i = \sum_{j=1}^{N} A_j K_{i,j} z_j \tag{3.48}$$

where i is the counter for the data points and A_j are the unknown coefficients. Although intuition would indicate that more accurate values of the parameters will be obtained as more terms are used, this is not the case. As is shown by Feddeev[65], the determinacy of the problem is directly related to the ratio of the maximum to the minimum eigenvalues of the kernel function (in matrix form). Simply put, if this ratio becomes too large (i.e., a large set of terms is used in the infinite series), then the stability of the solution is destroyed (this is similar to the constraints on the size of the parameter vector that is used in standard parameter estimation techniques).

For the solar receiver problem, the kernel of the equation is the direction term (Ω) and the known values are fluxes that are measured at the front face of the particle curtain. To develop the model, the computer program HELIOS[66] was used to obtain numerical estimates of these flux values at the target point of a receiver that is situated at the top of the CRTF Solar Tower at Sandia Laboratories in Albuquerque, New Mexico. The field is composed of 222 heliostats that are located on the north side of the tower. A vector of fluxes as a function of the solid angle is developed of the form

$$\mathbf{q_{solar}} = \left\{ \begin{array}{c} q_1(\theta_1, \Delta\theta_1; \phi_1, \Delta\phi_1) \\ q_2(\theta_2, \Delta\theta_2; \phi_2, \Delta\phi_2) \\ \vdots \\ q_n(\theta_n, \Delta\theta_n; \phi_n, \Delta\phi_n) \end{array} \right\} \tag{3.49}$$

The Fredholm problem is solved by assuming a functional form of the intensity as a function of the components of the direction vector, $\Omega(\theta, \phi)$. The

integration is carried out either analytically, for simple models, or numerically. The new model, with the corresponding parameters, is then used in a matrix solver algorithm to determine the best fit in a statistical sense to the data. These parameters are then placed into the expression for the intensity to provide a continuous function over solid angle.

The accuracy of the fit can be calculated in the standard statistical way (i.e., with the sum of the squared residuals and the pertinent variances). However, this goodness of fit calculation is based only on the flux data. It is conceivable, due to the unstable nature of the problem, that a "good" fit to the flux data would provide a poor estimation of the corresponding intensity distribution. For these reasons, and due to the complexity of a rigorous solution of the ill-posed problem, simplified models will be applied and the results for several different models of varying complexity will be analyzed to allow for an intensity distribution that is reasonably accurate. The details of this analysis are provided in Appendix A-1 and the results of the best models for each particular situation are presented in the relevant Chapters.

3.7 Formulation of the Convective Loss Term

The convective loss term in Eq. 3.41 may be written in the standard way as

$$Q_{conv} = \overline{h}_{eff}[T(x,y) - T_\infty] \tag{3.50}$$

The convection coefficient is stated as an effective value due to the type of medium. Since the medium chosen for the model actually is composed of both the air and the particles in the curtain, a global heat transfer coefficient for this type of geometry is required. As is standard for convection calculations, an empirical correlation is applied. A correlation by Bird, Stewart and Lightfoot[67] for packed beds has the form

$$\varepsilon_a \bar{j}_H = 2.06 Re_D^{-0.575} \tag{3.51}$$

where ε_a is the bed porosity (the subscript a denotes air in the present study) and $\bar{j}_H$ is the Colburn j-factor defined as

$$\bar{j}_H = \overline{St} Pr^{\frac{2}{3}} = \frac{\overline{Nu}}{Re_D Pr^{\frac{1}{3}}} \tag{3.52}$$

The curtain velocity as a function of fall height (used in the calculation of the Reynolds number) has been experimentally determined by researchers at Sandia[68]. The porosity will be determined in the present study and will be used not only to determine the convection coefficient but also to find the effective specific heat and the effective density, as was mentioned previously.

3.8 Numerical Solution Techniques

Some of the general details of the numerical techniques that are incorporated in the model are presented here. There are several specific points that will be mentioned as they become relevant in later Chapters.

To solve the EOT in the discrete ordinates formulation along with the particular form of the energy equation, an explicit finite difference technique is used. Standard first and second order accurate backward difference approximations are applied to the EOT, Eq. 3.22, to calculate the intensity distributions. For mixed heat transfer mode problems, the temperature distribution is also governed by a partial differential equation. The solution to the energy equation, for these cases, is obtained by differencing the derivatives in a manner similar to the approximations used in the EOT. The solutions are obtained simultaneously due to the coupling of the two fields through the emission term in the EOT. The radiative and thermal parameters, assumed constant for this model, are discussed in more detail in the results Chapters. Appendix A-2 presents the details of the differencing scheme and the resulting expressions for the EOT and the energy equation in mixed heat transfer mode situations. For radiative equilibrium, although the temperature distribution is no longer described by a

PDE, it is still an implicit function in the equation of transfer. A simultaneous solution technique will also be required for this case.

A more complicated problem must be addressed when the model is applied to the solar receiver problem. For the free-falling particle curtain, the system excitation is provided by the incident solar heat flux which is wavelength dependent. The spectral form of the EOT is solved for this case for energy in a wavelength band $\Delta\lambda$. The incident heat flux values that are provided by measurements or from HELIOS are integrated values over wavelength and, as such, need to be broken down into spectral components.

To accomplish this, a characteristic solar spectrum is needed. This spectrum could then be applied to the integrated flux values and the amount of power in each band could be determined. For generality, the model should be versatile with respect to the type of spectrum that is inputted. Several mathematical models have been developed that calculate the total energy under specified wavelength bands (i.e., integration under a curve from λ_1 to λ_2). Next, if measurements of the total integrated flux at a given location are available, the ratio of the area under each wavelength band to the total area (the integrated flux) will give the fraction of the total power that corresponds to the specified wavelength band.

To obtain a solution for this case, the spectral form of the EOT is solved on a wavelength band basis for each wavelength band that is specified by the user. The resulting intensity distribution, $I_\lambda(x, y, \Omega)$, is used in Eq. 3.23 to determine the spectral radiative flux vector. Eq. 3.19 is then used to integrate the flux values. This is accomplished using a simple Rhomberg integration routine (Wolford and Smith[69]). The total radiative flux vector may then be used in the energy conservation expressions (Eq. 3.33, 3.34, 3.35) to obtain the temperature distribution. The solution will proceed simultaneously due to the coupled nature of the equation system. This is done by first assuming a temperature distribution in the medium, then, the solution of the EOT will

provide the intensity field that is used to calculate the flux vector. These fluxes are then used in the energy equation to arrive at an updated value of the temperature field and the process is iterated to convergence.

Finally, the directional nature of the discrete ordinates approximation requires some attention during the development of the algorithm. One of the advantages of the discrete ordinates method is that it allows the effects of each boundary (i.e., two in each direction) to propagate into the solution of a partial differential equation that is only first order with respect to all spatial directions. It accomplishes this by forcing the directional nature of each boundary to effect the ordinate directions that have the same signs (i.e., are in the same direction). For example, for the boundary at $(0, y,)$ in the two-dimensional rectangular enclosure, the radiative effects of the wall are propagated into the medium only in ordinate directions that have positive values of μ. The intensity field in these directions is a function of the conditions at this boundary and the in-scattering term (assuming negligible emission). The intensities corresponding to negative μ values are only affected by the boundary condition at $(x = L_x, y)$ (and the in-scattering). The overall results are then properly recombined when quantities that require integration over solid angle are calculated (i.e., the flux or the intensity moments).

For this reason, the numerical solution of the EOT proceeds forward (i.e., from $x = 0 \rightarrow L_x$ and $y = 0 \rightarrow L_y$) when positive ordinates are being considered. For values of μ less than zero and positive ξ, the solution proceeds from $x = L_x \rightarrow 0$ and $y = 0 \rightarrow L_y$. Similar arguments hold for negative ordinates in all directions.

Chapter 4

One-Dimensional Model Verification

4.1 Introduction

The results of the discrete ordinates method applied to absorption-emission plane layer (1-D) problems are presented in this Chapter. The work of this Chapter is basically a model verification analysis and as such compares the discrete ordinates approximation to other numerical solutions believed to be accurate and, in limiting cases, to exact solutions that exist in the literature.

The Chapter includes the formulation of the 1-D discrete ordinates model and the pertinent forms of the energy equation. Boundary conditions are presented for the plane layer problem representing solid walls with constant radiative properties. The walls are assumed gray (or black) and diffuse (i.e., $\epsilon_w = \alpha_w = 1 - \rho_w$). The coupling between the energy and the radiative transport equation is addressed and the solution methods used to solve the problem for the cases of radiative equilibrium and internal energy generation are presented.

Results for two energy situations are then presented in terms of non-dimensional variables. Plots of temperature distributions and heat fluxes are given for both the radiative equilibrium and internal energy generation cases over a wide range of optical thicknesses.

4.2 Formulation of the One-Dimensional Model

The problem involves the calculation of the pertinent heat transfer quantities between two infinite, parallel, isothermal plates. The plates are assumed gray (or black) in nature and emit and reflect energy diffusely. To develop the discrete ordinates approximation, the medium is assumed to be gray, have uniform radiative and thermal properties that are independent of temperature and have a refractive index of unity. For the internal energy generation cases, the medium is assumed to generate energy uniformly and the wall temperatures for these cases are equal. Figure 4.1 illustrates the geometry of the situation in terms of the wall normal and the angle that defines the pertinent ordinate.

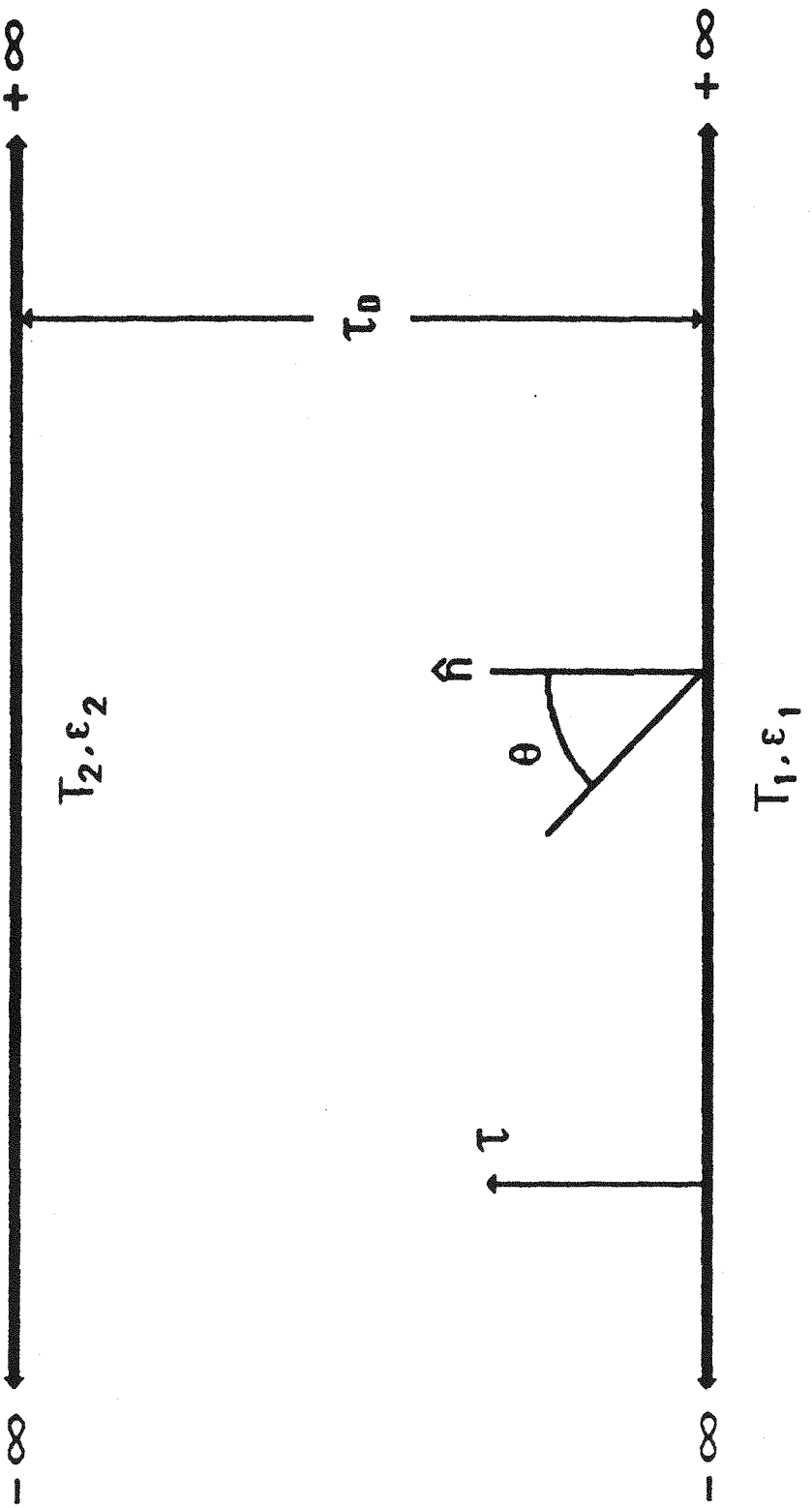

Figure 4.1: Planar Geometry

4.2.1 Equation of Radiative Transfer

The equation of transfer for a one-dimensional, diffuse gray absorbing-emitting (non-scattering) medium can be written as

$$\mu \frac{dI(x,\Omega)}{dx} = -\alpha I(x,\Omega) + \alpha I_b(x) \tag{4.1}$$

The above expression relates the change in the radiant intensity through the layer to the emission and the absorption of the medium where α is the uniform, temperature independent absorption coefficient. To maintain the one-dimensional nature of the problem, the angular dependence of the intensity can only be a function of the elevation angle (θ). So

$$\Omega = \Omega(\theta) \tag{4.2}$$

The optical thickness and it's differential are

$$\tau = \alpha x \tag{4.3a}$$

$$d\tau = \alpha dx \tag{4.3b}$$

Using Eqs. (4.3) in (4.1), we obtain

$$\mu \frac{dI(\tau,\theta)}{d\tau} + I(\tau,\theta) = I_b(\tau) \tag{4.4}$$

4.2.2 Energy Conservation

The temperature dependence of the intensity field is coupled to the EOT through the emission term, $I_b(\tau)$. A formulation of energy conservation will yield the governing equation for the temperature field. In this chapter, two cases were considered: 1) radiative equilibrium and 2) uniform internal energy generation.

For the radiative equilibrium case, an energy balance in the medium yields

$$\nabla \cdot \mathbf{q_r}(x) = 0 \tag{4.5}$$

where $\mathbf{q_r}(x)$ is the local radiative flux vector. Since emission is angularly uniform, the relationship between the intensity field and the temperature distribution can be obtained for the gray radiative equilibrium case from Eq. 3.36. The resulting expression is

$$\sigma T^4(\tau) = \hat{I}(\tau) \tag{4.6}$$

where σ is the Stefan-Boltzmann constant and the mean intensity at a point, $\hat{I}(\tau)$, is defined as

$$\hat{I}(\tau) \equiv \frac{1}{4\pi} \int_{\Omega=0}^{4\pi} I(\tau, \Omega) d\Omega \tag{4.7}$$

For the case of uniform internal energy generation, the energy equation relates the gradient of the radiative flux vector, $\mathbf{q_r}(\tau)$ to the volumetric generation rate, q'''. The resulting expression is

$$[\nabla \cdot \mathbf{q_r}(\tau)] = q''' \tag{4.8}$$

Substitution of the expression for the flux vector gradient (Eq. 3.36) into Eq. 4.8 yields the expression for the temperature distribution in the medium

$$4\alpha[\sigma T^4(\tau) - \frac{1}{4} \int_{\Omega=0}^{4\pi} I(\tau, \Omega) d\Omega] = q''' \tag{4.9}$$

The equation systems 4.4 and 4.6 (for radiative equilibrium) or 4.9 (for uniform internal energy generation) define the governing equation systems that describe the transport of radiative intensity and energy through the medium. They will be solved, along with their respective boundary conditions for the mean radiant intensity and the temperature distributions in the medium. The heat

flux at a point is obtained by integrating the intensity over all solid angles. The expression is

$$\mathbf{q_r}(\tau) = \int_{\Omega=0}^{4\pi} I(\tau, \Omega)\Omega d\Omega \tag{4.10}$$

4.2.3 Boundary Conditions

Even though the equation system represents a set of coupled equations, only the EOT is a differential equation. Mathematically, this system requires one boundary condition for the intensity at $x = 0$. However, since the medium may exist between two infinite walls that don't necessarily have identical radiative properties or participate, radiatively, in the same way, a general solution for the EOT can only be obtained if the boundary conditions are written for two dissimilar, participating walls. Classically, this has been accomplished by partitioning the intensity into two sets of directions for a one-dimensional problem.[1]

The two directions may be described by defining the product of the normal to the bounding surface and the particular direction in question, $\mathbf{n} \cdot \mathbf{\Omega}$. The boundary effects of any given surface will be propagated into the medium only in the directions for which this product is positive. In this way, the effects of each surface are "felt" only in those directions which may be called the "forward" directions of that surface. Figure 4.2 illustrates this situation.

The general expression for the boundary conditions (Eq. 3.40) can now be expressed in one-dimensional form for diffuse, gray boundaries as

$$I(x, \mathbf{\Omega}|_{\mathbf{n}\cdot\mathbf{\Omega}>0}) = \epsilon_w I_b(T) + \frac{\rho}{4\pi} \int_{\mathbf{n}\cdot\mathbf{\Omega}'<0} |\mathbf{n} \cdot \mathbf{\Omega}'| I(x, \mathbf{\Omega}') d\mathbf{\Omega}' \tag{4.11}$$

[1] For each added dimensional dependence to the problem, another direction cosine is defined. This has the effect of adding two more sets of directions to allow the effects of all four (for a 2-D problem) or all 6 (for a 3-D problem) bounding surfaces to be taken into consideration.

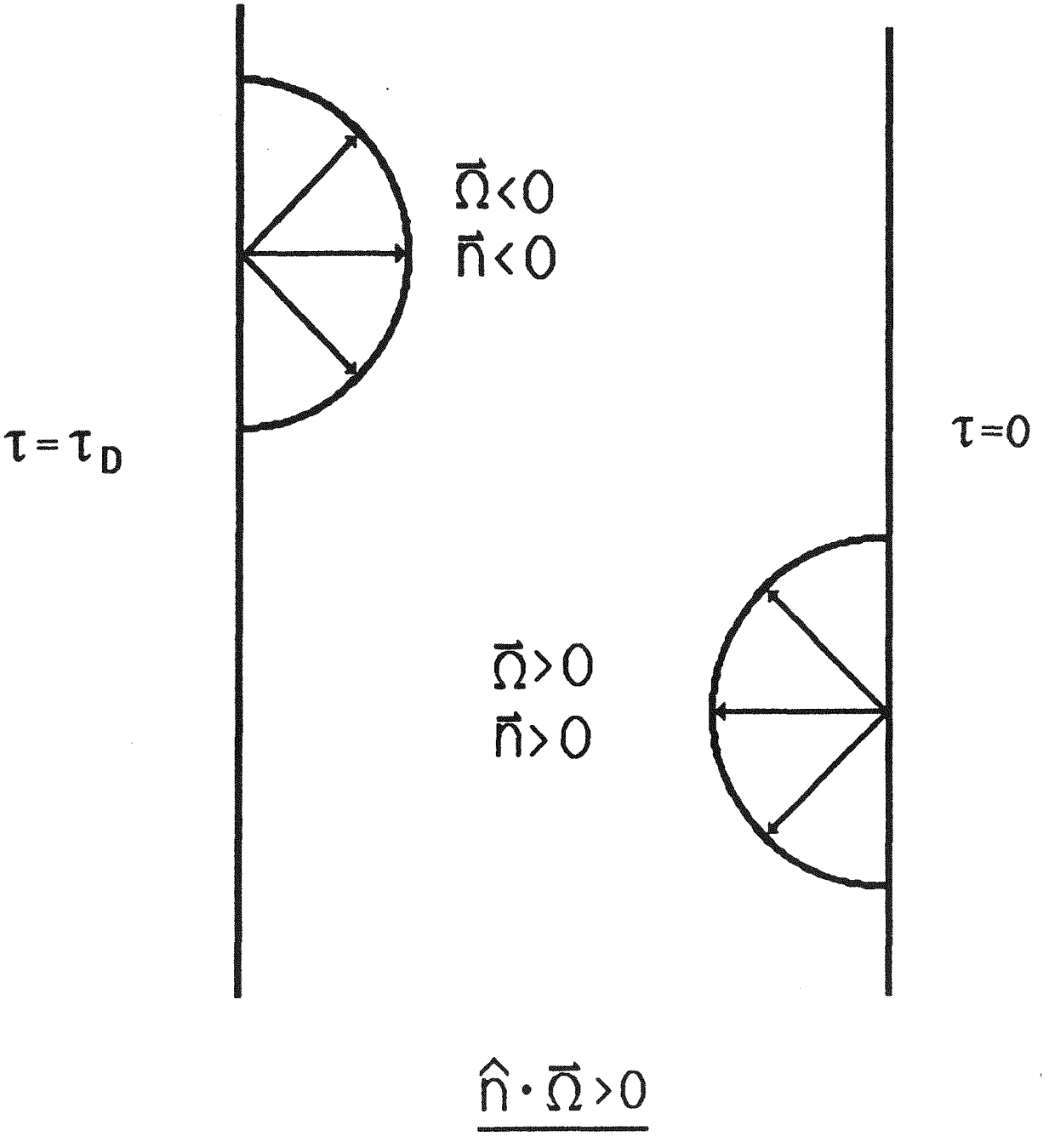

Figure 4.2: Directions of Propagation for Each Boundary

Notice that the integral in the above expression ranges over values of the inner product that are less than zero. This term represents the reflected component of the incoming radiant intensity. The first term adds the emitted power of the wall due to it's temperature. For a black wall, the expression simplifies to the expected result

$$I(x, \Omega|_{\mathbf{n}\cdot\Omega>0}) = I_b(T) \tag{4.12}$$

4.2.4 Discrete Ordinates Solutions

To obtain the solution to the main equation of transfer, Eq. 4.1, the intensity field is broken down into a discrete set of constant values representing the intensities in given directions or ordinates. The resulting one-dimensional expression for an absorbing-emitting medium is

$$\mu_m \frac{\partial I_m}{\partial \tau} + I_m = I_b(\tau) \quad m = 1, 2, ..., N \tag{4.13}$$

The solution of Eq. 4.13 will yield the set of intensities that result from the given boundary and internal generation conditions over the set of directions defined by μ_i, $i = 1, 2, ..., N$ where N is the number of directions involved.

Writing the general boundary condition, Eq. 4.11, in discrete ordinates form for each of the two surfaces, $\tau = 0$ and $\tau = \tau_D$, yields one boundary expression for each boundary that applies only over directions for which the product $\mathbf{n} \cdot \Omega$ is positive (as was previously mentioned). The application of the discrete ordinates formulation to the EOT allows the integral in the general boundary expression (Eq. 4.11) to be expressed in terms of a numerical quadrature technique in which the weights are simply the ordinate values used in the EOT. The expression for the $\tau = 0$ boundary is

$$I_m(\tau = 0) = \epsilon_{w1} I_{b,w1}(T_{w1}) + \frac{(1 - \epsilon_{w1})}{\pi} \sum_{\substack{n \\ \mu_n < 0}} w_n |\mu_n| I_n \tag{4.14a}$$

where the summation extends only over the incoming directions ($\mu_n < 0$). Eq. 4.14a will calculate the boundary intensity for the outgoing directions ($\mu_m > 0$) as a function of the temperature of the boundary ($I_{b,w1}(T_{w1})$) and the component of intensity that is reflected from the surface ($1 - \epsilon_{w1}$). The expression for the boundary at $\tau = \tau_D$ is

$$I_m(\tau = \tau_D) = \epsilon_{w2} I_{b,w2}(T_{w2}) + \frac{(1 - \epsilon_{w2})}{\pi} \sum_{\substack{n \\ \mu_n > 0}} w_n |\mu_n| I_n \qquad (4.14b)$$

where the summation extends only over the directions $\mu_n > 0$ and the intensity values calculated from Eq. 4.14b will be for the directions $\mu_m < 0$ only.

Since, for the cases of this Chapter, the resulting energy equation for either radiative equilibrium (Eq. 4.6) or uniform internal generation (Eq. 4.9) is not a differential equation, the solution to the set of governing equations only requires an approximation for the EOT, although the solution will still be iterative due to the implicit nature of the temperature dependence.

The approximation of the derivative in the EOT requires the imposition of a nodal grid over the domain. A standard grid is used allowing for different Δx and Δy values (for multi-dimensional problems). A simple first order finite backward difference is applied to the discrete ordinates derivative term. The resulting expression for the intensity value at interior node i along one of the ordinate directions, m, is

$$I_m^i = \left[\frac{\mu_m}{\Delta\tau} + 1\right]^{-1} \left(\frac{\mu_m}{\Delta\tau} I_m^{i-1} + I_b^i\right) \qquad (4.15)$$

The finite difference form of the relevant boundary conditions for the plane layer problem are written for the first node and for the N^{th} node using Eqs. 4.14a and 4.14b. The two expressions are

$$I_m^1 = \epsilon_{w1} I_{b,w1}(T_{w1}) + \frac{(1 - \epsilon_{w1})}{\pi} \sum_{\substack{n \\ \mu_n < 0}} w_n |\mu_n| I_n^1 \qquad (4.16a)$$

and

$$I_m^N = \epsilon_{w2} I_{b,w2}(T_{w2}) + \frac{(1-\epsilon_{w2})}{\pi} \sum_{\substack{n \\ \mu_n > 0}} w_n |\mu_n| I_n^N \qquad (4.16b)$$

Along with the intensity field, the temperature field is also discretized over the domain. The expressions that are used to calculate the temperature distribution in the medium are (from Eqs. 4.6 and 4.9)

$$I_b^i = \frac{\sigma T^{i^4}}{\pi} \qquad (4.17)$$

for the case of radiative equilibrium, and

$$\sigma T^{i^4} - \frac{1}{4} \sum_n w_n I_n^i = \frac{q'''}{4\alpha} \qquad (4.18)$$

for the internal generation case.

The equation system defined by Eqs. 4.15, 4.16 and either 4.17 (radiative equilibrium) or 4.18 (uniform internal generation) defines the 1-D problem to be solved. Since the system is implicit in temperature, an iterative solution algorithm is indicated. The solution is obtained by first assuming a temperature distribution in the medium. The EOT and it's boundary conditions (Eqs. 4.15 and 4.16) are then solved to determine the resulting intensity field based on these assumed temperatures. This intensity field is then numerically integrated to calculate the mean intensity (Eq. 4.7) and the result is used in either Eq. 4.17 or 4.18 to update the temperature distribution. The process is repeated until reasonable convergence is observed.

4.3 Results for the Radiative Equilibrium Case

Results for the solution of the governing equation system for the case of radiative equilibrium are presented in this Section. The problem was solved with

both black and diffuse gray walls as the boundaries. The results are compared to the work of Heaslet and Warming[70], which is considered a benchmark effort in the study of radiative transfer in participating media. The Heaslet and Warming study obtained a solution for an absorbing-emitting plane layer by solving two independent integral equations for the temperature and the flux distributions through the use of tabulated functions taken from Chandrasekhar[20] and Ambarzumian[44]. The solutions are considered to be highly accurate especially in predicting the emissive power distributions near the walls and, as such, are generally used as an "exact" solution for the non-scattering problem.

Figure 4.3 is a plot of the non-dimensional emissive power distribution as a function of optical depth for the plane layer (no internal generation) with black walls for various optical thicknesses. The plot compares the discrete ordinates approximations with the results of the Heaslet and Warming study. The walls are at temperatures T_1 and T_2 respectively. The non-dimensional emissive power is defined by

$$\hat{e}(\tau) = \frac{e(\tau) - e_{b,w1}}{e_{b,w2} - e_{b,w1}} = \frac{T^4(\tau) - T^4(0)}{T^4(\tau_D) - T^4(0)} \tag{4.19}$$

Since the curve is symmetrical, results are only shown from $\tau = 0$ to $\tau = \frac{\tau_D}{2}$.

Results are presented for optical thicknesses of 0.1, 1.0, and 10.0 for the 4-flux (S_2) and the 12-flux (S_4) approximations. The 24-flux results are not presented because the curve is virtually indistinguishable from the 12-flux model. The "exact" data are presented as points in the Figure. Although both the S_2 and the S_4 appear to provide reasonable predictions of the emissive power, the 12-flux model seems to indicate more accurate results near the wall in terms of both the emissive power values and their slopes. However, owing to the almost linear nature of the data near the wall, a realistic assessment of the ability of the model to predict these slopes is not possible.

Fortunately, for the gray wall case, the non-linearity of the emissive power distributions near the wall are much more pronounced. Figures 4.4 and 4.5

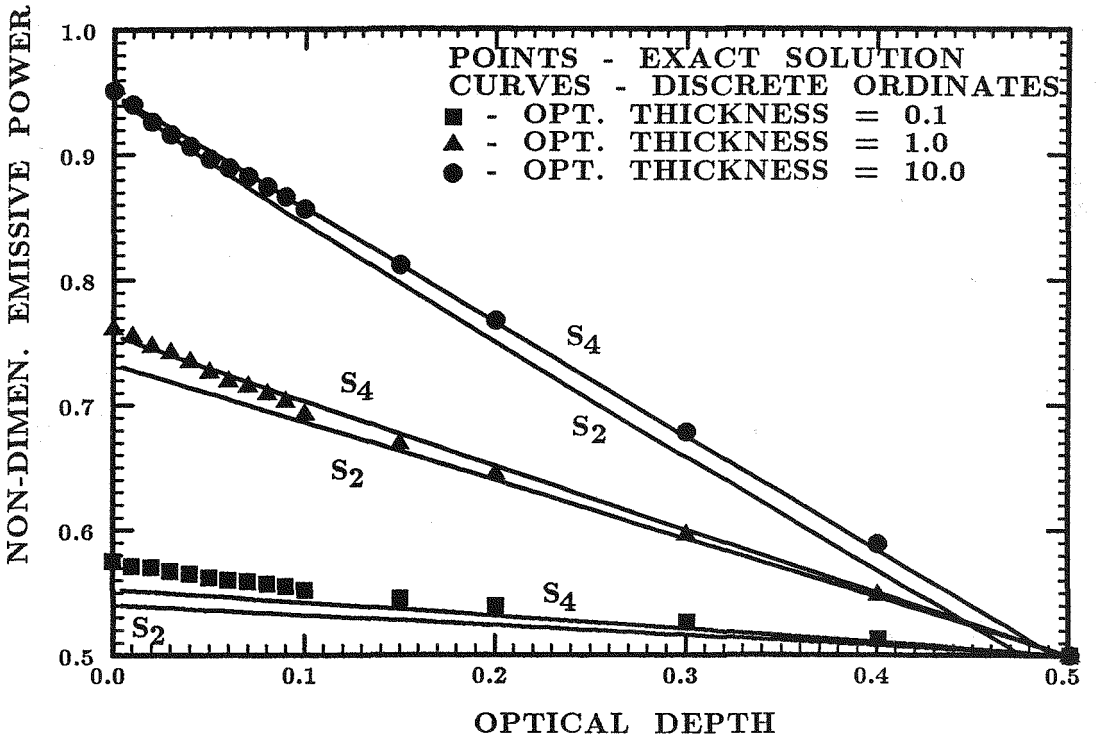

Figure 4.3: Non-Dimensional Emissive Power vs. Optical Depth (Black Walls, $T_{w1} = 1, T_{w2} = 0$)

present the solutions of the problem for several values of the total, hemispherical emissivity of the second wall. The curves present the emissive powers at $\hat{x} = 1$ (one of the walls) as a function of the optical thickness of the layer. For both plots, the emissivity of the first wall is held at $\epsilon_{w1} = 0.8$. The plot of Figure 4.4 shows that, for moderate values of ϵ_{w2} $(1.0, 0.5)$, while both models again provide reasonable predictions of the emissive power profiles, the 12-flux model is clearly more accurate for both the data and the apparent slope of the data.

It should be noted that, classically, approximate methods for solving the equation of transfer have tended to become significantly less accurate as the emissivities are reduced. As is clear from the curves, the magnitudes of the differences between the "exact" solutions and the model have increased from their values for the black wall case. This situation becomes dramatically evident

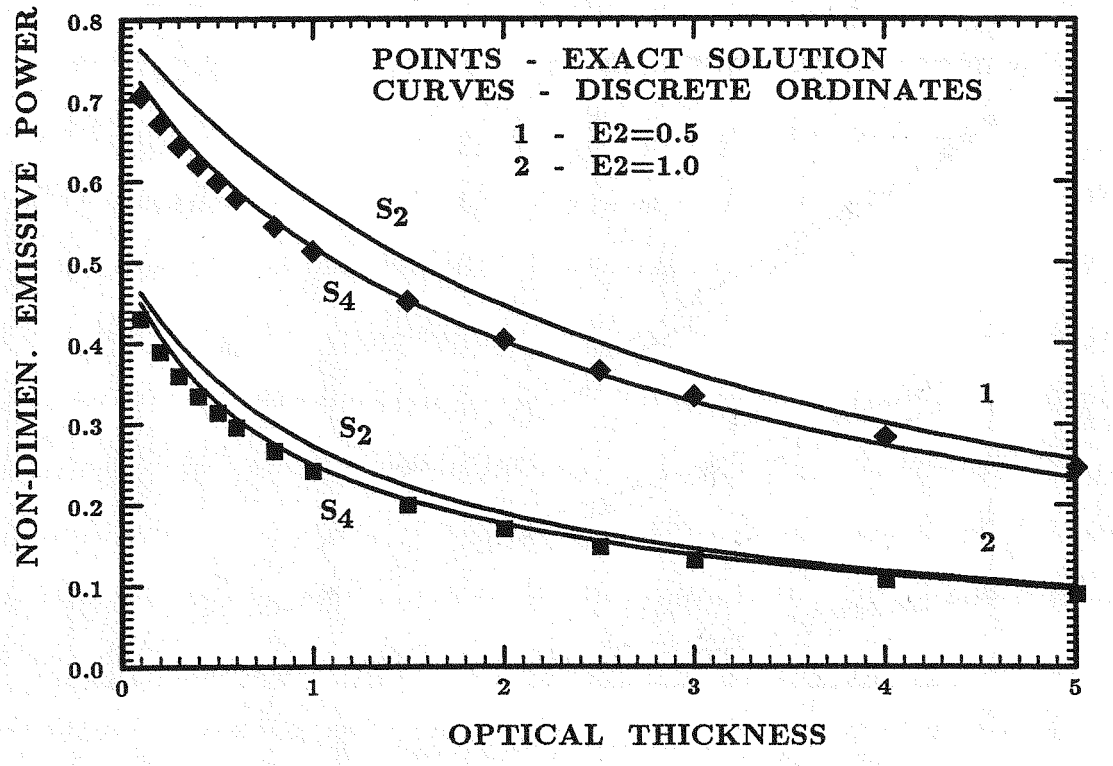

Figure 4.4: Non-Dimensional Emissive Power vs. Optical Thickness (Gray Walls, $\epsilon_{w1} = 0.8$, $T_{w1} = 1$, $T_{w2} = 0$)

as the emissivities are reduced still further. Figure 4.5 shows the results for ϵ_{w2} values of 0.3 and 0.1. In this Figure, the 4-flux model appears to provide a very poor prediction of the emissive power profiles and, in the curve for $\epsilon_{w2} = 0.1$, it seems to break down completely, predicting a positive slope where the data is negative. However, in both curves, the 12-flux model predicts the data and the slope of the data satisfactorily over all optical thicknesses.

Figures 4.6 and 4.7 are curves of the heat flux at the wall for the gray wall cases as a function of the optical thickness. Heat flux calculations, generally considered to be more important than emissive power or mean radiant intensity calculations, are also known to be more difficult to obtain accurately with radiation models.

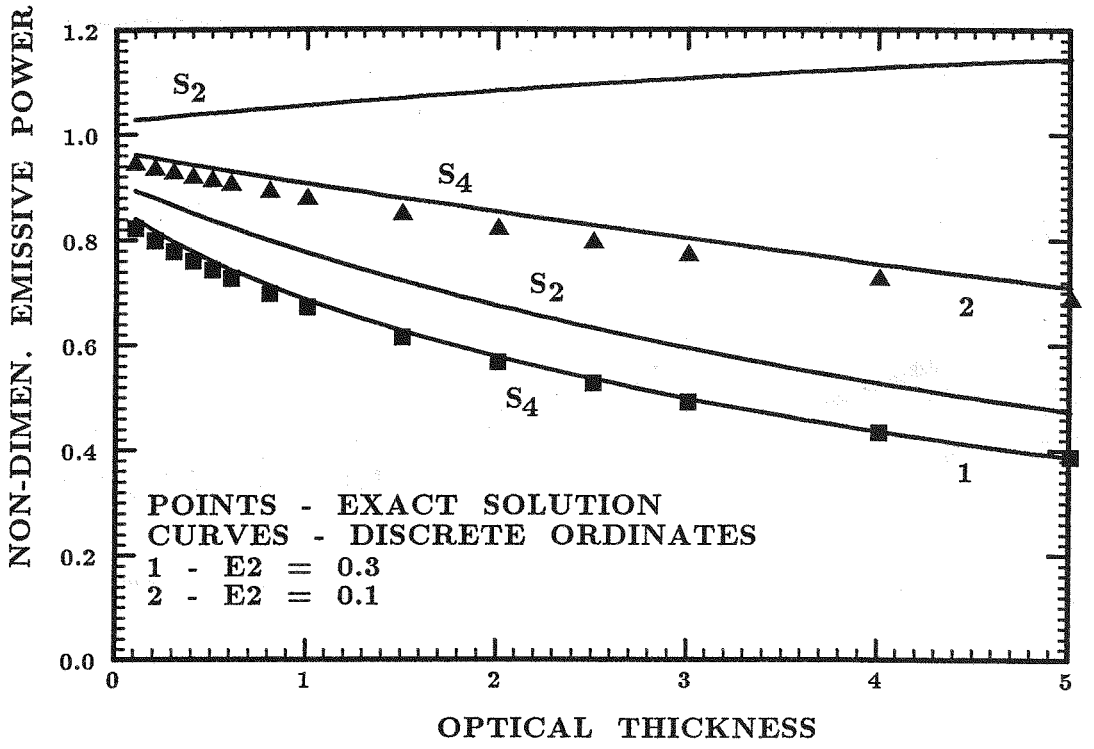

Figure 4.5: Non-Dimensional Emissive Power vs. Optical Thickness (Gray Walls, $\epsilon_{w1} = 0.8$, $T_{w1} = 1$, $T_{w2} = 0$)

The vertical axis in the Figures is a non-dimensional heat flux defined by

$$\hat{q} = \frac{q_{w1}}{\sigma T_{w1}^4 - \sigma T_{w2}^4} \tag{4.20}$$

and the emissivity of the first wall for the Figures is unity.

Both Figures indicate similar trends as compared to the emissive power results. For higher back wall emissivity, greater model accuracy is exhibited with the differences increasing as ϵ_{w2} decreases. Also, it is again apparent that the S_2 approximation, while providing reasonable results for solutions near the black wall case, predicts the radiative transport distributions poorly for the more general gray wall case. However, it is also clear that the S_4 approximation predicts the flux distribution with good accuracy ($\pm 5\%$) for moderate to high emissivities with relatively insignificant deviations down to $\epsilon_{w2} = 0.3$.

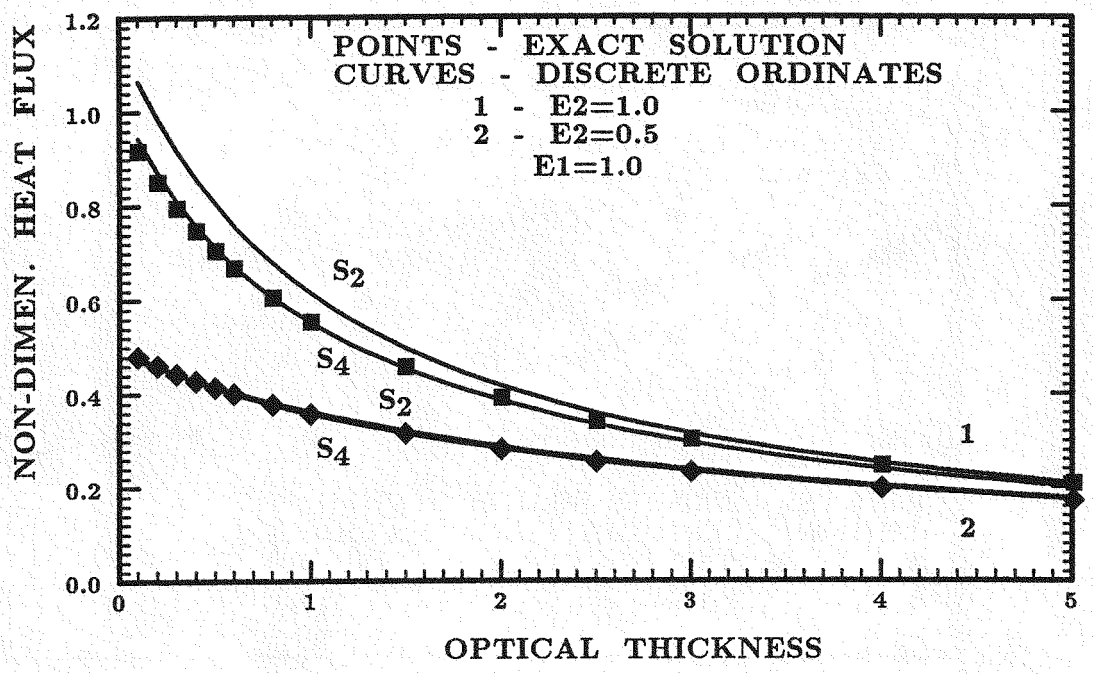

Figure 4.6: Non-Dimensional Heat Flux vs. Optical Thickness (Gray Walls, $\epsilon_{w1} = 1$, $T_{w1} = 1$, $T_{w2} = 0$)

The maximum error for the 24-flux approximation, 25%, was seen for highly reflective surfaces when the rear wall emissivity was 0.1.

Another indicator of the effectiveness of any participating medium radiative transfer solution is it's ability to accurately estimate the magnitude of the "temperature slip" at the wall. The "slip," which is a mathematical discontinuity in the temperature curve at the medium-wall interface, comes about as the result of assuming negligible conduction in the medium. In reality, there is no "slip" because the thermal effects of the wall will be propagated into the medium in the immediate vicinity of the wall through conduction as well as radiation. However, all radiation solutions that assume negligible conduction must exhibit this temperature slip to be considered valid. Heaslet and Warming developed an expression for estimating this slip and the discrete ordinates

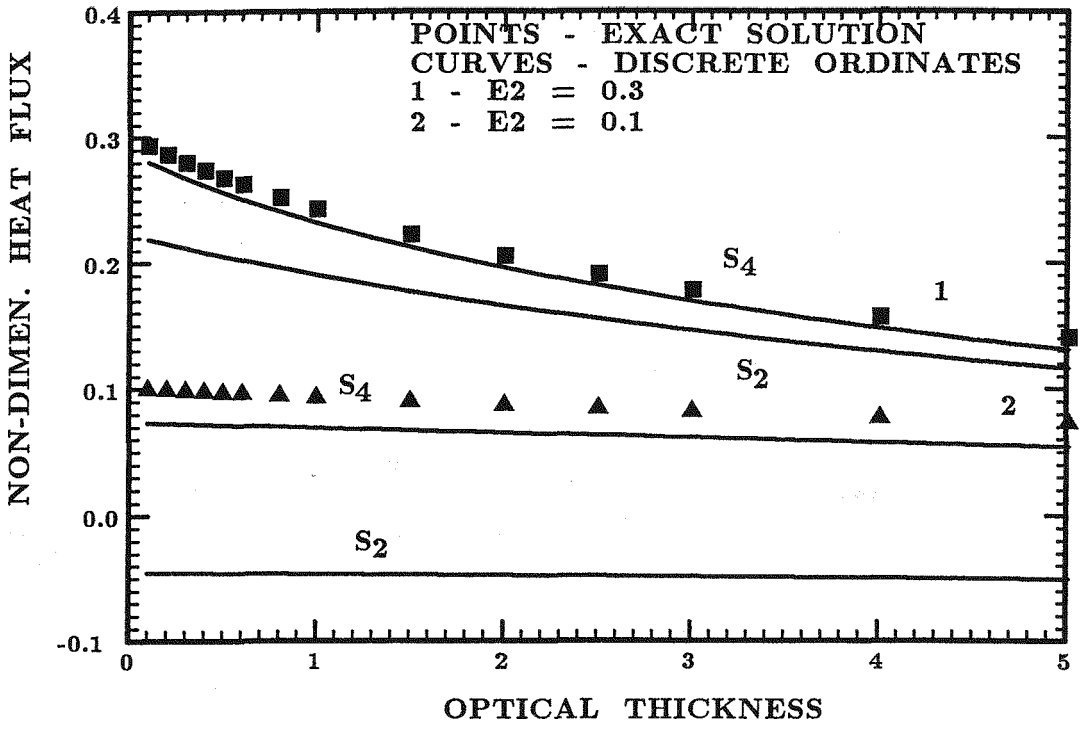

Figure 4.7: Non-Dimensional Heat Flux vs. Optical Thickness (Gray Walls, $\epsilon_{w1} = 1$, $T_{w1} = 1$, $T_{w2} = 0$)

model is compared to these results in Figure 4.8. The Figure is a plot of the non-dimensional temperature distribution in the medium at the interface defined by

$$\hat{T} = \frac{\sigma T^4(\tau_D) - \sigma T_{w2}^4}{\sigma T_{w1}^4 - \sigma T_{w2}^4} \tag{4.21}$$

versus optical thickness. As expected, when the optical thickness increases and the medium absorbs more energy per unit volume, the magnitude of the temperature slip decreases.

In Figure 4.8, the 4 flux and the 24 flux approximations are used (the improvement from the S_4 to the S_6 ordinate sets is negligible). Once again, it is apparent from the Figure that the 4 flux approximation, while providing a reasonable estimate of the slip, has significantly less accuracy than do the

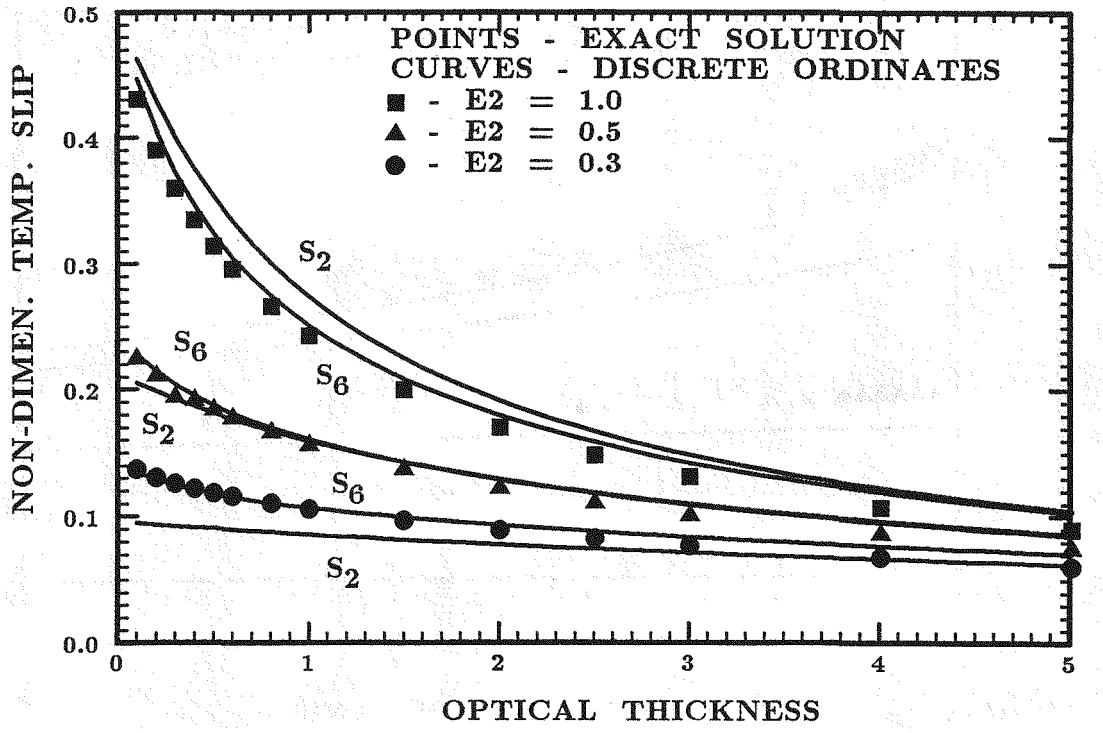

Figure 4.8: Non-Dimensional Temperature Slip at the Wall vs. Optical Thickness (Black and Gray Cases, $T_{w1} = 1$, $T_{w2} = 0$)

higher order models and, even though the computational time requirements are slightly more restictive for the higher order models, the increase in accuracy warrants their use.

4.4 Results for the Uniform Internal Generation Case

In this Section, results for the one-dimensional plane layer with uniform internal energy generation and cold walls of equal temperature are presented. Once again, the work of Heaslet and Warming is used as the standard. Results for the emissive power, the heat flux and the magnitude of the temperature slip are presented for both the black and gray wall cases for several optical thicknesses.

Figure 4.9 presents the non-dimensional emissive power in the plane layer

for the case of $T_{w1} = T_{w2} = 0$ and $q''' = 1.0$ as a function of the optical depth of the medium. The emissive power is now defined in terms of the generation term as

$$\hat{e} = \frac{\sigma T^4(\tau) - \sigma T_{w2}^4}{\frac{q'''}{\tau_D}(1+\alpha)} \tag{4.22}$$

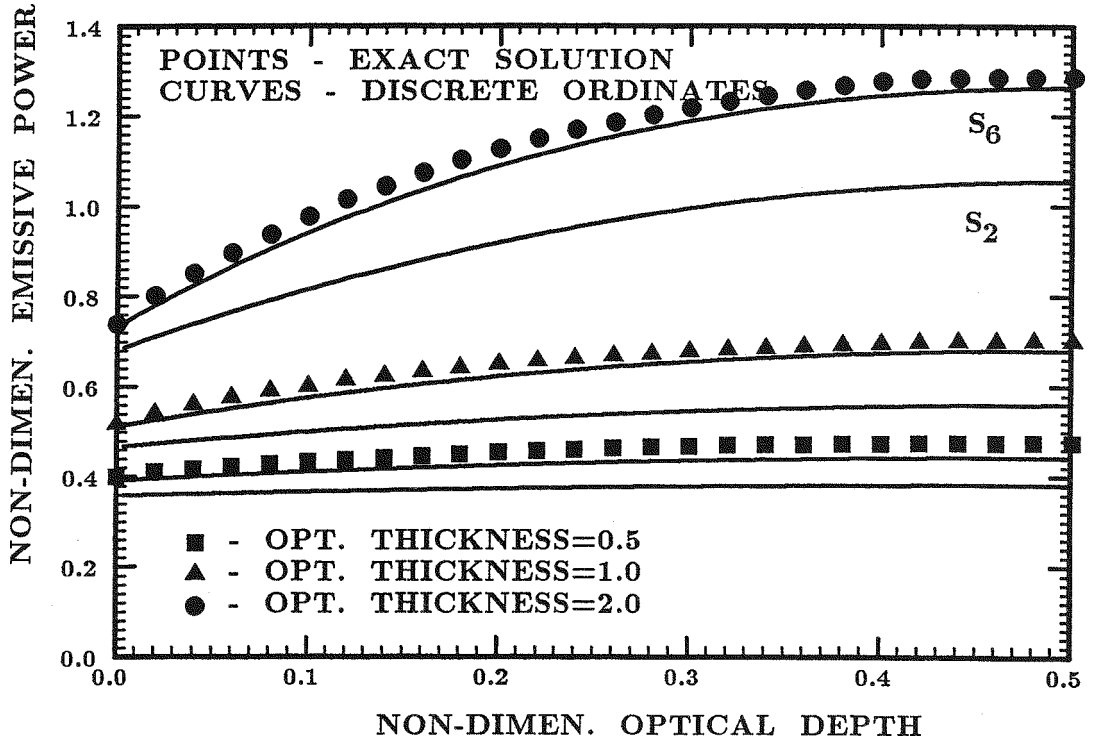

Figure 4.9: Non-Dimensional Emissive Power vs. Optical Depth (Black Walls, $q''' = 1$, $T_{w1} = T_{w2} = 0$)

In the Figure, curves for various optical thicknesses from 0.5 to 2 are presented. The relative accuracies of the discrete ordinates models are similar to the case of radiative equilibrium although, for the case of internal generation, the 4-flux model becomes **less** accurate as the optical thickness increases.

The dimensionless heat flux, defined as

$$\hat{q} = \frac{q_{w1}}{\frac{q'''}{\tau_D}}, \tag{4.23}$$

is plotted as a function of optical thickness for various values of the emissivity of the second wall in Figure 4.10. The emissivity of the first wall is set to 0.8 for all curves. Notice that, as observed previously, the accuracy of the 4 flux model decreases with the back wall emissivity. The higher order model seems to again provide a reasonable estimation of the heat flux for the generation problem.

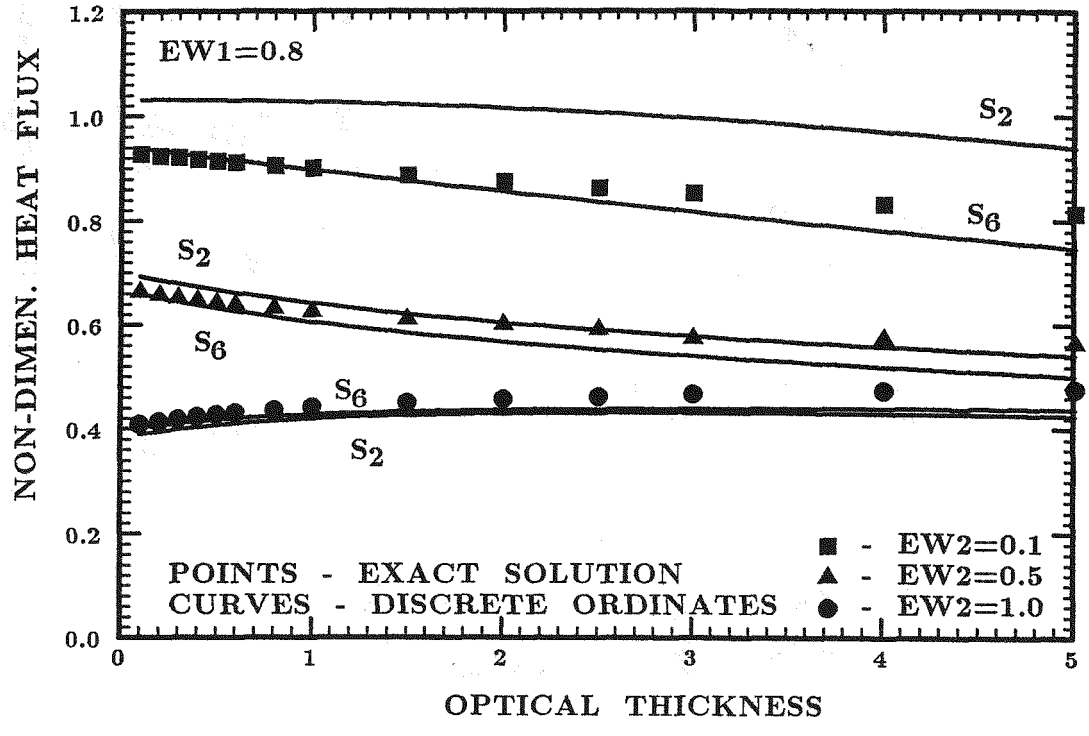

Figure 4.10: Non-Dimensional Heat Flux vs. Optical Thickness (Gray Walls, $\epsilon_{w1} = 0.8$, $q''' = 1$, $T_{w1} = T_{w2} = 0$)

Lastly, the non-dimensional temperature slip for the uniform internal generation case is plotted in Figure 4.11 as a function of optical thickness for various

rear wall emissivities. The slip is defined as

$$\hat{T} = \frac{\sigma T^4(\tau_D) - \sigma T_{w2}^4}{\frac{q'''}{\tau_D}} \tag{4.24}$$

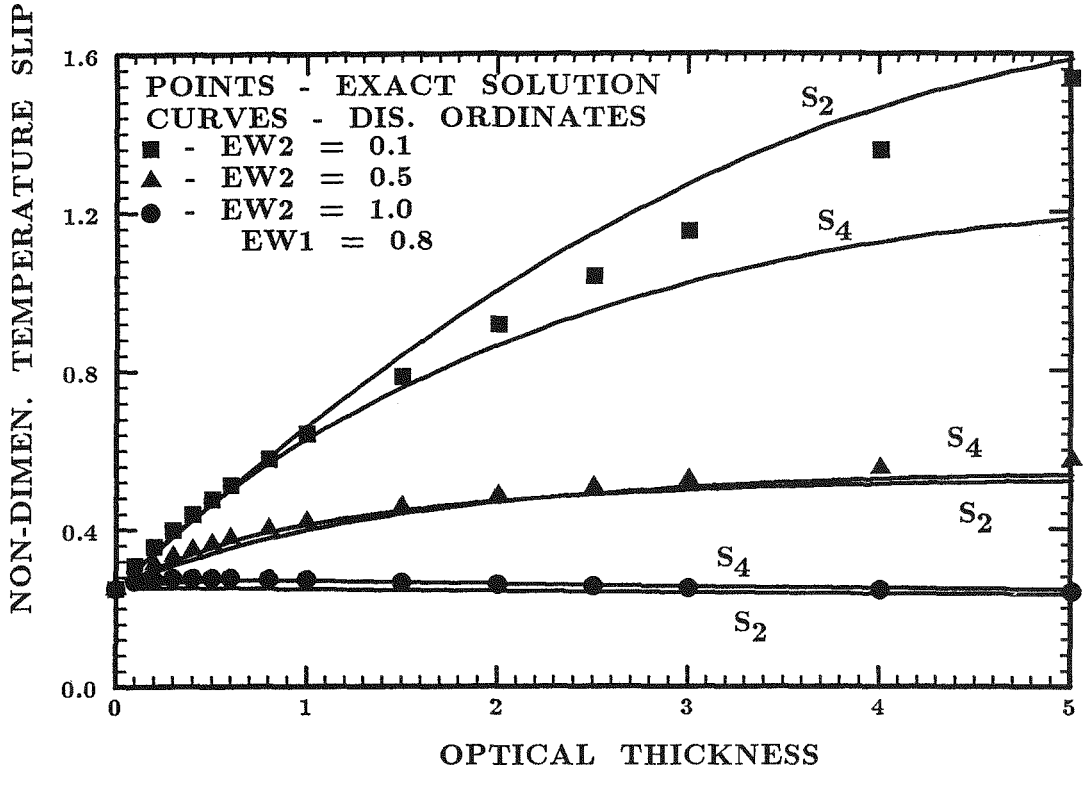

Figure 4.11: Non-Dimensional Temperature Slip vs. Optical Thickness (Black and Gray Cases, $\epsilon_{w1} = 1$, $q''' = 1$, $T_{w1} = T_{w2} = 0$)

In the Figure, the front wall emissivity is held at unity and the results are similar to the previous case (radiative equilibrium).

4.5 Summary

Results of a discrete-ordinates formulation of the one-dimensional equation of radiative transfer were compared to the work of Heaslet and Warming

which is generally considered an "exact" solution to the non-scattering radiation problem.

Solutions of the pertinent quantities (i.e., emissive power, heat flux and temperature slip) for both radiative equilibrium and uniform internal energy generation are obtained for a range of optical thicknesses and wall emissivities. In all cases, an S_4 approximation was used and compared to the exact solution as well as a higher order ordinate set.

For all cases considered, the higher order discrete ordinates approximations were found to be reasonable models of the problem providing predictions of the quantities within 5% of the exact solutions (with the exception of the very low wall emissivity problem). The 4 flux approximation was observed to be a poorer estimator than the higher order models and became less accurate as the reflective component of the radiative field increased (i.e., lower wall emissivities). It eventually broke down completely for a rear wall emissivity of 0.1. The large errors for the 4-flux model can be attributable to the ray effects that were described in Carlson and Lathrop[59].

Overall, it is apparent that the discrete ordinates approximation provides a satisfactory estimation of the intensity field if a 12-flux (S_4) or higher discrete ordinate set is used.

Chapter 5

Two-Dimensional Model Verification

5.1 Introduction

Extension of the basic discrete ordinates algorithm to two spatial dimensions and to include in-scattering is performed and the results are presented here. The geometry is a square enclosure with four black walls. The problem is set up such that one of the walls of the enclosure is hot ($T_h \neq 0$) and the others are maintained at $T_c = 0$.

The two-dimensional formulation of the EOT is presented as well as it's discrete ordinates equivalent. Due to the complexity of obtaining an accurate closed form solution for the multi-dimensional problem and since the emphasis of this Chapter is only to verify that the two-dimensional algorithm is correctly approximating the pertinent quantities, the solutions here are only presented for the black walled enclosure under radiative equilibrium conditions. Plots of surface heat flux in the vicinity of the hot wall are presented for the non-scattering case ($\sigma_s = 0$) and, for the non-absorbing case ($\alpha = 0$). The results are presented as plots of the mean radiant intensity at different locations in the medium.

Lastly, some algorithmic improvements were implemented into the solutions and the results of these activities are presented in the last Section of the Chapter.

5.2 Formulation of the Two-Dimensional Model

For this problem, four black, diffuse walls of equal length enclose the radiatively participating medium. Radiative transport is the only energy process that is considered. As before, the medium is assumed to be gray with uniform radiative properties and a refractive index of unity. A sketch of the geometry is provided in Figure 5.1.

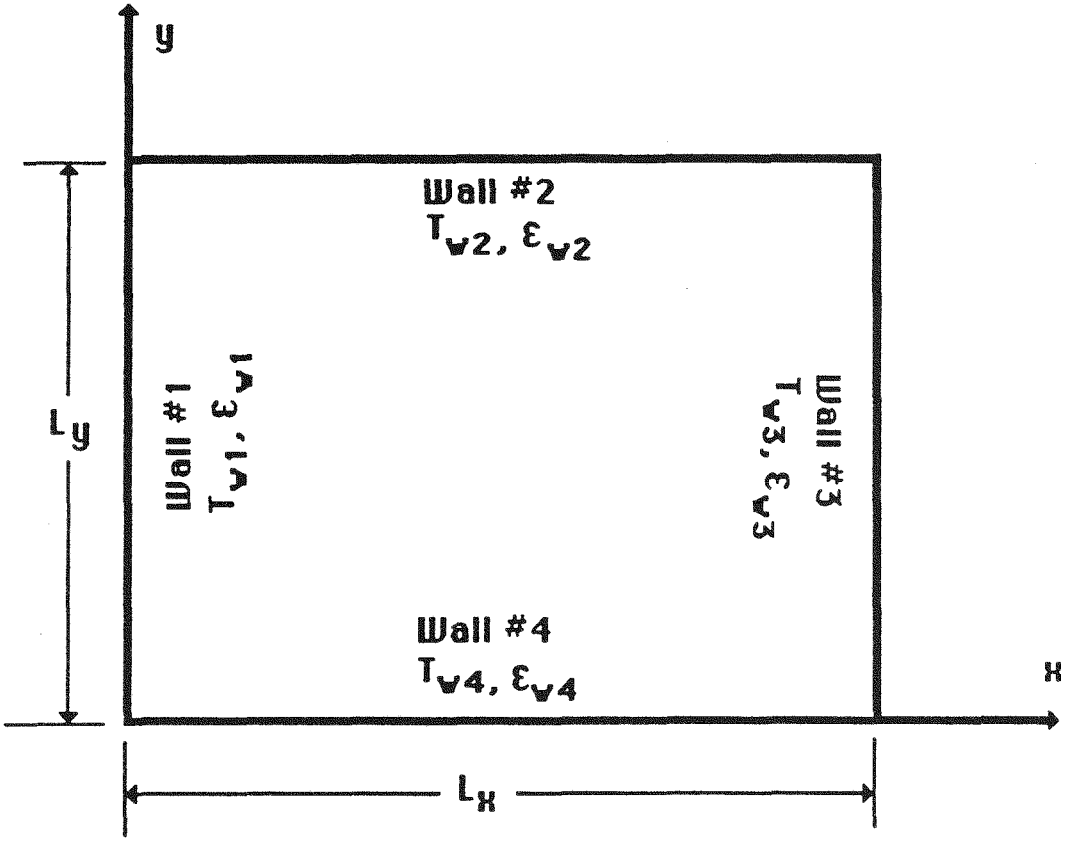

Figure 5.1: Square Enclosure Geometry

5.2.1 Equation of Radiative Transfer

The EOT for a diffuse gray medium can be written for the non-scattering case in cartesian coordinates as

$$\mu\frac{\partial I}{\partial x}(x,y,\Omega)+\xi\frac{\partial I}{\partial y}(x,y,\Omega)=-\alpha I(x,y,\Omega)+\alpha I_b(x,y) \tag{5.1}$$

and for the case of $\alpha = 0$, as

$$\mu\frac{\partial I}{\partial x}(x,y,\Omega)+\xi\frac{\partial I}{\partial y}(x,y,\Omega)=-\sigma_s I(x,y,\Omega)+\frac{\sigma_s}{4\pi}\int_{\Omega'=4\pi} I(x,y,\Omega')\Phi(\Omega',\Omega)d\Omega' \tag{5.2}$$

where σ_s is the scattering coefficient which has the same units as the absorption coefficient, α, namely, $1/L$.

The two equations above relate the spatial variation of the radiant intensity (LHS) to the attenuation of the intensity due to absorption in the medium and the increase in intensity due to emission by the medium (RHS) in the non-scattering case. For the non-absorbing case, the RHS of the equation of transfer represents the attenuation of the intensity due to out-scattering (i.e., energy that the medium is scattering out of the direction Ω) and the increase due to in-scattering (i.e., energy that is initially propagating in other directions but is scattered into the Ω direction at the point x, y). Due to the multi-dimensional nature of the problem, it is now necessary to introduce a second direction cosine to adequately define the direction vector. For this study, the direction cosine defined by μ lies along the x-axis and ξ lies along the y-axis. Consequently, the direction vector must be written in terms of the direction cosines as

$$\Omega = \Omega(\mu,\eta) \tag{5.3}$$

Assuming that the intensity is constant over small solid angles defined by the ordinates μ_m, ξ_m, $m = 1, 2, ..., N$ where N is the number of incremental

solid angles included in the sphere, the general two-dimensional EOT (Eqs. 5.1 and 5.2) can be written in discrete ordinates formulation as

$$\mu_m \frac{\partial I_m}{\partial x}(x,y) + \xi_m \frac{\partial I_m}{\partial y}(x,y) = -\alpha I_m(x,y) + \alpha I_b(x,y), \quad m = 1,2,...,N \tag{5.4}$$

for the non-scattering case and

$$\mu_m \frac{\partial I_m}{\partial x}(x,y) + \xi_m \frac{\partial I_m}{\partial y}(x,y) = -\sigma_s I_m(x,y) + \frac{\sigma_s}{4\pi} \sum_{m'} w_{m'} I_{m'} \Phi_{m' \to m}, \quad m = 1,2,...,N \tag{5.5}$$

for the non-absorbing case. In Eq. 5.5, $w_{m'}$ is the quadrature weighting factor. Note that, because of the discrete ordinates assumption, the in-scattering integral has been replaced with an appropriate form of numerical quadrature. Normally, Gaussian quadrature is used, requiring the ordinates to be the Gaussian quadrature points. While this simplifies the solution of the EOT, it still requires that an iterative procedure be used. The EOT may now be solved with ordinary PDE techniques applied iteratively.

In the case of the two dimensional analysis, the other solutions that are used for comparative purposes (i.e., the exact solution for the non-scattering case and the numerical zonal solution for the non-absorbing case) are presented only in terms of the radiant heat flux and the mean radiant intensity. Consequently, since few temperature results are available in the literature, it is not necessary to formulate and solve an energy conservation expression.

5.2.2 Boundary Conditions

For black walls, the general form of the boundary condition for a walled enclosure surrounding a diffuse gray enclosure (Eq. 3.44) reduces to the emission term which is directionally independent. The expression is

$$I(x,y,\mathbf{\Omega}|\mathbf{n}\cdot\mathbf{\Omega} > 0) = I_b(T_w) \tag{5.6}$$

where T_w is the temperature of the black wall.

In discrete ordinates formulation, Eq. 5.6 is simply written for each of the ordinate directions at each of the bounding surfaces according to the notation of Figure 5.1 as

$$I_m(x,0) = I_b(T_{w1}) \quad m = 1,2,...,N \tag{5.7a}$$

$$I_m(x,L_y) = I_b(T_{w2}) \quad m = 1,2,...,N \tag{5.7b}$$

$$I_m(0,y) = I_b(T_{w3}) \quad m = 1,2,...,N \tag{5.7c}$$

$$I_m(L_x,y) = I_b(T_{w4}) \quad m = 1,2,...,N \tag{5.7d}$$

For the curves in this Chapter, the emissive power of walls 2, 3, and 4 are maintained at zero while the emissive power of wall 1 is set to unity, so

$$I_b(T_{w1}) = \frac{e_b(x,0)}{\pi} = \frac{1}{\pi} \tag{5.8a}$$

and

$$I_b(T_{w2}) = I_b(T_{w3}) = I_b(T_{w4}) = 0 \tag{5.8b}$$

5.2.3 Discrete Ordinates Solutions

To solve the equation system defined by Eqs. 5.4 and 5.8 for the non-scattering case and by Eqs. 5.5 and 5.8 for the non-absorbing case, the enclosure was discretized and a first order finite difference technique was applied to the equations. Denoting the x-direction nodes with i and the y-direction nodes with j, the expression for the intensity at the interior nodes of the non-scattering medium becomes

$$I_m^{i,j} = \frac{1}{\eta_m}\left[\frac{\mu_m}{\Delta x} I_m^{i-1,j} + \frac{\xi_m}{\Delta y} I_m^{i,j-1} + \alpha I_b^{i,j}\right] \quad m = 1,2,...,N \tag{5.9}$$

where

$$\eta_m = \frac{\mu_m}{\Delta x} + \frac{\xi_m}{\Delta y} + \alpha \tag{5.10}$$

For the non-absorbing case, the emission term is dropped and the in-scattering quadrature term is added, the expression is

$$I_m^{i,j} = \frac{1}{\gamma_m}\left[\frac{\mu_m}{\Delta x} I_m^{i-1,j} + \frac{\xi_m}{\Delta y} I_m^{i,j-1} + \frac{\sigma_s}{4\pi}\sum_{m'=1}^{N} w_{m'}\Phi_{m'\to m} I_{m'}^{i,j}\right] \quad m = 1,2,...,N \tag{5.11}$$

where

$$\gamma_m = \frac{\mu}{\Delta x} + \frac{\xi_m}{\Delta y} + \sigma_s \tag{5.12}$$

For the case of equal node spacing in both directions (i.e., $\Delta x = \Delta y$) and defining M to be the number of nodes in each direction, the boundary conditions for the black walled problem in finite difference form become

$$I_m^{i,1} = I_m^{i,M} = I_m^{M,j} = 0 \tag{5.13}$$

for the cold walls and

$$I_m^{1,j} = \frac{1}{\pi} \tag{5.14}$$

for the hot wall (which provides the excitation for the problem).

The solution of the non-scattering problem is straightforward. Since there is no implicit nature in the interior node expression (Eq. 5.9), the solution may start from any wall and proceed forward (i.e., no iteration is required). As was previously mentioned, the implicit nature of the problem if in-scattering is included will require an iterative solution method. For this case, the intensity field is set to zero initially (except at the $x, 0$ boundary) and the interior expression is repeatedly solved until the intensity distribution converges to a satisfactory value.

As was discussed in Chapter 3, the effects of any particular bounding surface are only propagated in certain directions. The direction of solution is defined by the sign of the ordinate corresponding to that direction. So, calculations for the intensity in all positive y-direction ordinates (positive ξ_m) will

be affected by the hot wall at $x, 0$. In this way, each bounding surface only influences the intensities in all outgoing directions from that surface (i.e., the dot product of the surface normal and the ordinate along that axis is positive). These directionally localized intensities are then combined to determine the pertinent global non-dimensionalized quantities, either the heat flux or the mean radiant intensity.

5.3 Results for the Non-Scattering Problem

Results for the non-scattering problem defined by Eqs. 5.9 and 5.10 are presented in this Section. The problem was solved for the black walled case and the results compared to a closed form solution developed by Shah[71]. In that study, the author developed and solved a spatial integral expression formulated in terms of modified Bessel functions to calculate the heat flux along the hot wall.

Figures 5.2, 5.3 and 5.4 are the results of these calculations (compared to the discrete ordinates model predictions) for three different optical thicknesses. The vertical axis in the plots is the non-dimensionlized heat flux at the hot wall defined as

$$\hat{q}_{w1} = \frac{q_{w1}}{e_{b_{w1}}} \tag{5.15}$$

Like the in-scattering integral, the heat flux along a given direction (which is the integral of the product of the intensity and the direction over solid angle) can be calculated using the appropriate numerical quadrature. The finite difference formulation for the heat flux in the y-direction from Eq. 5.15 above becomes

$$\hat{q}^{i,1}_{w1} = \frac{\sum_{m=1}^{N} w_m \xi_m I^{i,1}_m}{e_{b_{w1}}} \quad i = 1, 2, ..., M \tag{5.16}$$

The horizontal axis is the non-dimensional optical position defined as

$$\hat{x} = \frac{\alpha x}{\alpha L_x} = \frac{\alpha x}{\tau_D} \tag{5.17}$$

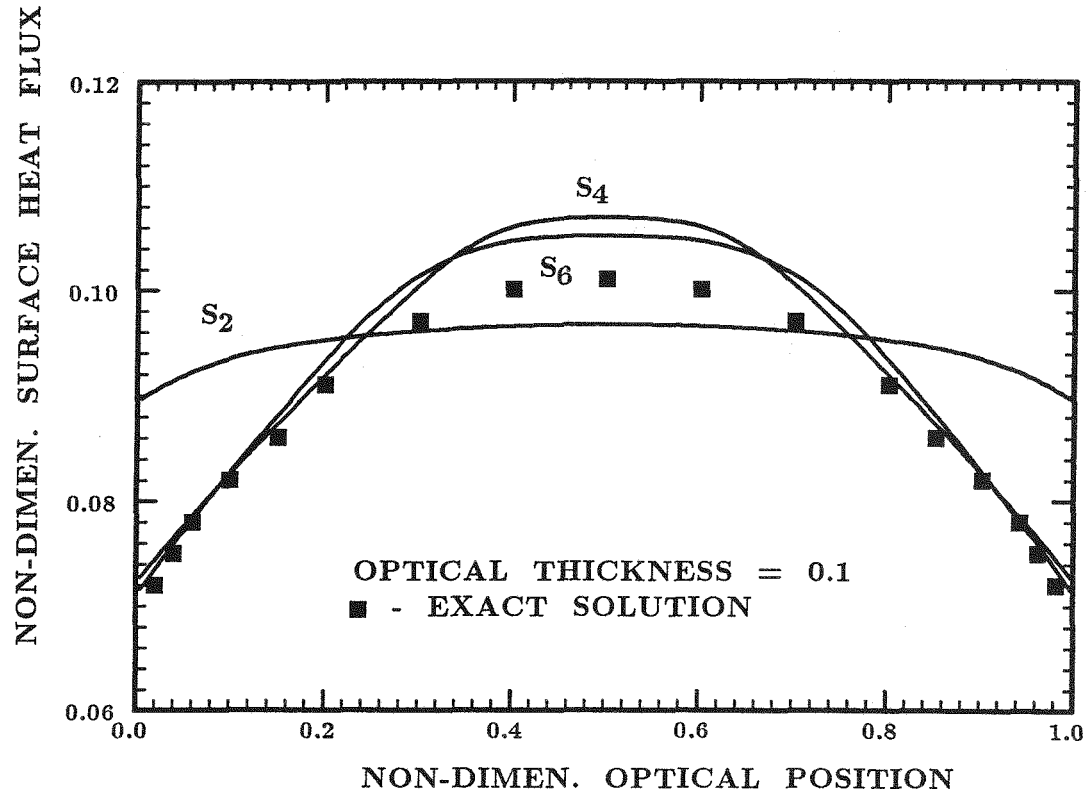

Figure 5.2: Non-Dimensional Surface Heat Flux vs. Optical Position for a Square Black Enclosure ($\tau_D = 0.1$, $T_{w1} = T_{w2} = T_{w3} = 0,\ T_{w4} = 1$)

where τ_D is the optical thickness.

Results are presented for optical thicknesses of 0.1, 1.0 and 10.0 for the 4-, 12- and 24-flux approximations (S_2, S_4, and S_6 respectively). The exact solution is presented as points in the Figures. In all three Figures, what was noticed in the one-dimensional solutions (Chapter 4) appears also to be true for the present case, i.e., the S_2 approximation is a relatively poor predictor of the surface heat fluxes for this problem. However, the higher order approximations appear to provide reasonable estimations of the flux. Maximum errors of 5.8% and 4.1% for the S_4 and S_6 models respectively occur at the low optical thicknesses and decrease as τ_D is increased. Once again, these deviations are attributed to the ray effects that are inherent in the discrete ordinates model.

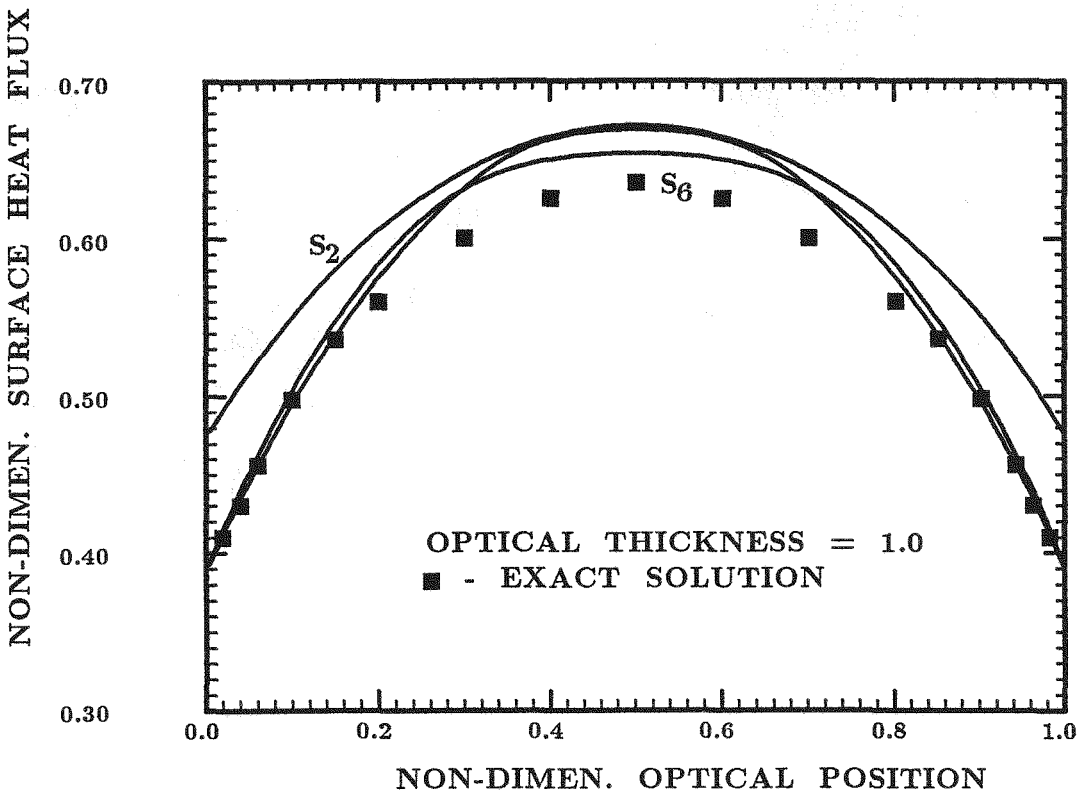

Figure 5.3: Non-Dimensional Surface Heat Flux vs. Optical Position for a Square Black Enclosure ($\tau_D = 1.0$, $T_{w1} = T_{w2} = T_{w3} = 0,\ T_{w4} = 1$)

In all three cases, the S_6 approximation provides a slightly more accurate prediction of the exact solution and, as is more evident in Figures 5.2 and 5.3, seems to more accurately match the shape of the curve (i.e., similar slopes along the entire $\hat{x}$ axis).

5.4 Results for the Non-Absorbing Problem

The solution for the non-absorbing problem is presented in Figures 5.5, 5.6 and 5.7. For these plots, the scattering was assumed isotropic (i.e., $\Phi(\Omega', \Omega) = 1$). Note that the horizontal axis in the Figures is now the optical position in the y-direction (not the x-direction as in the previous Figures). The curves show the non-dimensional mean radiant intensity (also known as the "zeroth

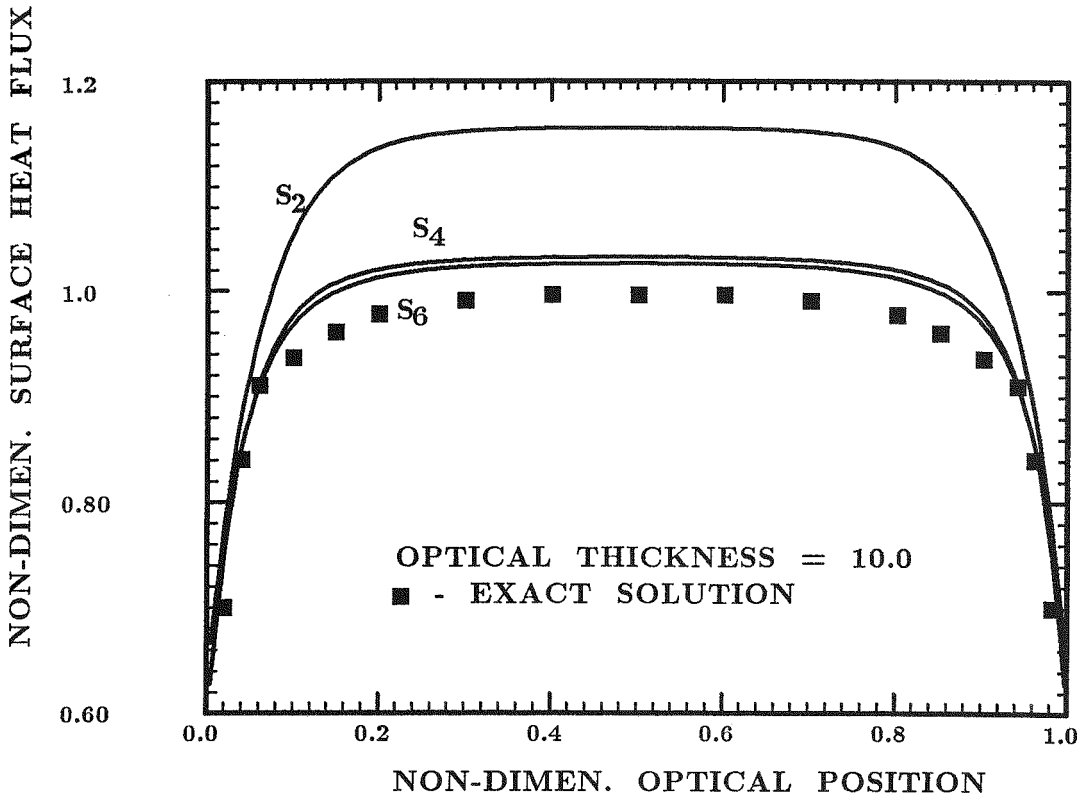

Figure 5.4: Non-Dimensional Surface Heat Flux vs. Optical Position for a Square Black Enclosure ($\tau_D = 10.$, $T_{w1} = T_{w2} = T_{w3} = 0,\ T_{w4} = 1$)

moment of intensity") defined by

$$\hat{G} = \frac{\int_{4\pi} I(x, 0, \Omega) d\Omega}{e_{b_{w1}}} \tag{5.18}$$

Replacing the integral with a quadrature technique and writing the results in finite difference form, we obtain

$$\hat{G} = \frac{\sum_{m=1}^{N} w_m I_m^{i',j}}{e_{b_{w1}}} \tag{5.19}$$

where

$$\frac{i'}{M} = 0.1,\ 0.3\ or\ 0.5 \tag{5.20}$$

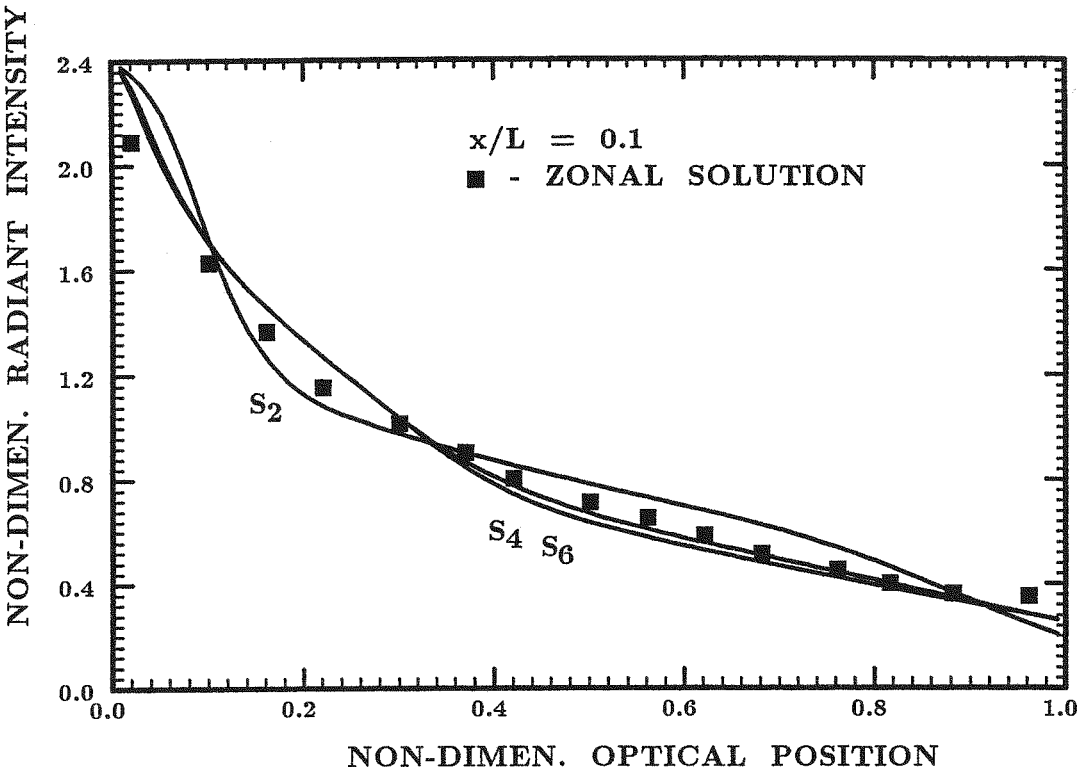

Figure 5.5: Non-Dimensional Mean Radiant Intensity vs. Optical Position for a Square Black Enclosure ($x/L_x = 0.1$)

The curves show the intensity from the hot wall at $x, 0$ to the cold wall at x, L_y at locations of 10% (Figure 5.5), 30% (Figure 5.6) and 50% (Figure 5.7) of the distance from the cold wall at $0, y$. Results are compared with a zonal model that is considered a standard solution to the scattering problem. The values were taken from another study (Fiveland[49]) that also performed these comparisons.

For most general approximations to the radiation transport equation, the types of problems that have the largest inherent errors associated with them are situations in which the scattering albedo (defined as the ratio of the scattering coefficient to the extinction coefficient) becomes large. For Figures 5.5, 5.6 and 5.7, the scattering albedo is unity (pure scattering) and, as the curves show, the errors in the model become more pronounced. For all three curves, the S_2

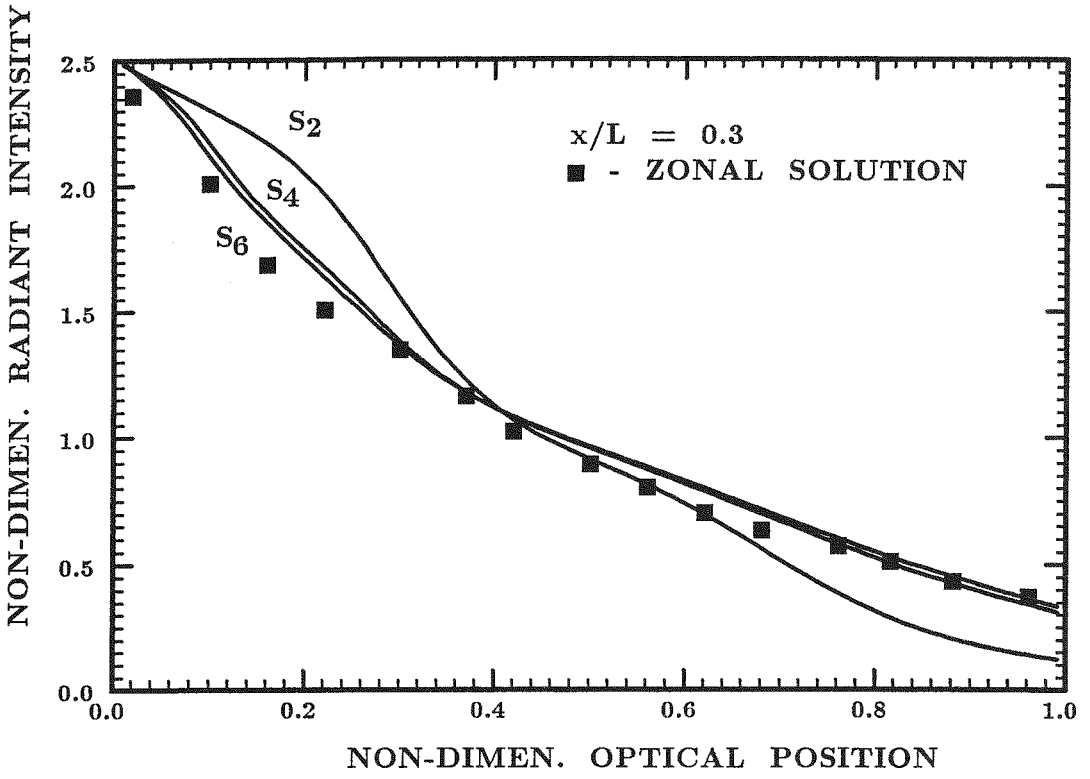

Figure 5.6: Non-Dimensional Mean Radiant Intensity vs. Optical Position for a Square Black Enclosure ($x/L_x = 0.3$)

approximation is again observed to be unsatisfactory in predicting pertinent radiative quantities. Also, the errors associated with the higher order models now appear to be higher than for the pure absorption case although they are still acceptable.

Notice from all three curves that the models over-estimate the radiant intensity near the hot wall and become progressively more accurate away from this boundary. Maximum errors of 13% at the hot wall occur for the higher order approximations with little improvement from the S_4 to the S_6 ordinate sets. Notice that, after the model "corrects" itself at $\hat{y} \approx 0.2$, the errors decrease significantly.

A comparison to the $P-N$ differential approximation (another popular multi-dimensional model) performed by Fiveland[49] shows that both approx-

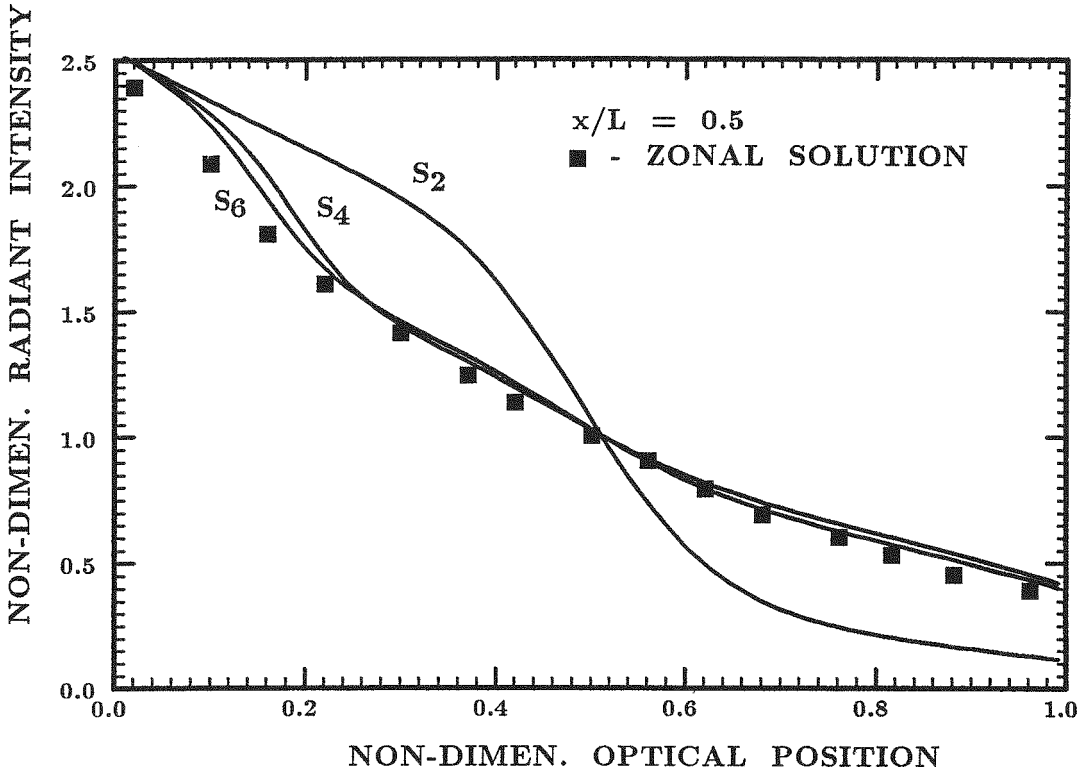

Figure 5.7: Non-Dimensional Mean Radiant Intensity vs. Optical Position for a Square Black Enclosure ($x/L_x = 0.5$)

imations predict the intensities with similar errors for the scattering problem (actually, the 12-flux discrete ordinates model is shown to have slightly smaller errors for this problem than the $P-3$ approximation).

5.5 Examination of Standard Numerical Parameters on Accuracy

To ensure that the accuracy of the numerical solution was not being effected by the noding density, the convergence criterion (for the pure scattering problem) and the order of the difference approximations, solutions of the model were obtained for a variety of different numerical parameters. The problem solved represented the most restrictive test of the model yet, i.e., the solution of the pure scattering enclosure problem to determine the mean radiant intensity distribution along the $\hat{y}$ axis for $x/L_x = 0.5$ (Figure 5.7). An S_4 approximation

was used since it has been shown that the S_2 ordinate set is an unsatisfactory estimator of the pertinent radiation quantities involved for both pure scattering and pure absorption problems. The convergence factor was applied such that the sum of the squared residuals (SSR) defined as the square of the difference of the mean radiant intensities at each of the nodes from one iteration to the next was smaller than a given epsilon.

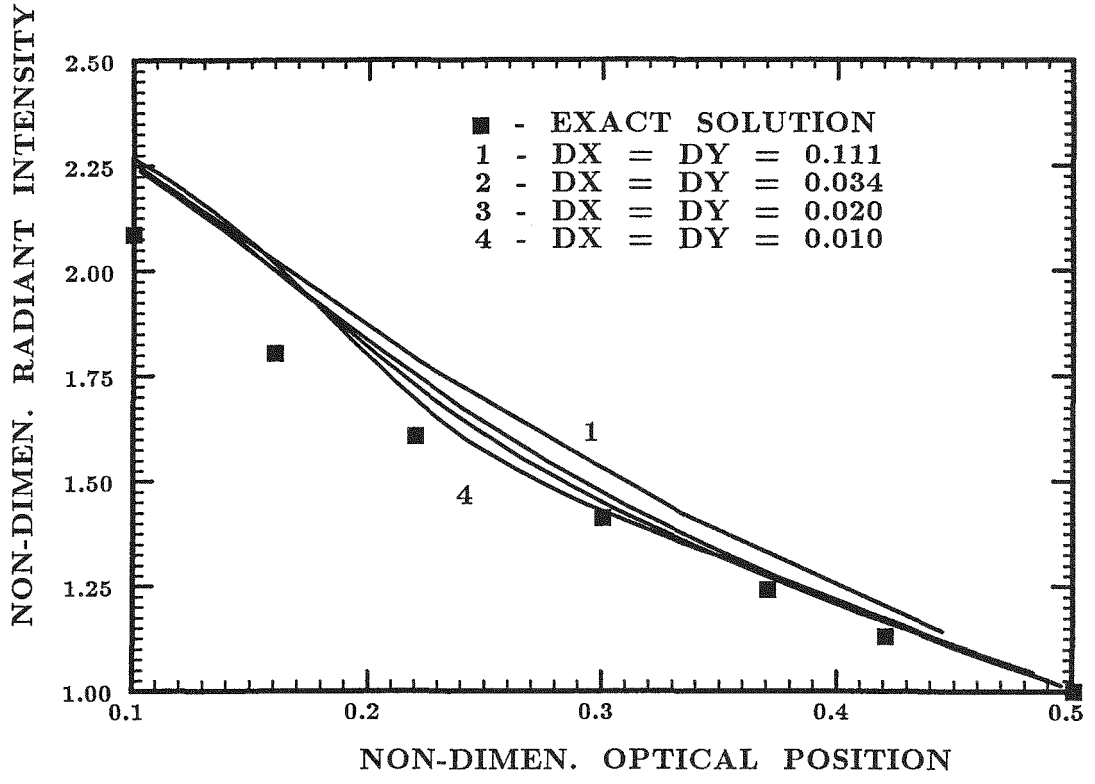

Figure 5.8: Effect of Noding Density on Accuracy of the Mean Radiant Intensity for the Pure Scattering Solution

Figure 5.8 shows the results of the model for various nodal densities from 100 nodes (10 in each direction) to 10,000 nodes (100 in each direction). The results show what might be expected. A more dense nodal packing leads to a slightly more accurate solution at the obvious expense of increased CPU times. The maximum CPU time for the model verification tests was 395 seconds for

the 24-flux pure scattering case for the 10,000 node execution. Obviously, for higher order flux models and dense nodal packing, the necessary CPU times do require consideration. (The maximum CPU time for the above tests was 395 seconds for the 10,000 node pure scattering problem.)

As far as varying the convergence criteria or applying a second or third order accurate finite difference expression on the spatial partial derivatives for solution of the pure scattering problem, the results showed imperceptible improvements when plotted in comparison to the zonal results. Plots, similar to Figure 5.8, did not show any significant changes in the model predictions for the 12-flux approximation. Convergence factors of 1, 0.5, 0.1 and 0.05 all showed practically no change in the accuracy of the model.

It should be noted that Carlson and Lathrop[59] have shown that the majority of the errors associated with the numerical application of the discrete ordinates technique comes from the lack of continuity of the intensity function. These errors, termed "ray effects" by the authors, arise because, for a certain emitting element in the medium located at at point x, y, there are several surrounding regions of the medium that lie along the boundary of two of the ordinate sets emanating from x, y. Along these boundaries, the intensity is mathematically discontinuous, so these potential absorbing elements are not able to "see" the emitted energy from the point x, y. These errors are most pronounced near heated boundaries and for highly absorbing media.

Notice that the Figure supports these statements. The increase in nodal packing, while slightly improving the accuracy of the approximation, does little to improve the model near the hot boundary. The errors at this boundary are overwhelmed by the so called "ray effects" which are inherent with the discrete ordinates approximation.

Clearly, the goal of any standard technique designed to increase solution accuracy by manipulating the numerical parameters (noding, convergence and the order of the difference approximations applied to the partial derivatives)

should be to force the "ray effects" to be the primary error at all points over the range of radiative parameters being considered. It is apparent that, in this case, only the noding density has any influence in reaching this goal. Varying convergence factors and increasing the order of the difference approximations has little or no effect (excluding unreasonable convergence criteria).

Chapter 6

Experimentation

6.1 Introduction

As was mentioned earlier in this report, obtaining an exact solution for the appropriate equation system to describe the energy transport processes occurring in a free-falling particle, direct absorption solar receiver is not feasable. Consequently, in order to characterize the pertinent quantities for design optimization, assumptions must be made and numerical models constructed to simulate the receiver cavity. Wherever possible, these models should be compared to some experimental data of the receiver. Also, it is often desirable to use experimentation to describe at least one of the major dependent variables in the physical system. In this way, the complexity of the governing equation system is reduced. Lastly, any model of a physical process will depend, in part, on the physical properties of the materials involved. Often, as is the case with the present study, the complexity of the situation warrants the choice of a combination of materials as the "active medium" to simplify the solution. Although much work may have been performed to determine the physical properties of many of the materials that make up the "medium," the relative weight of each of the materials as they appear in the particular situation must be determined. This determination is usually accomplished by measuring the critical parameters as they exist in the actual physical situation at hand.

It is clear that, to demonstrate the capability of the model to simulate the actual processes occurring (comparing the model to limiting case exact solutions does not completely satisfy) and to determine some of the physical parameters required to solve the model as it was developed, extensive experimentation must be performed before the accuracy of the model can be stated.

In the present study, the parameters appearing in the chosen formulation of the EOT and the energy conservation expression are the absorption coefficient, α, the scattering coefficient, σ_s, the scattering phase function, $\Phi(\Omega', \Omega)$, the porosities of the medium, ε_a and ε_p, the densities and specific heats of the air and the particles and the velocity of the curtain, v_y. Each of these quantities

must be determined before the model can be used. Also, the model will require the input of the boundary conditions for each particular test in order to compare the test data to the performance of the model. The procedures for determining these quantities, as well as the primary measurements (back surface flux and exit particle temperature), are discussed in this Chapter.

6.2 Radiative Properties

In the two-dimensional formulation of the equation of radiative transfer, there are three radiative properties that must be known about the medium to allow solution of the system; they are the absorption and scattering coefficients and the scattering phase function. For the free-falling curtain of absorbing particles, the medium consists of the particles and the interstitial air. This definition requires that these radiative parameters be determined for this "bulk" medium. So, experimental data taken of the curtain must be obtained. Research at Sandia into the compatibility of certain commercially available particles has revealed some information about the radiative properties of the proppants that are used in the present study. Part of the research on the proppants was an optical characterization of their radiative properties performed by Stahl, Griffin, Matson and Pettit[22]. The authors measured, among other things, the single particle scattering phase function and the single scattering albedo, defined as

$$w_0 = \frac{\sigma_s}{\sigma_s + \alpha} = \frac{\sigma_s}{\kappa} \tag{6.1}$$

where κ is known as the extinction coefficient.

Assuming that only single scattering events occur (i.e., multiple scattering is negligible), the single particle scattering phase function will represent the scattering behavior of the *curtain*. The single scattering assumption is justified by noting that the average clearance between particles in the medium is much larger than the clearance that would be required for multiple scattering to

occur. Also, for absorbing particles that scatter in the geometrical regime (i.e., size parameter, $\frac{\pi d}{\lambda}$, much greater than unity), the scattering phase function is thought to be linearly anisotropic (as was reported in Chapter 2). The measurements made in the Stahl report corroborate this and provide a Legendre polynomial approximation of the phase function that uses the first two terms of the infinite series which is the usual way to characterize a linear anisotropically scattering particle.

Since the scattering albedo has been measured (the results are reported in the work by Stahl et al.[22]) and the phase function has been characterized, measurements of the absorption coefficient (or the extinction coefficient) are required. The extinction coefficient can be a function of temperature in the medium and wavelength. The formulation of the EOT for the present model assumes constant radiative and thermal properties. The measurements of the albedo, although obtained over a number of particle flow rates, were not set-up to address the spectral or temperature dependence. Without any knowledge of the spectral or temperature dependence of the particle curtain, measurements of the extinction coefficient would need to show that the constant property assumption was justified.

To accomplish these measurements, a tuneable dye laser was used to provide energy to the curtain at wavelengths in the solar region. The curtain was provided by a flow device designed to deliver a 6 inch wide curtain of varying thickness to the test area. The flow device consisted of a particle storage hopper out of which the particles were fed directly to the test section. Both the hopper and the capture tank were insulated to allow for solar testing and a wind break was placed across the left and right sides of the test area to decrease the spreading of the curtain. A schematic of the flow device is presented in Figures 6.1a and 6.1b. This device will be discussed further in Sections 6.4 and 6.6.

The test involved measuring the incident and transmitted energy from the curtain. To determine the extinction coefficient from these measurements,

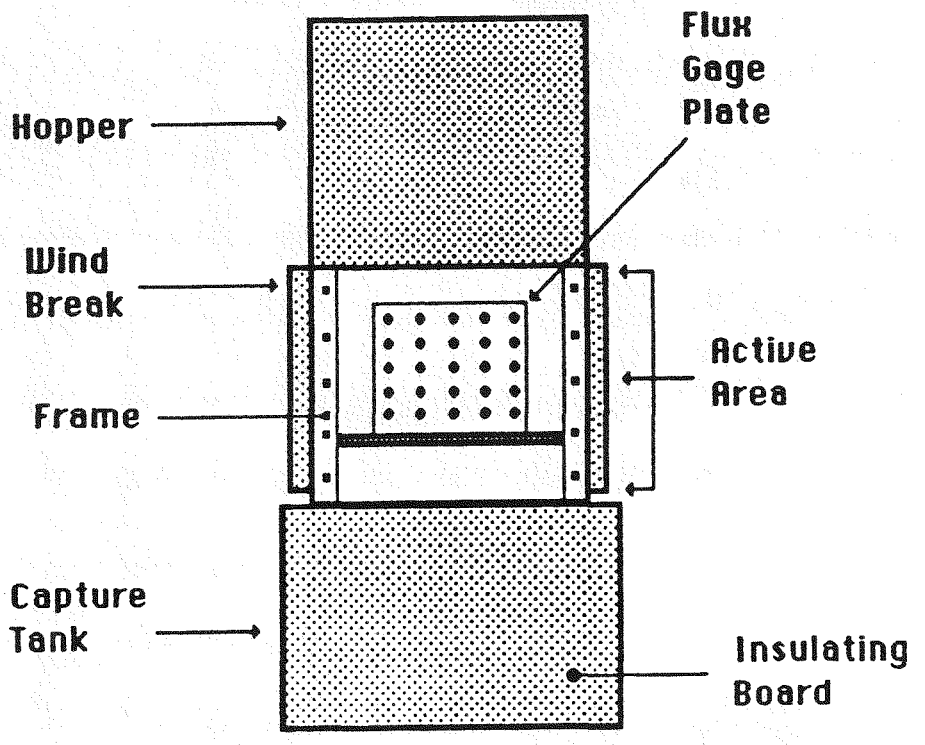

Figure 6.1a: Schematic Diagram of Particle Flow Device (Front View)

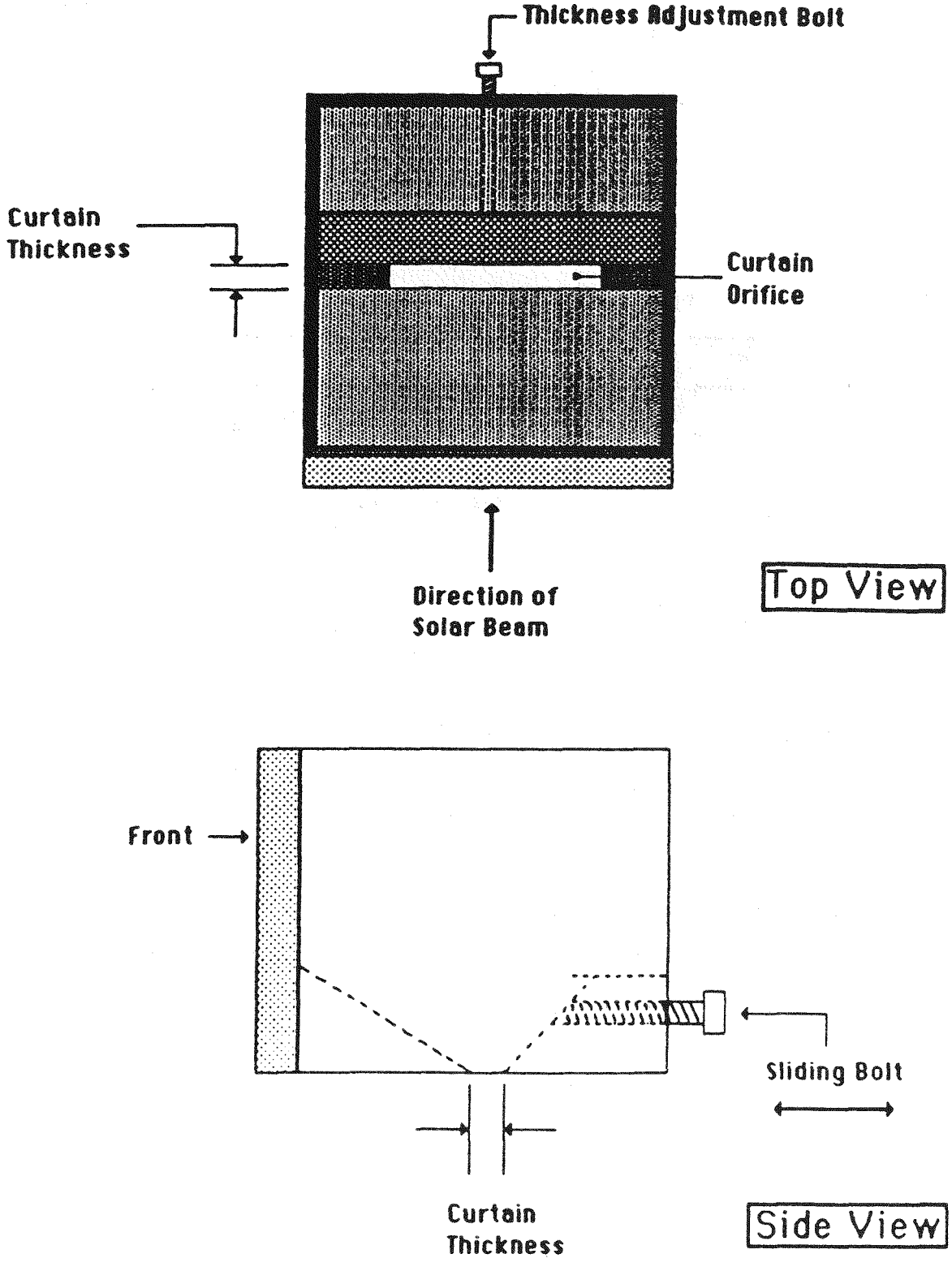

Figure 6.1b: Schematic Diagram of Particle Flow Device (Top and Side Views)

consider spectral radiation of intensity $I_\lambda(x)$ impinging on an absorbing and scattering layer with thickness Δx as shown in Figure 6.2. The intensity exiting the layer has been changed by an amount $dI_\lambda(x)$ to $I_\lambda(x + \Delta x)$.

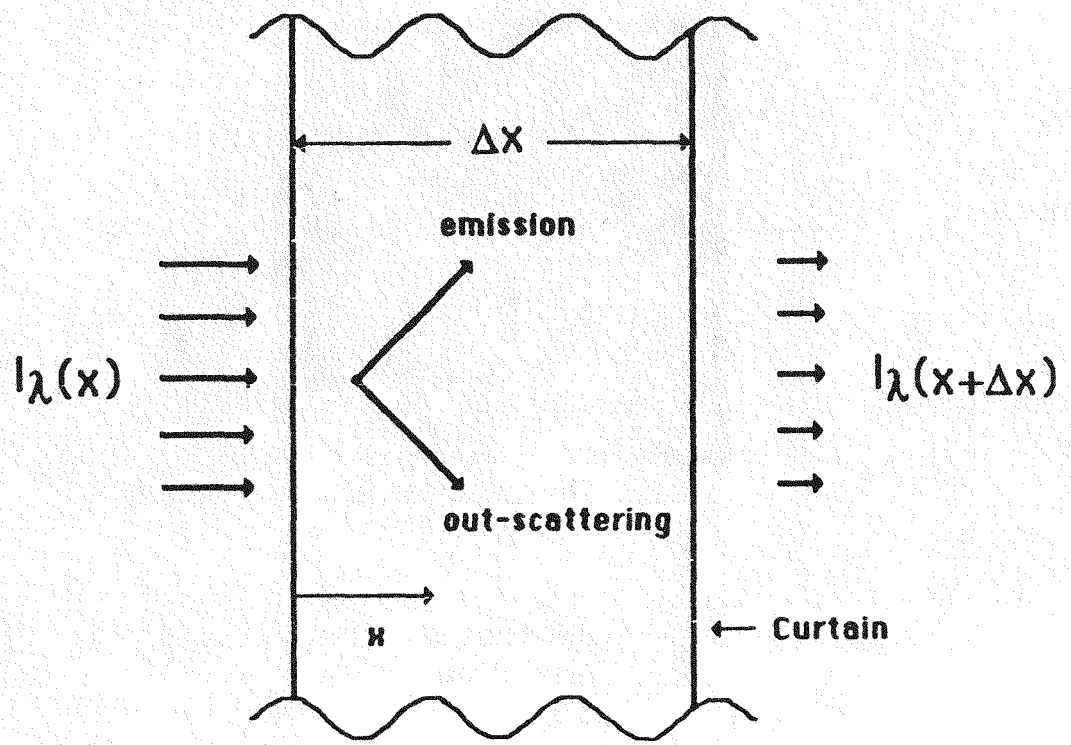

Figure 6.2: Normally Incident Intensity on Curtain Layer

If the medium is cool (i.e. emission is negligible), then, as the radiation passes through the layer, the intensity will be attenuated due to absorption and scattering and it will be increased by the in-scattering effects. Ignoring the in-scattering effects and defining a proportionality constant (the extinction coefficient) as $\kappa_\lambda(x)$, the decrease in the intensity can be written as

$$dI_\lambda(x) = -\kappa_\lambda(x) I_\lambda(x) dx \tag{6.2}$$

Integration of Eq. 6.2 over the path length gives

$$ln \frac{I_\lambda(x + \Delta x)}{I_\lambda(x)} = -\int_x^{x+\Delta x} \kappa_\lambda(x^*) dx^* \tag{6.3}$$

or, in a more general form and considering the medium to start at $x = 0$,

$$I_\lambda(x) = I_\lambda(0)e^{\left[-\int_0^x \kappa_\lambda(x^*)dx^*\right]} \tag{6.4}$$

Eq. 6.4 is known as Bouguer's Law, Lambert's Law or Beer's Law and shows that the attenuation of radiation along a path through a participating medium with negligible in-scattering is exponential in nature.

To relate the extinction coefficient to the ratios of the laser energies, κ is assumed to have no spatial dependence. Eq. 6.3 is then simplified to

$$ln\frac{I_\lambda(x)}{I_\lambda(0)} = -\kappa_\lambda x \tag{6.5}$$

The extinction coefficient then becomes

$$\kappa_\lambda = -\frac{1}{x}ln\frac{I_\lambda(x)}{I_\lambda(0)} \tag{6.6}$$

Figure 6.3 illustrates the experimental concept of the tests. The laser beam is created by pumping a dye laser and expanding and collimating the beam before it is directed into the particle curtain. The pump laser is a Spectra-Physics Model 2030 $18W$ Argon Ion being used at the 514 nm line. The pump laser provides energy to a Spectra-Physics Model 375B Dye Laser that directs the pump beam through a high velocity horizontal dye jet. The dye that was used for these tests was Rhodamine 590 which has a center wavelength at 590 nm and ranges from 570 to 650 nm. To record the incident and transmitted power levels, a Newport Corporation Model 818-SL Photosensor head was used with a Model 835 Optical Power Meter. The power meter allows for detection of continuous wavelength variations in the laser light.

To allow satisfactory measurement accuracy, the laser beam is collimated before it reaches the particle curtain. In this way, it is not necessary to move the detector to read the incident and transmitted energies. After exiting the

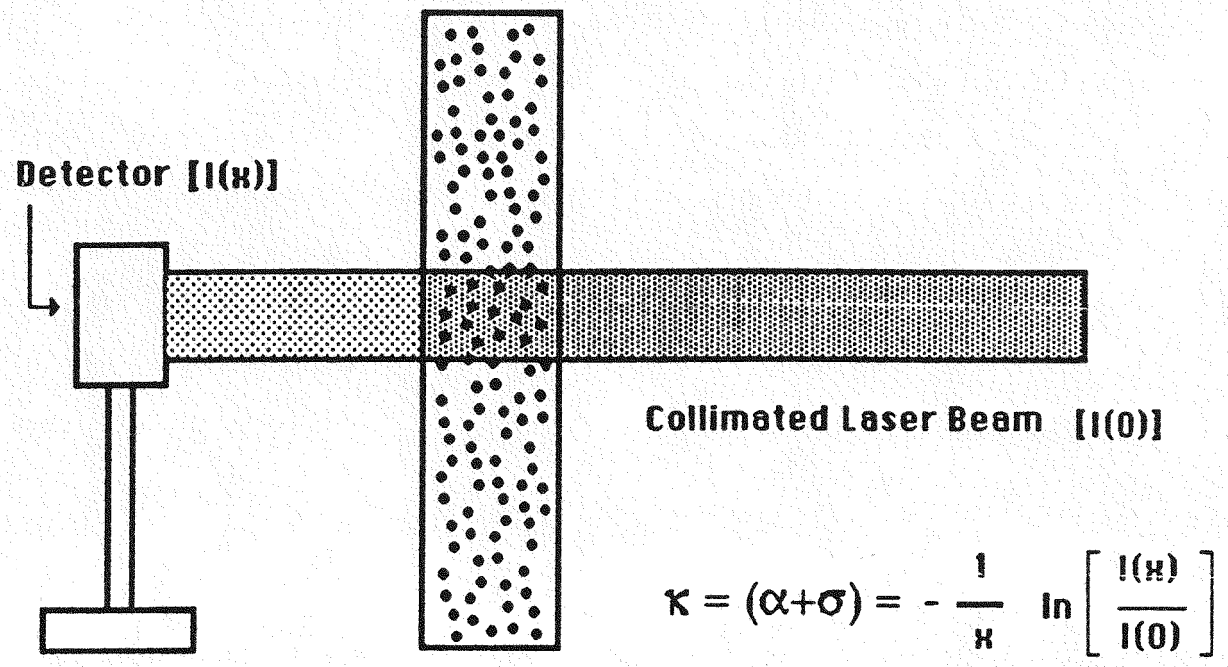

Figure 6.3: Schematic of Extinction Coefficient Measurements

dye laser, the beam is first re-directed and elevated to the height of the test section. Next, the beam is directed through a ten power microscope objective to produce a spherical wavefront. A 2 inch positive lens is positioned such that the distance between the objective and the lens is the focal length of the lens. This has the effect of producing a collimated beam (approximately 1.5 inches in diameter) through the test section of the flow device. To reduce any noise or non-collimated light from reaching the detector, an aperture stop is placed between the positive lens and the flow device. Figure 6.4 shows a photograph of the collimation system. The detector is then positioned such that it's entire active area is illuminated by the collimated laser beam.

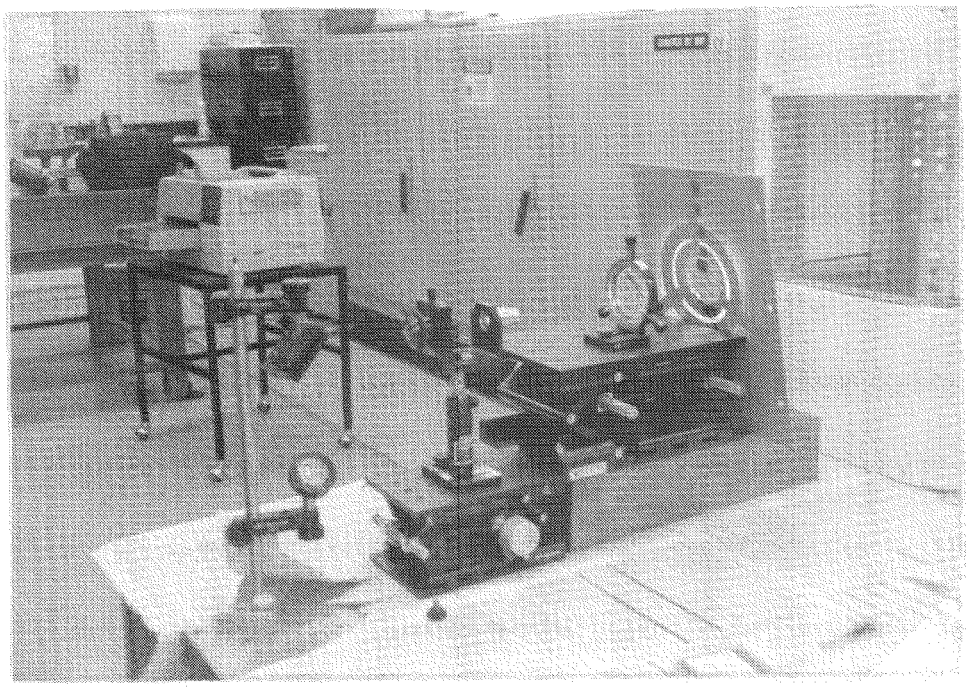

Figure 6.4: Collimation Optics for Extinction Measurements

It was desired to measure a constant value for κ independent of curtain thickness (flow rate) or wavelength. To address the spectral nature of the

extinction, readings were taken at several different wavelengths over the range of the dye laser. Flow rate dependence was considered by taking energy ratio readings for different curtain thicknesses. However, as the photograph in Figure 6.5 attests, very thin curtains will give erroneous readings. This is due to the fact that the detector can "see" portions of the laser beam at particular times (i.e., an instantaneous opening in the curtain allows the laser beam to pass through unaffected). Because of this, the experimental set-up required a certain minimum curtain thickness to eliminate any of this direct reading noise. Initial tests confirmed that the detector LCD readout was practically unreadable for these thin curtains. The reading fluctuated significantly until the curtain thickness was increased beyond the point where the porosity of the particle flow became independent of flow rate.

Figures 6.5 and 6.6 illustrate this point. Figure 6.5 is a photograph of a thin curtain test (with the room lights on for photographic purposes, for actual tests, the room lights were off). Notice that, in the Figure, both the point of contact of the beam on the curtain and the detector face are visible from the front face of the test device. It is clear that, for the curtain thickness in the Figure, the reading would not represent the actual extinction of the medium. However, as the thickness is increased as in Figure 6.6, the detector cannot be seen from the front of the flow device. For this case, the reading on the detector became fairly steady.

Another interesting point that was noticed during these initial tests was that, as the supply of particles in the hopper began to dwindle, the reading changed from a fairly constant value and began to increase. This increase continued until the curtain "split" apart because the hopper was practically empty at which point the detector reading was very close to the pre-flow reading. The post flow reading was actually slightly less then the pre-flow reading due to the dust that slowly settled back into the capture tank after the test. It was clear that the height of the particles above the exit of the hopper, to some extent,

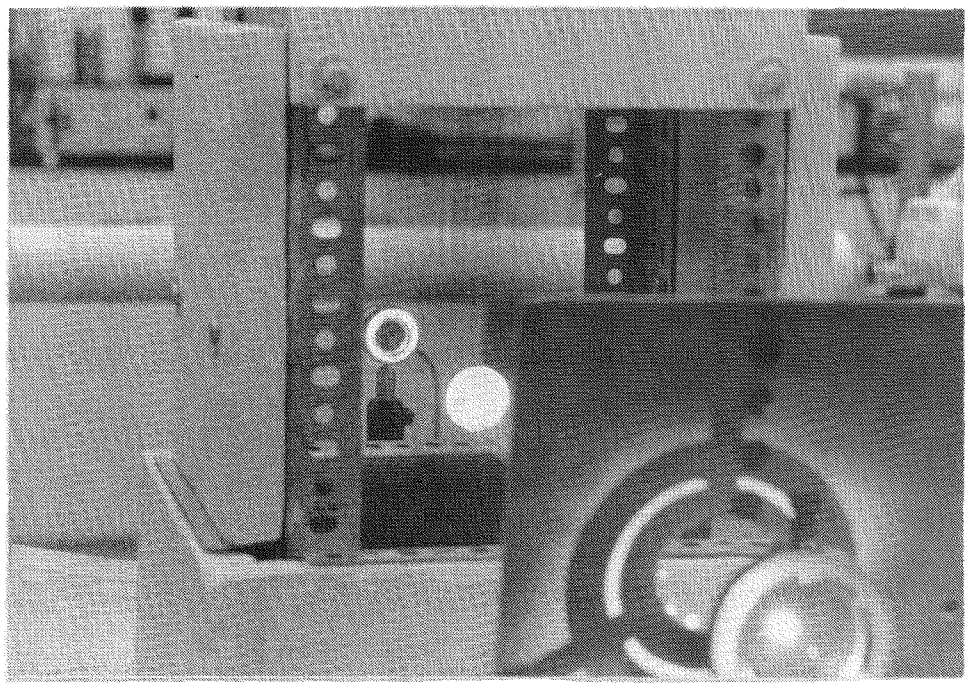

Figure 6.5: Thin Curtain Extinction Test

affected the flow rate through the test area. This occurred only as the particle height in the hopper became low, at which point, it is assumed, the flow rate decreased due to a decrease in the gravity-induced pressure at the exit of the hopper. It is anticipated that, for a DAR system using the free-falling particle curtain, a constant flow rate is the desirable design situation. Consequently, the constant (slightly fluctuating) readings taken during the constant flow rate segments of the test were considered the correct readings for the transmitted laser power.

As was mentioned, the actual testing took place in the laser lab of the Optics and Material Sciences Laboratory at New Mexico State University. The room was darkened completely to avoid any indirect energy reaching the detector. Tests were performed for curtain thicknesses ranging from 7 to 13 mm (the maximum the device could produce). A photograph of a dark room test is

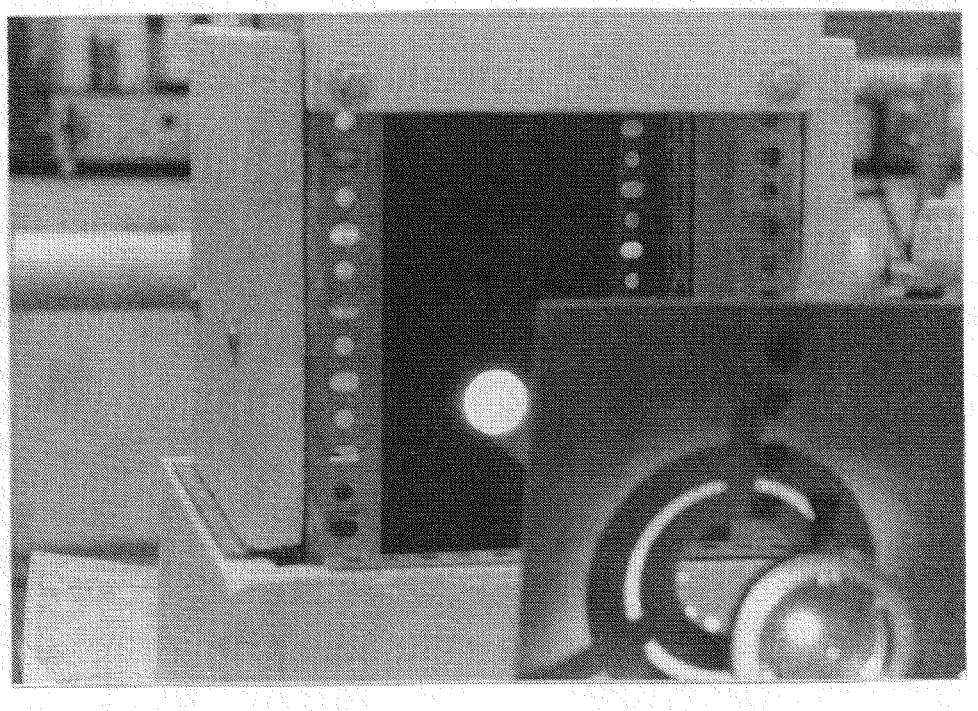

Figure 6.6: Thick Curtain Extinction Test

shown in Figure 6.7. The results of the tests are included in the next Chapter.

6.3 Particle Velocity Characterization

To adequately formulate a model to determine the exit temperature of the particles, knowledge of the curtain velocity is necessary. A momentum conservation expression with the appropriate boundary conditions could be formulated and solved simultaneously with the EOT formulation and the energy equation. However, to reduce the number of governing equations, measurements of the velocity can be made and these data can be used in the energy equation. Researchers at Sandia[71] have measured the velocity as a function of fall height in the cavity for the Norton Masterbeads^{TM} using laser Doppler velocimetry (LDV). Measurements were made for cold and hot particles and results showed that some spreading of the curtain occurred during the hot particle tests. This

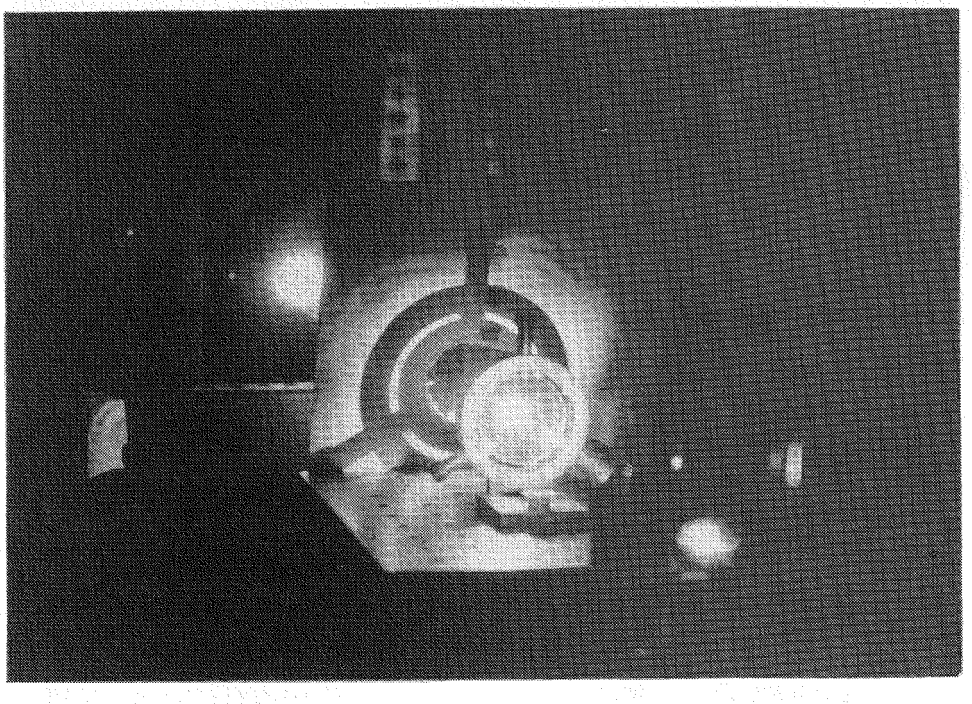

Figure 6.7: Extinction Coefficient Measurement Test

spreading was believed to be caused by the entrainment of air into the curtain and buoyancy forces created when the air warms up along with the particles. For the present study, however, the actual cavity fall height and the overall increase in the curtain temperature were much smaller than those used in the Sandia study. Consequently, the assumption of a one-dimensional velocity profile is justified.

The formulation of the energy expression described in Chapter 3 includes the velocity (assumed constant) and the spatial derivative of the temperature. Since the functional relationship of the velocity can be considered known (a curve fit of the LDV data will yield $v_y = f(y)$), the finite differenced form of the energy equation is simply solved at any given vertical node, j, by calculating the velocity at this height and using that value in the iterative process to solve for the temperature distribution in the curtain.

Using a standard ordinary least squares curve fitting technique, a third order polynomial was fit to the LDV data to obtain an expression of the from

$$v_y(y) = A + By + Cy^2 + Dy^3 \left[\frac{m}{sec}\right] \tag{6.7}$$

The coefficients of the curve fit were found to be

$$A = 0.844137$$

$$B = 5.034810$$

$$C = -1.875972$$

$$D = 0.260033$$

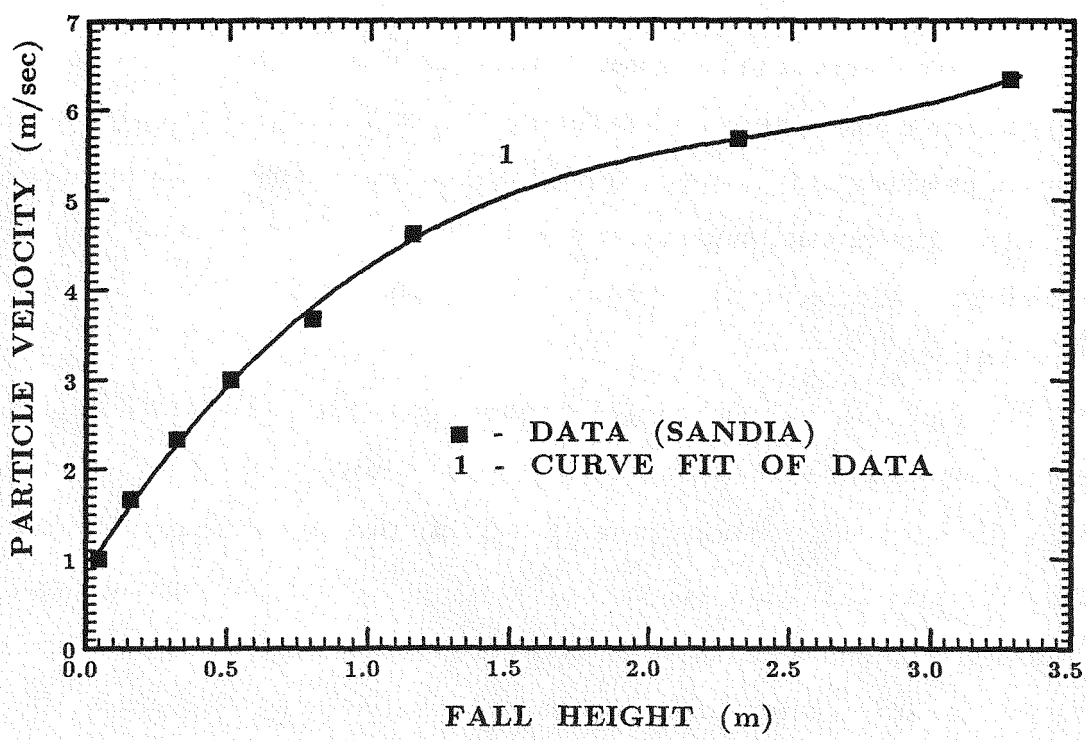

Figure 6.8: Curve Fit of Velocity Data

Figure 6.8 is a plot of the Sandia data (points on the curve) and the approximation of the data obtained through the curve fit.

6.4 Determination of the Curtain Porosity

As described in Chapter 3, to determine the values of the properties appearing in the energy equation (i.e., the effective density and the effective specific heat as well as the convection coefficient), the values of the porosities of both the air and the particles in the curtain are required. Recall that the "medium," as defined by the formulation of the EOT and the energy equation, consists of both the air and the particles in the curtain and, as such, the properties appearing in the equations must be representative of the "bulk" effects of the curtain. Since the extinction coefficient and the single scattering albedo were measured through a falling curtain, these values are not the values of particles alone but represent the combination of the two materials in the medium.

Likewise, to determine the density and the specific heat of the medium, a combination, based on comparative volumes, was suggested in Chapter 3. The expressions for these two properties can be written then in terms of the relative volumes of the particles and the air to the total volume as

$$\rho_{eff} = \varepsilon_a \rho_a + \varepsilon_p \rho_p \tag{6.8}$$

and

$$c_{p_{eff}} = \varepsilon_a c_{p_a} + \varepsilon_p c_{p_p} \tag{6.9}$$

where ε_a and ε_p are called the porosities and are defined on a volumetric basis as

$$\varepsilon_a = \frac{\forall_a}{\forall} \tag{6.10a}$$

and

$$\varepsilon_p = \frac{\forall_p}{\forall} \tag{6.10b}$$

Eqs. 6.10a and 6.10b can be combined to yield the expected result of the relationship between the porosities

$$\varepsilon_a + \varepsilon_p = 1 \tag{6.11}$$

It was necessary to determine the porosities of the curtain experimentally. This was accomplished through knowledge of the mean diameter and density of the particles. A description of the experimental process follows.

First, particle flow rates for various curtain thicknesses were determined. Using the same flow device described in a previous Section, we conducted timed tests in which the particle flow was allowed to continue for a set amount of time. This amount of time was determined by observing several flow tests at each of the two flow rates that were used. It was desired to only record flows in which the flow rate was known to be fairly constant.[1]The flow was started and a stop watch was engaged. At a given time, the flow and the stop watch were both suddenly halted. The total number of particles that fell into the capture tank during the time interval were then weighed. Since the density and mean diameter of an individual particle were known (see Hruby[17]), the mean mass of an individual particle can be calculated as

$$m_p = \rho_p \forall_p = \rho_p \frac{\pi d^3}{6} \tag{6.12}$$

Given the mass flow rate of the particles from the test (this value is obtained by dividing the weight of the particles from the test by the total time of the test recorded by the stop watch), the number flow rate of the particles, N_t in *number of particles/sec*, is determined as

$$N_t = \frac{\dot{m}}{m_p} \tag{6.13}$$

[1] As was discussed earlier, it was felt that the flow rate slowly decreased as the supply of particles in the hopper dwindled. The flow rate tests were conducted before this variation could occur while the level of particles in the hopper was substantial.

The number flow rate of the particles can now be converted to the number of particles per unit volume through knowledge of the velocity of the particles as a function of fall height. The velocity at any point in the test section can be determined by measuring the distance from the inlet to this point (defined as y_1) in the test section and calculating the velocity of the curtain based on this fall height (Eq. 6.7). Dividing the number flow rate of the particles by this velocity yields the number of particles in the curtain from the inlet at $y_0 = 0$ to the given point at $y = y_1$. Since the width (Δz) and the thickness (Δx) can also be measured, the number of particles per unit volume, $N_\forall$, is found from

$$N_\forall = \frac{N_t}{v(y_1)\Delta z \Delta x} \left[\frac{number\ of\ particles}{cm^3} \right] \tag{6.14}$$

The porosities are then calculated by determining the total volume of the particles that exist in the total volume defined by $(y_1 - y_0)\Delta x \Delta z$ by multiplying the volume density of the particles, $N_\forall$, by the volume of a single particle (based on the mean diameter). The expression is obtained by noting that the volume density of the particles in the medium, $N_\forall$, actually represents the number of particles that exists in a defined volume element of the medium, i.e., $N_\forall = \frac{(\#\ of\ particles)}{\forall}$. The result yields the ratio of the volume of particles to the total volume through the expression

$$\varepsilon_p = \forall_p N_\forall \left[\frac{cm^3(particles)}{cm^3(curtain)} \right] \tag{6.15}$$

From ε_p the porosity of the air is simply found from

$$\varepsilon_a = 1 - \varepsilon_p \tag{6.16}$$

It was anticipated that the value of $N_\forall$ would be constant for curtain thicknesses above the minimum value discussed in the Section on extinction coefficient measurements. The results of the tests are presented in Chapter 7.

6.5 Measurement of Angular Dependence of Incident Flux

Recall that, to determine the front face boundary condition, the solution of an "ill-posed" Fredholm integral equation must be obtained. The boundary condition is formulated to relate the intensity distribution at the front face of the curtain to the incident heat flux impinging on the curtain as the result of the solar concentrator system. The relationship between the flux and the intensity provides the basis for the difficulty. The heat flux represents the intensity distribution integrated over all solid angles as

$$q_{r,\lambda}(\mathbf{r_b}, \Delta\theta, \Delta\phi) = \int_{\theta_1}^{\theta_2} \int_{\phi_1}^{\phi_2} I_\lambda(\mathbf{r_b}, \theta', \phi') cos\phi' sin\phi' d\phi' d\theta' \qquad (6.17)$$

where $\mathbf{r_b}$ is the spatial location on the boundary.

As was previously discussed, the problem involves determining the local front face intensity distribution from measurements of the heat flux taken at the surface. Consequently, it is necessary to measure the angular dependence of the incoming heat flux from the concentrator. This was accomplished through the use of a flux gage with a limited field of view. Rather than constructing a new device for this purpose, a normal incidence pyroheliometer (NIP) was used (see Figure 6.9). This instrument is normally used for measuring the direct solar flux and, as such, has a field of view limited to the solid angle that the sun subtends at the surface of the earth. The aperture is circular with an angular field of view along both the altitudinal and azimuthal axes of 5.7°.

The NIP was mounted at the test area of the solar furnace on a two angle, altitude-azimuth mount with graduations for both angles. Figure 6.10a illustrates the positioning of the NIP on the test stand and Figure 6.10b illustrates the definition of the two angles that are discussed in the report.

Tests were conducted with the NIP well insulated in order to protect it from damage and to reduce erroneous readings due to emission from the NIP material. Readings were taken across the face of the concentrator at zero elevation and across the top of the concentrator (elevation $\approx 18°$) at several points for each "sweep." The voltage readings from the NIP were converted to flux

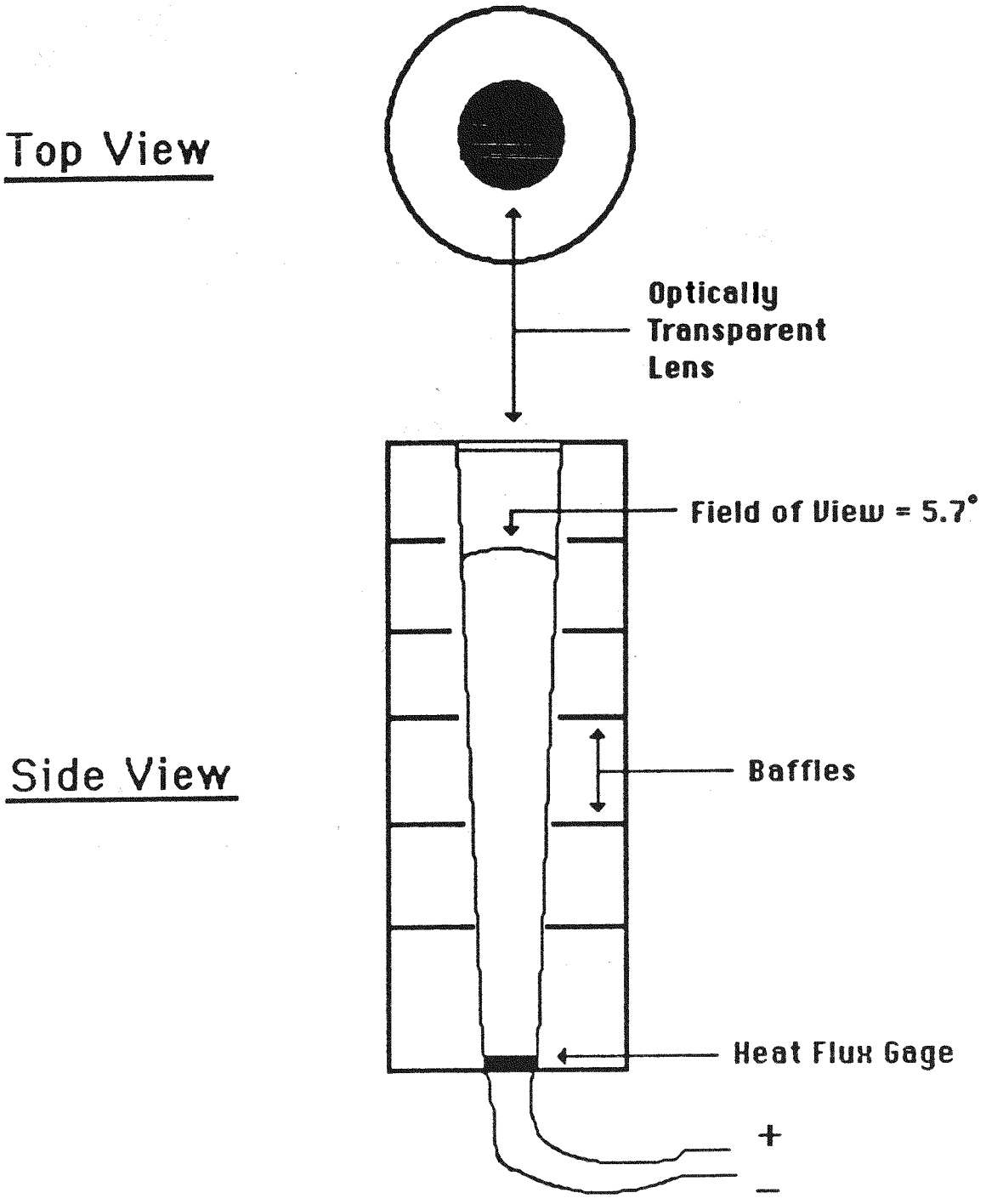

Figure 6.9: Normal Incidence Pyroheliometer

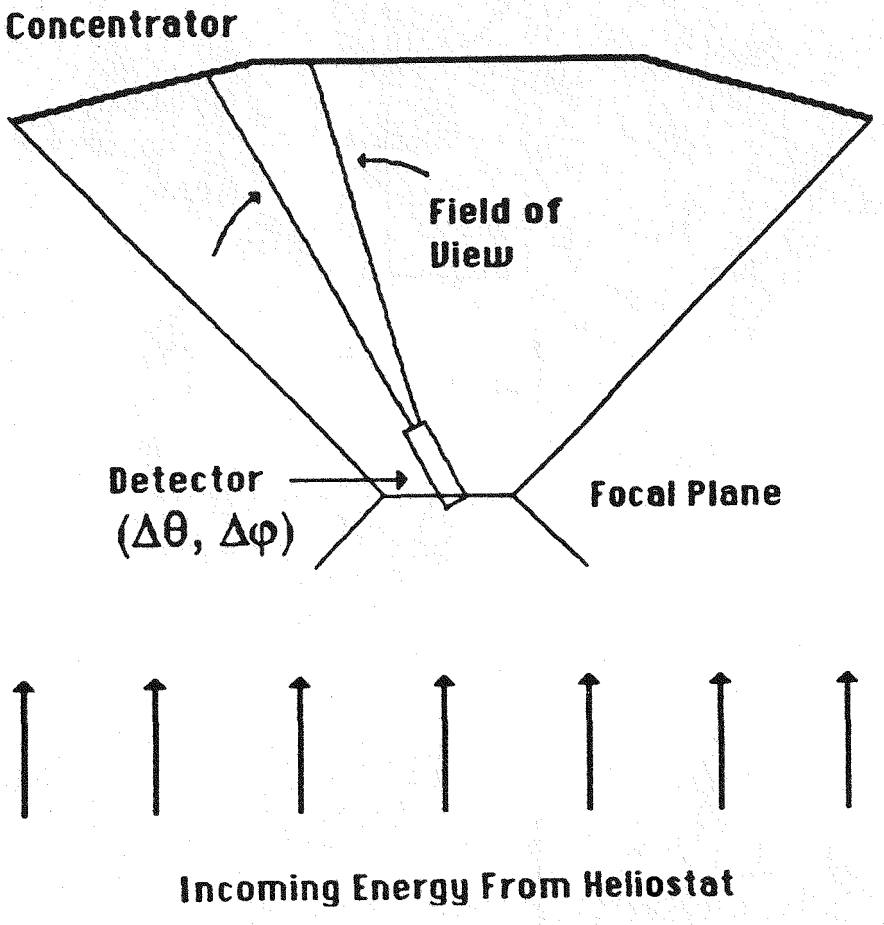

Figure 6.10: Positioning of the NIP for Angular Flux Measurements

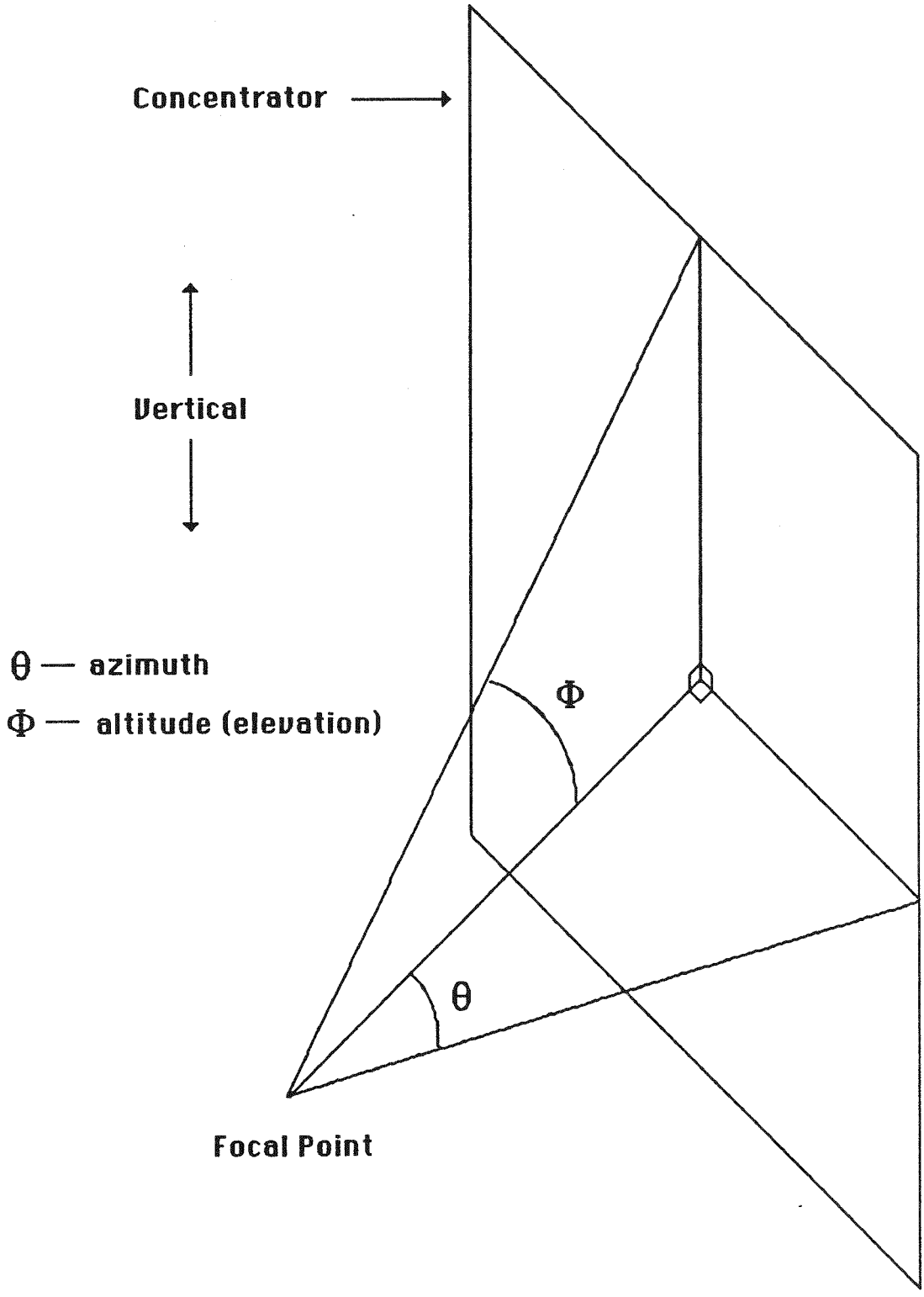

Figure 6.10b: Altitude (Elevation) and Azimuth Angles For the Solar Concentrator

readings using the calibration factor determined for the particular NIP used. Tests were only conducted when the concentrator was "full" (i.e., the position of the sun was such that the heliostat could illuminate the entire concentrator). The magnitude of the flux readings was not as important as was the variation of the readings over the concentrator as a normalization procedure was used for each specific flow test. In this way, it was only necessary to perform these angular tests once. (However, this does require that the actual flux tests also be conducted only when the concentrator is full.) With the flux readings from the concentrator characterization, the boundary fluxes for a particular test of the flow system would be determined by normalizing the angular data to the average flux measured on the day of the actual test.

Several angular tests were performed and the results are detailed in Appendix A-3. Similar trends were observed on several different days with several different solar conditions implying that, as long as the concentrator was full, the comparative magnitudes of the fluxes at the test stand were only functions of the angular position of the NIP. This helped determine that the NIP readings were successfully characterizing the nature of the concentrator and were not functions of solar position or environmental conditions.

A discussion of the normalization procedure and the development of the boundary flux (and intensity) models which provides the solution of the Fredholm integral problem is provided in the next Chapter.

6.6 Primary Flux and Temperature Measurements

The results of the experimentation comprising the secondary phase of the testing plan can now be put to use in the model of the transport processes to predict the flux and temperature distributions in the curtain with the eventual goal of comparing these results to the experimental data collected in the primary phase of the testing. The extinction coefficient, the porosities, the curtain velocity, and the angular characterization of the concentrator now allow for comparison of the model results to data comprised of measurements of the back surface fluxes (transmitted) and the average exit temperatures. These readings are performed using the variable area flow device mentioned previously.

Also, as was discussed in an earlier Section, the front face fluxes need to be measured in order to combine them with the results of the angular concentrator measurements to determine the boundary intensity distribution.

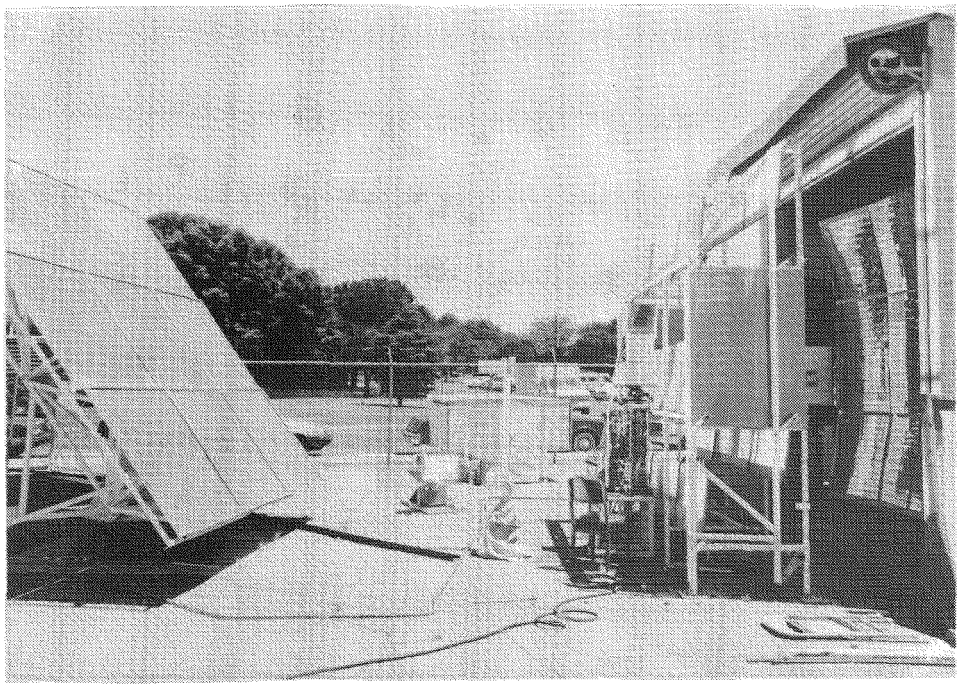

Figure 6.11: NMSU Solar Furnace Facility

The particle flow device, used previously in the determination of the curtain extinction coefficient and the porosities, is designed to provide an even particle curtain of constant width and variable thickness to the test area. The solar furnace, a photograph of which is shown in Figure 6.11, delivers a high heat flux concentration to a spot that is roughly a 6 inch diameter circle. Consequently, the flow device was designed to produce a curtain with a thickness slightly greater than the solar beam. The height of the test section of the device was determined by physical size limitations of the furnace (blocking and shadowing effects reduce the effectiveness of the concentrator). The hopper can hold sufficient particles to allow approximately 10 seconds of flow at the maximum curtain thickness, 13 mm. However, it was anticipated that most data runs

would be performed at significantly lower thicknesses (i.e. $< 8\ mm$) for which flow could continue for well over 30 seconds. Photographs of the device (front and top views) are shown in Figures 6.12a and 6.12b.

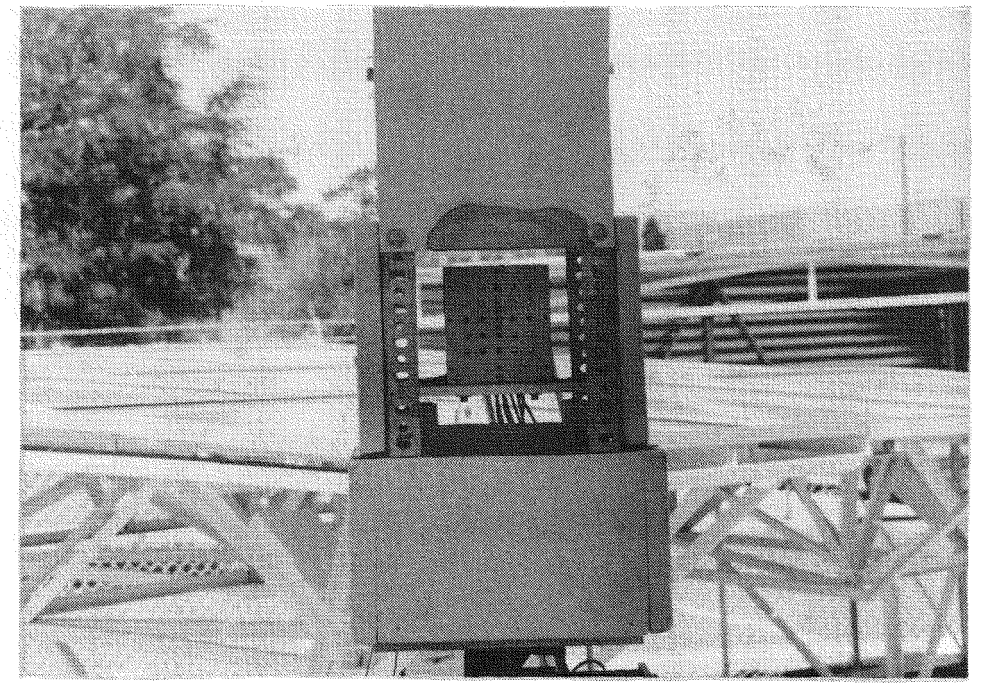

Figure 6.12a: Front View of Flow Device With Flux Gage Plate and Thermocouple Funnel

The test section of the flow device was designed to allow access to the front and back of the section (front defined as the side of the device facing the solar concentrator). To prevent any curtain spreading due to wind and to help even out the heat flux across the width of the curtain, pieces of insulating board were attached to the sides of the device (seen in Figure 6.12a). The front of the hopper as well as the entire capture tank were also insulated with the same material (mostly to prevent thermal damage to the hopper and capture tank).

The measurements of the heat fluxes were performed using standard cir-

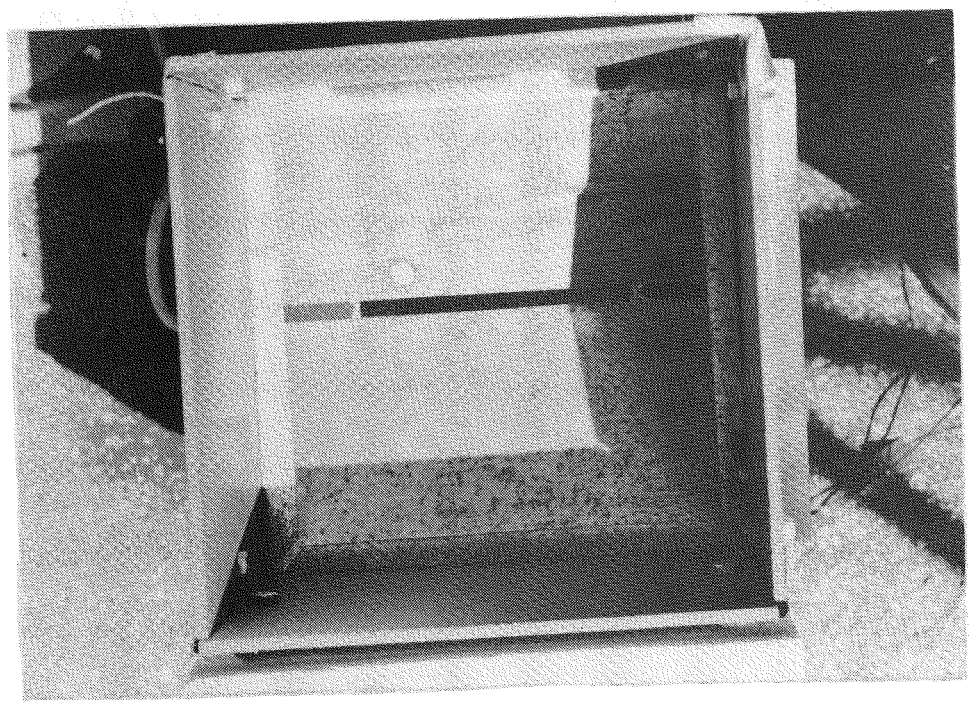

Figure 6.12b: Top View of Flow Device Detailing the Hopper Design

cular foil heat flux gages mounted to a water cooled copper plate. Both front and rear surface heat fluxes were measured. Figures 6.13a and 6.13b illustrate the concept.

The copper plate, visible in Figure 6.12a and shown from the rear with the flux gages installed in Figure 6.14, was designed to hold 25 threaded heat flux gages. The front surface has been painted white to prevent emission from the plate adding noise to the flux gage reading (the white coating reduces the absorption of energy by the plate itself). For the present study, 9 heat flux gages were installed on the plate in a cross pattern as is shown in Figure 6.14.

Only the readings from the vertical column of gages were used in the model due to the assumption of a two-dimensional intensity field in the x and y directions. As is illustrated in Figure 6.15, the development of the numerical model allowed for intensity variations along the height (y-direction) and through the

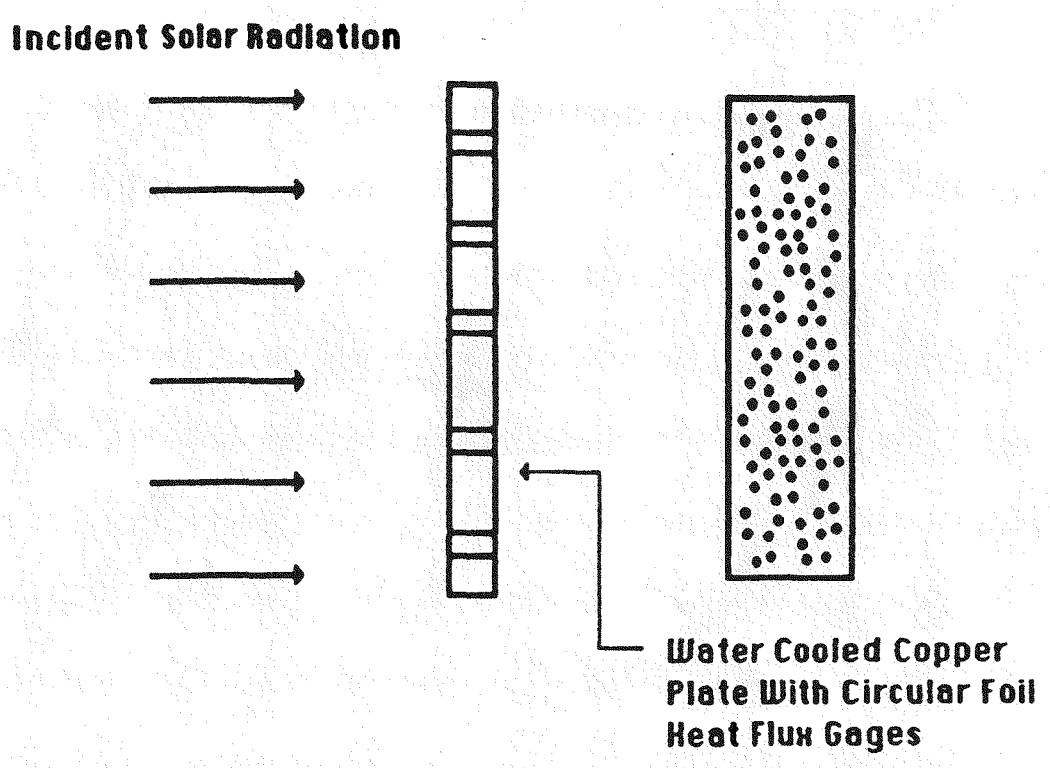

Figure 6.12a: Sketch of Front Surface Flux Measurement Concept

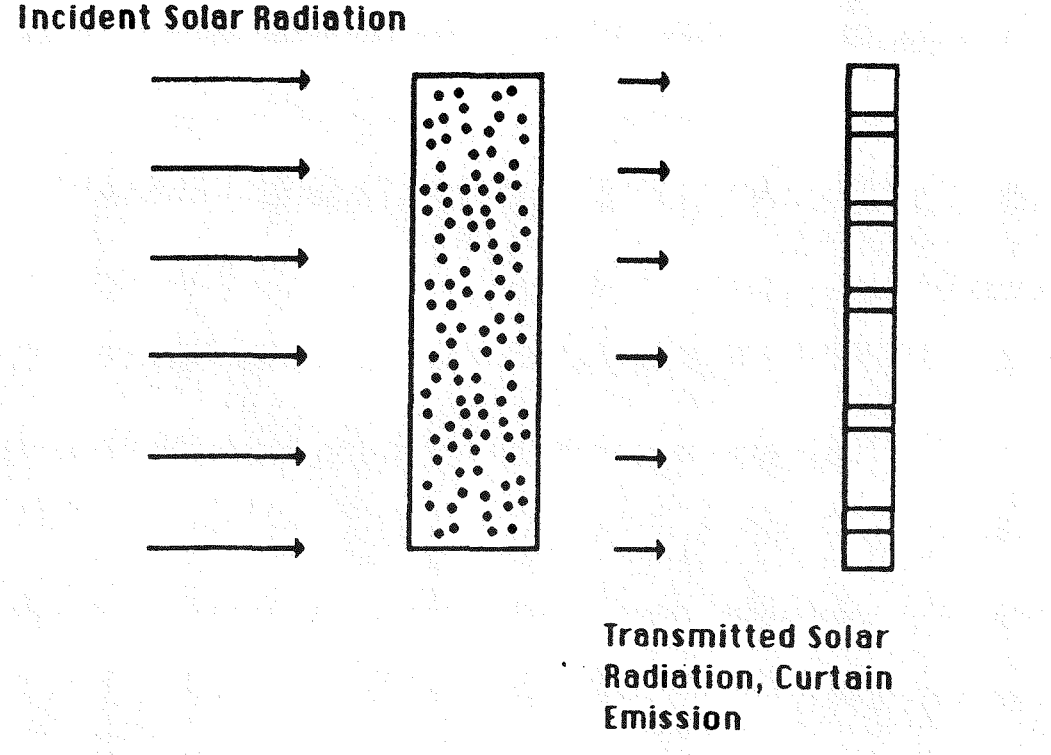

Figure 6.12b: Sketch of Rear Surface Flux Measurement Concept

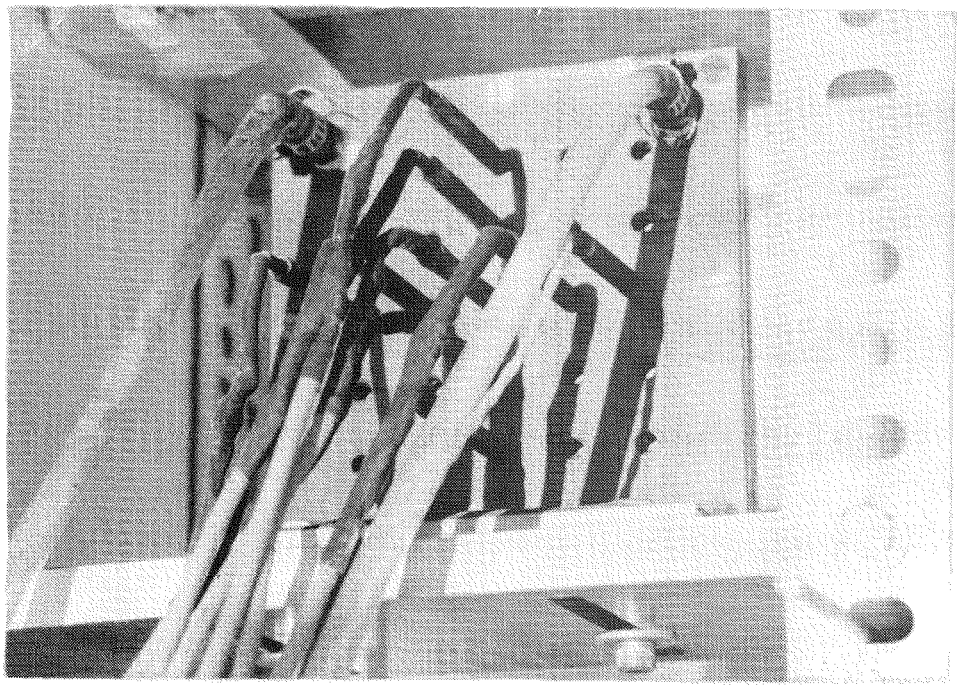

Figure 6.14: Rear View of Copper Plate With Flux Gages Installed

thickness (x-direction) of the curtain. The leads from the heat flux gages were connected to an HP-3054 data logger system (DAS). An HP-85 processor was used to control an HP-3497A and to make the conversions from the voltage readings into heat flux values given the calibration factors of each of the flux gages. The flux gages were made available for the present tests by Sandia National Laboratory's Solar Furnace Facility. Calibration of the gages was performed at Sandia in a well controlled manner. Consequently, the flux gage calibration is assumed to be correct and the factors provided by Sandia were used directly in the DAS without any check of their validity.

The flux gage plate was mounted on a plate which was attached to the rear supporting columns of the device. Long linear cuts were made in this support plate to allow movement of the gage plate forward or backward. This allowed proper positioning of the flux gages to help increase the accuracy of the

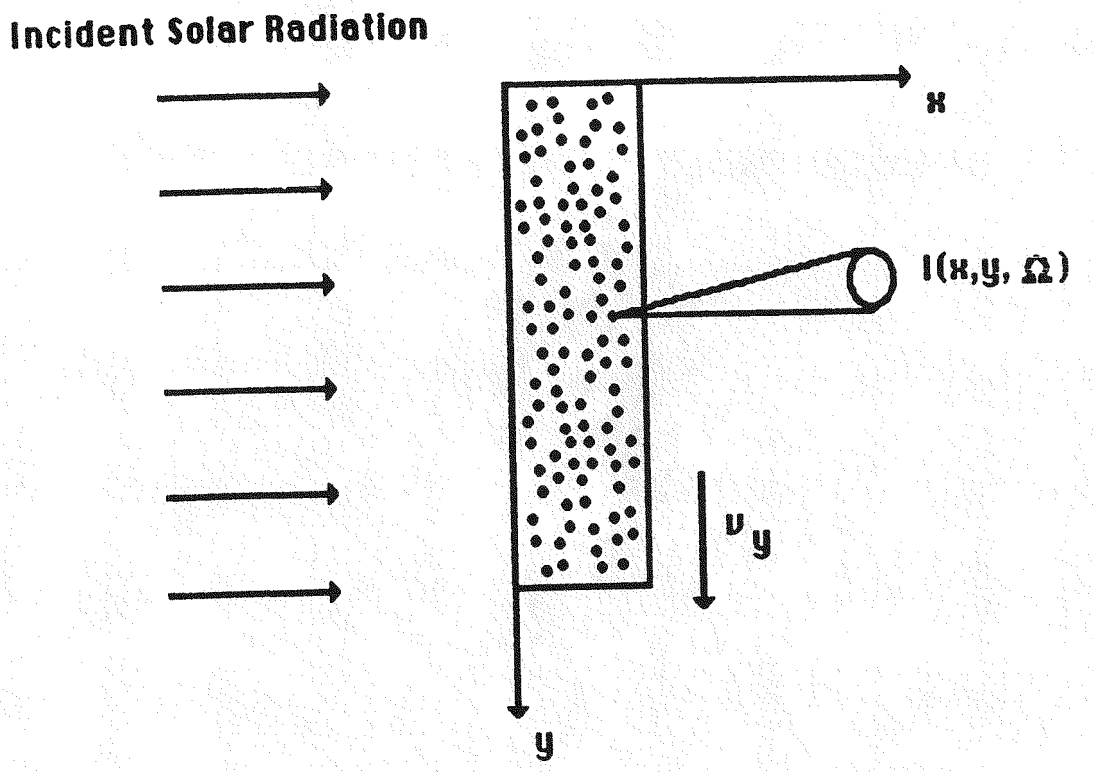

Figure 6.14: Geometry of the Free-Falling Particle Curtain

measurements.[1] These cuts can be seen in the lower part of the photograph in Figure 6.14.

Measuring the exit temperature of the particles is a rather difficult process. Obviously, recording the temperature of one of the particles is prohibitive (if possible). It was felt that standard optical techniques to obtain accurate temperature readings were unsatisfactory. A thermographic method would have difficulty determining the actual bulk or average temperature of the curtain because it would "see" only the particles and air near the face of the curtain that it was directed towards. Consequently, since the curtain does not have a solid boundary but is defined by the flowing particles and the interstitial air,

[1] The divergence of the solar beam in the vicinity of the test area is significant. Consequently, small movements along the axis of the concentrator normal can significantly alter the flux readings. It is important to position the gage plate as close to the rear surface of the curtain as possible.

most standard optical techniques would fail. It would be necessary to find a technique (such as two-color pyrometry) that could somehow differentiate between the particles near the "boundary" of the curtain and record an actual bulk temperature.

Researchers at Sandia addressed this problem using standard thermocouples specially mounted to record the temperature of the air immediately surrounding the particles (with a small contribution from the particles themselves whenever they actually contact the thermocouple junction). A report by Hruby, Steeper, Evans, and Crowe[72] details the measurements made of the temperature of a curtain of particles by using a "sampling cup" which consisted of a stainless steel foil cup fitted with a thermocouple. The cup was cylindrical in shape with a short length and a hole drilled into the bottom to allow the particles to escape. In effect, the concept relies on slowing the particles down enough to allow another body to come to thermal equilibrium with the particles. Then, the temperature of the second body is recorded using standard thermocouple techniques.

Accuracy would be high if the cup had enough time to reach equilibrium with the particles in the curtain. However, if the particles are allowed to remain in the cup for too long, they will begin to cool and the thermocouple readings will become inaccurate.

For the present study, this concept was used with a slightly different design. Instead of using a cup, a funnel device was constructed to force the curtain to funnel through a thin area. (A sketch of the concept is provided in Figure 6.16.) The funnel was designed with the same width as the curtain (slightly larger than the solar beam at the test stand) but it had a much smaller thickness than the curtain thicknesses used in the tests. At the base of the funnel, mounted vertically, was a thin bar (approximately $6'' \times 1'' \times \frac{1}{16}''$ in size). The material of the bar was copper which was chosen due to it's high thermal conductivity. Holes for fine gage thermocouples were drilled into the thin side of the bar

from the bottom approximately half the distance to the top ($\frac{1}{2}''$). Hypodermic thermocouples [1] were then placed into the holes to measure the temperature of the copper bar.

It was anticipated that the particles in the curtain would be forced to slow down as they passed through the funnel to very low velocities. As this happened, the particles would cover or surround the copper bar. This would cause the highly conductive copper bar to come to thermal equilibrium with the particles and the embedded thermocouples could then record these temperatures. The funnel was constructed out of the same insulating board that was used in the particle flow device in order to preserve the temperature of the particles as they passed through it and to eliminate any external energy effects from reaching the copper bar. Eye hooks were mounted into the insulating board and thin rods were used to hang the device under the test area of the curtain. Photographs of the device from the top and from the side showing the positioning of the hypodermic thermocouples are shown in Figures 6.17a and 6.17b. Figure 6.18 shows the orientation of the temperature measuring tool under the test area of the flow device.

Preliminary tests showed that this "funnel thermocouple" was effective (in terms of covering the bar with particles for a sufficient amount of time) within a range of curtain thicknesses from approximately 3 mm to approximately 8 mm. Below this range, the particle flow was not sufficient to significantly "clog" the funnel and, for these particles flow rates, most of the copper bar was not exposed to the particles. Above this range, the large particle flow rates overwhelmed the funnel and particles spilled over the top of the device. Obviously, the desired situation is when the copper bar is well covered by particles but the overall flow through the funnel is enough to ensure that the residence time of the particles is small enough to not allow them to cool significantly.

[1] The thermocouples were Omega brand Model HYP-2, type T hypodermic thermocouples with an outside diameter of $0.032''$.

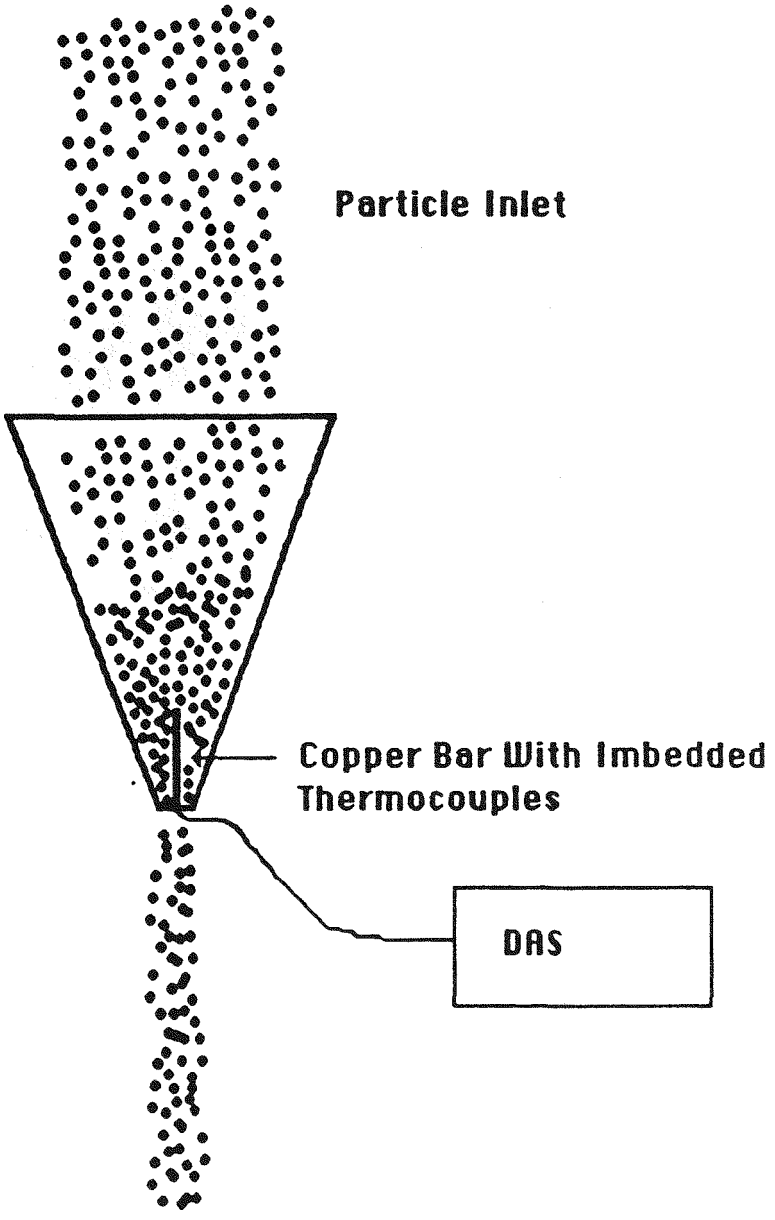

Figure 6.15: Schematic of Temperature Measuring Device

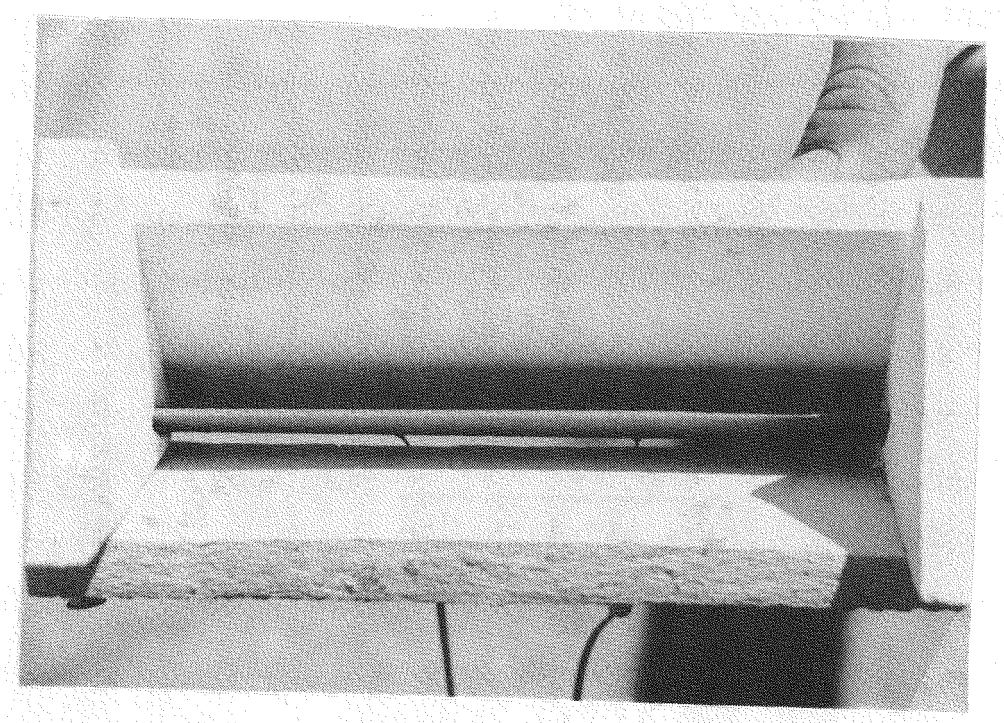

Figure 6.17a: Top View of Particle Temperature Measurement Device

Actual testing of the system involved filling the hopper with particles and initiating the flow by sliding the wooden plate at the bottom of the hopper open to the desired curtain thickness. Initially, the required model inputs (i.e. the front face fluxes and the inlet particle temperature) were recorded separately. However, uneven tracking of the heliostat system to follow the "motion" of the sun across the sky led to significant errors in the data. Between the time the front fluxes were measured and the test was run, changes in the character of the solar beam due to tracking adjustments sometimes caused the rear surface fluxes to be measured *greater* than the front fluxes.

The test routine was amended to allow the recording of the front surface fluxes immediately after the rear surface fluxes were measured. This was ac-

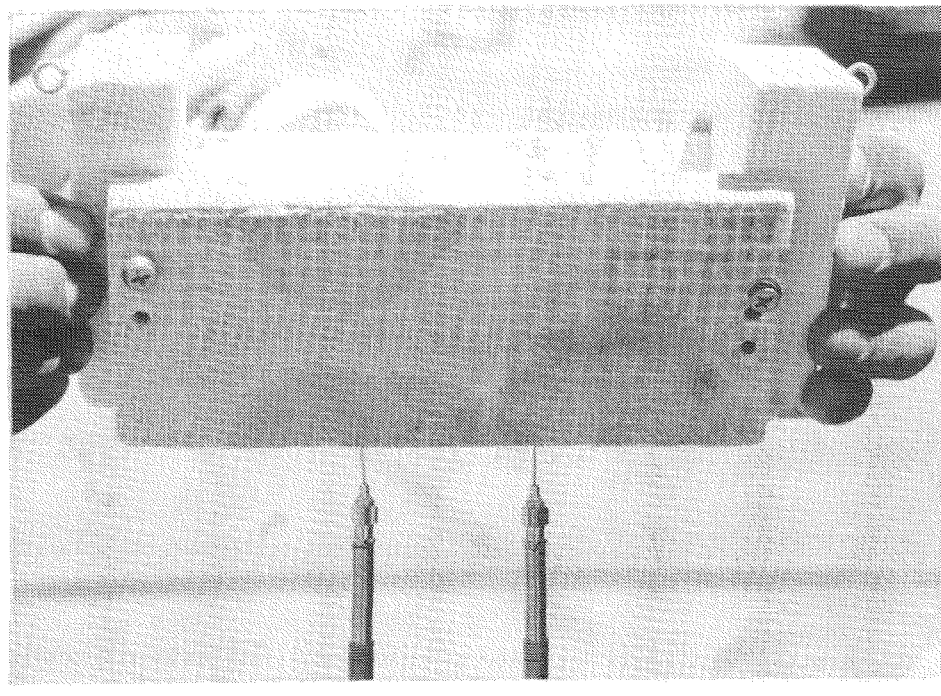

Figure 6.17b: Front View of Particle Temperature Measurement Device

complished by allowing the hopper to completely drain itself of the particles, and the fluxes measured at that moment were used as the incident heat flux on the curtain. Unfortunately, this test procedure did not allow the flux gage plate to be moved to the plane that represents the front of the curtain since the time required for this operation would cause the same tracking errors to occur. However, since the maximum thickness of the curtain for the tests was 8 mm, the error associated with the beam divergence over this distance was assumed negligible (certainly much smaller than the tracking errors noticed initially).

Figures 6.19 and 6.20 show a test run in progress. Figure 6.19 shows the particle curtain being illuminated by the solar beam and the next Figure shows the flux gage plate as it looks immediately after the flow has ceased. Both

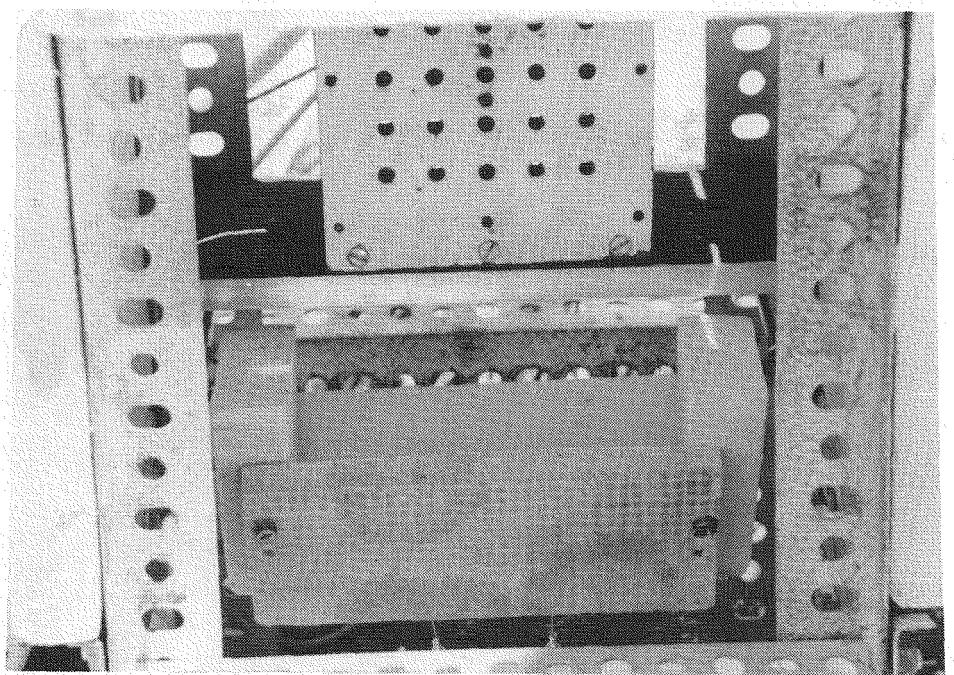

Figure 6.18: Orientation of Temperature Measuring Tool in Particle Flow Device

photographs were taken through an opening in the center of the concentrator that allows viewing of the test object with the attenuator in the open position.

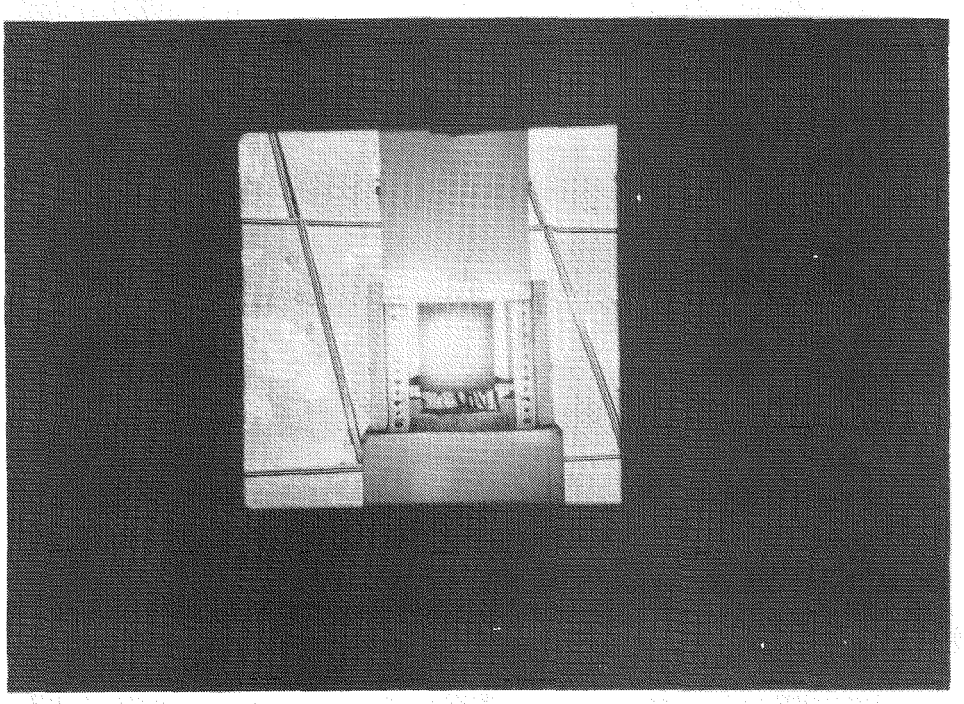

Figure 6.19: Test Run During Particle Flow

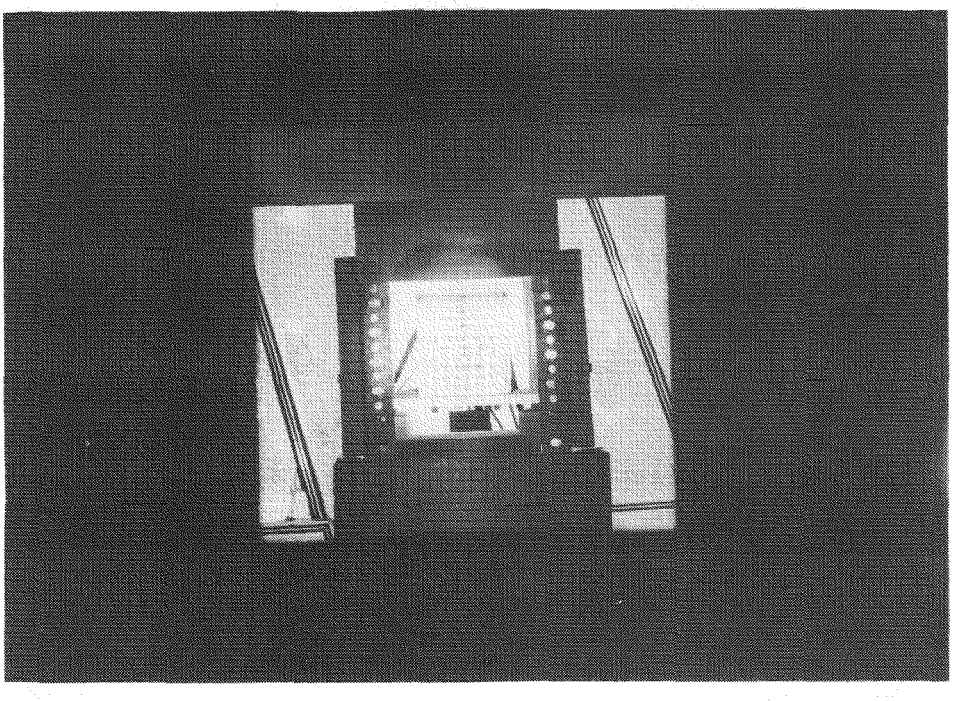

Figure 6.20: Test Run Showing Incident Flux Measurement Immediately After Cessation of Flow

Chapter 7

Experimental Results and Comparisons

7.1 Introduction

The results of both the secondary and primary phases of the experimentation are presented in this Chapter. Each of the major measurements that were performed are reported in separate Sections of the Chapter. The results of tests to determine a constant value for the extinction coefficient are presented in tabular form in Section 7.2.

Section 7.3 presents the experimentally determined values of the curtain porosities (air and particle). The calculation process used to determine the porosities from measurements of the particle flow rates and knowledge of other physical characteristics of the curtain (i.e., size and mass of the particles and the curtain velocity) is described. The values for the effective density and the effective specific heat of the curtain are presented after the porosities have been determined.

After determination of the properties and the physical parameters of the curtain and given the measurements of the angular fluxes from the concentrator, the specific boundary fluxes for a given test were measured as described in the previous Chapter. These fluxes were used to determine the incident intensity distribution on the front face of the curtain through the solution of the Fredholm integral problem. This process is described in detail in Section 7.4. The results of the boundary intensity model development and it's corresponding heat flux model are presented in graphical form.

Using the inputs of the boundary intensity and the inlet particle temperature, the model is now able to predict the transmitted flux through the curtain and the average exit temperature of the curtain.[1] Comparisons of these quantities as estimated by the model are made with the data recorded in the test runs. Results for the transmitted flux for a range of curtain thicknesses are presented

[1] Actually, the model can predict the heat flux and temperature distributions within the curtain itself, however, since obtaining measurements of these values would significantly alter the character of the curtain and due to feasablility constraints, comparisons were only made of the transmitted flux and the average exit temperature of the particles.

in Section 7.5 while the temperature results are presented in Section 7.6. The details of the finite differencing scheme for the equation system formulated for the present case (i.e., the solar receiver problem) are presented in Appendix 2 along with the final forms of the expressions as they are used in the body of the computer code.

Section 7.7 presents the results of a calibration test performed on the thermocouple device. The calibration was conducted to possibly explain the effects of the transient response of the copper bar on the actual particle temperatures.

To determine the effects of measurement errors of the model inputs on the model predictions of the transmitted flux and the average exit temperature, a sensitivity analysis was performed and the results are presented in Section 7.8. A plot of the modified sensitivity coefficients for the heat flux is included as well as a table for the average exit temperature.

7.2 Extinction Coefficient Measurements

As given in Stahl et al.[22], the single scattering albedo for the particle curtain was measured to be 0.1 $\pm$ 0.01. The scattering albedo represents the ratio of the scattering coefficient to the extinction coefficient, the latter being the summation of the absorption and scattering coefficients. The measurements of the extinction coefficient were performed as described in the previous Chapter. Tests were conducted for several different curtain thicknesses from 5 to 13 mm with the majority of data taken at the maximum thickness, 13 mm.

As was discussed previously, the extinction coefficient for the model developed for the present study was assumed independent of wavelength. Consequently, the dye laser was used to validate this assumption. Results indicated that very little, if any, spectral dependence exists. There was no change in the measurements (performed at a thickness of 13 mm) as the laser was swept from approximately 570 nm to 630 nm. Consequently, the assumption of spectral independence was felt to hold over the entire solar spectrum (even those

Table 7.1: Extinction Coefficient Results

Approx. Wavelength (nm)	**Curtain Thickness** (mm)	**Extinction Coefficient** ($1/mm$)
570	13	0.293
570	13	0.303
580	13	0.322
590	13	0.296
590	13	0.299
630	13	0.305
630	13	0.230
630	13	0.194
580	8.5	0.379
580	7	0.358
580	5	0.494
630	5	0.343

wavelengths that lie outside the range of the dye laser).

Table 7.1 presents the results of the experiments. The data in the Table constitute the tests in which it was felt the reading had become fairly stabilized and, as such, are the most representative of the actual extinction behavior of the curtain. Also, by using Bouguer's Law in the calculation of the extinction coefficient, in-scattering has been neglected. Realistically, the power detector

would read the amount of energy that is transmitted through the curtain *and the amount that is scattered into the direction of the laser beam propagation.* As was discussed in Chapter 6, in-scattering has been assumed negligible and, since the single scattering albedo has been measured to be 0.1, the uncertainty associated with this assumption is well within the experimental error associated with reading the power meter.

The mean value of the above tests is

$$\kappa = 0.318 \pm 0.075 \left[\frac{1}{mm}\right] \tag{7.1}$$

7.3 Curtain Porosity Measurements

The test procedure to measure the porosities of the air and the particles in the curtain was detailed in Chapter 6. The results of the tests are presented here. Data were taken for two curtain thicknesses (i.e., two particle flow rates) and, with knowledge of the particle velocity as a function of the fall height and the volume and density of a single particle, the curtain porosities were calculated.

The data and the subsequent calculations made of the data to obtain the porosities are presented in Appendix A-4. The results of the tests are

$$\varepsilon_p = 0.590 \pm 0.053 \tag{7.2}$$

and

$$\varepsilon_a = 1 - \varepsilon_p = 0.410 \pm 0.053 \tag{7.3}$$

As was anticipated, the porosities calculated for the two different curtain thicknesses were found to be independent of the particle flow rate.

If the measured values for the porosities are used in the expressions for the effective curtain density and the effective curtain specific heat, Eqs. 3.42 and

3.43, the thermal properties for the curtain are found to be

$$\rho_{eff} = \varepsilon_a \rho_a + \varepsilon_p \rho_p = 2342.78 \left[\frac{kg}{m^3}\right] \tag{7.4}$$

and

$$c_{p_{eff}} = \varepsilon_a c_{p_a} + \varepsilon_p c_{p_p} = 864.22 \left[\frac{J}{kg - K}\right] \tag{7.5}$$

7.4 Front Surface Boundary Intensity Distribution

As was discussed in Chapter 3, the determination of the front face intensity distribution involves the solution of a Fredholm integral equation. The solution is obtained by assuming a functional form for the intensity and determining the parameters that appear in the integrated form of the functional relationship which is a model of the boundary heat flux distribution. These fluxes, measured in terms of their dependence on altitudinal and azimuthal angles, are determined by measuring the angular variation of the heat flux at the test stand. The solution process involves several steps, each of which is discussed in the order they are performed.

7.4.1 Flux Data

As was discussed in Section 6.5, the angular dependence of the incident heat flux coming from the concentrator was measured. The data, taken on clear days and only when the position of the sun is such that the illumination from the heliostat completely covers the concentrator area, are assumed to be representative of the true angular dependence of the concentrator. The variation of the solar conditions is removed from these data by normalizing it with respect to the insolation measured at the front face for each particular test.

The total heat flux data taken immediately after a flow test were used to produce a function for the flux in terms of the vertical position on the plate.

Since the heat flux distribution at the focal area of many solar concentrator systems is generally believed to be Gaussian in nature, the flux gage data were first curve fit using a Gaussian formulation. This step was taken to make the "test" of the model less extreme (i.e., if only the data were used, the model would "see" several step changes in the flux level for each flux gage data point) by determining a smooth continuous function for the incident flux. The curve fitting technique was a standard ordinary least squares method. To obtain the fits, the flux at the edge of the copper plate was assumed to be zero. Since the diameter of the "spot" at the solar furnace is slightly less than the length of one side of the copper plate, this assumption was considered valid. Also, it was felt that any error associated with this assumption would be insignificant except in the regions very near the edges of the plate.

Figure 7.1 is a plot of the flux data and the Gaussian curve fit for one of the test runs. The functional formulation for the curve fit is defined in terms of the distance along the vertical of the plate, y, as

$$q^*(y) = Ae^{\frac{-(y-y_0)^2}{B}} \tag{7.6}$$

where A, y_0, and B are the parameters that the curve fitting routine determines.

Physically, A represents the maximum magnitude of the data. This maximum is measured at the peak (the center of the solar "spot") which is determined to exist at the vertical location y_0. The parameter B is a measure of the "spread" of the Gaussian function defined by the variation of the flux from the maximum at y_0 to zero at $y = 0, L_y$.

7.4.2 Normalized Angular Flux Data

To eliminate the differences in solar conditions from the time the angular tests were performed to the conditions that exist on the day of the particular flow test, the angular flux data were normalized by dividing by the average of the total fluxes recorded at each of the flux gage locations measured on the day

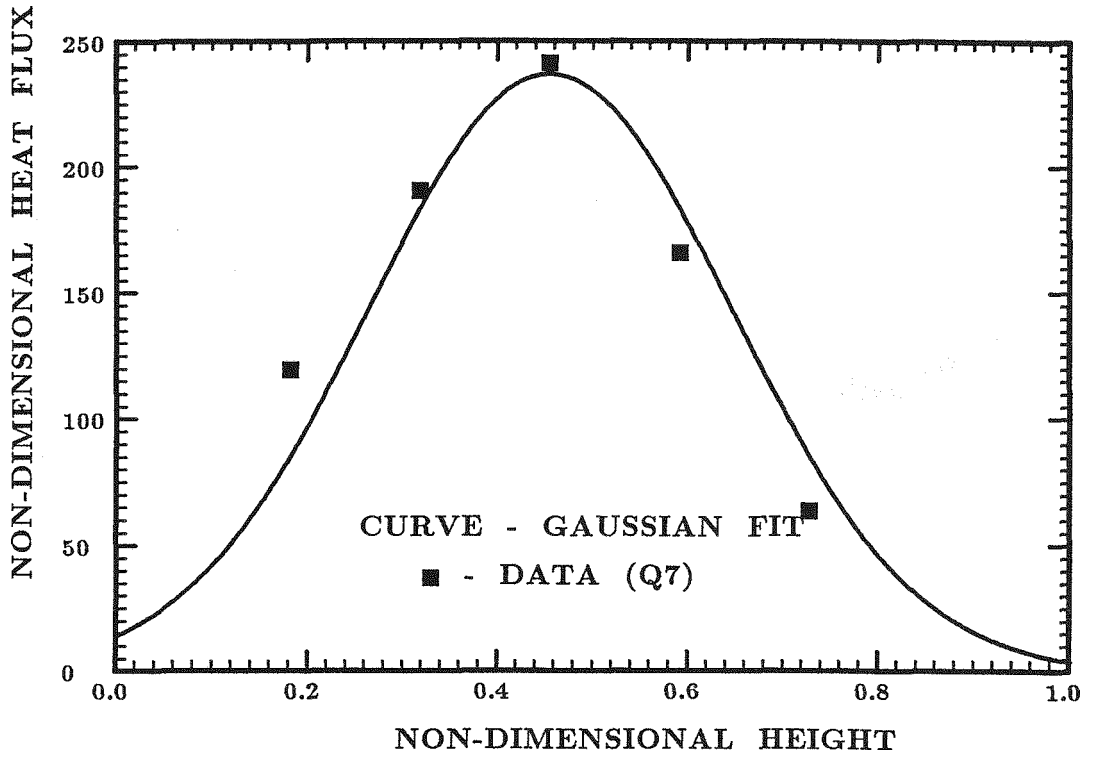

Figure 7.1: Front Face Total Heat Flux vs. Height (Data and Gaussian Curve Fit, Test Run *Q7*)

of the flow test. This resulted in a set of flux values as a function of the two angles (the elevation and the azimuth, see Figure 6.10b) that were assumed to be the fractions of the total energy measured at the copper plate coming from that direction on that particular day. These values now contained the effects of the local solar conditions and the specific concentrator characteristics that the solar furnace demonstrated.

Unfortunately, difficulties were encountered in attempting to measure the flux at non-zero elevation angles. Since the cone angle defined by the concentrator at the test section is relatively large, small errors in the placement of the NIP (most especially the location of the flux gage in the NIP) produced large discrepencies in the readings. Several tests were taken on several different days of clear skies with the concentrator completely illuminated by the helio-

stat. Readings taken only minutes apart varied significantly for elevation angles other than zero. However, due to the position of the attenuator in the full open position (see Figure 6.10), it was difficult to align the NIP with confidence that the attenuator was not interfering with the readings. Also, since the center of rotation of the device that the NIP was mounted on was not precisely at the position of the heat flux gage near the base of the NIP cylinder housing, when the device was adjusted to a different angle, the position of the heat flux gage would not now be at the focus of the concentrator.

Plots of the normalized heat flux data for test run $Q7$ are presented in Figures 7.2a and 7.2b illustrating the significant differences between the zero and non-zero elevation data. Figure 7.2a is the data for an elevation angle of zero while Figure 7.2b is at an elevation angle of 15.2°. Clearly, the variation of the heat flux coming from the concentrator is significant. Since the concentrator is composed of many small *flat* mirrors aligned towards the focal point, misalignment of a set of these mirrors in any one particular area of the concentrator would significantly reduce the flux reading being measured by a limited field of view device such as the NIP. Note that, due to the problems initially observed in measuring the fluxes at non-zero elevations, confidence was less for these readings than for the zero elevation readings.

The readings taken at zero elevation warrant discussion. The maximum heat flux was consistently observed near the left side of the concentrator (if viewing from the focal point towards the concentrator) which corresponds to positive values for the azimuthal angle. The plot shows the fairly smooth yet unexpected variation of the flux for the zero elevation case. Once again, it was believed that this behavior was caused by the alignment of the individual mirrors. Although repeatability was difficult for any of these flux readings, the zero elevation readings showed the same variation for all tests conducted.

Due to the difficulties that were observed for the non-zero elevation data, it was felt that, in order to minimize the potential for inclusion of large sources

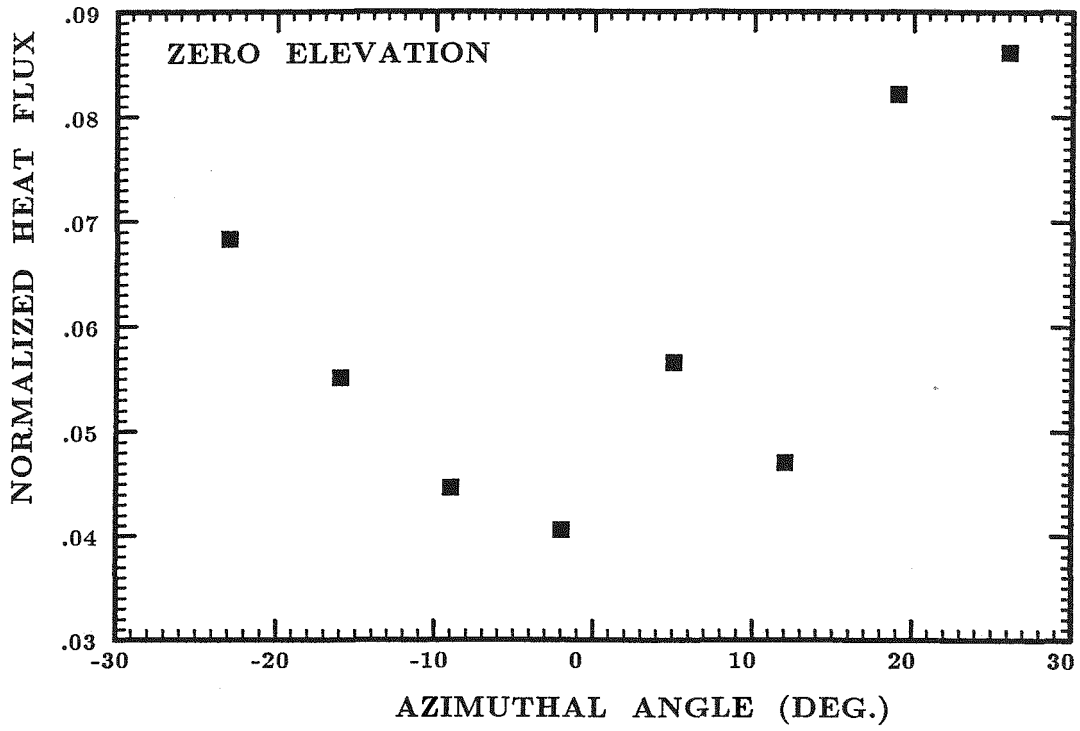

Figure 7.2a: Normalized Angular Front Face Heat Flux Distribution (Test Run $Q7$, Zero Elevation)

of measurement error, only the zero elevation data would be used to estimate the angular flux and intensity functions. Also, as will be discussed later in this Section, the solution of the Fredholm integral problem was more accurate if only the zero elevation fluxes were used (since the differences in the behavior of the zero and non-zero elevation readings were significant). The front face intensity distribution was developed by assuming that the concentrator was symmetric in both the altitudinal (ϕ) and azimuthal (θ) directions. The zero elevation flux readings were used alone to determine the parameters in the intensity and corresponding heat flux models.

7.4.3 Boundary Intensity and Heat Flux Models

Once the normalized angular heat fluxes have been determined for the

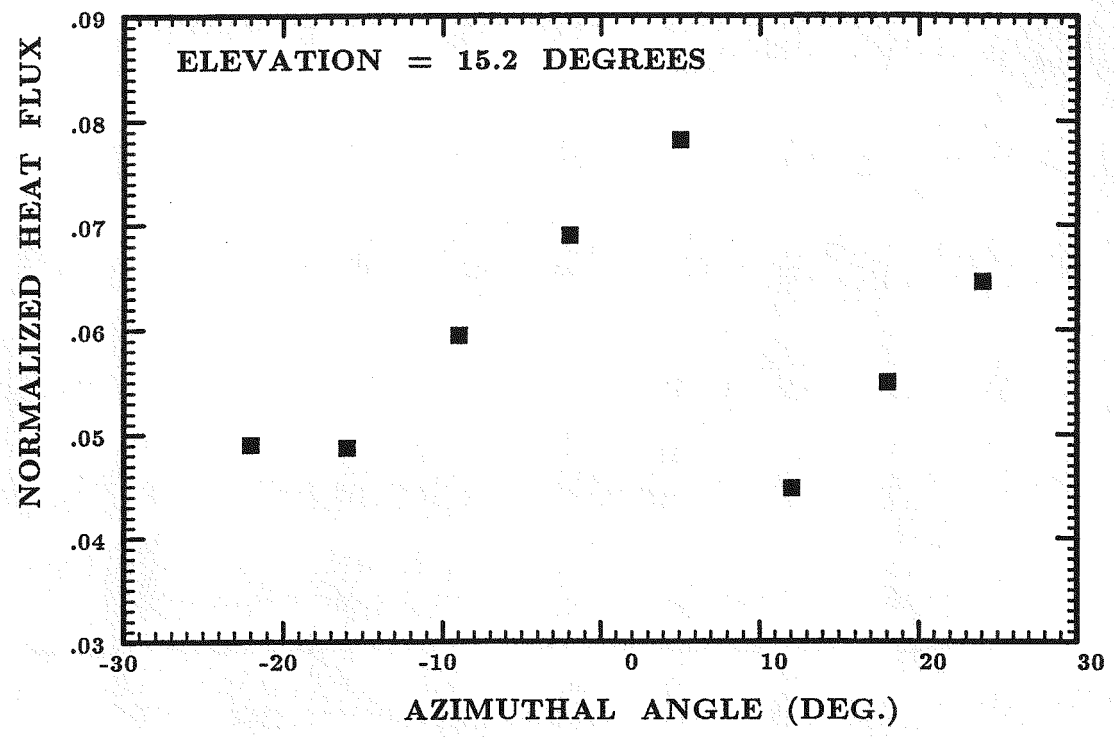

Figure 7.2b: Normalized Angular Front Face Heat Flux Distribution (Test Run *Q*7, 15.2° Elevation)

specific test under consideration, the solution to the Fredholm integral problem is obtained. This is accomplished by assuming a functional form for the boundary intensity and determining which parameter values best fit the heat flux data after the function has been integrated. As was mentioned previously, the concentrator is assumed symmetric about both the vertical and horizontal directions, so the data points from the zero elevation sweep of the NIP are used for the problem.

The choice for the intensity function was made based on the apparent behavior of the concentrator. The expression relating the heat flux to the intensity is

$$q_{i,\lambda}(\mathbf{r_b}, \Delta\theta, \Delta\phi) = \int_{\phi_1}^{\phi_2} \int_{\theta_1}^{\theta_2} I_\lambda(\mathbf{r_b}, \theta', \phi') cos\theta' sin\theta' d\theta' d\phi' \qquad (7.7)$$

where θ is the angle defined by the angular flux data due to the assumption of azimuthal symmetry described earlier.

Notice that, if *sin* or *cos* behavior is observed for the heat flux, assuming a *sin* or *cos* function for the intensity will *not* yield the same function for the flux after integration through Eq. 7.7 above. Initial models attempted to describe the *intensity* in standard trigonometric forms. These models yielded difficult and physically unrealistic flux functions that were incapable of accurately describing the heat flux. Appendix A-1 lists some of the models that were tried for the intensity and their corresponding fluxes.

Eventually, it was decided to choose a simple trigonometric form for the *heat flux.* This was accomplished by choosing a function for the intensity that would deliver the desired heat flux expression after the solid angle integration was performed. The "best" model was observed to be a combination of *sin* and *cos* functions with separate parameters for each term. The model for the intensity was defined as

$$I_\lambda(\mathbf{r_b}, \theta) = \frac{\beta_1}{cos\theta} + \frac{\beta_2}{sin\theta} + \frac{\beta_3}{cos\theta sin\theta} \tag{7.8}$$

which, as observations of the form of Eq. 7.7 indicate, will yield trigonometric forms for the heat flux distribution.

The resulting integrated form of Eq. 7.8 which is the heat flux model is

$$q_{i,\lambda}(\mathbf{r_b}, \theta, \Delta\theta, \phi, \Delta\phi) = \beta_1'(cos\theta_i - cos\theta_{i+1}) + \beta_2'(sin\theta_{i+1} - sin\theta_i) + \beta_3' \tag{7.9}$$

where the new parameters are defined in terms of the non-primed parameters as

$$\beta_1' = \beta_1(\Delta\phi) \tag{7.10a}$$

$$\beta_2' = \beta_2(\Delta\phi) \tag{7.10b}$$

and

$$\beta_3' = \beta_3(\Delta\phi) \tag{7.10c}$$

where $\Delta\phi = \phi_{i+1} - \phi_i$. Since azimuthal symmetry was assumed, $\Delta\phi$ (as well as $\Delta\theta$) represents the field of view of the NIP and is therefore a constant.

Once the model for the intensity distribution has been chosen and it's corresponding heat flux function determined, the parameters are now estimated through a typical OLS (ordinary least squares) parameter estimation routine. As described above, the output of the parameter estimation method will be the primed values of the parameters as defined in Eqs. 7.10. The assumption that these parameter estimates are valid in the intensity function forms the basis of the solution to the Fredholm integral problem.

The routine that was used is part of the IMSL software package and is designed to solve the typical non-square OLS problem. The routine, *LSBRR* and *DLSBRR* for double precision programs, solves a linear least squares problem with iterative refinement. The refinement algorithm is developed in Björk[73],[74]. *LSBRR* calculates the QR decomposition with pivoting of the coefficient matrix. The diagonal elements of the coefficient matrix are tested against a tolerance value to force satisfactory conditioning of the matrix before the iterative refinement process is applied.

Given the data over the angle θ and the functional formulation for the heat flux, the IMSL routine was able to determine values for β_1', β_2' and β_3' that fit the flux data reasonably well. Figure 7.3 is a plot of the results for the test run. The plot shows the flux as a function of the angle θ. The results of the parameter estimation routine are plotted (curve) along with the actual data (points). The average error magnitude, defined in terms of the total number of data points used, N, as

$$e_q = \frac{\sum_{i=1}^{N} |q_{data} - \hat{q}|}{N} \tag{7.11}$$

for all of the test runs[1] was 9%.

[1] Recall that the data for these tests are the angular concentrator flux values normalized by the average total flux reading for a given test run. Consequently, the error associated with

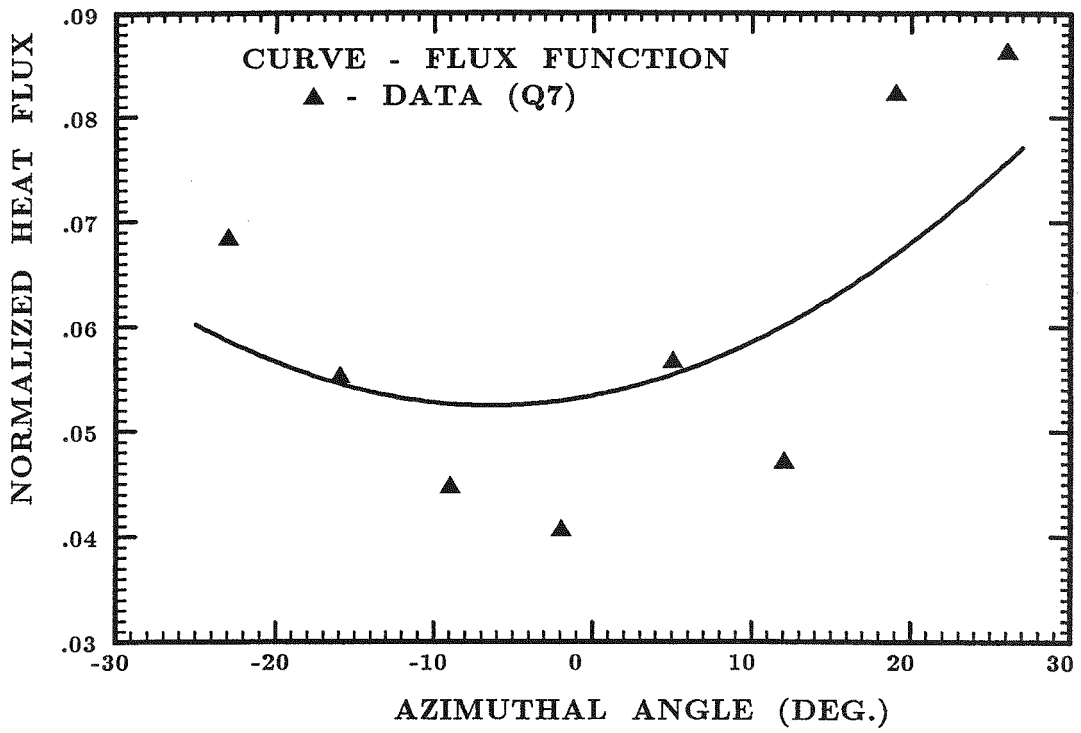

Figure 7.3: Comparison of Front Face Data to Estimated Flux Distribution (Test Run *Q*7)

It was necessary to determine the parameters that best fit the data for all flow tests conducted. The determination of the parameters for the boundary intensity distribution is performed in a separate program than the main program which is the EOT/energy conservation solver. The parameter set is fed into the main program and the model for the intensity is used to determine the intensity in the ordinate directions. Since the intensity model is couched in terms of the angles involved with the NIP experiments, the angles that correspond to the discrete ordinate direction cosines are calculated by projecting the ordinates down onto the same set of axes that was used for the NIP experiments.

It should be noted that, even though one half of the ordinates of each

---

the estimation routine will always be the same, regardless of the value of the average total flux.

set correspond to forward directions (i.e., into the curtain at the front face), only a few of these will represent angular directions that fall within the total solid angle subtended by the solar furnace concentrator at the test stand. Consequently, for the S_4 approximation (12-flux), only 3 ordinates correspond to allowable directions for the geometry of the system. The S_6 (24-flux) approximation contains 6 acceptable directions while the 2-flux model contains no allowable directions. Intensities along forward directions that do not fall within the concentrator solid angle are set to zero. In this way, the 2-flux discrete ordinates approximation cannot be applied. Once all the ordinate direction cosines have been broken down into their respective angles, the model calculates the intensities for those angles within the prescribed concentrator cone angle. The result is an intensity distribution that is zero for most directions (i.e., those that are "backward" facing and those that lie outside the proper field of view) and positive for all of the others.

7.4.4 Numerical Check of the Boundary Intensity Model

In an effort to illustrate some measure of accuracy of the boundary intensity model, after the intensity distribution was calculated for the front face boundary, the *total* heat flux along the boundary was "re-calculated" by numerically integrating the intensity values (not by using the analytically integrated intensity function). The expression relating the intensity to the heat flux is written in Gaussian quadrature formulation as

$$\hat{\hat{q}}_\lambda(\mathbf{r_b}) = \sum_{i=1}^{N} w_i I_{i,\lambda} \Omega_i \tag{7.12}$$

The results of this calculation should reproduce the total heat fluxes measured at the front face for a particular flow test. The plots for these calculations are presented in the next Section along with the model's estimation of the measured transmitted fluxes for each of the flow tests that produced "good" data

(i.e., data that displayed fairly constant flux readings both during the flow and after cessation of the flow).

7.5 Transmitted Flux Comparisons (Model and Data)

The measurements of the transmitted flux at each of the vertical flux gage locations on the copper plate are compared with the flux predictions by the model. The results are presented in this Section.

Tests were conducted for a range of curtain thicknesses that fall within the allowable values as dictated by the effectiveness of the temperature measuring device. Results are presented graphically in two separate plots for each test run. The first plot illustrates the incident flux measurements and the numerical "re-calculation" of the front surface flux obtained by integrating the boundary intensity distribution over solid angle as described above. The transmitted flux through the particle curtain, both the data and the numerical predictions, are presented in the second plot. The plots are presented in order of increasing curtain thickness with both plots for a given test presented together.

Experimental error bounds are presented in each of the plots for the flux data points that are included. The measurement errors in the flux data are primarily caused by two major factors: 1.) the inherent error associated with the circular foil heat flux gage (usually this error is biased above the actual flux value due to lack of precise information concerning the absorption qualities of the black coating) and 2.) errors that were observed due to imperfect orientation of the solar beam on the copper plate.

The second of these error terms, which is difficult to quantify, is mostly caused by changes in the heliostat alignment due to tracking adjustments. These changes often have the result that the flux distribution on the plate before the change is slightly different than the distribution that is recorded after the adjustment has occurred. For the data presented in this Section, the heliostat was both manually adjusted (in an effort to reduce this orientation er-

ror) and automatically adjusted with the tracker. In both cases, the orientation error was observed.

Quantitatively, the inherent flux gage error is usually approximated as $\pm 5\%$ of the maximum rated capability of the flux gage. The orientation error, for purposes of necessity, was also assumed to be $\pm 5\%$ of the rated maximum. These errors were combined in a root sum squares (RSS) sense (i.e., $\omega_q = \sqrt{\omega_{gage}^2 + \omega_{orientation}^2}$, where ω represents the uncertainty value of the indicated quantity) to yield the overall measurement error for any given flux gage reading. The actual determination of the error bounds that are shown in the plots is discussed in the next Section.

7.5.1 Thin Curtain Results

Two sets of data were used for comparisons that had curtain thicknesses less than 3.5 mm. Data from two test runs, $Q7$ and $Q8$, are compared with the predictions determined by the model. The results are presented in Figures 7.4 and 7.5 for $Q7$ and 7.6 and 7.7 for $Q8$. All the plots in this section have the vertical axis defined as a non-dimensional heat flux

$$\hat{q} = \frac{\mathbf{q_r}}{\sigma T_{inlet}^4} \tag{7.13}$$

where $\mathbf{q_r}$ is the total radiative heat flux at that particular vertical location and T_{inlet} is the uniform inlet curtain temperature obtained through measurements taken with the temperature measuring device before the attenuator of the solar furnace had been opened.

The horizontal axis is the non-dimensional vertical distance defined as

$$\hat{y} = \frac{y}{L_y} \tag{7.14}$$

As was discussed earlier, after obtaining a front face intensity distribution by estimating the parameters that appeared in the integrated heat flux

form of the assumed intensity distribution, the front face heat flux was "re-calculated" (i.e., the integral performed using Gaussian quadrature as defined by the discrete ordinates approximation) to provide some information regarding the accuracy of the intensity distribution. Since the forcing function for the initial parameter estimation of the heat flux was obtained by curve fitting a Gaussian type function to the measured data, the "re-calculated" fluxes exhibit this Gaussian shape also.

The error bounds that are shown in the plots are determined by considering the flux reading uncertainty, ω_q (discussed in the previous Section) along with the uncertainty in the measurement of the inlet particle temperature. The final error value is determined through a standard Kline-McLintock[75] analysis according to the following expression

$$\omega_{\left(\frac{q}{\sigma T_{inlet}^4}\right)} = \sqrt{\left(\frac{\partial\left\{\frac{q}{\sigma T_{inlet}^4}\right\}}{\partial q}\right)^2 \omega_q^2 + \left(\frac{\partial\left\{\frac{q}{\sigma T_{inlet}^4}\right\}}{\partial T_{inlet}}\right)^2 \omega_{T_{inlet}}^2} \qquad (7.15)$$

Since the particles and the thermocouple funnel were given sufficient time to reach ambient temperature before a flow test, and since the particles were flowing for several seconds before the attenuator was opened, the measurement errors associated with the *inlet* particle temperatures were assumed to be only a factor of the inherent errors in the hypodermic thermocouples, $\pm 1°C$. Given the values for the temperature errors and the flux errors described above, Eq. 7.15 is used for every data point to determine the upper and lower bounds on the flux readings presented in the plots to follow.

Figures 7.4 and 7.6 are the plots of the front face heat fluxes as a function of the vertical height along the copper flux gage plate for test runs $Q7$ and $Q8$ respectively. In both Figures, it is apparent that the numerical prediction of the local heat flux overestimates the measured values at all locations on the plate. A clear increase in accuracy is shown with the higher order (S_6) discrete

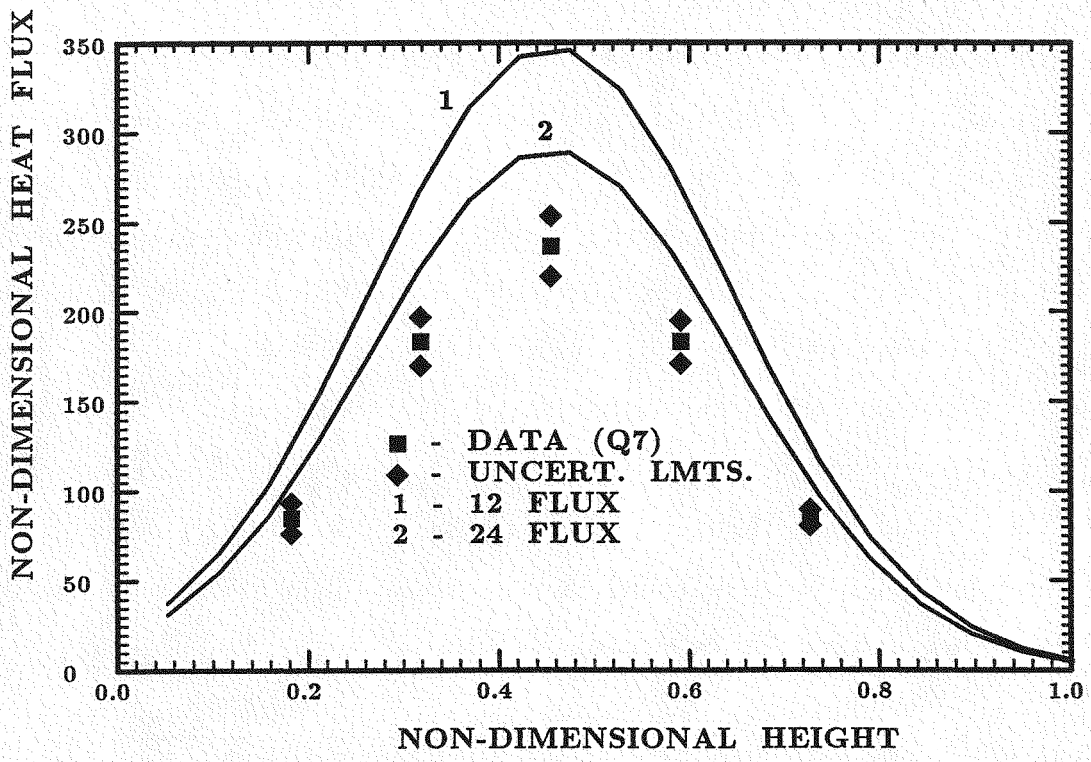

Figure 7.4: Non-Dimensional Front Face Heat Flux Comparison (Test Run $Q7$, $L_x = 3.175mm$, Thin Curtain)

ordinates model.[1]

The deviations for Figures 7.4 and 7.6 range from a minimum of 17.8% to a maximum of 27.6% for the S_6 (24-flux) approximation. Even though it appears in the Figures that the maximum deviation occurs at or near the center of the flux gage plate, the actual error magnitude is similar for all of the flux gage readings. It should be noted that, in the discussion to follow for the rest of this Section, all deviations are those between the 24-flux (S_6) approximation and the data. Since the higher order approximation is clearly more accurate and the computational requirements associated with running the S_6 approximation are not significantly more costly, the 24-flux model is used for all comparisons.

[1] Recall that, for the 24-flux approximation, only 6 directions fall within the solid angle defined by the field of view of the concentrator at the test section.

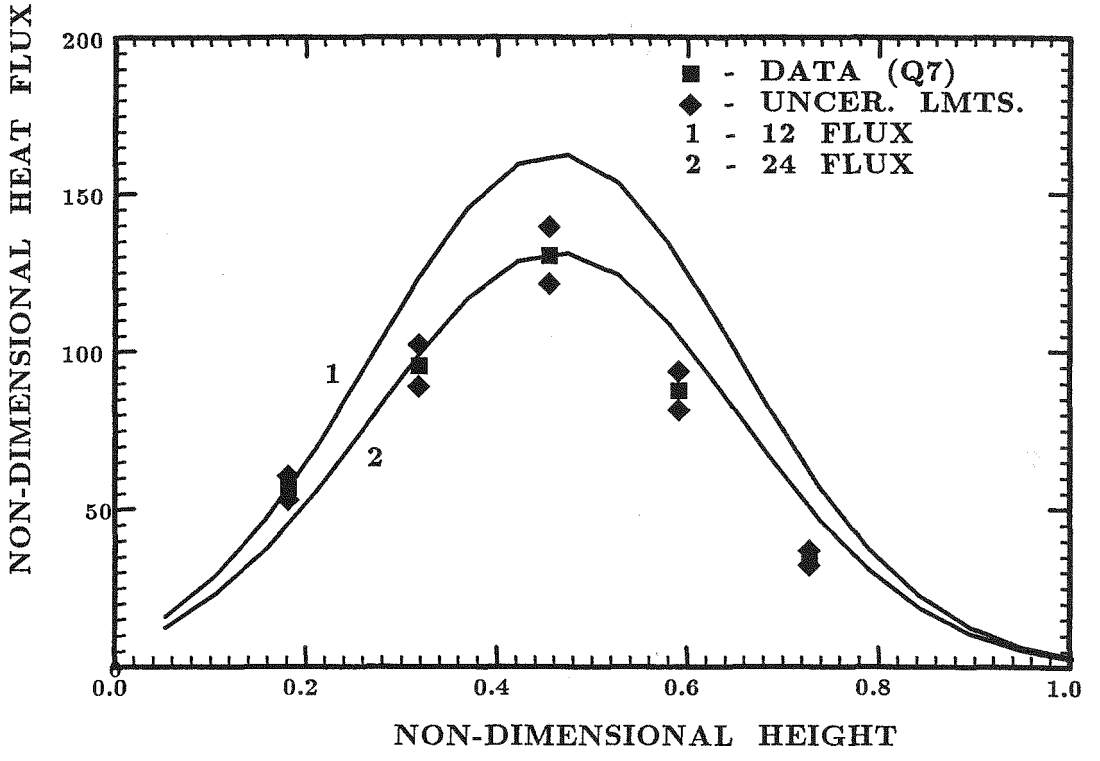

Figure 7.5: Non-Dimensional Transmitted Flux Comparison (Test Run $Q7$, $L_x = 3.175mm$, Thin Curtain)

It is clear from the Figures that the "re-calculation" of the front face flux through the integration of the intensity distribution values overestimates the actual flux measurements. In all of the subsequent Figures (the even numbered Figures are the front face fluxes, odd numbered Figures indicate transmitted flux), the model overestimates the measured heat flux. Recall that, in the discussion of the concentrator characterization experiments, one "sweep" of the concentrator consisted of approximately 50°. The intensity model parameters (obtained through estimation from the flux data) are determined over this angular range. However, the discrete ordinates model, for both the 12- and 24-flux approximations will only have a few angles that will fall within the limited field of view of the solar furnace system. Typically, estimations of data through the use of some known function with a set of parameters will, over the range of the

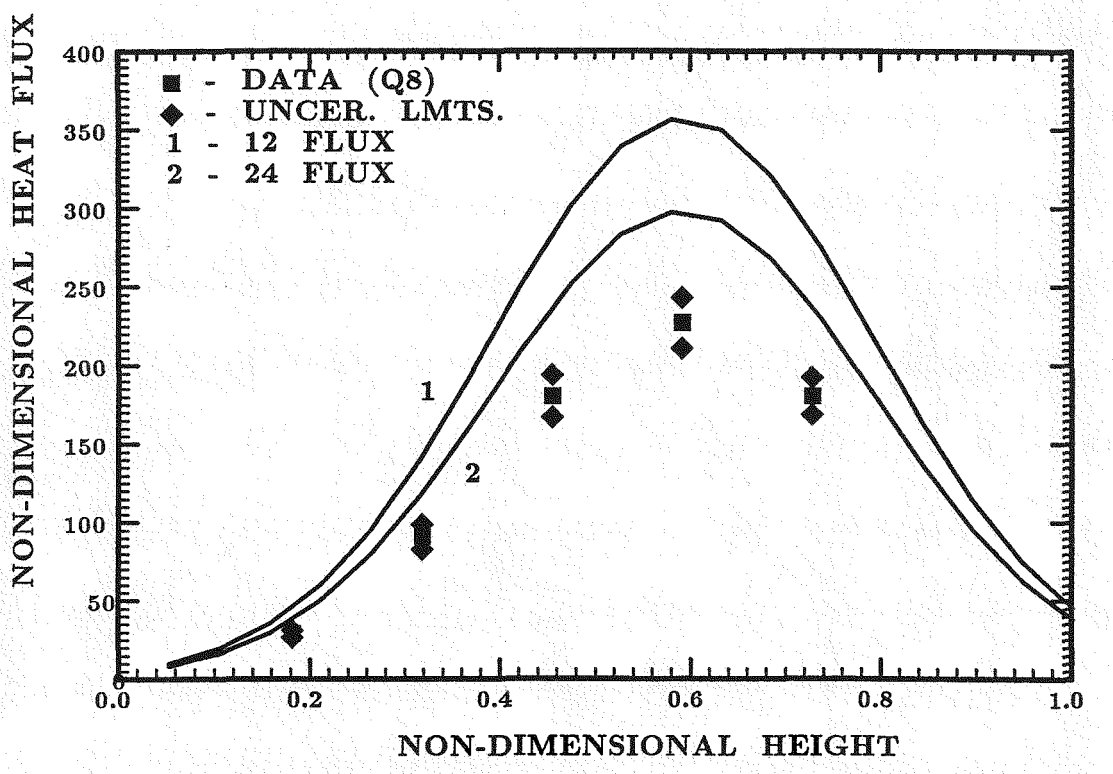

Figure 7.6: Non-Dimensional Front Face Heat Flux Comparison (Test Run $Q8$, $L_x = 3.175mm$, Thin Curtain)

independent variable used, have regions of both overestimation and underestimation. It is conceivable that, for the small set of angles used in the discrete ordinates model (3 for the S_4 and 6 for the S_6 sets), the intensity distribution is in a region of overestimation of the data by the function. This would have the effect of causing the model to always overestimate the front face flux data as it seems to do in all of the even numbered Figures.

Also, recall that the inaccuracies involved with the determination of the front face flux from a numerical integration of the intensity field are additive through the calculations that were performed to reach these values. Initially, the front face flux data were curve fit using a Gaussian function. Then, the parameters that appear in the analytical integration of the intensity field were determined using this Gaussian representation of the data along with the re-

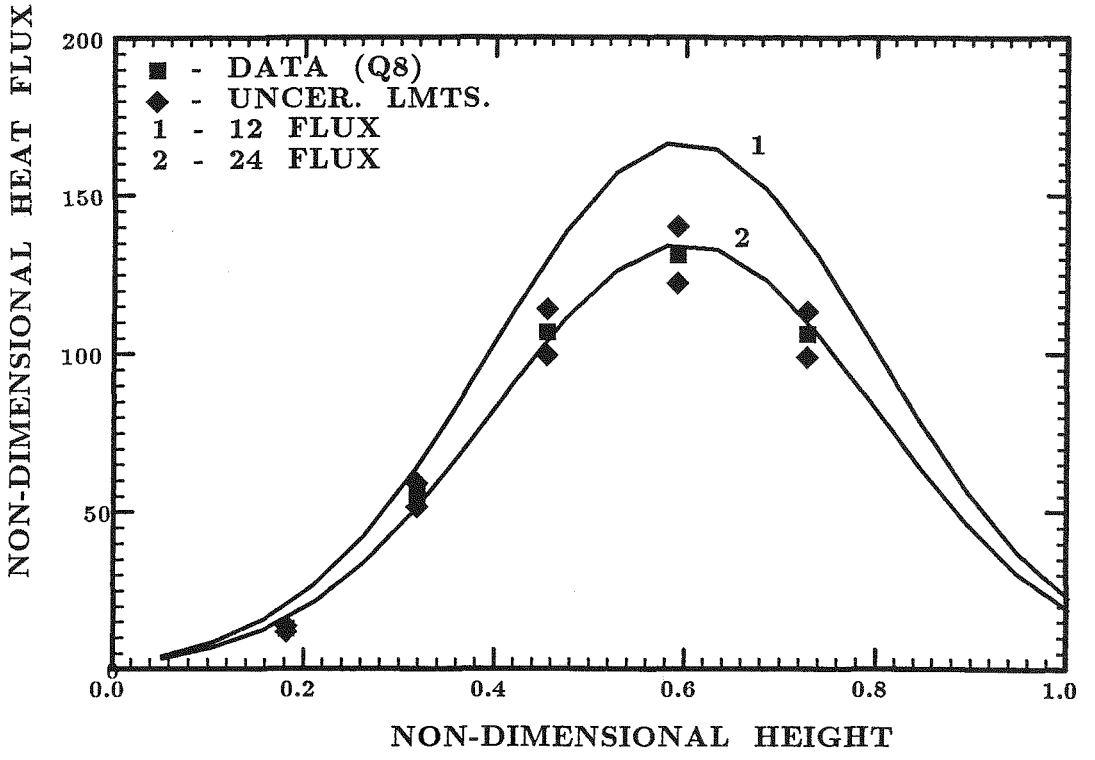

Figure 7.7: Non-Dimensional Transmitted Flux Comparison (Test Run $Q8$, $L_x = 3.175mm$, Thin Curtain)

sults from the concentrator characterization tests. Next, the intensity field was determined by projecting the ordinates down onto the coordinate axes and evaluating the intensity function, with the parameters found previously, at the resulting angles. Finally, to obtain the re-calculated fluxes, these numerical intensity values were integrated using Gaussian quadrature. Clearly, the numerical errors involved with this set of computational steps could cause the final solution (the curves in the plots of the front face fluxes) to be inaccurate.

However, for all of the front face plots presented in this Section, the largest deviation of the model from the data is the 27.6% observed at the position of the first data point in Figure 7.6 (test run $Q8$). This would seem to indicate that the intensity model chosen and the predicted parameters determined from the flux data produced results that were acceptable.

For the thin curtain trials ($Q7$ and $Q8$), the results of the model in predicting the transmitted flux distribution are also reasonable. The deviations ranged from a low of -0.5% at the peak reading in Figure 7.5 to a high of 24.8% near the top of the plate ($\hat{y} \approx 0.2$) in Figure 7.7.

The deviations in these two Figures are maximum near the plate edges for both trials and become small near the center. Notice that, although the front face boundary flux calculations consistently overestimated the data, the transmitted flux predictions do not. In Figure 7.5, the model initially under-predicts the transmitted flux. It eventually passes through a point where, if the Gaussian curve fit of the data was shown, it would cross this curve ($\hat{y} \approx 0.3$). For the rest of the flux readings from $\hat{y} \approx 0.3$ to the bottom of the plate at $\hat{y} = 1$, the model over-predicts the data.

In Figures 7.6 and 7.7, the shape of the flux data deviates slightly from what was noticed in the previous two plots. The peak reading for this test, as is clear from an observation of the front face flux in Figure 7.6, is offset with the maximum reading occurring at $\hat{y} = 0.6$. Obviously, the test stand and the flow device were not correctly aligned vertically. From the Figures, the model seems to do a reasonable job of reproducing this offset flux profile and predicts the fluxes with small error ($< 10\%$) over most of the flux gage plate from $\hat{y} \approx 0.3 \rightarrow 1$. The ability of the model to accurately predict the flux shapes comes from the use of the front face flux data to obtain a Gaussian curve fit. Recall that, in these curve fits, the location of the peak was one of the parameters that was determined. This information resulted in the determination of the boundary intensity profile. Consequently, the model is capable of predicting reasonable flux shapes even when the solar "spot" has been incorrectly aligned.

7.5.2 Intermediate Curtain Thickness Results

The front face flux plots for the intermediate curtain thickness tests, as expected, show that the model also provides reasonable predictions of the bound-

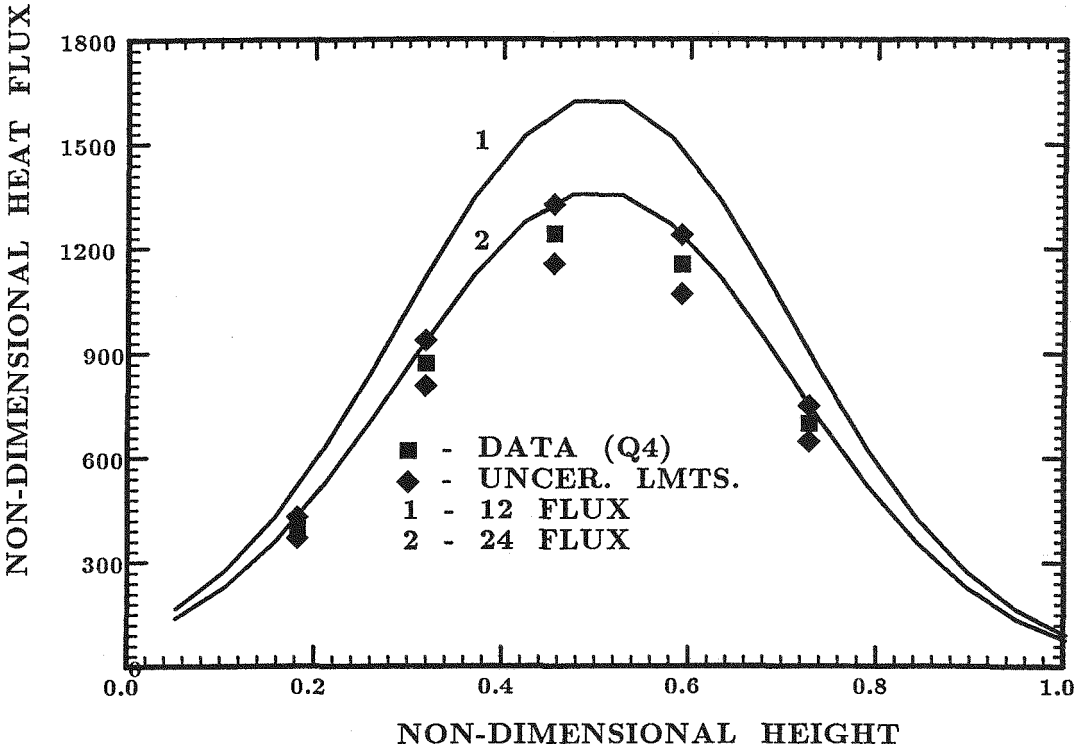

Figure 7.8: Non-Dimensional Front Face Heat Flux Comparison (Test Run $Q4$, $L_x = 4.366mm$, Intermediate Curtain)

ary intensity distribution. The intermediate curtain tests are designated $Q4$, $Q5$ and $Q16$. The deviations between the 24-flux approximation and the measured data range from 3.8% to 9.4% for the three plots. Once again, the errors were slightly larger near the edges of the plate than in the center and, at all points, the model overestimated the data for both the 12- and 24-flux approximations. In all of the front face flux plots (for all thicknesses), the model not only predicts the flux data values but it also seems to match the slope of the curve with reasonable accuracy.

The transmitted flux plots (Figures 7.9, 7.11 and 7.13) show results similar to the thin curtain plots. However, the maximum deviations exhibited on this plot are significantly higher than those for the thin curtain cases. Once again, the maximum errors occur near the plate boundaries. Edge errors for the three

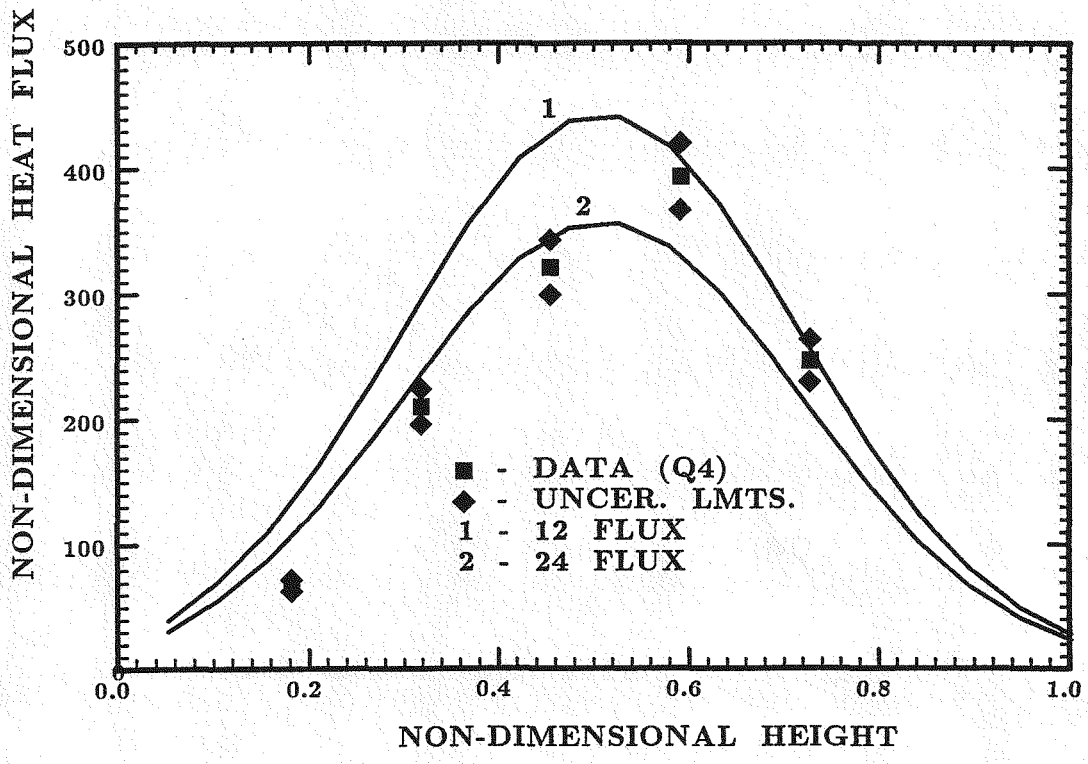

Figure 7.9: Non-Dimensional Transmitted Flux Comparison (Test Run $Q4$, $L_x = 4.366mm$, Intermediate Curtain)

plots shown are 38.6% ($Q4$), 59.9% ($Q5$) and 76.1% ($Q16$). As is clear from the plots, the errors near the data point at $\hat{y} \approx 0.2$ are the largest. Near the peak reading, errors ranged from -23% to 5.4%. Notice that, in all three plots, the peak reading seems to have moved from somewhere between the second and third readings ($\hat{y} \approx 0.5$) to the location of the third flux gage at $\hat{y} = 0.6$. This apparent propagation of the peak reading can be attributed to changes in the position of the heliostat. The solar tracking system can slightly alter the position of the heliostat such that the peak flux is not kept exactly at the center of the plate. This adjustment can occur after the transmitted readings have been recorded but before the hopper is emptied of particles. The front face fluxes are recorded at this time. This behavior is noticed in all of the transmitted flux plots except Figures 7.5 and 7.7 which are the results of

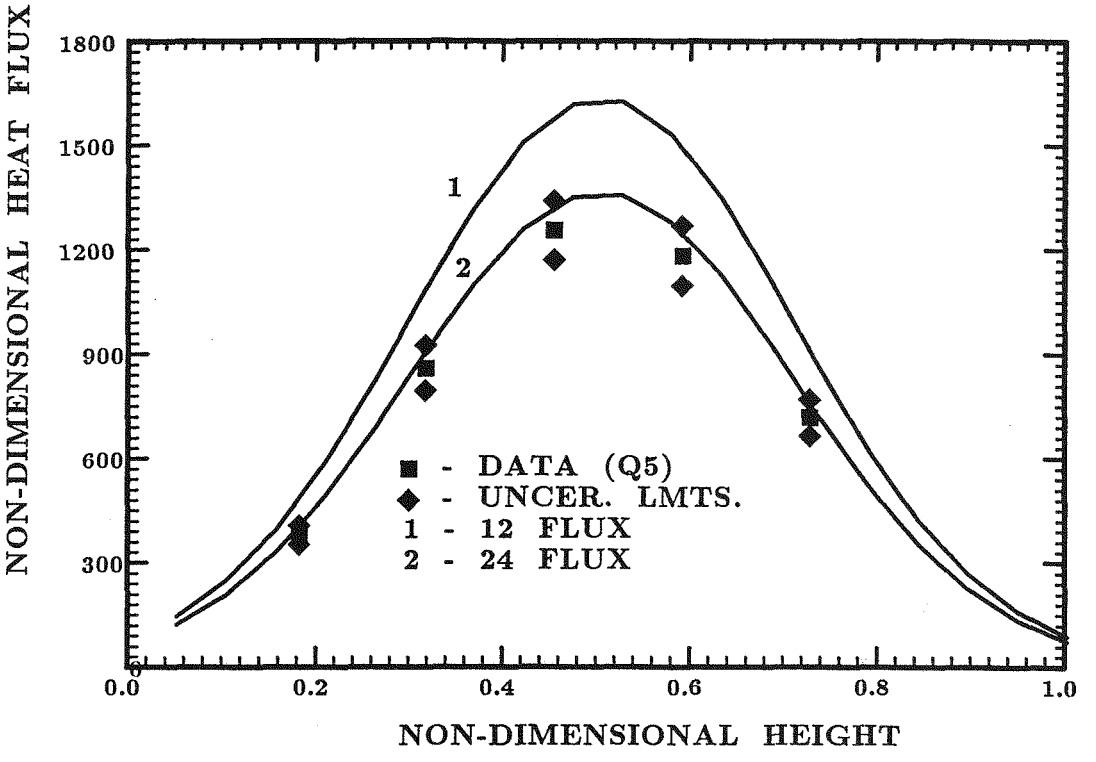

Figure 7.10: Non-Dimensional Front Face Heat Flux Comparison (Test Run $Q5$, $L_x = 4.366mm$, Intermediate Curtain)

the thin curtain tests although, in other preliminary tests with thin curtains, tracking adjustment error **was** observed. Consequently, the indications are that curtain thickness plays *no role* in terms of these tracking adjustment errors.

The movement of the peak certainly plays a significant part in explaining the large errors near the top of the plate. As the Figures indicate, the peak reading moves to a location lower on the flux gage plate (i.e., $\hat{y}_{p_{trans}} > \hat{y}_{p_{incident}}$). This has the effect of producing a flux reading at the topmost location ($\hat{y} = 0.2$) that is low. As stated above, the model overestimates the data consistently (which occurs for all of the plots in which the peak reading moves between the recording of the transmitted and incident fluxes). It is thought that these deviation values are not indicative of the ability of the model to estimate the edge fluxes but rather are caused by the adjustment of the heliostat in between flux

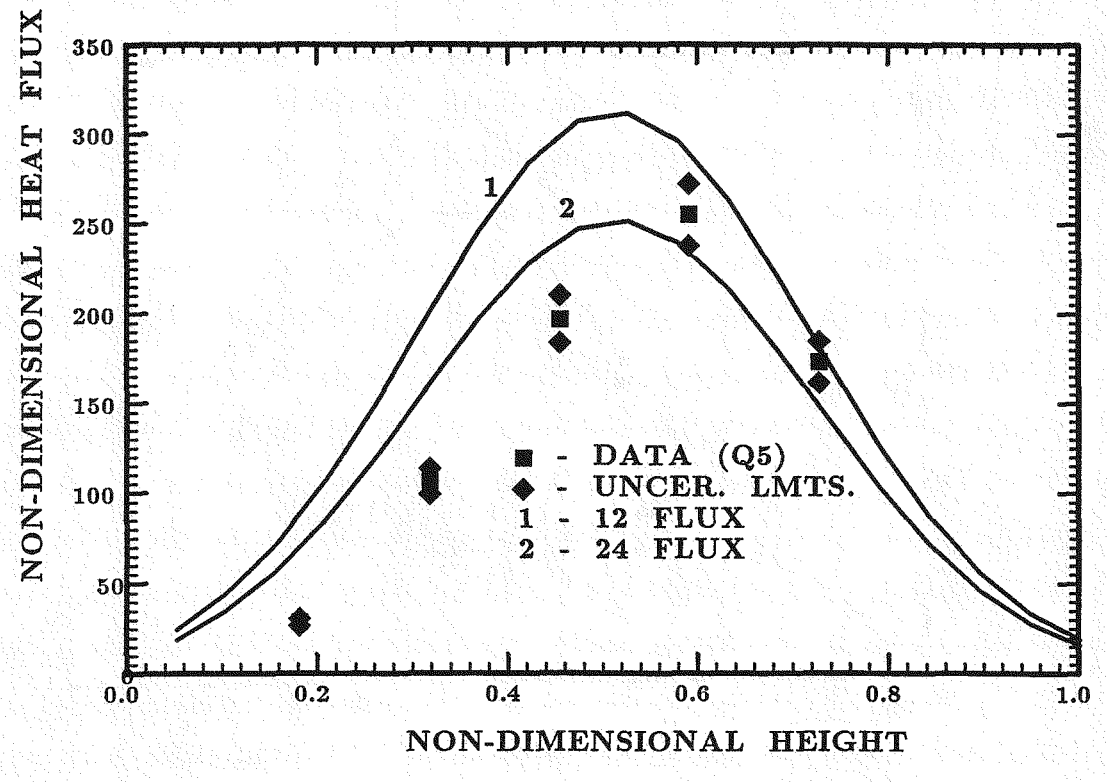

Figure 7.11: Non-Dimensional Transmitted Flux Comparison (Test Run $Q5$, $L_x = 4.366mm$, Intermediate Curtain)

readings. As was illustrated in the thin curtain plots (Figures 7.5 and 7.7) in which this peak reading movement is not observed, the errors associated with the model predictions are much lower.

The errors near the peak for the three intermediate plots are much more reasonable. However, this is also slightly misleading since the model peak value and the data peak value don't coincide. If the errors near the center of the plate are "re-calculated" as the percentage difference from the peak value of the model to the peak value of the data, the errors are reduced significantly for the plots of test runs $Q4$ (from -23% to -10.4%) and $Q5$ (from -12.4% to -1.4%). The error in Figure 7.13 (test run $Q16$) increased slightly from 5.4% to 7.6%. This suggests that, if the data were somehow recorded simultaneously such that adjustments to the heliostat made by the tracking system did not

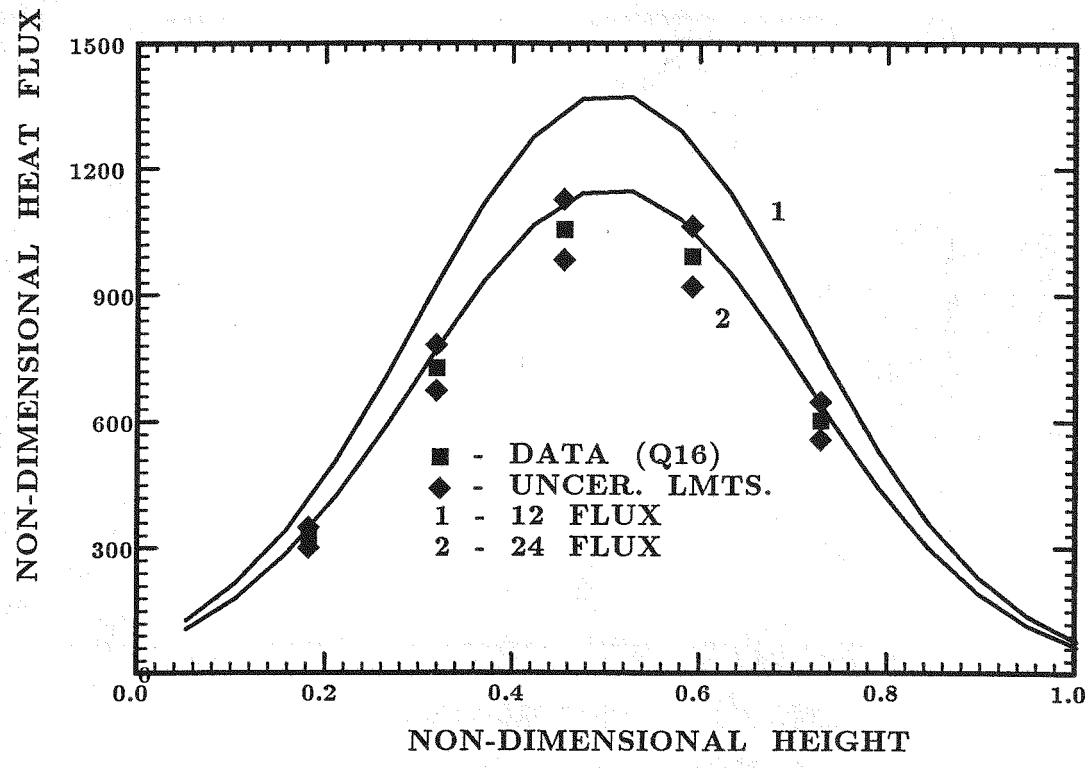

Figure 7.12: Non-Dimensional Front Face Heat Flux Comparison (Test Run $Q16$, $L_x = 5.556mm$, Intermediate Curtain)

effect the readings, the model predictions would be more reasonable.

7.5.3 Thick Curtain Results

As was noticed before, the model provides a reasonable prediction of the front face heat fluxes for the test runs for the thick curtains. Figures 7.14, 7.16 and 7.18 are the results for the incident flux profiles for test runs $Q12$, $Q17$ and $Q15$ that correspond to curtain thicknesses of 5.95 mm, 6.747 mm and 7.54 mm, respectively. Maximum and minimum errors for the model predictions of the incident flux in each of the Figures are 14.4%, 10.1% for Figure 7.14, 11%, -2.2% for Figure 7.16 and 14.7%, 13.8% for Figure 7.18. Notice that, in all three Figures, the peak of the curves (both for the data and the model) appears to lie between the second and third flux gage locations in the vicinity

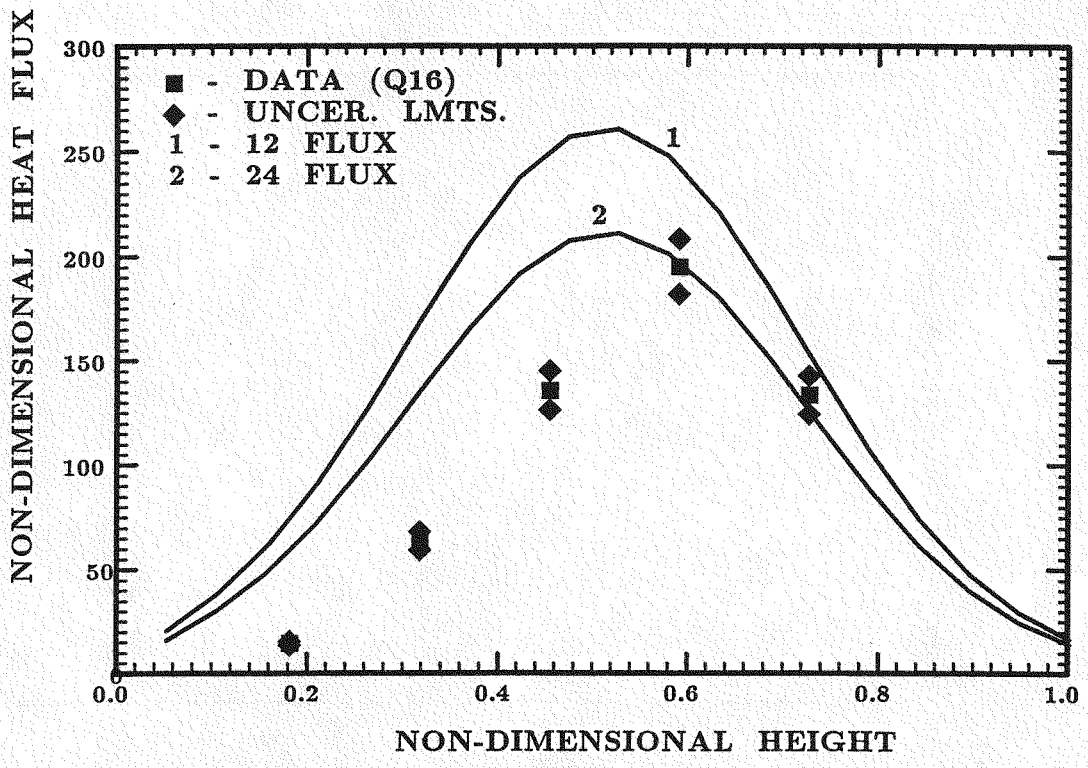

Figure 7.13: Non-Dimensional Transmitted Flux Comparison (Test Run $Q16$, $L_x = 5.556mm$, Intermediate Curtain)

of $\hat{y} \approx 0.5$. As the transmitted flux Figures show, the movement of the peak due to tracking adjustments seems to have occurred in these three tests also.

Figures 7.15, 7.17 and 7.19 are the plots of the transmitted flux data and the model predictions of the flux for test runs $Q12$, $Q17$ and $Q15$, respectively. These tests are the results of curtain thicknesses that were close to the maximum particle flow rate that the temperature device could handle. Also, at the increased particle flow rates for these thicker curtains, the particle supply in the hopper would be exhausted so quickly that obtaining reasonable transmitted flux data became difficult.

Test run $Q15$ represented the upper limit on curtain thickness with a thickness of 7.54 mm. At this thickness, it was only possible to obtain three complete sets of transmitted flux data that displayed the necessary leveling off in order

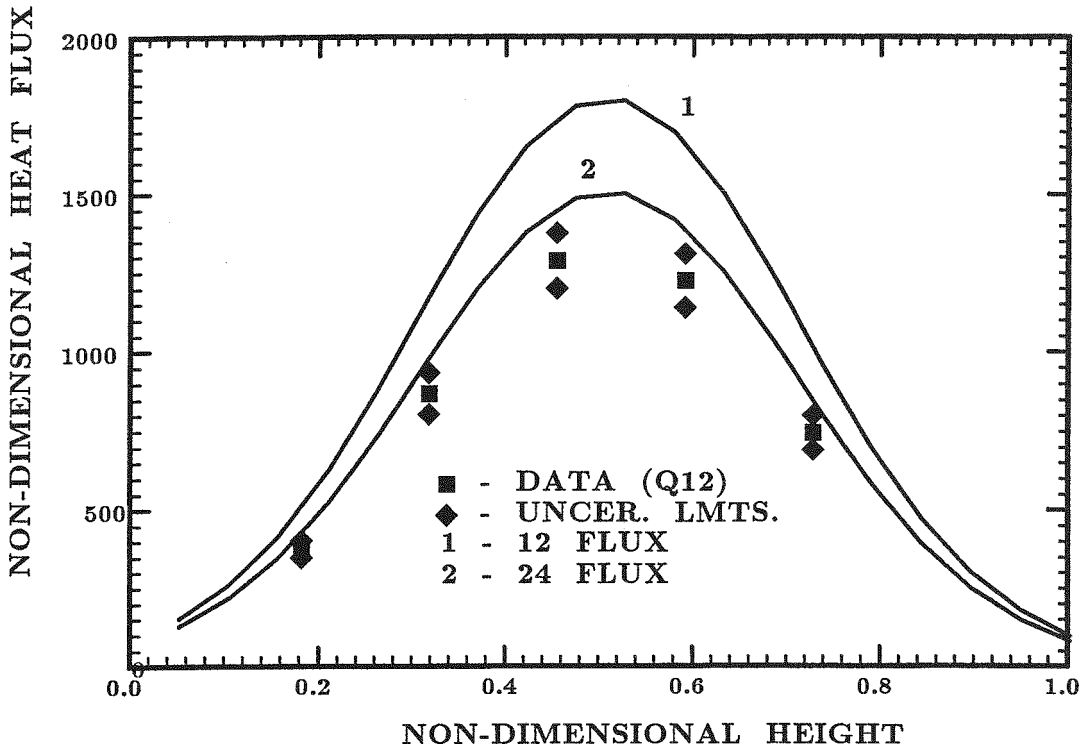

Figure 7.14: Non-Dimensional Front Face Heat Flux Comparison (Test Run $Q12$, $L_x = 5.95mm$, Thick Curtain)

to be considered steady-state. Recall that, due to the slow response of the flux gages, the transmitted readings for each test slowly increased from the moment the attenuator was completely opened and eventually leveled off. In some cases, the flux readings did not level off before the flow ceased when the hopper emptied. The readings at this leveling off point were considered the actual transmitted fluxes. Then, as the hopper supply was exhausted, the readings once more ramped up until they leveled off at the incident flux readings. Some readings were taken at curtain thicknesses greater than 7.54 mm (i.e., 9.128 and 9.92 mm), but the data from these readings did not level off before the hopper emptied.

Errors for these runs are maximum at the first flux gage location (as is true of all of the plots in which the peak reading appears to have propagated

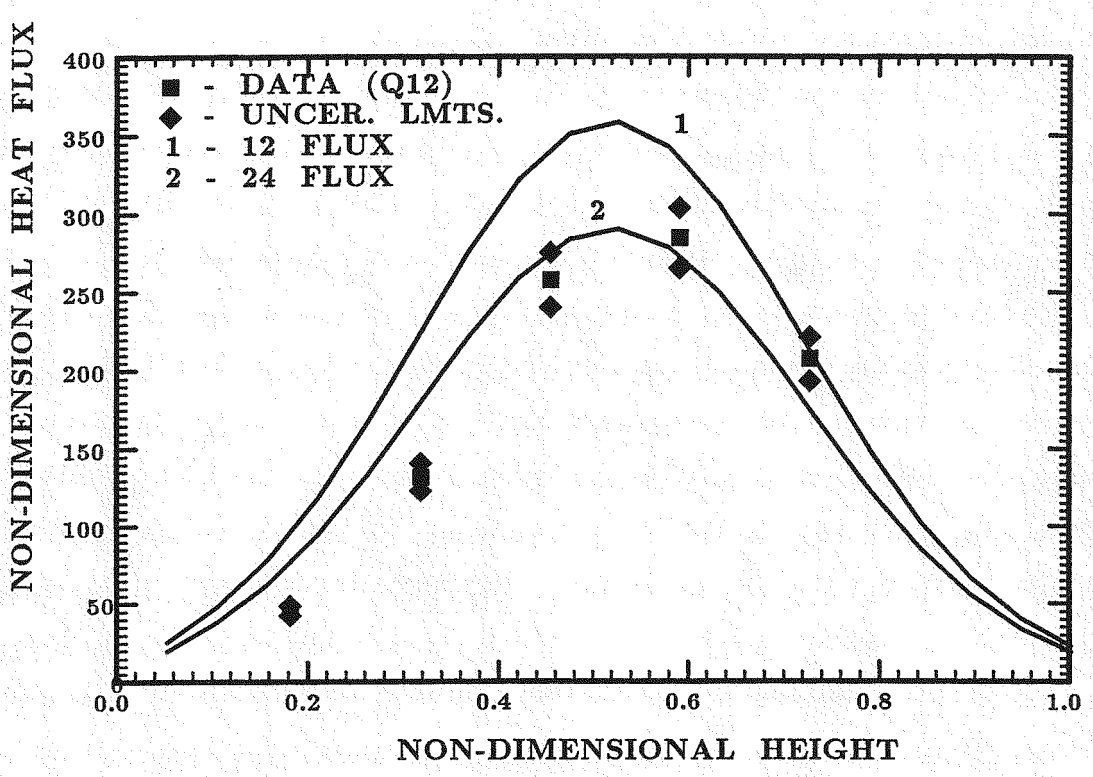

Figure 7.15: Non-Dimensional Transmitted Flux Comparison (Test Run $Q12$, $L_x = 5.95mm$, Thick Curtain)

downward). The error values at these locations are 41.9%, 69.9% and 22.1% for Figures 7.15, 7.17 and 7.19, respectively. Errors at the apparent location of the peak for each of the Figures are -7.6%, -43.6% and 1.9%, respectively. As was noticed for the intermediate curtain results, if the errors are calculated between model peak and data peak, the errors are changed to -2.1%, -27.4% and -4.7%, respectively. Notice that significant improvements are noticed for two of the three plots while the error in Figure 7.19 is reasonable for both calculations.

As is clear in Figure 7.17, the data readings at flux gage locations 4 and 5 (the peak reading and the next lower one), appear to be inconsistent with the first three readings. This may be attributable to the tracking adjustments mentioned earlier. Clearly, the errors between the model and the data for

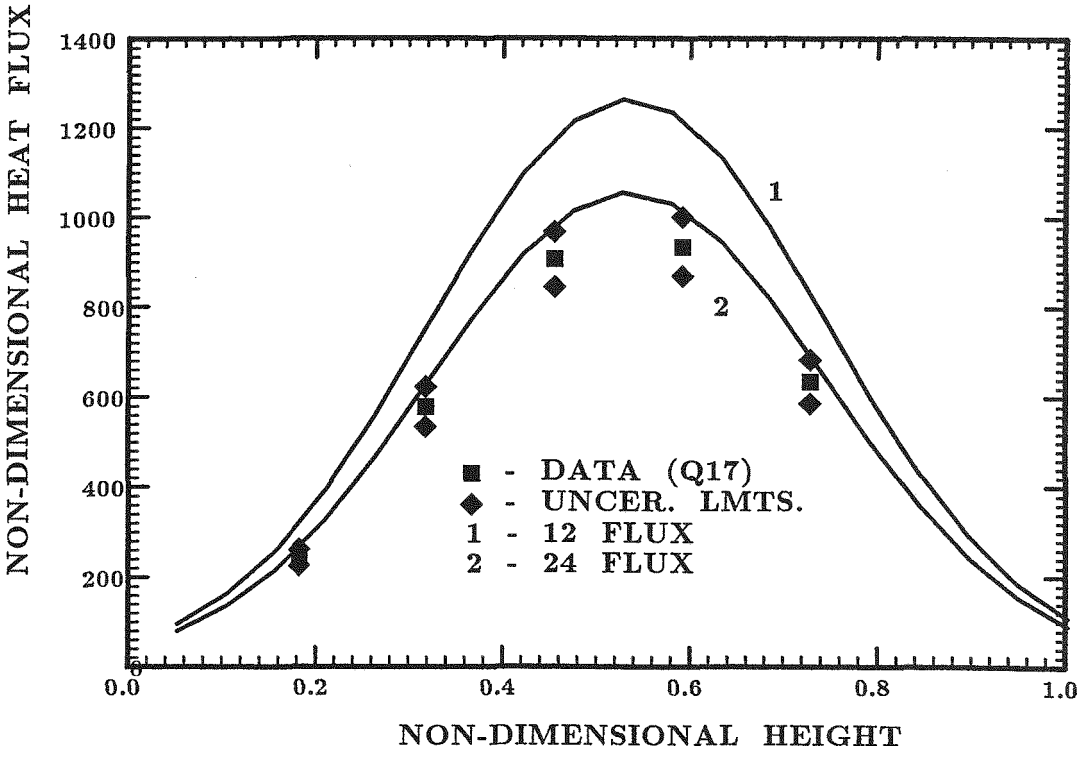

Figure 7.16: Non-Dimensional Front Face Heat Flux Comparison (Test Run $Q17$, $L_x = 6.747mm$, Thick Curtain)

these two locations are not representative of the performance of the model as is indicated in the other plots. It may be deduced that the experimental error associated with the data presented in Figure 7.17 is comparitively larger than for the other test runs presented in this Section.

7.6 Average Exit Temperature Comparisons (Model and Data)

The results of the solution of the conservation of energy expression are presented in this Section. The temperature distribution is calculated by the model simultaneously with the EOT and, as was described in previous Chapters, the process is repeated until the intensity and temperature fields converge to a prescribed tolerance from one iteration to the next. The measurements of the average exit temperature of the particles, as was also described previously, were

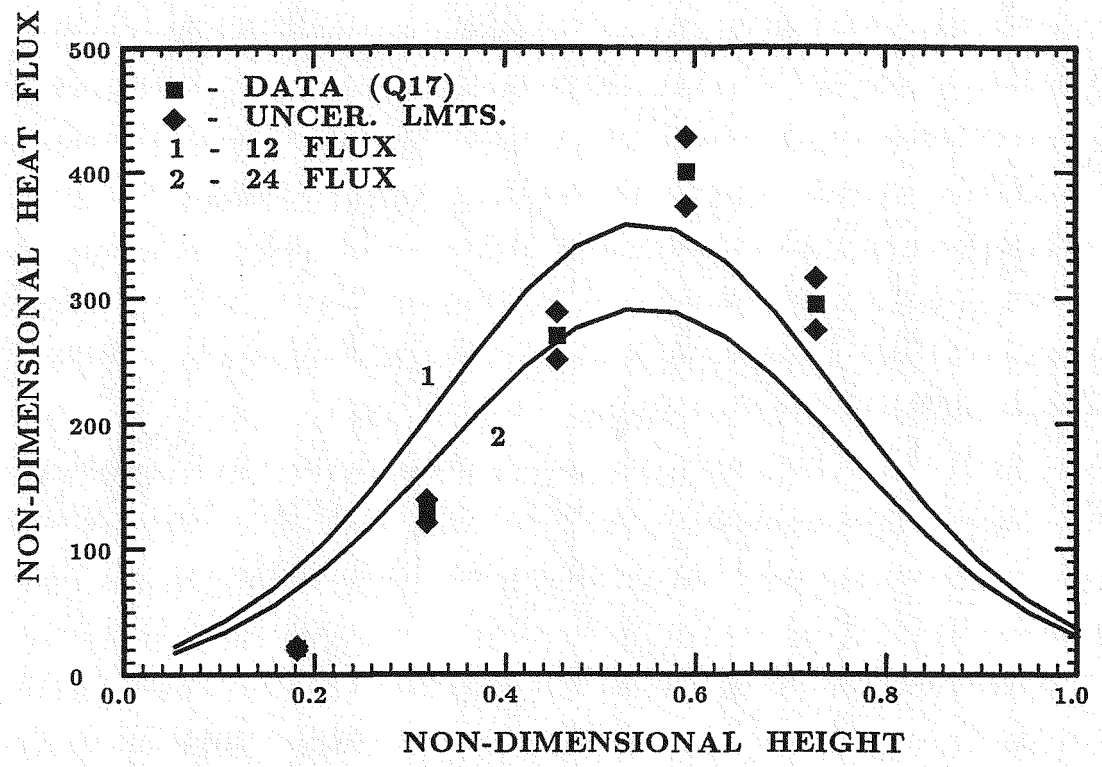

Figure 7.17: Non-Dimensional Transmitted Flux Comparison (Test Run $Q17$, $L_x = 6.747mm$, Thick Curtain)

difficult and it was anticipated that the experimental error would be significant.

The results for the average exit temperature are presented in Table 7.2 for all of the test runs that were discussed above. The table shows the test run designation along with the curtain thickness for that run and the measured inlet particle temperature. The inlet temperature is the value that is used as the input for the model for the intial temperature distribution in the curtain. Although the model is capable of predicting the temperature distribution in the medium, the experimental program only produced what must be considered the average exit values. Consequently, to calculate the same values in the model, the temperature distribution along the x-direction (direction into the curtain) at the vertical location $\hat{y} = 1$ was averaged in the usual way.

The last column of the Table presents the deviations between the data read-

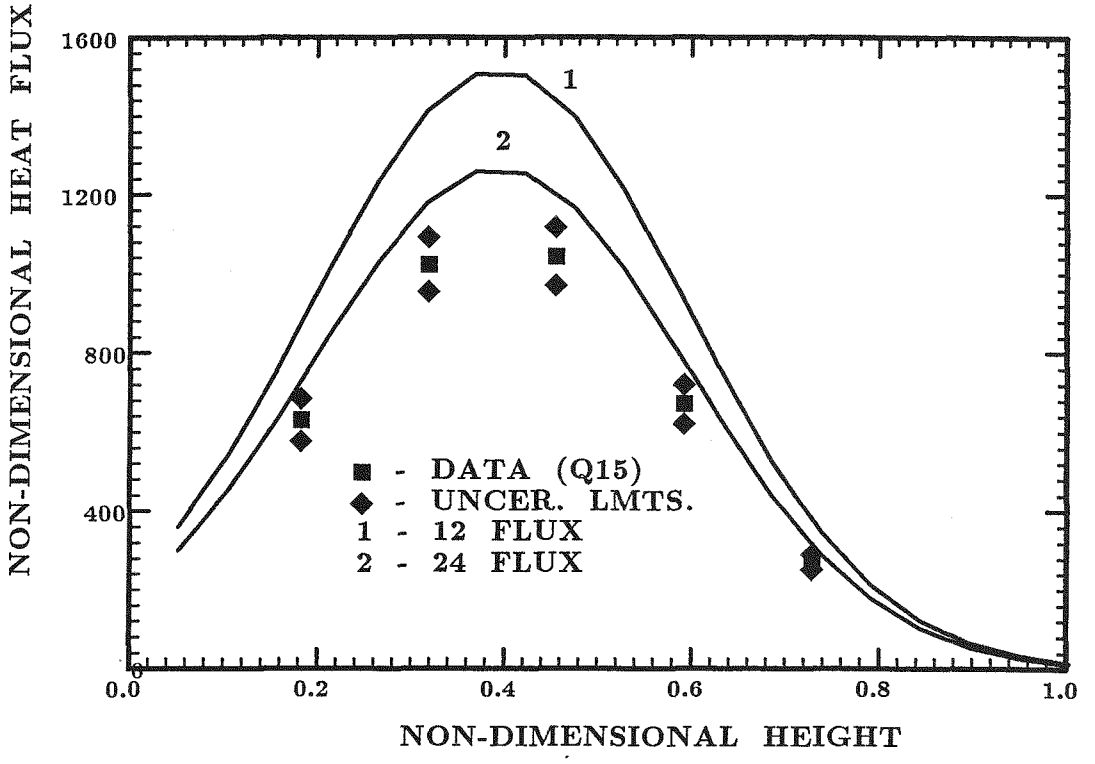

Figure 7.18: Non-Dimensional Front Face Heat Flux Comparison (Test Run $Q15$, $L_x = 7.54mm$, Thick Curtain)

ings and the model (for the S_6 approximation only) in the form of a percentage difference defined in terms of the differences between the exit temperature of the data (and the model) and the measured inlet temperature as

$$\% \; difference = \frac{[T_{data_{exit}} - T_{data_{inlet}}] - [T_{model_{exit}} - T_{data_{inlet}}]}{[T_{data_{exit}} - T_{data_{inlet}}]} \qquad (7.16)$$

As is indicated in the Table, the magnitude of the deviations ranged from a low of 8.4% to a high above 45% for the 24-flux approximation. Clearly, the predictions of the model and the measured values are significantly different. For the cases in which the model underestimated the exit temperature, the 12-flux model predicted the exit temperature more accurately than did the 24-flux model. This was only considered coincidental, however, due to the fact

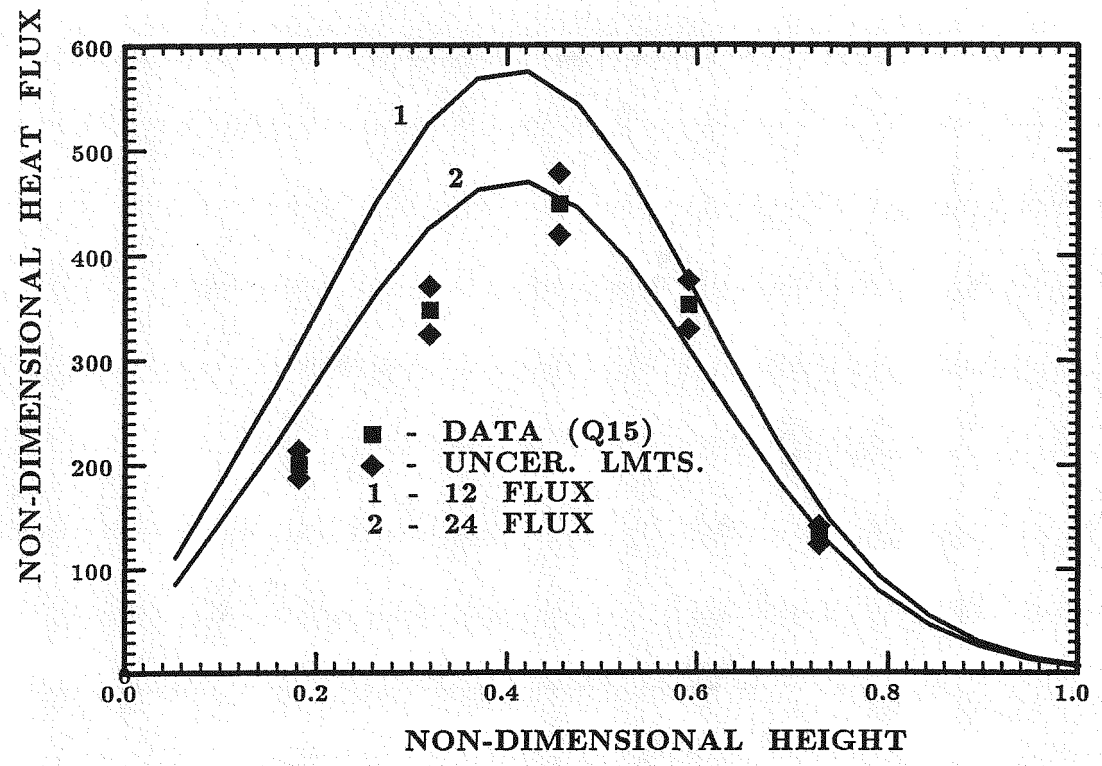

Figure 7.19: Non-Dimensional Transmitted Flux Comparison (Test Run $Q15$, $L_x = 7.54mm$, Thick Curtain)

that the 12-flux model consistantly overpredicted the incident flux distribution which certainly led to an overestimation of both the transmitted heat flux and the exit temperature. The significant differences between the model and the data suggest that some consideration of the measurement error associated with the temperature measuring device is in order.

Due to the complexity of the measurement process and to the uncertainty of the measurements of the curtain porosities (used to determine the thermal properties), the specific reason for the large deviation is unknown. Certainly it may be stated with reasonable confidence that the measurements have a significant amount of experimental error. The thermocouples embedded in the thin copper bar are actually measuring the temperature of the bar. The contact area of the particles on the bar is very small for a given particle. Consequently,

Table 7.2: Temperature Results

Test Run	L_x (mm)	T^*_{inlet}	T^*_{avg} (data)	T^*_{avg} (S_4)	T^*_{avg} (S_6)	Diff. (%)
Q7	3.175	87.13	90.59	91.31	91.20	-17.6
Q8	3.175	88.05	91.14	92.35	92.23	-35.3
Q4	4.366	80.62	84.65	85.90	85.49	-20.8
Q5	4.366	83.95	92.87	88.52	88.24	51.9
Q16	5.556	79.76	85.52	84.01	83.66	32.2
Q12	5.950	77.35	84.28	82.2	81.77	36.2
Q17	6.747	83.12	86.38	88.41	87.92	-47.2
Q15	7.540	77.78	82.32	83.27	82.70	-8.4

$(*$ - all temperature results in $^\circ F)$

the copper bar is actually in contact with both the air in the curtain and the particles as they pass through the device. Also, there will be a characteristic time lag (and a spatial temperature gradient) between the actual temperatures of the medium and the recorded temperatures of the copper bar. This effect was neglected in the model by assuming the copper bar to be a lumped system (i.e., the high conductivity and relatively small thickness of the copper would cause any temperature gradients from the outer wall to the thermocouple junctions to be suffuciently small to be ignored). The actual effects of spatial temperature gradients and temperature time lags could be determined by solving the conduction problem associated with the copper bar. A first approximation analysis of the problem (i.e., transient conduction in a copper bar with simplistic boundary conditions) would show that the value recorded by the thermocouples was

actually **less** than the true temperature of the particles. This could have the effect of decreasing the deviations for the cases in which the model overestimated the temperatures (cases $Q7$, $Q8$, $Q4$, $Q17$ and $Q15$), while making the deviation values for the other cases larger.

A calibration procedure was consequently conducted for the temperature measuring device to determine the effects of the time lag on the thermocouple readings. The results of these tests are presented in Section 7.7.

Due to the low absorption of the air in the solar spectrum, it is anticipated that the funnelling process, caused by the shape of the temperature measuring device, forces the air near the copper bar to be warmed to the temperature of the particles. This will allow the copper bar to come to thermal equilibrium at the actual temperature of the particles in the curtain. However, it is clear that the hypodermic thermocouples will actually measure a temperature that is less than the temperature of the particles. Temperature gradients from the outside surface of the copper bar to the location of the thermocouples along with cooling of the bar caused by the inefficient transfer of heat from the particles to the air that is in contact with the bar indicate that the thermocouples will be underestimating the actual exit temperature. To determine the magnitude of this underestimation, an energy balance may be performed on the copper bar. However, it is anticipated that the calibration procedure will justify the assumption of lumped capacitance in the copper (i.e., the actual spatial temperature gradient from the surface to the thermocouple location inside the bar is negligible).

Another source of error is caused by assuming that the thermocouples will be reading the *average* exit temperature. Even if the device was properly positioned under the hopper exit area, the particles would still not contact the copper bar uniformly. Particles near the leading and trailing edges of the curtain would not contact the bar as easily as those closer to the central plane. This would cause the copper bar to not experience the effects of the cooler particles

at the trailing edge and the hottest particles along the front face. Also, any slight misalignment of the funnel device below the hopper exit could cause the particle curtain to contact the bar unevenly (i.e., in such a way that one part of the curtain would "weight" the readings away from the true average reading) causing the thermocouple readings not to be indicative of the *average* of the curtain as a whole.

Recall that the model was developed assuming no transient energy storage effects. Also, the thermal properties of the medium were assumed constant and were written as a weighted sum of the properties for the air and the particles with the weighting function defined volumetrically in terms of the porosities of each material in the curtain. Certainly, any errors in either the physical representation of the thermal properties (in terms of the volumetrically based porosities) or in the measurement of the porosity would add to the inaccuracies of the model. The sensitivity of the model to measurement errors in the porosity is discussed in the next Section.

Lastly, the convection loss term was modeled using a correlation developed for a fluidized bed system.[1]

Certainly, the numerical uncertainty associated with these assumptions should be considered when judging the effectiveness of the model to predict the temperature field. It is clear that a more sophisticated model of the thermal properties and of the exchange of energy in general is needed to more accurately estimate the temperaure distribution. In all probability, the thermal (and radiative) properties of the system are not constant and the development of an energy model should consider this.

One important capability of the model is it's ability to describe the tem-

[1] While convection correlations are generally considered to only be accurate to within $\pm 20\%$, the errors associated with the present convection calculations are not thought to be extensive due to the relatively low temperatures acheived by the particles as they pass through the solar beam.

perature distribution in the interior of the particle curtain. Ultimately, the factors that will effect the decisions concerning the design of any direct absorption receiver will include the temperature drop that will be observed for the given medium and solar concentration system. In this way, the effects of walls and other boundaries that may participate in the energy transfer can be determined. Although it was not feasable to experimentally describe the interior temperature distribution, the model does provide some indication of the magnitudes of the temperature gradients from the front of the curtain to the rear. A table of the interior temeprature distribution for one of the test runs is included in Appendix 6.

7.7 Calibration of the Thermocouple Funnel Device

In an effort to determine if the transient effects of the thermocouple funnel device were causing the errors observed in the comparisons of the model to the temperature data, a calibration procedure was conducted. The copper bar, which is a highly conductive material, was as thin as was practical to allow implantation of the hypodermic thermocouples. This non-zero thickness certainly would cause the temperature readings taken by the thermocouples to lag the actual temperature of the outside surface of the bar. Both spatial and temporal temperature gradients would exist that would add to the experimental error of the thermocouple/copper bar system. The transient effects can be observed by forcing a known boundary condition on the outer surface of the bar and observing the temperature readings of the thermocouples.

This calibration procedure was simple and only involved preheating the particles to a known initial temperature. This was accomplished in an industrial oven and the preheat temperature was monitored not only by the built in temperature probe in the oven but also by a separate thermocouple that was placed into the center of the particles as they sat in a metallic canister.

After the particles had achieved the desired uniform initial temperature

(the thermocouple probe in the particles was placed at several different heights to ensure that no stratification was occurring), the canister was removed from the oven and the particles were quickly poured through the particle flow device. As the particles flowed through the thermocouple funnel, the temperature was recorded in the same way as during the flow tests at the solar furnace.

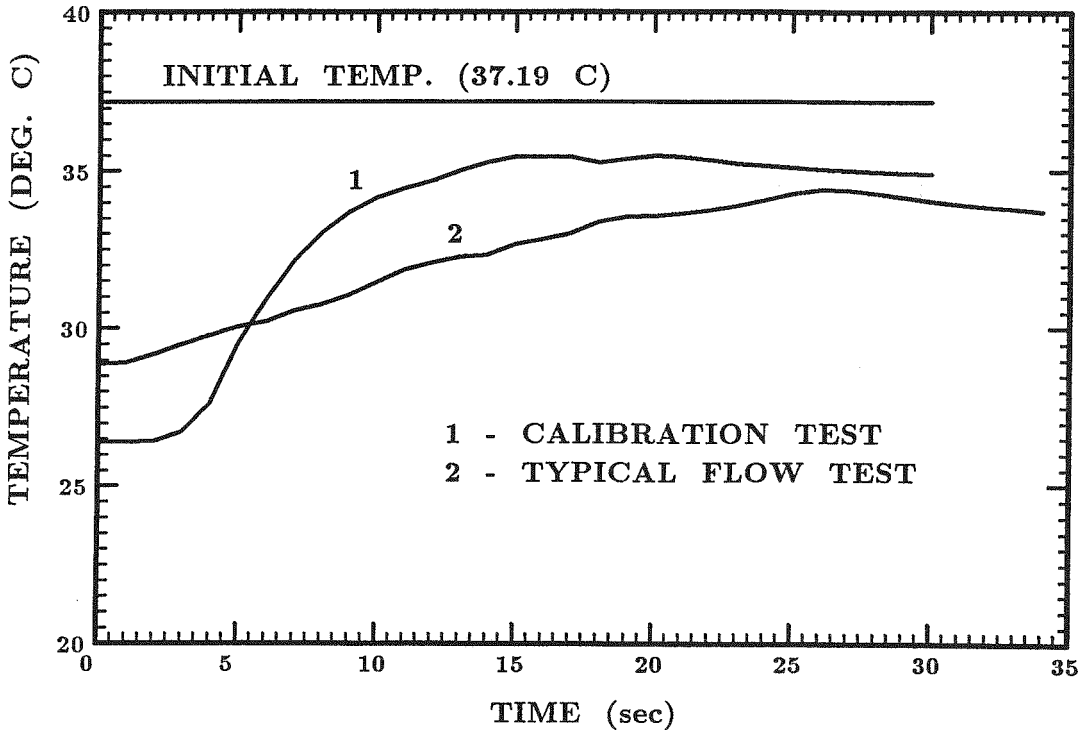

Figure 7.20: Transient Response of the Copper Bar Thermocouple System

A plot of the results is presented in Figure 7.20 with the initial temperature shown as a horizontal line. Also included in the Figure is a typical temperature curve from one of the actual solar furnace tests. An observation of the curves in the Plot indicates that the response of the thermocouple funnel device has a characteristic time constant on the order of 10 to 15 *seconds*.

The temperature that was used as the average exit temperature for the

experimental data was the peak value that is clearly observable on the curve. At this point, the hopper emptied and the particle flow stopped. Since a typical test displayed a gradual positive slope throughout the duration of the particle flow (which ceased when the flow ended), it was assumed that, as long as the time period that elapsed from the opening of the attenuator was significantly greater than the time constant of the system, the time lag in the thermocouple readings would be negligible.

As is clear from the plot, at the point that the hopper emptied, the elapsed time for the flow test was sufficiently longer than the time constant observed in the calibration procedure and this temperature reading was considered the constant value for that particular test. Accordingly, the assumption that the thermocouples readings were fairly accurate at this moment seems to be validated.

It is also clear, however, that more accurate thermocouple readings could be obtained by considering not only the transient storage of energy in the curtain (through a re-formulation of the energy conservation equation) but also the transient variation of the temperature readings. Through the use of a calibration curve similar to the one in Figure 7.20, it would be possible to correct for temporal (and spatial) temperature gradients, although this would require taking the thermocouple measurements as function of time. Even greater accuracy might be achieved by solving a multi-dimensional, transient energy balance on the copper bar itself. Unfortunately, an accurate representation of the boundary conditions for the particle flows would be difficult.

7.8 Sensitivity of the Model to Measurement Error

In order to determine the relative importance of the different quantities that were measured during the course of this project on the performance of the model, a sensitivity analysis was conducted. Values of the measured quantities that were used as inputs to the model (i.e., absorption coefficient, curtain poros-

ity, incident heat flux, and inlet temperature) were perturbed a small amount and the model was re-executed to determine the difference that this perturbation had on the outputted values (i.e., the average exit temperature and the transmitted heat flux.) This analysis was performed by calculating the sensitivity coefficients that related the outputted values of the model to the inputted measurements.

The sensitivity coefficient is the ratio of the change in the desired output quantity to the change in the inputted measurement value. Mathematically, it can be expressed as the partial derivative of the outputted term with respect to the inputted measurement. Defining the sensitivity coefficient as Γ_p where p is the specific parameter that is being considered, the expression that would be used for the heat flux data becomes

$$\Gamma_p = \left.\frac{\partial q}{\partial p}\right|_{point\ n} \tag{7.17}$$

where n represents the independent variable that pertains to the particular output distribution.

Normally the above expression is used to construct the sensitivity matrix which is eventually used to solve a parameter estimation problem to determine the corresponding parameter values (Γ_p, $p = 1, 2, ..., N_p$, where N_p is the number of parameters in the model). However, in order to provide a comparitive basis for determination of relative importance of certain measured quantities, a set of *modified* sensitivity coefficients is calculated by multiplying the coefficient defined above by the measured value of the particular quantity. This has the effect of removing the dimensionality of the perturbed measurement from the calculated value (i.e., the final values have the units of the outputted data quantity that is being investigated). The expression is written for the realistic case where it is impossible to calculate the partial derivatives analytically because the model is actually the solution to a set of partial differential equations by

perturbing the measured data value and observing the effects on the outputted data point.

For the present project, the modified sensitivity coefficients were calculated for the two outputted quantities, the transmitted flux and the exit temperature as

$$\Gamma_{\alpha,\hat{q}} = \alpha \frac{\Delta \hat{q}}{\Delta \alpha} \tag{7.18a}$$

$$\Gamma_{\alpha,T_{exit}} = \alpha \frac{\Delta \hat{T}_{exit}}{\Delta \alpha} \tag{7.18b}$$

$$\Gamma_{\varepsilon_p,\hat{q}} = \varepsilon_p \frac{\Delta \hat{q}}{\Delta \varepsilon_p} \tag{7.19a}$$

$$\Gamma_{\varepsilon_p,T_{exit}} = \varepsilon_p \frac{\Delta T_{exit}}{\Delta \varepsilon_p} \tag{7.19b}$$

$$\Gamma_{\beta_j,\hat{q}} = \beta_j \frac{\Delta \hat{q}}{\Delta \beta_j} \tag{7.20a}$$

$$\Gamma_{\beta_j,T_{exit}} = \beta_j \frac{\Delta T_{exit}}{\Delta \beta_j} \tag{7.20b}$$

for j = 1,2,3 for the three parameters in the boundary intensity (and heat flux) function (see Eq. 7.8), and

$$\Gamma_{T_{inlet},\hat{q}} = T_{inlet} \frac{\Delta \hat{q}}{\Delta T_{inlet}} \tag{7.21a}$$

$$\Gamma_{T_{inlet},T_{exit}} = T_{inlet} \frac{\Delta T_{exit}}{\Delta T_{inlet}} \tag{7.21b}$$

for the absorption coefficient, the curtain porosity, the front face heat flux and the inlet particle temperature measurements respectively.

The above calculations were applied to the model results of test run $Q8$ using a 10% perturbation on each of the above described quantities (there are six in all). The results for the transmitted heat flux predictions, which provide

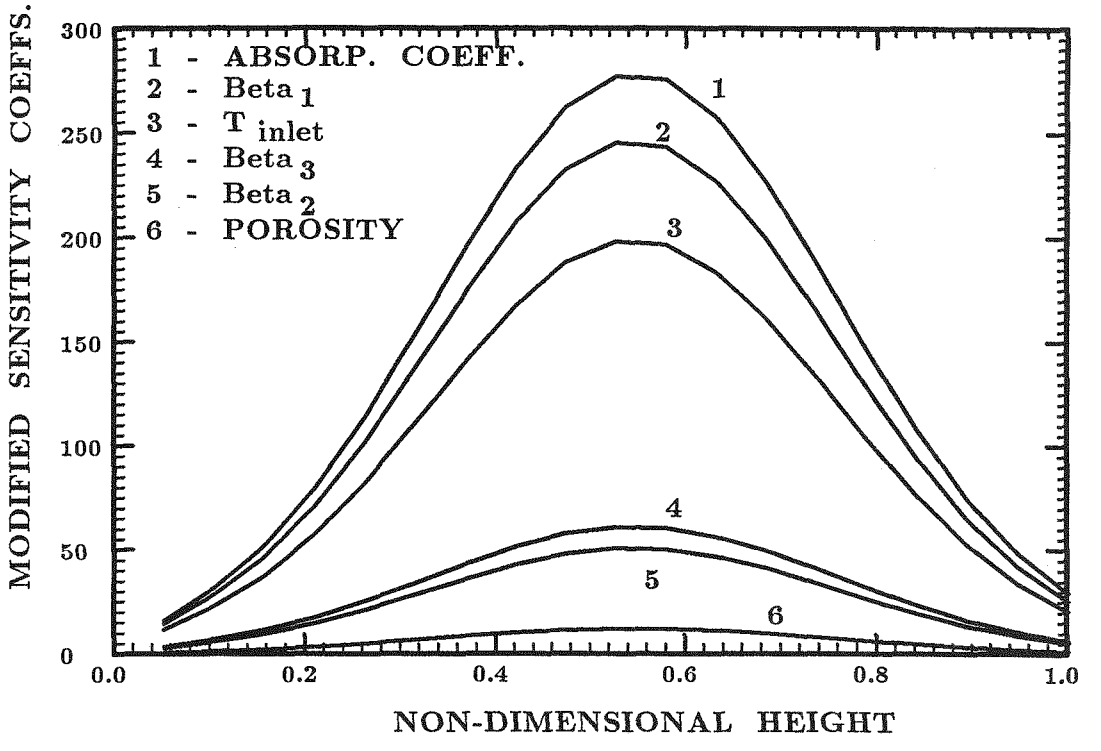

Figure 7.21: Effect of Measurement Error of Input Quantities on Predictions of Transmitted Heat Flux

a direct comparison of the relative importance of each of the measured inputs, are presented in Figure 7.21.

It is clear from the plot that the top three curves, the absorption coefficient (1), the first parameter in the boundary function, β_2, (2), and the inlet particle temperature (3), are of significantly greater importance than the lower three curves due to their higher sensitivities in the computer model estimations of the transmitted heat flux. The plot clearly indicates that experimental accuracy in the determination of these three parameters is more critical in obtaining model predictions of the heat flux that are of satisfactory accuracy although the magnitude of the difference is not enough to justify ignoring any of the reported measured values.

Notice that, while a 10% perturbation was applied to the measured values,

the propagation of that difference is not linear. The resulting percentage differences in the model predictions for the peak transmitted heat flux (at $\hat{y} = 0.5263$) for the six parameters discussed are 1) 9.5% for the absorption coefficient, 2) 8.4% for β_1, 3) 6.8% for T_{inlet}, 4) 2.1% for β_3, 5) 1.7% for β_2, and 6) 0.42% for ε_p. Fortunately, the resulting difference in the readings is not more than 10% for any of the terms discussed.

The results of the sensitivity analysis in terms of the effects of the six measured inputs to the outputted exit temperature are presented in Table 7.3. The first column in the Table indicates the particular parameter that is being considered, the second and third columns show the model predictions of the temperature increase for the unperturbed and perturbed models, respectively. The fourth column is the percent difference in the two predictions defined as

$$\%error = \frac{(\Delta T)_{unperturbed} - (\Delta T)_{perturbed}}{(\Delta T)_{unperturbed}} \tag{7.22}$$

and the fifth column is the value of the modified sensitivity coefficients defined by Eqs. 7.18b, 7.19b, 7.20b and 7.21b.

Clearly, all of the reported measurements with the exception of the absorption coefficient play a crucial role in the ability of the model to predict the average exit temperature. The results that are shown in the Table may help explain the reasons for the significant discrepancies that were observed between the model's prediction of the temperature and the recorded values. Obviously, the significant amount of experimental error (most of it qualitative in nature) and the high sensitivity of the model to any measurement error suggests that more accurate data be obtained not only for the measurement of the exit temperature but also for the measured input values.

7.9 Summary

The results of the experimental tests that were conducted to allow the

Table 7.3: Exit Temperature Sensitivity on Erroneous Inputs

Perturbed Input Measurement	$(\Delta T)_{unpert}$ ($^\circ F$)	$(\Delta T)_{pert}$ ($^\circ F$)	Error (%)	Modified Sensitivity Coefficient ($^\circ F$)
α	4.8	2.71	43.5	27.1
ε_p	4.8	4.81	-0.2	48.1
β_1	4.8	4.19	12.7	41.9
β_2	4.8	4.43	7.7	44.3
β_3	4.8	4.34	9.6	43.4
T_{inlet}	4.8	4.13	12.9	41.3

model that was developed to be compared with actual results from a solar receiver application were presented and discussed.

The secondary phase consisted of experimentation to determine some of the radiative and thermal properties needed for the model. The extinction coefficient was measured using a tuneable dye laser and the absorption coefficient was determined from this value and previous work performed to determine the single scattering albedo.

The curtain porosities were measured to allow calculation of the density and specific heats of the curtain. The results showed that the porosities were constant for different flow rates which was expected.

The intensity field along the front face of the curtain was obtained through measurements of the angular variation of the heat flux arriving at the test stand from the concentrator. This data, taken with a limited field of view device (a NIP), characterized the behavior of certain sections of the concentrator. When the total heat flux at the front face was measured, the data obtained were used

along with the NIP characterization to determine the intensity distribution along the front face. The accuracy of these calculations was illustrated by re-calculating the front face flux from the intensity values and comparing them back to the measured values. Reasonable errors were observed (within 28%) for these calculations.

The transmitted flux distribution and the average exit temperatures were obtained as the solution to the model and compared to the data taken during the primary phase of the testing. The results illustrated that the 24-flux approximation was a reasonable predictor of the flux values measured. Significant edge deviations were observed in tests in which the heliostat tracking system was thought to have altered the position of the peak flux on the flux gage plate. (Although the differences became acceptable when "peak-to-peak" deviations were calculated.) However, in test in which little or no tracking adjustment was noticed between the recording of the transmitted and the incident fluxes, deviations within $\pm 25\%$ were observed.

A sensitivity analysis was conducted that illustrated that care should be taken in trying to reproduce any of the measurements of the inputted values. In terms of the transmitted heat flux, measurement errors in the inputted values will be slightly reduced as they propagate through the model and are manifested in the predictions of the flux. However, the sensitivity of the model in terms of it's ability to predict the temperature field to the measured input values is much greater. It is clear that more accurate temperature measurements should be obtained and improvements in the energy conservation part of the model should be performed to reduce the sensitivity of the model to the measurement errors.

Chapter 8

Summary, Conclusions and Recommendations

8.1 Summary

The investigation of advanced solar central receiver designs was furthered in this study by considering a solar absorbing, free-falling particle curtain as the active medium in a direct absorption system. The study consisted of the development of a general, algorithmically simple numerical model to address the problem of the multi-dimensional radiative field that will exist if the particles in the curtain are heated enough to make emission significant. The model was developed so as to allow easy coupling with other process governing equations (namely, conservation of energy) to allow comparison to experimental data recorded at the NMSU Solar Furnace Facility. Some secondary phase data were taken to aid in the determination of some of the properties defined in the system of equations governing the intensity and temperature fields in the particle curtain.

The discrete ordinates approximation, wherein the intensity field is assumed to be composed of discrete constant values defined over several incremental solid angles, was formulated for the problem. Some solutions of the problem for one- and two-dimensional cases in conditions of radiative equilibrium and uniform internal energy generation were obtained and compared to other solutions generally considered to be highly accurate (i.e., exact solutions and other proven numerical models). One-dimensional results were compared to an exact formulation developed by Heaslet and Warming[69] in Chapter 4. Errors within 10% were observed for both the S_4 (12-flux) and the S_6 (24-flux) approximations for all cases in which the wall emissivities were both above 0.3. As stated in Carlson and Lathrop[59], it is apparent that continuity discrepancies, called "ray effects," cause these errors. Slightly larger errors occurred for ϵ_{w1} or ϵ_{w2} values of 0.1. The 4-flux (S_2) approximation, while observed to be a fair predictor of the radiative field for large wall emissivities, quickly became unsatisfactory as the reflective component at the boundary became large.

Two-dimensional results were compared to a zonal solution that is a computational model developed to solve multi-dimensional problems. Results within 13% were observed for all 12- and 24-flux cases in the black walls, pure scattering situation. Maximum deviations were observed near the hot wall for all scattering results with the differences quickly diminishing away from this surface. Results for the pure absorption problem displayed deviations within 6% at all optical thicknesses for the 12- and 24-flux models. Once again, the 4-flux model was observed to be inaccurate for most realistic situations in multi-dimensional problems while the higher order approximations provided accurate predictions of the pertinent quantities.

Experimental measurements of the extinction coefficient and the curtain porosity (the ratio of the volume of solid particle material in an elemental volume of the curtain to the total volume) were used along with data determined from previous studies to determine the thermal and radiative properties needed for the solution. The velocity of the particles as they fall through the active area of the receiver cavity was measured by researchers at Sandia[71] and this information was used to remove the need to solve the conservation of momentum problem as well as the energy and radiation problems.

The front face boundary condition, defined as a Fredholm integral problem, was determined using measurements of the angular variation of the heat flux reaching the test area from the solar furnace concentrator along with the measurements of the total heat flux at the front face for each test run. The Fredholm problem was solved by assuming a functional form for the boundary intensity distribution as a function of the polar angles associated with a spherical coordinates system and analytically integrating this expression to determine the corresponding expression for the heat flux. The unknown parameters appearing in this heat flux expression are then estimated to best fit (in a least squares sense) the concentrator data. When these parameter values are used in the intensity function, the boundary intensity values for each of the appro-

priate discrete ordinates directions are obtained. A check of the accuracy of these calculations was performed by "re-calculating" the boundary heat flux by numerically integrating the intensity values. Plots of these calculations revealed reasonable deviations between the data and the model.

Total solutions for the intensity and temperature distributions were then obtained and were compared to the primary phase of the experimentation. Tests were conducted that recorded the transmitted heat flux and the average exit temperature of the curtain. Comparisons to the data revealed that the model was a reasonable estimator of the transmitted heat flux especially in cases when the front face and transmitted fluxes were recorded without any adjustment of the heliostat in between. Results of the temperature comparisons indicated slightly more significant errors between the model and the data. While this may be attributable, in part, to unreasonable definitions of the thermal properties (ρ and c_p), it was felt that the experimental error associated with the data, caused by the practical difficulties involved with attempting to measure the temperature of a 357 μm particle, was large.

8.2 Conclusions

A multi-dimensional discrete ordinates radiation model has been developed to characterize the flux and temperature distributions in a free-falling particle curtain used as the medium in a solar receiver. It is clear that reasonably accurate distributions of the pertinent heat transfer quantities were predicted by the model. Comparsons to one- and two-dimensional exact solutions and other well accepted numerical solutions showed that, for absorption dominated problems, the model accurately predicts the emissive power, heat flux and temperature distributions.

For the solar receiver case, the model solved a Fredholm integral problem to determine the front face intensity distribution given heat flux data at the front surface. Results of these calculations showed satisfactory agreement when the

set of "re-calculated" front face fluxes from the assumed intensity distribution was compared with the measured flux values.

An experimental program to measure the transmitted flux and the exit temperature also produced estimations of the extinction coefficient and the porosities of the materials in the curtain. Comparisons of the model to the transmitted flux and average exit temperature data showed good agreement between the two. For cases in which the heliostat tracking system did not adjust between the recording of the transmitted flux and the incident flux, reasonable errors were observed at all points along the diameter of the solar spot at the test area.

8.3 Recommendations

It is clear that the development of a general multi-dimensional radiative transfer model of sufficient accuracy has received a significant amount of attention in the literature. While there are several models that can address specific problems, there are only a few that have the generality needed to develop an algorithmically efficient model that can easily be incorporated into a computer code that obtains solutions for realistic physical systems that are charaterized by strong coupling between the respective physical quantities.

While there has been some investigation into the applicability of utilizing the discrete ordinates model for multi-dimensional problems, little has been done to verify that the model provides reasonable predictions of measured experimental data for these physically coupled systems. Certainly more research should be performed in terms of obtaining accurate heat flux, temperature and even velocity experimental data to satisfactorily test the discrete ordinates approximations.

In the present study, it was assumed that the temporal storage term in the energy conservation equation was negligible. While it was thought that this term would only contribute a small amount to the overall temperature

distribution, the temperature data showed a gradual positive slope with time for the flow tests. Calibration tests confirmed that the transient response of the thermocouple system did not cause this to occur which would indicate that there were transient effects being observed. Consequently, any and all improvements of the energy equation formulation for the model are recommended. Also, more sophisticated temperature recording techniques should be implemented to more accurately determine the temperature of the particles in the curtain.

Lastly, more accurate information concerning the thermal and radiative properties should be obtained. The present study assumed all properties to be constant (independent of wavelength, temperature, spatial location, etc.). Certainly, more accurate solutions can be obtained by determining the behavior of all properties in terms of the independent variables in the governing equations. Unfortunately, this addition would require a re-formulation of the basic equations and would certainly increase the computational demands to obtain a solution. Consequently, research into the area of algorithmic optimization of the model for the computer should be considered if attempting to expand the solution to account for varying properties. Also, because the characterization of the solar concentrator, which eventually yielded the data used to solve the Fredholm problem, proved difficult, it is recommended that more accurate and repeatable data of the angular variation of the flux be recorded with emphasis on the data points that lie at non-zero elevation angles.

Lastly, the definition of the density and the specific heat for the curtain required obtaining values for the particle and air porosities in the curtain. This occurred because of the definition of the medium as both the particles and the entrained air in the curtain. It is possible that a re-formulation of the basic equations could be developed by separating the particles and the air in the curtain. While this would simplify the determination of the thermal and radiative properties for the problem, it would significantly increase the overall complexity due to the increased number of equations that would have to be solved simul-

taneously. Consequently, it is anticipated that slightly higher accuracy could be obtained if some research is performed concerning the actual physical relationship that exists between the two materials in the curtain. The thermal and radiative properties could then be defined in terms of this studied behavior and the assumption of the two material curtain could remain intact.

References

(1)- Flamant, G., "Theoretical and Experimental Study of Radiant Heat Transfer in a Solar Fluidized-Bed Receiver," *AIChE J.*, Vol. 28, No. 4, July 1982, pp.529-35.

(2)- Flamant, G., and G. Olalde, "High Temperature Solar Gas Heating Comparison Between Packed ad Fluidized-Bed Receivers - *I*," Solar Energy, Vol. 31, No. 5, 1983, pp. 463-71.

(3)- Flamant, G., Olalde, G., and D. Gauthier, "High Temperature Solar Gas Solid Receivers," *Alternative Energy Sources V. Part B: Solar Applications*, edited by T. N. Veziroglu, Elsevier Science Publishers, B. V. Amsterdam, 1983.

(4)- Kubelka, P. and F. Munk, "Ein Beitak zur Optik der Ferbanstriche," *Zeistschrift für Technische Physik*, No. 11, 1931, pg. 593.

(5)- Chen, J. C., and S. W. Churchill, "Radiant Heat Transfer in Packed Beds," *AIChE J.*, Vol. 9, No. 1, 1963, pg. 35.

(6)- Hamaker, H. C., "Radiation and Heat Conduction in Light Scattering Material," *Philips. Res. Repts.*, Vol. 2, 1947, pg. 55, 103, 112.

(7)- Siegel, R., and J. R. Howell, Thermal Radiation Heat Transfer, Second Ed., McGraw-Hill Book Company, New York, New York, 1972.

(8)- Bachovchin, D.M., Archer, D.H., Keairns, L.M., and L.M. Thomas, "Design and Testing of a Fluidized-Bed Solar Thermal Receiver," Final Report by Westinghouse R&D Center and Georgia Institute of Technology to the Solar Energy Research Institute, Aug. 1980, Subcontract No. XP-9-8321-1.

(9)- Bachovchin, D. M., Archer, D. H., Neale, D. H., Brown, C. T., and J. M. Lefferdo, "Development and Testing of a Fluidized-Bed Solar Thermal Receiver," Proc. 1981 Annual Meeting of Amer. Section International Solar Energy Society, TJ810-T56-81.

(10)- Neale D. H., and R. A. Cassanova, "Solar Thermal Hydrogen Pro-

duction with a Direct Flux Chemical Reactor," presented at 6^{th} Miami International Conference on Alternative Energy Sources, Dec. 1983.

(11)- Neale D. H., and R. A. Cassanova, "Water Gas Production with a Solar Thermal Direct Flux Chemical Reactor," presented at 22^{nd} ASME/AIChE National Heat Transfer Conference, Aug. 1984.

(12)- Hunt, A.J., Ayer, P. H., Miller, F., Russo, R., and W. Yuen, "Solar Radiant Processing of Gas-Particle Systems for Producing Useful Fuels and Chemicals," presented at 23^{rd} ASME/AIChE National Heat Transfer Conference, Aug. 1985.

(13)- Hunt, A. J., "A New Solar Thermal Receiver Utilizing a Small Particle Heat Exchanger," LBL Report LBL-8520, presented at 14^{th} Intersociety Energy Conversion Engineering Conference, Aug. 1979.

(14)- Fisk, W. J., Wroblewski, D. E., Jr., and A. J. Hunt, "Performance Analysis of a Windowed High Temperature Gas Receiver Using a Suspension of Ultra-Fine Carbon Particles as the Absorber," LBL Report LBL-10100, presented at Amer. Session of International Solar Energy Society Annual Meeting, June 1980.

(15)- Hunt, A. J., and C. T. Brown, "Solar Test Results of an Advanced Direct Absorption High Temperature Gas Receiver (SPHER)," LBL Report LBL-16497, Proceedings of the 1983 Solar World Congress, Perth, Australia, Aug. 1983.

(16)- Hunt, A. J., "Solar Radiant Heating of Small Particle Suspensions," LBL Report LBL-14077, Symposium Series *Fundamentals of Solar Energy*, Vol. 3, 1982.

(17)- Hruby, J. M., "A Technical Feasibility Study of a Solid Particle Solar Central Receiver for High Temperature Applications," Sandia Report SAND86-8211, March 1986.

(18)- Crowe, C., Sharma, M., and D. Stock, "The Particle-Source-in-Cell

(PSI-Cell) Model for Gas-Droplet Flows," *Journal of Fluids Engr.*, 1977, pp. 325-32.

(19)- Houf, W. G., and R. Greif, "Radiative Transfer in a Solar Absorbing Particle Laden Flow," Sandia Report SAND84-8929, presented at the 23^{rd} ASME/AIChE National Heat Transfer Conference, Aug. 1985.

(20)- Chandrasekhar, S., Radiative Transfer, Dover Publications Inc., NY, NY, 1960.

(21)- Hellmann J. R., and G. L. Messing, "Sintering of Course Ceramic Particulates," Sandia Report SAND85-0064.

(22)- Stahl, K. A., Griffin, J. W., Matson, B. S., and R. B. Pettit, "Optical Characterization of Solid Particle Solar Central Receiver Materials," Sandia Report SAND85-1215.

(23)- Prescott, G. H., and B. R. Steele, "A Particle Curtain Generator for Optical Property Measurements of Solid Particles," Sandia Report SAND84-8255.

(24)- Hellmann, J. R., and R. C. Bradt, "Strengths of Proppant Thermal Transfer Media," Sandia Report, to be published.

(25)- Stahl, K. A., Griffin, J. W., and R. B. Pettit, "Optical Properties of Solid Particle Receiver Materials *II*: Diffuse Reflectance of Norton Master Beads^{tm} at Elevated Temperatures," presented at SPIE meeting, San Diego, Calif., Aug. 1985.

(26)- Griffin, J. W., Stahl, K. A., and R. B. Pettit, "Optical Properties of Solid Particle Solar Central Receiver Materials *I*: Angular Scattering and Extinction Characteristics of Norton Master Beads^{tm}," presented at SPIE meeting, San Diego, Calif., Aug. 1985.

(27)- Klier, K., "Absorption and Scattering in Plane Parallel Turbid Media," *J. Opt. Soc. Am.*, Vol. 62, 1948, pp. 882-85.

(28)- Kubelka, P., "New Contribution to the Optics of Intensity Light-

Scattering Materials, Part *I*," *J. Opt. Soc. Am.*, Vol. 38, 1948, pp. 448-57.

(29)- Armaly, B. F., and T. T. Lam, "Influence of Refractive Index on Reflectance from a Semi-Infinite Absorbing-Scattering Medium with Collimated Incident Radiation," *Int. J. Heat Mass Transfer*, Vol. 18, 1975, pp. 893-99.

(30)- Sagan, C., and J. Pollack, "Anisotropic Nonconservative Scattering and the Clouds of Venus," *J. Geophys. Res.*, Vol. 72, 1967, pp. 469-74.

(31)- Domoto, G., and W. Wang, "Radiative Transfer in Homogeneous Non-Gray Media with Nonisotropic Particle Scattering," *J. Heat Transfer*, Vol. 96, 1974, pp. 385-90.

(32)- Brewster, M. Q., and C. L. Tien, "Examination of the Two-Flux Model for Radiative Transfer in Particular Systems," *Int. J. Heat Mass Transfer*, Vol. 25, No. 12, 1982, pp. 1905-07.

(33)- Daniel, K. J., Laurendeau, N. M., and F. P. Incropera, "Prediction of Radiation Absorption and Scattering in Turbid Water Bodies," *J. Heat Transfer*, Vol. 101, 1979, pp. 63-67.

(34)- Viskanta, R., Ungan, A., and M. P. Mengüç, "Predictions of Radiative Properties of Pulverized Coal and Fly-Ash Polydispersions," *ASME*, Paper 81-HT-24, 1981.

(35)- Incropera, F. P., and W. G. Houf, "A Three-Flux Method for Predicting Radiative Transfer in Aqueous Suspensions," *ASME - J. of Heat Transfer*, Vol. 101, 1979, pp. 496-501.

(36)- Berquam, J. B., and R. A. Seban, "Heat Transfer by Conduction and Radiation in Absorbing and Scattering Materials," *ASME - J. ofHeat Transfer*, Vol. 93, No. 1, 1971, pp. 236-41.

(37)- Sanders, C. F., and J. M. Lenoir, "Radiative Transfer Through a Cloud of Absorbing-Scattering Particles," *AIChE J.*, Vol. 18, No.

1, 1972, pp. 155-60.

(38)- Duntely, S. Q., "Light in the Sea," *J. Opt. Soc. Am.*, Vol. 53, No. 1, 1963, pp. 214-220.

(39)- Privoznik, K. G., Daniel, K. J., and F. P. Incropera, "Absorption, Extinction and Phase Measurements for Algal Suspensions of Chlorella Pyrenoidosa," *J. Quan. Spectrosc. Radiat. Transfer*, Vol. 20, 1978, pp. 345-52.

(40)- Breig, W. F., and A. L. Crosbie, "Two-Dimensional Radiative Equilibrium: Boundary Fluxes for a Finite Medium Subjected to Cosine Varying Radiation," *J. Quant. Spectrosc. Radiat. Transfer*, Vol. 15, 1975, pp. 163-79.

(41)- Crosbie, A. L., and T. L. Linsenbardt, "Two-Dimensional Isotropic Scattering in a Semi-Infinite Medium," *J. Quant. Spectrosc. Radiat. Transfer*, Vol. 19, 1978, pp. 257-84.

(42)- Crosbie, A. L., and R. L. Dougherty, "Two-Dimensional Isotropic Scattering in a Semi-Infinite Cylindrical Medium," *J. Quant. Spectrosc. Radiat. Transfer*, Vol. 20, 1978, pp. 151-73.

(43)- Crosbie, A. L., and J. W. Koewing, "Two-Dimensional Radiative Transfer in a Finite Scattering Planar Medium," *J. Quant. Spectrosc. Radiat. Transfer*, Vol. 21, 1979, pp. 573-95.

(44)- Ambarzumian, V. A., "Diffuse Reflection of Light by a Foggy Medium," *Doklady Akad. Nauk. SSSR*, Vol. 38, 1943, pp. 229-32.

(45)- Jefferies, J. T., *Optica Acta*, Vol. 2, 1955, pg.109.

(46)- Bellman, R., Kalaba, R., and S. Ueno, "Invariant Imbedding and Diffuse Reflection from a Two-Dimensional Flat Layer," *Icarus*, Vol. 1, 1963, pp. 297-303.

(47)- Bellman, R., and R. Kalaba, "On the Principle of Invariant Imbedding and Propagation Through Inhomogeneous Media," *Proc. Nat. Acad. Sci. USA*, Vol. 42, 1956, pp. 629-32.

(48)- Bellman, R., and R. Kalaba, "On the Principle of Invariant Imbedding and Diffuse Reflection from Cylindrical Regions," *Pro. Nat. Acad. Sci. USA*, Vol. 43, 1957, pp. 514-17.

(49)- Harshvardhan, Weinman, J. A., and R. Davies, "Transport of Infrared Radiation in Cuboidal Clouds," Goddard Space Flight Center, Greenbelt, Maryland, 1981.

(50)- Davies, R., "The Effect of Finite Geometry on the Three-Dimensional Transfer of Solar Irradiance in Clouds," *J. Atmos. Sci.*, Vol. 35, 1978, pp. 1712-25.

(51)- Weinman, J. A., and R. Davies, "Thermal Microwave Radiance from Horizontally Finite of Hydrometeors," *J. Geophys. Res.*, Vol. 83, 1978, pp. 3099-107.

(52)- Yang, Y. S., Howell, J. R., and D. E. Klein, "Radiative Heat Transfer Through a Randomly Packed Bed of Spheres by the Monte Carlo Method," *ASME - J. of Heat Transfer*, Vol. 105, May 1983, pp. 325-32.

(53)- Fiveland, W. A., "Discrete-Ordinates Solutions of the Radiative Transport Equation for Rectangular Enclosures," *ASME - J. ofHeat Transfer*, Vol. 106, Nov. 1984, pp. 699-706.

(54)- Ratzel, A., and J. Howell, "Two-Dimensional Radiation in Absorbing, Emitting, Scattering Media Using the P-N Approximation," *ASME* Paper No. 82-HT-19, 1982.

(55)- Modest, M. F., "Radiative Equilibrium in a Rectangular Enclosure Bounded by Gray Walls," J. Quant. Spectrosc. Radiat. Transfer, Vol. 15, No. 6, 1975, pp. 445-61.

(56)- Cartigny, J. D., "Radiative Transfer with Dependent Scattering of Particles," PhD Dissertation, Univ. of Calif. Berkeley, 1984.

(57)- Brewster, M. Q., and C. L. Tien, "Radiative Transfer in Packed Fluidized Beds: Dependent Versus Independent Scattering," *J. of*

Heat Transfer, Vol. 104, 1982, pp. 573-79.

(58)- Truelove, J. S., "Three-Dimensional Radiation in Absorbing, Emitting, Scattering Media Using the Discrete-Ordinates Approximation," *J. Quant. Spectrosc. Radiat. Transfer*, Vol. 39, No. 1, 1988, pp. 27-31.

(59)- Carlson, B. G., and K. D. Lathrop, *Transport Theory-The Method of Discrete-Ordinates in Computing Methods in Reactor Physics*, edited by Greenspan, Kelber, and Okrent; Gordon and Breach, New York, 1968.

(60)- Schuster, A., "Radiation Through a Foggy Atmosphere," *Astrophys. J.*, Vol. 21, 1905, pp. 1-22.

(61)- Schwarzschild, K., "Equilibrium of the Sun's Atmosphere," *Ges. Wiss.*, Gottingen, *Nachr., Math-Phys. Klasse*, Vol. 1, 1906, pp. 41-53.

(62)- Lee, C. E., "The Discrete S_n Approximation to Transport Theory," *Lawrence Livermore Laboratory Report LA2595*, 1962.

(63)- Tikhonov A. N., and V. L. Arsenin, *Methods of Solving Ill-Posed Problems*, Nauka, Moscow, 1974.

(64)- Markovsky, A., "Development and Application of Ill-Posed Problems in the USSR," *Appl. Mech. Rev.*, Vol. 41, No. 6, June 1988.

(65)- Faddeev, D. K., and V. N. Faddeeva, *Computational Methods of Linear Algebra*, Phys-Math. Publ., Moscow, 1963.

(66)- Biggs, F., and C. N. Vittitoe, "The Helios Model for the Optical Behavior of Reflecting Solar Concentrators," Sandia Laboratories Report # SAND76-0347, March 1979.

(67)- Bird, R. B., Stewart, W. E., and E. N. Lightfoot, *Transport Phenomena*, Wiley, New York, 1966.

(68)- Hruby, J.M., and V.P. Burolla, "Solid Particle Receiver Experiments: Velocity Measurements," Sandia National Laboratory Re-

port, SAND84-8238.

(69)- James, M. L., Smith, G. M., and J. C. Wolford, *Applied Numerical Methods for Digital Computation With Fortran and CSMP*, Second Edition, Harper and Row, New York, 1977.

(70)- Heaslet, M. A., and R. F. Warming, "Radiative Transport and Wall Temperature Slip in an Absorbing Planar Medium," *Int. J. Heat Mass Transfer*, Vol. 8, 1965, pp. 979-994.

(71)- Shah, N., "New Method of Computation of Radiation Heat Transfer in Combustion Chambers," Ph.D. Dissertation, Dept. of Mechanical Engineering, Imperial College of Science and Technology, University of London, 1979.

(72)- Hruby, J. M., Steeper, R. R., Evans, G. H., and C. T. Crowe, "An Experimental and Numerical Study of Flow and Convective Heat Transfer in a Freely Falling Curtain of Particles," Sandia Laboratory Report, SAND86-8714.

(73)- Björak, Åke, "Iterative Refinement of Linear Least Squares Solutions I," *BIT*, Vol. 7, 1967, pp. 322-337.

(74)- Björak, Åke, "Iterative Refinement of Linear Least Squares Solutions II," *BIT*, Vol. 8, 1968, pp. 8-30.

(75)- Holman, J. P., Experimental Methods for Engineers, McGraw-Hill, New York, New York, 1978.

Appendix 1

Development of Boundary Intensity Models

As was discussed in previous Chapters, the determination of the intensity at the front face of the receiver, the area at which the solar beam is directed, involves the solution of an ill-posed Fredholm integral problem. The reason for this is the inability to actually measure the intensity. The related measureable quantity is the heat flux and the expression that relates the two quantities is integral in nature. The heat flux represents a weighted integration of the intensity over solid angle where the weighting function is the direction vector. The expression, which is Eq. 3.46, is

$$q_{i,\lambda}(\mathbf{r_b}, \Delta\theta, \Delta\phi) = \int_{\phi_1}^{\phi_2} \int_{\theta_1}^{\theta_2} I_\lambda(\mathbf{r_b}, \theta', \phi') cos\theta' sin\theta' d\theta' d\phi' \qquad (A.3.1)$$

It is desired to obtain the intensity distribution along the boundary $\mathbf{r_b}$ from measurements of the angular variation of the heat flux being delivered to the test section by the concentrator. This type of problem is solved be assuming the functional form for the *intensity* and integrating this function to obtain the flux. In the present study, the integration of the intensity function was performed analytically due to the sufficiently simple models chosen.

The parameters appearing in the intensity model and their corresponding counterparts in the flux function may then be estimated in a least squares sense to best fit the flux data.

Several models were attempted before the decision was made to use the model that was presented in Chapter 7 (Eq. 7.7). The steps taken to fully develop a model will be illustrated below with an example of a very simple intensity model. Then a partial list of some of the models chosen will be presented along with the average errors associated with the "fitting" process for that model. These errors were used, along with observations of the shapes of the models in relationship to the apparent shape of the data, to choose the best model for use in the main program to solve the energy and radiation problems for the direct absorption receiver.

As was mentioned, models that were dependent on only one angle variable seemed to give much better results than if both the altitude and azimuth angles were included. Because of this, the flux dependence on angle was assumed symmetric about both the vertical and horizontal axes. Consequently, only models in terms of θ will be discussed here although it should be stated that the decision to use only one angular variable was made after developing several two angle models and comparing them to the results of single angle ones.

To explain the model development process, consider the simple case of a one parameter model for the intensity of

$$I_\lambda(\theta) = \beta_{1_\lambda} cos\theta \qquad (A.3.2)$$

where β_{1_λ} is the parameter. Notice that the wavelength dependence is included in the parameter. This dependence will be determined by breaking the intensity values in the solar bandwidths into respective components that are determined by calculating the percentage of energy that lies under the specified bandwidth.

If we define the direction cosine as

$$\mu = cos\theta \qquad (A.3.3)$$

then Eq. A.3.2 can be written as

$$I_\lambda(\mu) = \beta_{1_\lambda} \mu \qquad (A.3.4)$$

The heat flux function can be determined by integration of the form

$$q_{i,\lambda}(\mu, \phi) = \int_{\phi_1}^{\phi_2} \int_{\mu_1}^{\mu_2} \beta_{1_\lambda} \mu^2 d\mu d\phi \qquad (A.3.5)$$

Integrating eventually gives

$$q_{i,\lambda}(\mu, \phi) = \beta_{1_\lambda} \left[\frac{\mu_2^3 - \mu_1^3}{3} \right] (\phi_2 - \phi_1) \qquad (A.3.6)$$

Notice that the ϕ dependence in the above expression actually represents the field of view of the data (i.e. the $\Delta\phi$ defined by the measurement technique). This value is a known constant since the NIP has a well defined field of view. Consequently, the expression can be re-written as

$$q_{i,\lambda}(\mu) = \beta'_{1_\lambda} \left[\mu_2^3 - \mu_1^3\right] \qquad (A.3.7)$$

where

$$\beta'_{1_\lambda} = \beta_{1_\lambda} \frac{\Delta\phi}{3} \qquad (A.3.8)$$

The least squares solution will yield the value for β'_{1_λ} which is then related to the parameter that appears in the intensity function through the above expression. For the least squares system, the sensitivity coefficients are defined as

$$\left.\frac{\partial q_{i,\lambda}}{\partial \beta'_{1_\lambda}}\right|_j = (\mu_2^3 - \mu_1^3) \quad j = 1, 2, 3, ..., N \qquad (A.3.9)$$

where N is the number of data points. The solution for the unknown parameter is determined using an IMSL routine that solves the non-square system without taking inverses to avoid any ill-conditioning that might arise. For this model, the average error (defined as the arithmetic mean of the magnitudes of the deviations at each data point) was $> 20\%$. Clearly, this simplified model is unsatisfactory in describing the intensity field at the front face.

Partial Listing of Models Considered

(1) Linear, One Parameter

$$I_\lambda(\theta) = \beta_{1_\lambda}\theta$$

$$q_{i,\lambda} = \beta_{1_\lambda}(\Delta\phi) \int_{\theta_i}^{\theta_{i+1}} \theta cos\theta sin\theta d\theta$$

In this case, the integral was performed numerically using Gaussian quadrature. The results, as expected, were poor.

(2) Linear, Two Parameter

$$I_\lambda(\theta) = \beta_{1_\lambda}\theta + \beta_{2_\lambda}$$

$$q_{i,\lambda} = \beta_{1_\lambda}(\Delta\phi)\int_{\theta_i}^{\theta_{i+1}} \theta cos\theta sin\theta d\theta + \int_{\theta_i}^{\theta_{i+1}} cos\theta sin\theta d\theta$$

A slight improvement is noticed over the previous model, however, at this point it was becoming apparent that a polynomial function was not satisfactory as a model for the intensity. To check a higher order model was tried.

(3) Quadratic, Three Parameter

$$I_\lambda(\theta) = \beta_{1_\lambda}\theta^2 + \beta_{2_\lambda}\theta + \beta_{3_\lambda}$$

$$q_{i,\lambda} = \beta_{1_\lambda}(\Delta\phi)\int_{\theta_i}^{\theta_{i+1}} \theta^2 cos\theta sin\theta d\theta$$

$$+ \int_{\theta_i}^{\theta_{i+1}} \theta cos\theta sin\theta d\theta + \int_{\theta_i}^{\theta_{i+1}} cos\theta sin\theta d\theta$$

The assumption that a polynomial formulation for the intensity is an unacceptable model is validated with this particular model. Average errors of $> 20\%$ were observed for all of the above models with no improvement occurring from a first order to this second order model. A slight improvement was noticed when a third order polynomial was applied. However, the large values for the errors and the fact that the plots of the flux and intensity functions did not appear to resemble the data satisfactorily led the author to eliminate any type of polynomial curves for the intensity function.

(4) Trigonometric, Two Parameter

$$I_\lambda(\theta) = \beta_{1_\lambda} cos\theta + \beta_{2_\lambda}$$

$$q_{i,\lambda} = \beta_{1_\lambda}(\Delta\phi)\int_{\theta_i}^{\theta_{i+1}} cos^2\theta sin\theta d\theta + \int_{\theta_i}^{\theta_{i+1}} cos\theta sin\theta d\theta$$

For this model, the resulting heat flux function is a term with a cubic cosine dependence and a term that is second order in cosine or sine which was not expected to deliver accurate results when fit to the data. Consequently, the errors were again large (> 20% for the average error), and the model was discarded.

(5) Trigonometric-Linear Combination, Two Parameter

$$I_\lambda(\theta) = \beta_{1_\lambda} cos\theta + \beta_{2_\lambda}\theta$$

$$q_{i,\lambda} = \beta_{1_\lambda}(\Delta\phi)\int_{\theta_i}^{\theta_{i+1}} cos^2\theta sin\theta d\theta + \int_{\theta_i}^{\theta_{i+1}} \theta cos\theta sin\theta d\theta$$

Again, this combination resulted in an unsatisfactory function for the flux, a cubic cosine term and a fairly complex term involving θ and $cos\theta$, $sin\theta$ dependence. Although this model was significantly more accurate than the previous model, the errors were still large and the curve shape was unacceptable. A third parameter was added on the above intensity expression to add a constant to the intensity model. However, this addition only added another trignometric term in the flux function and was still considered inappropriate. At this point (after trying several variations on the trigonometric and linear models) it was decided that a simple trigonnometric formulation for the *heat flux* would be more appropriate for the data.

To accomplish this, it would be necessary to divide out the trigonometric dependence on the assumed intensity function. The first simplistic model is explained below.

(6) Reciprocal Trigonometric, One Parameter

$$I_\lambda(\theta) = \frac{\beta_{1_\lambda}}{cos\theta sin\theta}$$

$$q_{i,\lambda} = \beta_{1_\lambda}(\Delta\phi)\int_{\theta_i}^{\theta_{i+1}} d\theta = \beta_{1_\lambda}\Delta\phi\Delta\theta$$

Since the resulting integrated flux function is dependent only on $\Delta\phi$ and $\Delta\theta$, and since the field of view of the NIP is constant, this model actually represents a constant valued flux function. Clearly this is not the optimal model but it does show that it is possible to actually choose the model for the *flux.*

(7) Reciprocal Trigonometric, One Parameter

$$I_\lambda(\theta) = \frac{\beta_{1_\lambda}}{cos\theta}$$

$$q_{i,\lambda} = \beta_{1_\lambda}(\Delta\phi)\int_{\theta_i}^{\theta_{i+1}} d\theta = \beta_{1_\lambda}\Delta\phi(cos\theta_i - cos\theta_{i+1})$$

It became clear with the application of this model that choosing a trigonometric formulation for the heat flux was a satisfactory model for the problem. Average errors of $< 15\%$ were observed for this model and it was anticipated that even better results could be obtained by formulating slightly more sophisticated models.

(8) Reciprocal Trigonometric, Two Parameter

$$I_\lambda(\theta) = \frac{\beta_{1_\lambda}}{cos\theta} + \frac{\beta_{2_\lambda}}{cos\theta sin\theta}$$

$$q_{i,\lambda} = \beta_{1_\lambda}\Delta\phi(cos\theta_i - cos\theta_{i+1}) + \beta_{2_\lambda}(\Delta\phi)(\Delta\theta)$$

Notice that this model actually represents a cosine term plus a constant for the flux function. Significantly better results were obtained with this model (an average error of < 13).

It should be noted that even though the concentrator data was assumed symmetric (i.e. all of the data at non-zero elevation angles was not used in this devlopment), several of the above models were tried by incorporating a second

angle dependence and using the non-zero elevation data. However, the inclusion of the "extra" data into the model increased the average errors of the model in all cases and it was still thought that the symmetric assumption was justified.

(9) Final Model, Reciprocal Trigonometric, Three Parameter

$$I_\lambda(\theta) = \frac{\beta_{1_\lambda}}{cos\theta} + \frac{\beta_{2_\lambda}}{sin\theta} + \frac{\beta_{3_\lambda}}{cos\theta sin\theta}$$

$$q_{i,\lambda} = \beta_{1_\lambda}(\Delta\phi)(cos\theta_i - cos\theta_{i+1}) + \beta_{2_\lambda}(\Delta\phi)(sin\theta_{i+1} - sin\theta_i)$$

As discussed in the body of the report, this is the model that was finally used to fit to the flux data. This is the first model that had an average error of $< 10\%$ for the symmetric data and seemed to exhibit reasonable agreement with the apparent shape of the data.

Appendix 2

Finite Difference Approximations of the Governing Equations

The finite difference scheme that was employed to obtain the numerical solution to the two equation system is discussed in this Appendix. Due to the relative complexity of the governing equation system, first order differences were applied to both of the spatial derivatives that appear in the interior equations. This discussion is only presented for the two-dimensional case.

The final form of the EOT and the energy equation for the solar particle problem are

$$\mu\frac{\partial I_{m,\lambda}}{\partial x}(x,y)+\xi\frac{\partial I_{m,\lambda}}{\partial y}=-\kappa I_{m,\lambda}+\alpha I_{b,\lambda}+\frac{\sigma_s}{4\pi}\sum_{m'}w_{m'}\Phi_{m'\rightarrow m}I_{m',\lambda} \quad (A.2.1)$$

and

$$\rho_{eff}c_{p_{eff}}v_y\frac{dT}{dy}(x,y)=-[\nabla\cdot\mathbf{q_r}(x,y)]+h_{eff}[T(x,y)-T_\infty] \quad (A.2.2)$$

As has been discussed, the radiative flux vector divergence is found from performing an intensity balance on an element of the medium. The resulting expression is

$$\begin{aligned}[\nabla\cdot\mathbf{q_r}(x,y)] =& 4\int_{\lambda=0}^{\infty}\Big\{\alpha_\lambda[e_{\lambda,b}(T)-\pi\hat{I}_\lambda(x,y)]+\\ &\frac{\sigma_s}{4}\int_{\Omega_i=4\pi}I_\lambda(x,y,\Omega_i)\hat{\Phi}(\Omega_i)d\Omega_i\Big\}d\lambda\end{aligned} \quad (A.2.3)$$

where

$$\hat{\Phi}(\Omega_i)=\frac{1}{4\pi}\int_{\Omega=4\pi}\Phi(\Omega,\Omega_i)d\Omega \quad (A.2.4)$$

The formulation of the governing equations for this problem require two boundary conditions for the intensity problem (one at the top of the curtain and one for the front face) and one for the temperature problem (at the top). The boundary temperature is simple the input of the data point that is measured

for each test. The intensity at the top of the curtain is simply the emission of the particles at the inlet temperature of the curtain. Although this term could be neglected for room temperature range tests, it was included to allow for pre-heating of the particles in possible later designs. As has been discussed, the front face intensity distribution is determined through a solution of the Fredholm integral problem that relates the measured fron face heat flux to the front face intensity distribution. The discussion of this process is handled elsewhere.

To obtain a numerical solution to the equation system described above, the domain is discretized simply allowing for different but uniform node spacings in each of the two coordinate directions, (x, y). Due to the limited memory capabilities of the machine because the intensity array was 4-dimensional (two spatial and one angular coordinates and the wavelength dependence), the nodal spacing for the curtain was limited to 20 nodes in the vertical (y) direction and 10 nodes in the thickness (x) direction.

Simple backward first order differences were applied to the first order spatial derivatives in the two expressions with the out-scattering, emission and in-scattering terms on the RHS of the EOT (Eq. A.2.1) evaluated at the forward node. The resulting EOT expression is

$$\mu_m \left(\frac{I^{i,j}_{m,\lambda} - I^{i-1,j}_{m,\lambda}}{\Delta x} \right) + \xi_m \left(\frac{I^{i,j}_{m,\lambda} - I^{i,j-1}_{m,\lambda}}{\Delta y} \right) = -\kappa I^{i,j}_{m,\lambda} + \alpha I^{i,j}_{m,\lambda} + \frac{\sigma_s}{4\pi} \sum_{m'} w_{m'} \Phi_{m' \to m} I^{i,j}_{m',\lambda} \qquad (A.2.5)$$

Recall that the scattering phase function is written in terms of the direction cosines and some parameters that are defined in Chapter 3.

Collecting the explicit terms of $I^{i,j}_{m,\lambda}$ from the above expression gives

$$I^{i,j}_{m,\lambda} = \left[\frac{\mu_m}{\Delta x} + \frac{\xi_m}{\Delta y} + \kappa\right]^{-1} \left\{ \frac{\mu_m}{\Delta x} I^{i-1,j}_{m,\lambda} + \frac{\xi_m}{\Delta y} I^{i,j-1}_{m,\lambda} + \alpha I^{i,j}_{b,\lambda} + \frac{\sigma_s}{4\pi} \sum_{m'} w_{m'} \Phi_{m' \to m} I^{i,j}_{m,\lambda} \right\} \tag{A.2.6}$$

Notice that the in-scattering source term must be written in terms of the intensity at the present node, i, j, to be correct. This necessitates the use of an iterative procedure at each node to determine the overall intensity field. Also, notice that the coupling between the two equations comes about in the emission term, $I^{i,j}_{b,\lambda}$. Although this isn't another implicit intensity term (since it is directionally independent), it is dependent on the local temperature of the medium at that node and, as such, is a term that causes the algorithm to be iterative in nature in order to obtain a solution.

The quantity in square brackets can be written by defining the finite difference "parameter" as

$$\eta_m = \frac{\mu_m}{\Delta x} + \frac{\xi_m}{\Delta y} + \kappa \tag{A.2.7}$$

The final expression for the intensity distribution at the interior nodes beceomes

$$I^{i,j}_{m,\lambda} = \frac{1}{\eta_m} \left\{ \frac{\mu_m}{\Delta x} I^{i-1,j}_{m,\lambda} + \frac{\xi_m}{\Delta y} I^{i,j-1}_{m,\lambda} + \alpha I^{i,j}_{b,\lambda} + \frac{\sigma_s}{4\pi} \sum_{m'} w_{m'} \Phi_{m' \to m} I^{i,j}_{m,\lambda} \right\} \tag{A.2.8}$$

Recall that the boundary condition for the intensity distribution is obtained by assuming a fuctional form for the intensity field and then determining the unknown parameters through an estimation routine that best fits the front face *flux* data. The model has the form

$$I_\lambda(\mathbf{r_b}, \theta) = \frac{\beta_1}{cos\theta} + \frac{\beta_2}{sin\theta} + \frac{\beta_3}{cos\theta sin\theta} \tag{A.2.9}$$

The angular flux data taken as a characterization of the solar furnace concentrator is normalized by the average of the front face flux readings for the particular test. Consequently, once the parameters have been estimated, the intensity field at the boundary, in finite difference form, can be written

$$I_{\lambda}^{1,j} = q_{Gaussian}^{1,j} \left[\frac{\beta_1}{cos\theta} + \frac{\beta_2}{sin\theta} + \frac{\beta_3}{cos\theta sin\theta} \right] \qquad (A.2.10)$$

where $q_{Gaussian}^{i,j}$ is a curve fit of the front face fluxes. Recall that the front face fluxes were used in a Gaussian curve fit routine to determine a more realistic variation of the flux from one node to the next. If the data is used directly, the flux distribution will appear as a series of step changes and, as such, will represent an unusually difficult "test" of the model.

The energy equation is similarly differenced with the final result written as

$$T^{i,j} = T^{i,j-1} + \gamma_{eff} \left[-(\nabla \cdot \mathbf{q_r}) + h_{eff}(T^{i,j} - T_{\infty}) \right] \qquad (A.2.11)$$

where

$$\gamma_{eff} = \frac{\Delta y}{\rho_{eff} c_{p_{eff}} v_y} \qquad (A.2.12)$$

The flux vector divergence is determined by applying a Gaussian quadrature analysis to Eq. A.2.3. The resulting expression is a triple summation expression in terms of the mean radiant intensity, the emission, and an in-scattering term that is characterized by the integral of the phase function which is the *probability* function corresponding to Φ (a probability density).

A solution is obtained by first setting the entire temperature field to the inlet value. Next, the EOT is solved (for the first iteration, the in-scattering term is set to zero) for the intensity distribution. This step usually requires no more than 4 iterations once the in-scattering term is included in the calculations. The flux vector divergence is calculated and the results are used in the energy expression to determine a new prediction for the temperatures. The

process is repeated until the average exit temperature and the transmitted flux distribution converge to a preselected tolerance (for the test runs in Chapter 7, this value was 0.01 for both quantities).

Appendix 3

Solar Furnace Concentrator Characterization

As described in Chapters 6 and 7, the variation of the heat flux with angle at the test stand of the solar furnace was measured. The tests were conducted using a normal incidence pyroheliometer (NIP) placed on an altitude-azimuth angularly graduated mount. The description of the data that was used in the development of the boundary intensity distribution is provided in the body of this study, this Appendix simply presents the data that was obtained from the tests in order to allow future researchers to have this information available.

The tests were performed between April 4 and April 11, 1989 within two hours of solar noon. As has been discussed, it was necessary to only take this data when the sun position was such that the heliostat completely filled the concentrator. Data was taken at elevations of 0° and 18° (along the horizontal centerline and along a horizontal line near the top of the concentrator). Sweeps along the bottom of the concentrator proved impossible due to the position of the open attenuator.

The NIP was well insulated and was positioned such that the heat flux gage near the base of the device was at the focal point of the system. The data from the tests is presented below in tabular form along with some comments concerning the solar conditions present during the run. The DAS (a Hewlett-Packard system) converted the data from voltages to fluxes using the conversion factor determined for the particular NIP through standard calibration techniques.

Table A.3.1: Concentrator Data

Elevation = 0°

Azimuth Angle	Test #1 $\frac{W}{cm^2}$	Test #2 $\frac{W}{cm^2}$	Test #3 $\frac{W}{cm^2}$
25.5°	6320.53	5859.20	6502.38
18.5°	6265.53	5050.20	6200.04
11.5°	3369.10	3700.1	3553.07
4.5°	3131.22	3943.70	4276.46
-3.5°	3775.91	3220.45	3066.75
-10.5°	3985.49	4315.24	3376.67
-17.5°	4075.91	5135.12	4164.52
-25.0°	4899.13	5347.65	5157.62

Elevation = 18.2°

Azimuth Angle	Test #1 $\frac{W}{cm^2}$	Test #2 $\frac{W}{cm^2}$	Test #3 $\frac{W}{cm^2}$
22.5°	4106.95	*	4880.00
15°	3936.03	*	4155.69
7.5°	5623.00	*	3384.93
1.5°	5921.44	*	5895.64
-5.5°	5575.18	*	5208.83
-12.5°	4043.40	*	4493.7
-20.5°	3974.01	*	3699.66

Appendix 4

Determination of the Curtain Porosity

As was discussed in the main body of this report, the specific heat, the density and the heat transfer coefficient were all defined in terms of the porosities of the air and the particles in the curtain. This comes about due to the assumption that the "medium" is the air and the particles together. In order to consider the two components separately, the number of governing equations would effectively double and obtaining information into some of the relevant quantities (most especially the velocity of the air) would be difficult.

The porosity is simply defined as the ratio of the volume taken up by the particles or the air in a given volume of the "medium." The definitions can be expressed as

$$\rho_{eff} = \varepsilon_a \rho_a + \varepsilon_p \rho_p \tag{A.4.1}$$

$$c_{p_{eff}} = \varepsilon_a c_{p_a} + \varepsilon_p c_{p_p} \tag{A.4.2}$$

and, for the convection loss term,

$$\varepsilon_a \frac{\overline{Nu}}{Re_D Pr^{\frac{1}{3}}} = 2.06 Re_D^{-0.575} \tag{A.4.3}$$

The measurements that eventually led to the calculation of the porosity are explained in this Appendix.

Initially, timed flow tests were conducted to determine the mass flow rate of the particles for two different curtain thicknesses. Table A.4.1 illustrates the results of these tests. The tests were conducted by suddenly opeing the flow device to the proper thickness. This was actually accomplished by pre-setting the opening before the particles were poured into the hopper. While the orifice was manually blocked by a hand held obstruction, the particles were added to the hopper. The test was initiated by suddenly removing the obstruction and, at the same instant, starting a timer. Before the hopper emptied (the flow rate gradually changes as the particle supply dwindles), the obstruction was suddenly replaced and the timer stopped simultaneously. The particles that

Table A.4.1: Mass Flow Rate Tests

Curtain Thickness (mm)	Total Weight (lbs)	Time Interval (sec)
13	19.75	6.51
13	17.75	6.08
13	20.0	5.96
13	21.0	5.97
7.5	12.0	6.34
7.5	13.0	6.08
7.5	11.0	6.37
7.5	12.25	5.87

flowed through the orifice during that time interval were the ones that were weighed.

Since the density of the particle is known (measured by Sandia) and optical measurements of the mean diameter have been performed, the mean mass of a single particle can be calculated simply as

$$m_p = \rho_p \forall_p = \rho_p \frac{\pi d^3}{6} \qquad (A.4.4)$$

Substituting in the measured values gives

$$m_p = (3970)\left[\frac{kg/m^3}{particle}\right]\frac{\pi}{6}(357\times 10^{-6})^3[m^3] = 9.458\times 10^{-8}\left[\frac{kg}{particles}\right] \qquad (A.4.5a)$$

Converting to English units yields

$$m_p = 4.29 \times 10^{-8} \left[\frac{lbs}{particle} \right] \qquad (A.4.5b)$$

If the total weight of the particles that ended up in the capture tank is divided by the mass/particle values just calculated, the result will be the total number of particles that took part in the test. The number flow rate of the particles (defined as the number of particles flowing through the orifice per unit time) is the easily calculated by dividing the total number of particles that were weighed by the time interval of the test. The results of these calculations are presented in Table A.4.2.

Table A.4.2: Number Flow Rate Calculations

Curtain Thickness *(mm)*	**Total Particles** *(millions)*	**Time Interval** *(sec)*	**Number Flowrate** *(millions/sec)*
13	460.366	6.51	70.718
13	413.747	6.08	68.050
13	466.193	5.96	78.220
13	489.503	5.97	81.994
7.5	279.716	6.34	44.119
7.5	303.026	6.08	49.840
7.5	256.406	6.37	40.252
7.5	285.543	5.87	48.644

Next, the number flow rate of the particles is divided by the velocity of the particles in the curtain at any pre-chosen vertical location. This is possible since the velocity data as a function of fall height is known and has been curve fit. The choice of the vertical location is arbitrary because the final result of these calculations, the porosities, is a ratio of volumes. Choosing the vertical location just defines the volume that will be considered. The results of these calculations are divided by the two fixed spatial dimensions of the curtain, the thickness and the width. This yields the number of particles per unit volume. Table A.4.3 illustrates the final calculations to determine this value.

Table A.4.3: Number Density of Particles

Curtain Thickness (*mm*)	**Number Flowrate** (*millions/sec*)	**Particles per Meter Vert.** (*millions/m*)	**Number Density** (*thousands/cm*^{3})
13	70.718	45.077	22.752
13	68.050	43.377	21.894
13	78.220	49.860	25.167
13	81.994	52.266	26.381
7.5	44.119	28.123	24.605
7.5	49.840	31.770	27.795
7.5	40.252	25.658	22.448
7.5	48.644	31.007	27.128

Notice that, as expected, the number density of the particles does not appear to be a dependent on the curtain thickness. It was felt that, above a

certain critical thickness at which the weight of the particles in the hopper no longer effects the flow rate, the number density of the particles in the curtain would be constant.

Finally, the actual volume of the particles in the elemental volume of the medium is determined by multiplying the number of particles per unit volume by the mean volume of a given particle. This yields the ratio of the volume of particles in a given elemental volume of the medium, which is the particle porosity, ε_p. The air porosity is simply determined by noting that, in formulating the theoretical model, it was assumed that only air and the particles exist in the medium. Consequently, the porosities of the two materials must sum to unity. The results are presented in the final table, Table A.4.4.

Table A.4.4: Calculation of Porosities

Curtain Thickness (mm)	**Number Density** $(thousands/cm^3)$	**Porosity of Particles** $(cm^3_{particles}/cm^3)$	**Porosity of Air** (cm^3_{air}/cm^3)
13	22.752	0.542	0.458
13	21.894	0.522	0.478
13	25.167	0.600	0.400
13	26.381	0.628	0.372
7.5	24.605	0.586	0.414
7.5	27.795	0.662	0.338
7.5	22.448	0.535	0.465
7.5	27.128	0.646	0.354

The average values of the above porosities are calculated and the final result is

$$\varepsilon_p = 0.590 \pm 0.053 \qquad (A.4.6)$$

and

$$\varepsilon_a = 0.410 \pm 0.053 \qquad (A.4.7)$$

Appendix 5

A Listing of the

Main Computer Programs

Program Intensity_Estimation

```
C-----------------------------------------------------------------------C
C                                                                       C
C                  PROGRAM: INTENSITY_ESTIMATION                      C
C                                                                       C
C    THIS PROGRAM DETERMINES THE PARAMETER SET THAT BEST FITS THE       C
C    NORMALIZED ANGULAR FLUX DATA.  THE CONCENTRATOR DATA IS NOR-       C
C    MALIZED BY DIVIDING IT BY THE AVERAGE READING OF THE               C
C    TOTAL FRONT SURFACE FLUX MEASURMENTS.  THEN, AN OLS ESTIMATOR      C
C    IS USED TO DETERMINE THE PARAMETER SET FOR THE FLUX                C
C    AND INTENSITY FUNCTIONS                                            C
C                                                                       C
C-----------------------------------------------------------------------C
      IMPLICIT REAL*8 (A-H,O-Z)
      REAL*8 INTEGRAL, INT1, INT2, INT3, INT4
      PARAMETER (IDIM_DATA = 22, IDIM_PAR = 5)
      DIMENSION X(IDIM_DATA, IDIM_PAR), BETA(IDIM_PAR)
      DIMENSION THETA_1(IDIM_DATA), THETA_2(IDIM_DATA), RES(IDIM_DATA)
      DIMENSION PHI_1(IDIM_DATA), PHI_2(IDIM_DATA), FLUX(IDIM_DATA)
      DIMENSION DTHETA(IDIM_DATA), DPHI(IDIM_DATA), TAVG(IDIM_DATA)
      DIMENSION PAVG(IDIM_DATA), DBETA(IDIM_PAR), RHS(IDIM_DATA)
      DIMENSION COEF(20,IDIM_PAR), FXT(IDIM_PAR), FXNORM(IDIM_DATA)
      OPEN (UNIT=2, STATUS='NEW', FILE='COEFF')
      OPEN (UNIT=3, STATUS='NEW', FILE='FLUXDAT')
C
C-----     INPUT SECTION
C
      FMAX = 6502.3825
      TOL = 0
      N_COEFF = 3
      I_TERMS = 2
      N_DATA = 8
      N_READS = 5
C
C-----     INITIALIZATION
C
      PI = 4.0 * ATAN(1.0)
C
C-----     READING IN THE FLUX AND ANGLE DATA
C
      OPEN (UNIT=8, STATUS='UNKNOWN', FILE= 'NIP.DAT')
      DO I_DATA = 1, N_DATA
       READ(8, *) I_PT, PX, TX, FXX, FXX, P, T, FX
       T0 = - 50.
       DT = 5.7 / 2.0
       DP = 5.7 / 2.0
       THETA_1(I_DATA) = (T0 + (T - DT)) * PI / 180.
       THETA_2(I_DATA) = (T0 + (T + DT)) * PI / 180.
       PHI_1(I_DATA) = (P + 90.+ DP) * PI / 180.0
       PHI_2(I_DATA) = (P + 90. - DP) * PI / 180.0
       TAVG(I_DATA) = (THETA_1(I_DATA)+THETA_2(I_DATA)) / 2.0
       PAVG(I_DATA) = (PHI_1(I_DATA)+PHI_2(I_DATA))/2.0
       FLUX(I_DATA) = FX * FMAX
       DTHETA(I_DATA) = DT
```

```
        DPHI(I_DATA) = DP
        T1 = THETA_1(I_DATA) * 180.0 / PI
        T2 = THETA_2(I_DATA) * 180.0 / PI
        P1 = PHI_1(I_DATA) * 180.0 / PI
        P2 = PHI_2(I_DATA) * 180.0 / PI
       END DO
       CLOSE (UNIT=8)
 70    FORMAT(2X,F8.3,3X,F8.3,3X, F8.3, 3X, F8.3, 5X,F9.3)
C
C-----      READING IN THE FLUX GAGE INCIDENT READINGS
C
       SUMFX = 0.0
       DO I_NODES = 1, N_READS
        WRITE(6,200)I_NODES
        READ(6,*)FXT(I_NODES)
        SUMFX = SUMFX + FXT(I_NODES)
       END DO
C
C-----      DETERMINING THE AVERAGE VALUE OF THE READINGS
C
       FXINPUT = SUMFX / N_READS
       WRITE(6,*)'FXINPUT=',FXINPUT
 200   FORMAT(///,4X,'ENTER FLUX READING #',I1,' ...',$)
C
C-----      STARTING THE LOOP OVER THE NODES, TO DETERMINE A PARAMETER
C-----      SET FOR EACH FLUX GAGE READING
C
      DO I_NODES = 1, N_READS
       WRITE(6,210)I_NODES
 210   FORMAT(//,'FOR FLUX GAGE READING NUMBER ...',I2,//)
C
C-----      NORMALIZING THE NIP READINGS
C
       OPEN (UNIT=11, STATUS='NEW', FILE='FLUXES')
       DO I = 1, N_DATA
        FXNORM(I) = FLUX(I) / FXINPUT
C
C-----      PRINTING THE NORMALIZED VECTOR WITH THE ANGLES
C
        TT1 = TAVG(I) * 180. / PI - TO
        PP1 = PAVG(I) * 180. / PI - 90.
        WRITE(11,*) TT1, PP1, FXNORM(I)
       END DO
       CLOSE (UNIT=11)
C
C-----      DETERMINING THE SENSITIVITY COEFFICIENTS AND THE
C-----      RIGHT HAND SIDE
C
 1     DO I_X = 1, N_DATA
        X(I_X,1) = COS (THETA_1(I_X)) - COS (THETA_2(I_X))
        X(I_X, 2) = 1.0
        X(I_X,3) = SIN (THETA_2(I_X)) - SIN (THETA_1(I_X))
        RHS(I_X) = FXNORM(I_X)
      END DO
```

```
C
C-----      SOLVING THE OLS PROBLEM USING IMSL ROUTINE "DLSBRR"
C
      CALL DLSBRR(N_DATA, N_COEFF, X, IDIM_DATA, RHS, TOL,
     !            BETA, RES, KBASIS)
C
C-----      CALCULATING THE SSR AND PRINTING THE RESULTS
C
      SUMP = 0.0
      SSR = 0.0
      DO I = 1, N_DATA
       SSR = SSR + RES(I)**2
       PERC = RES(I)/FXNORM(I) * 100.0
       SUMP = SUMP + ABS(PERC)
 100  END DO
      SUMP = SUMP / (N_DATA)
      WRITE(6,60)SSR,SUMP
C
C-----      CHECKING THE RESULTS BY CALCULATING THE FLUX DISTRIBUTION
C
      DO I = 1, N_DATA
       Q = BETA(1) * X(I,1) + BETA(2) * X(I,2) + BETA(3) * X(I,3)
       Q = Q * FXINPUT
       WRITE(6,*)'Q=',Q,'T1=',THETA_1(I),THETA_2(I)
      END DO
C
C-----      SETTING THE PARAMETER SETS INTO THE PROPER NODAL POSITIONS
C
      IF (I_NODES .EQ. 1) THEN
       DO I = 1, 5
        DO J = 1, N_COEFF
         COEF( I, J) = BETA(J)
        END DO
       END DO
      ELSE IF (I_NODES .EQ. 2) THEN
       DO I = 6, 8
        DO J = 1, N_COEFF
         COEF( I, J) = BETA(J)
        END DO
       END DO
      ELSE IF (I_NODES .EQ. 3) THEN
       DO I = 9, 11
        DO J = 1, N_COEFF
         COEF( I, J) = BETA(J)
        END DO
       END DO
      ELSE IF (I_NODES .EQ. 4) THEN
       DO I = 12, 14
        DO J = 1, N_COEFF
         COEF( I, J) = BETA(J)
        END DO
       END DO
      ELSE IF (I_NODES .EQ. 5) THEN
       DO I = 15,20
```

```
          DO J = 1, N_COEFF
           COEF( I, J) = BETA(J)
          END DO
         END DO
        END IF
C
C-----      RESETTING THE PARAMETER SET FOR ONE READING TO ZERO
C-----      SINCE THE PROBLEM MUST BE SOLVED FOR EVERY FLUX GAGE READING
C
        DO J = 1, N_COEFF
         BETA(J) = 0.0
        END DO
C
C-----      ENDING THE NODAL LOOP AND PRINTING THE RESULTS
C
       END DO
       DO I = 1, 20
        WRITE(6,120)I,(COEF(I,J), J = 1, N_COEFF)
        WRITE(2,120)I,(COEF(I,J), J = 1, N_COEFF)
       END DO
C
C-----      FORMAT STATEMENTS
C
 10    FORMAT(//,5X,'INPUT N_COEFF...',$)
 11    FORMAT(//,5X,'INPUT KMAX, N_DATA, L AND N_COEFF...',$)
 12    FORMAT(//,5X,'INPUT L...',$)
 20    FORMAT(I2,1X,I3,2X,F8.5,2X,F8.5,2X,F5.1,2X,F5.1)
 30    FORMAT(I2,1X,I3,2X,F5.3)
 49    FORMAT(1X, 'I',5X, 'DTHETA',5X, 'DPHI',8X, 'DATA', 9X, 'RES',
     !       5X, 'PERCENT',/,72('-'))
 50    FORMAT( 1X, I2, 2X, F7.3, 2X, F7.3, 3X, F10.7, 3X, F10.7,3X, F8.3)
 60    FORMAT(15X,'THE SSR IS...',F12.8,/,15X,
     !   'THE AVERAGE PERCENT ERROR IS...',F5.2)
 110   FORMAT(5X,F20.16,5X,F20.16)
 120   FORMAT(3X,I3,3X,F15.5, 3X, F15.5, 3X, E15.7, 3X, E15.7)
C
 999   CLOSE (UNIT=2)
       STOP
       END
```

Program SPECTRA

```
C-----------------------------------------------------------------------C
C                                                                       C
C                                                                       C
C                        PROGRAM: SPECTRA                               C
C                                                                       C
C                                 Solid                                 C
C                                 Particle curtain                      C
C                                 Energy                                C
C                                 Characterization utilizing a          C
C                                 Two-Dimensional                       C
C                                 Radiative                             C
C                                 Analysis                              C
C                                                                       C
C                                                                       C
C                                                                       C
C                                        WRITTEN BY:                    C
C                                                                       C
C                                        MICHAEL RIGHTLEY               C
C                                                                       C
C                                                                       C
C   THIS PROGRAM CALCULATES THE INTENSITY AND TEMPERATURE               C
C   DISTRIBUTIONS IN A FREE-FALLING SOLID PARTICLE SOLAR CENTRAL        C
C   RECEIVER.  IT UTILIZES A DISCRETE ORDINATES APPROXIMATION TO        C
C   MODEL THE INTENSITY FIELD.  THE BOUNDARY INTENSITY DISTRIBUTION     C
C   IS DETERMINED THROUGH THE ASSUMED INTENSITY FUNCTION AND THE        C
C   PREVIOUSLY CALCULATED PARAMETER VALUES.  FIRST ORDER FINITE         C
C   DIFFERENCES ARE APPLIED TO BOTH THE DISCRETE ORDINATES              C
C   FORMULATION OF THE EOT AND TO THE ENERGY EXPRESSION AND AN          C
C   ITERATIVE LOOP IS SET UP TO ALLOW THE USER TO CHOOSE THE DESIRED    C
C   NUMBER OF ITERATIONS (CONVERGENCE FOR ALL CASES HAS BEEN OBSERVED   C
C   AFTER 10 TO 15 ITERATIONS).                                         C
C                                                                       C
C-----------------------------------------------------------------------C
      REAL L, KAPPA, L_X, L_Y, INTENSITY_LAM, LAMBDA1, INTENSITY
      REAL LAMBDA2, LAMBDA_AVG, MU, I_LAM_FLUX, I_BLACK_YO
      PARAMETER (IDIM_X=30, IDIM_Y=60, IDIM_LAM=7, IDIM_M=24)
      DIMENSION INTENSITY_LAM(IDIM_X, IDIM_Y, IDIM_M, IDIM_LAM)
      DIMENSION INTENSITY(IDIM_X, IDIM_Y, IDIM_M), FX_INPUT(IDIM_Y)
      DIMENSION I_LAM_FLUX(IDIM_Y, IDIM_M, IDIM_LAM), BFLUX(IDIM_Y)
      DIMENSION T(IDIM_X,IDIM_Y), MU(IDIM_M), XI(IDIM_M), WEIGHT(IDIM_M)
      DIMENSION ETA(IDIM_M), I_BLACK_YO(IDIM_LAM), DELQ(IDIM_X, IDIM_Y)
      DIMENSION FLUX_LAM(IDIM_X, IDIM_Y, IDIM_LAM), FLUX(IDIM_X, IDIM_Y)
      DIMENSION FX_CAL(IDIM_Y), FXDATA(IDIM_Y)
C
C-----     SUBROUTINE INPUT IS CALLED TO DETERMINE THE NEEDED
C-----     INPUTS FROM THE USER
C
      CALL INPUT(L_X, L_Y, NODES_X, NODES_Y, N_LAM1, N_LAM2, ALPHA,
     *           SIGMA_S, PHI, N_ORDS, T_INLET, DX, DY,
     *           FX_INPUT, IDIM_Y, FXDATA)
C
C-----     SUBROUTINE YOBOUND IS CALLED TO DETERMINE THE BOUNDARY
C-----     INTENSITIES AT THE TOP OF THE CURTAIN.
C
```

```
      CALL YOBOUND(T_INLET, N_LAM1,N_LAM2, INTENSITY_LAM,
     *             NODES_X, IDIM_X, IDIM_Y,
     *             IDIM_LAM, IDIM_M, N_ORDS, I_BLACK_YO)
C
C-----     SUBROUTINE ORDINATES DEFINES THE ORDINATES AND THE WEIGHTS
C-----     FOR THE DISCRETE ORDINATES METHOD
C
      CALL ORDINATES(N_ORDS, MU, XI, ETA, WEIGHT, IDIM_M)
C
C-----     SUBROUTINE XOBOUND IS CALLED TO DETERMINE THE BOUNDARY
C-----     INTENSITIES ON THE FRONT OF THE CURTAIN WHERE THE
C-----     INCIDENT SOLAR ENERGY IS IMPINGING.
C
      CALL XOBOUND(NODES_Y, INTENSITY, N_ORDS, MU, XI, ETA, IDIM_X,
     *             IDIM_Y, IDIM_M, FX_INPUT, WEIGHT, FX_CAL,
     *             FX_CALMAX, DY)
C
C-----     SUBROUTINE SPECTRUM IS CALLED TO BREAK THE INCIDENT FLUX
C-----     DOWN INTO ITS SPECTRAL COMPONENTS.
C
      CALL SPECTRUM(INTENSITY, I_LAM_FLUX, IDIM_X, IDIM_Y, IDIM_LAM,
     *              IDIM_M, N_LAM1, N_ORDS, NODES_Y)
C
C-----     SUBROUTINE EOT WILL SOLVE THE EQUATION OF TRANSFER,
C-----     SPECTRALLY, AT EACH NODE FOR THE ORDINATE DIRECTIONS.
C
      CALL EOT(INTENSITY_LAM, N_LAM1, N_LAM2, NODES_X, NODES_Y,
     *         L_X, L_Y, IDIM_X, IDIM_Y, IDIM_M, IDIM_LAM, MU, XI,
     *         WEIGHT, N_ORDS, INTENSITY, FLUX, T, FLUX_LAM,
     *         PHI, DX, DY, SIGMA_S, T_INLET, I_LAM_FLUX, I_BLACK_YO,
     *         ALPHA, DELQ, E_POWER, BFLUX, FX_INPUT, FX_CAL, FXDATA,
     *         FX_CALMAX)
C
      STOP
      END
C-------------------------------------------------------------------------C
C                                                                         C
C  THIS SUBROUTINE PROMPTS THE USER FOR THE NECESSARY INPUT               C
C  INFORMATION.                                                           C
C                                                                         C
C-------------------------------------------------------------------------C
      SUBROUTINE INPUT(L_X, L_Y, NODES_X, NODES_Y, N_LAM1, N_LAM2,
     *                 ALPHA, SIGMA_S, PHI, N_ORDS, T_INLET, DX, DY,
     *                 FX_INPUT, IDIM_Y, FXDATA)
      DIMENSION FX_INPUT(IDIM_Y), FXDATA(IDIM_Y)
      REAL KAPPA, L_X, L_Y
C
C-----     INPUTTING THE CURTAIN THICKNESS
C
      WRITE(6,10)
      WRITE(6,20)
      READ(*,*) L_X
      L_X = L_X / 10.
      L_Y = 13.97
      NPOINTS = 5
```

```
C
C-----     FIXING THE NODAL GRID
C
      NODES_X = 10
      NODES_Y = 20
      DX = L_X / NODES_X
      DY = L_Y / (NODES_Y - 1)
C
C-----     READING IN THE FRONT FACE FLUX DATA FOR LATER
C-----     CONVERSION TO THE BOUNDARY INTENSITIES (5 IS THE
C-----     NUMBER OF READINGS)
C
      WRITE(6,90)
      READ(5,*)I_DEF
      IF (I_DEF .EQ. 0) THEN
       WRITE(6,80)
       DO I = 1, NPOINTS
        WRITE(6,70)I
        READ(5,*)FX
        IF (I .EQ. 1) THEN
         FX_INPUT(1) = FX
         FX_INPUT(2) = FX
         FX_INPUT(3) = FX
         FX_INPUT(4) = FX
         FX_INPUT(5) = FX
        ELSE IF (I .EQ. 2) THEN
         FX_INPUT(6) = FX
         FX_INPUT(7) = FX
         FX_INPUT(8) = FX
        ELSE IF (I .EQ. 3) THEN
         FX_INPUT(9) = FX
         FX_INPUT(10) = FX
         FX_INPUT(11) = FX
        ELSE IF (I .EQ. 4) THEN
         FX_INPUT(12) = FX
         FX_INPUT(13) = FX
         FX_INPUT(14) = FX
        ELSE
         FX_INPUT(15) = FX
         FX_INPUT(16) = FX
         FX_INPUT(17) = FX
         FX_INPUT(18) = FX
         FX_INPUT(19) = FX
         FX_INPUT(20) = FX
        END IF
       END DO
      ELSE
C
C-----     TO MAKE INPUTTING EASIER, THE DATA FROM THE TESTS THAT
C-----     WERE USED ARE INPUT HERE AS PERMANENT DATA
C
       WRITE(6,100)
       READ(5,*)NFILE
```

```
IF (NFILE .EQ. 7) THEN
 FX_INPUT(1) = 57920.33
 FX_INPUT(2) = 57920.33
 FX_INPUT(3) = 57920.33
 FX_INPUT(4) = 57920.33
 FX_INPUT(5) = 57920.33
 FX_INPUT(6) = 92419.63
 FX_INPUT(7) = 92419.63
 FX_INPUT(8) = 92419.63
 FX_INPUT(9) = 116991.01
 FX_INPUT(10) = 116991.01
 FX_INPUT(11) = 116991.01
 FX_INPUT(12) = 80426.93
 FX_INPUT(13) = 80426.93
 FX_INPUT(14) = 80426.93
 FX_INPUT(15) = 30785.48
 FX_INPUT(16) = 30785.48
 FX_INPUT(17) = 30785.48
 FX_INPUT(18) = 30785.48
 FX_INPUT(19) = 30785.48
 FX_INPUT(20) = 30785.48
ELSE IF (NFILE .EQ. 8)THEN
 FX_INPUT(1) = 15940.73
 FX_INPUT(2) = 15940.73
 FX_INPUT(3) = 15940.73
 FX_INPUT(4) = 15940.73
 FX_INPUT(5) = 15940.73
 FX_INPUT(6) = 54692.433
 FX_INPUT(7) = 54692.433
 FX_INPUT(8) = 54692.433
 FX_INPUT(9) =  92010.503
 FX_INPUT(10) = 92010.503
 FX_INPUT(11) = 92010.503
 FX_INPUT(12) = 110487.887
 FX_INPUT(13) = 110487.887
 FX_INPUT(14) = 110487.887
 FX_INPUT(15) = 80853.553
 FX_INPUT(16) = 80853.553
 FX_INPUT(17) = 80853.553
 FX_INPUT(18) = 80853.553
 FX_INPUT(19) = 80853.553
 FX_INPUT(20) = 80853.553
ELSE IF (NFILE .EQ. 12)THEN
 FX_INPUT(1) = 174000.49
 FX_INPUT(2) = 174000.49
 FX_INPUT(3) = 174000.49
 FX_INPUT(4) = 174000.49
 FX_INPUT(5) = 174000.49
 FX_INPUT(6) = 412441.23
 FX_INPUT(7) = 412441.23
 FX_INPUT(8) = 412441.23
```

```
 FX_INPUT(9) =  557202.39
 FX_INPUT(10) = 557202.39
 FX_INPUT(11) = 557202.39
 FX_INPUT(12) = 564179.57
 FX_INPUT(13) = 564179.57
 FX_INPUT(14) = 564179.57
 FX_INPUT(15) = 344742.27
 FX_INPUT(16) = 344742.27
 FX_INPUT(17) = 344742.27
 FX_INPUT(18) = 344742.27
 FX_INPUT(19) = 344742.27
 FX_INPUT(20) = 344742.27
ELSE IF (NFILE .EQ. 15)THEN
 FX_INPUT(1) = 345778.33
 FX_INPUT(2) = 345778.33
 FX_INPUT(3) = 345778.33
 FX_INPUT(4) = 345778.33
 FX_INPUT(5) = 345778.33
 FX_INPUT(6) = 437564.67
 FX_INPUT(7) = 437564.67
 FX_INPUT(8) = 437564.67
 FX_INPUT(9) =  468617.67
 FX_INPUT(10) = 468617.67
 FX_INPUT(11) = 468617.67
 FX_INPUT(12) = 314740.33
 FX_INPUT(13) = 314740.33
 FX_INPUT(14) = 314740.33
 FX_INPUT(15) = 126025.67
 FX_INPUT(16) = 126025.67
 FX_INPUT(17) = 126025.67
 FX_INPUT(18) = 126025.67
 FX_INPUT(19) = 126025.67
 FX_INPUT(20) = 126025.67
ELSE IF (NFILE .EQ. 4)THEN
 FX_INPUT(1) = 196713.57
 FX_INPUT(2) = 196713.57
 FX_INPUT(3) = 196713.57
 FX_INPUT(4) = 196713.57
 FX_INPUT(5) = 196713.57
 FX_INPUT(6) = 418726.44
 FX_INPUT(7) = 418726.44
 FX_INPUT(8) = 418726.44
 FX_INPUT(9) =  545615.42
 FX_INPUT(10) = 545615.42
 FX_INPUT(11) = 545615.42
 FX_INPUT(12) = 545868.72
 FX_INPUT(13) = 545868.72
 FX_INPUT(14) = 545868.72
 FX_INPUT(15) = 329435.71
 FX_INPUT(16) = 329435.71
 FX_INPUT(17) = 329435.71
```

```
 FX_INPUT(18) = 329435.71
 FX_INPUT(19) = 329435.71
 FX_INPUT(20) = 329435.71
ELSE IF (NFILE .EQ. 5)THEN
 FX_INPUT(1) = 182981.94
 FX_INPUT(2) = 182981.94
 FX_INPUT(3) = 182981.94
 FX_INPUT(4) = 182981.94
 FX_INPUT(5) = 182981.94
 FX_INPUT(6) = 429956.24
 FX_INPUT(7) = 429956.24
 FX_INPUT(8) = 429956.24
 FX_INPUT(9) =  563836.87
 FX_INPUT(10) = 563836.87
 FX_INPUT(11) = 563836.87
 FX_INPUT(12) = 572774.45
 FX_INPUT(13) = 572774.45
 FX_INPUT(14) = 572774.45
 FX_INPUT(15) = 345879.92
 FX_INPUT(16) = 345879.92
 FX_INPUT(17) = 345879.92
 FX_INPUT(18) = 345879.92
 FX_INPUT(19) = 345879.92
 FX_INPUT(20) = 345879.92
ELSE IF (NFILE .EQ. 6)THEN
 FX_INPUT(1) = 118834.47
 FX_INPUT(2) = 118834.47
 FX_INPUT(3) = 118834.47
 FX_INPUT(4) = 118834.47
 FX_INPUT(5) = 118834.47
 FX_INPUT(6) = 381789.96
 FX_INPUT(7) = 381789.96
 FX_INPUT(8) = 381789.96
 FX_INPUT(9) =  565425.4
 FX_INPUT(10) = 565425.4
 FX_INPUT(11) = 565425.4
 FX_INPUT(12) = 636021.61
 FX_INPUT(13) = 636021.61
 FX_INPUT(14) = 636021.61
 FX_INPUT(15) = 446337.81
 FX_INPUT(16) = 446337.81
 FX_INPUT(17) = 446337.81
 FX_INPUT(18) = 446337.81
 FX_INPUT(19) = 446337.81
 FX_INPUT(20) = 446337.81
ELSE IF (NFILE .EQ. 16)THEN
 FX_INPUT(1) = 156356.95
 FX_INPUT(2) = 156356.95
 FX_INPUT(3) = 156356.95
 FX_INPUT(4) = 156356.95
 FX_INPUT(5) = 156356.95
```

```
          FX_INPUT(6) = 348157.41
          FX_INPUT(7) = 348157.41
          FX_INPUT(8) = 348157.41
          FX_INPUT(9) =  463759.09
          FX_INPUT(10) = 463759.09
          FX_INPUT(11) = 463759.09
          FX_INPUT(12) = 463937.03
          FX_INPUT(13) = 463937.03
          FX_INPUT(14) = 463937.03
          FX_INPUT(15) = 283033.40
          FX_INPUT(16) = 283033.40
          FX_INPUT(17) = 283033.40
          FX_INPUT(18) = 283033.40
          FX_INPUT(19) = 283033.40
          FX_INPUT(20) = 283033.40
         ELSE IF (NFILE .EQ. 17)THEN
          FX_INPUT(1) = 118954.23
          FX_INPUT(2) = 118954.23
          FX_INPUT(3) = 118954.23
          FX_INPUT(4) = 118954.23
          FX_INPUT(5) = 118954.23
          FX_INPUT(6) = 291606.29
          FX_INPUT(7) = 291606.29
          FX_INPUT(8) = 291606.29
          FX_INPUT(9) =  407880.0
          FX_INPUT(10) = 407880.0
          FX_INPUT(11) = 407880.0
          FX_INPUT(12) = 439180.02
          FX_INPUT(13) = 439180.02
          FX_INPUT(14) = 439180.02
          FX_INPUT(15) = 319162.39
          FX_INPUT(16) = 319162.39
          FX_INPUT(17) = 319162.39
          FX_INPUT(18) = 319162.39
          FX_INPUT(19) = 319162.39
          FX_INPUT(20) = 319162.39
         END IF
        END IF
C
C-----      CONVERTING THE FLUXES TO W/m2
C
        DO I = 1, NODES_Y
         FX_INPUT(I) = FX_INPUT(I) / 100.0**2
        END DO
C
C-----      FIXING THE SPECTRAL BANDS AND OTHER RADIATIVE PROPERTIES
C
        N_LAM1 = 5
        N_LAM2 = 2
        ALPHA = 3.0
        SIGMA_S = 0.1 * ALPHA / 0.9
C
C-----      INPUTTING THE NUMBER OF ORDINATE DIRECTIONS DESIRED
```

```
C
      WRITE(6,63)
      READ(*,*) N_ORDS
      WRITE(6,64)
C
C-----     INLET PARTICLE TEMPERATURE
C
      READ(*,*) T_INLET
      T_INLET = ((T_INLET - 32.) * 5. / 9.) + 273.
      WRITE(6,65)
C
C-----     FORMAT STATEMENTS
C
 10   FORMAT(////,5X,'INPUT SECTION FOR THE CURTAIN GEOMETRY',///)
 20   FORMAT(10X,'CURTAIN DEPTH ALONG INCOMING FLUX ',
     *       'VECTOR (L_X) IN MILLIMETERS? ',$)
 21   FORMAT(//,10X,'CURTAIN HEIGHT (L_Y) IN METERS? ',$)
 22   FORMAT(//,10X,'NUMBER OF NODES IN X DIRECTION? ',$)
 23   FORMAT(//,10X,'NUMBER OF NODES IN Y DIRECTION? ',$)
 30   FORMAT(////,5X,'INPUT SECTION FOR WAVELENGTH BANDS',///)
 40   FORMAT(10X,'NUMBER OF BANDS DESIRED IN THE SOLAR ',
     *       'SPECTRAL RANGE',/,10X,'(0.3 TO 1.1 MICROMETERS) ',
     *       '...',$)
 41   FORMAT(//,10X,'THE NUMBER OF BANDS DESIRED IN THE IR RANGE',/,
     *       10X,'(1.1 TO 10 MICROMETERS)... ',$)
 50   FORMAT(////,5X,'INPUT SECTION FOR RADIATIVE PROPERTIES',///)
 60   FORMAT(10X,'CONSTANT ABSORPTION COEFFICIENT (1/m)? ',$)
 61   FORMAT(//,10X,'CONSTANT SCATTERING COEFFICIENT (1/m)? ',$)
 62   FORMAT(//,10X,'CONSTANT PHASE FUNCTION (EITHER A 0 OR A 1)? ',$)
 63   FORMAT(//,10X,'NUMBER OF ORDINATE DIRECTIONS DESIRED (4,12,24)? '
     *       ,$)
 64   FORMAT(//,10X,'AVERAGE INLET PARTICLE TEMPERATURE (FAHRENHEIT)? '
     *              ,$)
 65   FORMAT(////)
 70   FORMAT(20X,'READING OF FLUX GAGE #',I1,' (W/m2)...',$)
 80   FORMAT(///,10X,'INPUT SECTION FOR THE FLUX GAGE READINGS',//)
 90   FORMAT(//,10X,' ENTER A ZERO FOR INPUTTTED VALUES...',$)
 100  FORMAT(//,10X,'ENTER THE NUMBER OF THE DATA FILE... Q',$)
C
      RETURN
      END
C-----------------------------------------------------------------------C
C                                                                       C
C  THIS SUBROUTINE DETERMINES THE INTENSITY ALONG THE Y=0               C
C  BOUNDARY (I.E. THE PARTICLE INLET POINT).  IT CALCULATES THE         C
C  EMISSIVE POWER OF THE PARTICLES THROUGH PLANCKS DISTRIBUTION         C
C  AND DIVIDES BY PI TO DETERMINE THE INTENSITY SINCE THIS              C
C  EMISSION IS DIFFUSE.                                                 C
C                                                                       C
C-----------------------------------------------------------------------C
      SUBROUTINE YOBOUND(T_INLET, N_LAM1, N_LAM2, INTENSITY_LAM,
     *                   NODES_X, IDIM_X,
```

```
     *                    IDIM_Y, IDIM_LAM, IDIM_M, N_ORDS, I_BLACK_YO)
      REAL INTENSITY_LAM, LAMBDA1, LAMBDA2, LAMBDA_AVG
      REAL I_BLACK_YO
      DIMENSION INTENSITY_LAM (IDIM_X, IDIM_Y, IDIM_M, IDIM_LAM)
      DIMENSION I_BLACK_YO(IDIM_LAM)
      PI = 4.0 * ATAN(1.0)
      C2 = 14388.0
      SIGMA = 5.729E-08
C
C-----     DETERMINING THE SPECTRAL RANGE AND THE BANDWIDTHS
C
      D_LAM1 = (1.1 - 0.3) / FLOAT(N_LAM1)
      D_LAM2 = (10.0 - 1.1) / FLOAT(N_LAM2)
      N_LAMT = N_LAM1 + N_LAM2
      LAMBDA1 = 0.3
C
C-----     CALCULATING THE F(0 TO LAMBDA) FACTORS TO INTEGRATE PLANCKS
C-----     DISTRIBUTION FOR LAMBDA1
C
       TLAM1 = LAMBDA1 * T_INLET
       V1 = C2 / TLAM1
       IF(V1.GE.2.0)THEN
        SUM = 0.0
        DO I = 1,40
         SUM = SUM + (EXP(-I*V1)/FLOAT(I)**4)
     *               * (((I*V1 + 3)*I*V1 + 6)*I*V1 + 6)
        END DO
        FOL1 = (15.0/PI**4) * SUM
       ELSE
        FOL1 = 1 - (15./PI**4) * V1**3 * (1./3. - V1/8. + V1**2/60.
     *         - V1**4/5040. + V1**6/272160. - V1**8/13305600.)
       END IF
C
C-----     FOR LAMBDA2
C
      D_LAM = D_LAM1
      DO I_NLAM = 1,N_LAMT
       LAMBDA2 = LAMBDA1 + D_LAM
       TLAM2 = LAMBDA2 * T_INLET
       V2 = C2 / TLAM2
       IF(V2.GE.2.0)THEN
        SUM = 0.0
        DO I = 1,40
         SUM = SUM + (EXP(-I*V2)/FLOAT(I)**4)
     *               * (((I*V2 + 3)*I*V2 + 6)*I*V2 + 6)
        END DO
        FOL2 = (15.0/PI**4) * SUM
       ELSE
        FOL2 = 1 - (15./PI**4) * V2**3 * (1./3. - V2/8. +
     *         V2**2/60. - V2**4/5040. + V2**6/272160.
     *              - V2**8/13305600.)
       END IF
C
C-----     THE EMISSIVE POWER IS JUST THE DIFFERENCE IN THE F FACTORS
C-----     MULTIPLIED BY THE INLET TEMPERATURE TO THE FIFTH POWER, THE
```

```
C-----      STEPHAN BOLTZMANN CONSTANT, AND THE EMITTANCE WHICH
C-----      IS EQUAL TO THE ABSORPTANCE
C
       E_POWER = (FOL2 - FOL1) * T_INLET**5 * SIGMA
C
C-----      DETERMINING THE INTENSITY BY DIVIDING BY PI DUE TO
C-----      THE DIFFUSE NATURE OF THE PARTICLE EMISSION
C
       I_BLACK_YO(I_NLAM) = E_POWER / PI / 100.0**2
       DO I = 1,NODES_X
        DO I_DIR = 1, N_ORDS
         INTENSITY_LAM(I, 1, I_DIR, I_NLAM) = I_BLACK_YO(I_NLAM)
        END DO
       END DO
C
       LAMBDA1 = LAMBDA2
       FOL1 = FOL2
       TLAM1 = TLAM2
       IF(LAMBDA2 .GE. 1.1)THEN
        D_LAM = D_LAM2
       END IF
      END DO
      RETURN
      END
C-----------------------------------------------------------------------C
C                                                                       C
C   THIS SUBROUTINE SETS THE INTENSITIES AT THE X=0 BOUNDARY.           C
C   THE VALUES HAVE BEEN DETERMINED THROUGH THE PARAMETER ESTIMATION    C
C   METHOD THAT MODELS THE INTENSITIES FROM EXPERIMENTAL DATA.          C
C                                                                       C
C-----------------------------------------------------------------------C
      SUBROUTINE XOBOUND(NODES_Y, INTENSITY, N_ORDS, MU, XI, ETA,
     !                   IDIM_X, IDIM_Y, IDIM_M, FX_INPUT, WEIGHT,
     !                   FX_CAL, FX_CALMAX, DY)
      REAL INTEGRAL, MU, INTENSITY
      DIMENSION INTENSITY(IDIM_X, IDIM_Y, IDIM_M), WEIGHT(IDIM_M)
      DIMENSION MU(IDIM_M), XI(IDIM_M), ETA(IDIM_M)
      DIMENSION BETA(20,4), FX_INPUT(IDIM_Y), FX_CAL(IDIM_Y)
      DIMENSION FLUX_C(20)
C
C-----      INITIALIZATION
C
      PI = 4.0 * ATAN(1.0)
      N_COEFF = 3
      DP = 5.7 * PI / 180.
      DH = DP / 2.
      TO = 50. * PI /180.
C
C-----      A AND B ARE THE GAUSSIAN CURVE FIT PARAMETERS FOR
C-----      THE INPUTTED FRONT FLUX TERM
C
      A = 458006.648588
      B = - 17.421543
      XO = 7.442046
C
C-----      TC1 AND TC2 ARE THE ANGULAR LIMITS DEFINING THE CONE
```

```
C-----      OF RAYS FROM THE CONCENTRATOR.  ANY ORDINATE DIRECTIONS
C-----      OUTSIDE THIS CONE WILL REPRESENT A BOUNDARY INTENSITY OF
C-----      ZERO.
C
      TC1 = -85. * PI / 180.
      TC2 = -35. * PI / 180.
C
C-----      CALCULATING THE AVERAGE INCIDENT FLUX WHICH IS THE VALUE USED
C-----      IN THE NORMALIZATION OF THE NIP DATA
C
      SUMFX = 0.0
      DO J = 1, 5
       SUMFX = SUMFX + FX_INPUT(J)
      END DO
C
C-----      READING IN THE COEFFICIENTS TO BE USED
C
      OPEN (UNIT=3, STATUS='UNKNOWN', FILE='COEFF.DAT')
      DO I = 1, NODES_Y
       READ(3,*) IX, BETA(I,1), BETA(I,2), BETA(I,3)
      END DO
      DO I = 1, NODES_Y
       DO J = 1, N_COEFF
        BETA(I,J) = BETA(I,J)  / DP
       END DO
       WRITE(6,10) (BETA(I,J)*DP, J = 1, N_COEFF)
      END DO
      CLOSE (UNIT=3)
 10   FORMAT(1X, 3(F12.6,5X))
C
C-----      DETERMINING THE SENSITIVITY COEFFICIENTS
C
      DO I_DIR = 1, N_ORDS
C
C-----      DETERMINING THE ANGLES OF THE ORDINATES
C
        THETA_QUAD = ATAN (XI(I_DIR)/SQRT(ETA(I_DIR)**2 + MU(I_DIR)**2))
        PHI_QUAD = ATAN(ETA(I_DIR) / MU(I_DIR))
        IF (MU(I_DIR) .GE. 0) THEN
         THETA_TOT = THETA_QUAD
         PHI_TOT = PHI_QUAD
        ELSE
         IF (XI(I_DIR) .GE. 0) THEN
          THETA_TOT = PI / 2. + ABS(THETA_QUAD)
         ELSE
          THETA_TOT = PI + ABS(THETA_QUAD)
         END IF
         IF (ETA(I_DIR) .GE. 0) THEN
          PHI_TOT = (PI / 2. + ABS(PHI_QUAD))
         ELSE
          PHI_TOT = (PI + ABS(PHI_QUAD))
         END IF
        END IF
        PHI_TOT = 90. * PI / 180.
        THETA_TOT = THETA_TOT - TO
```

```
         IF (MU(I_DIR) .GE. 0) THEN
          TT = THETA_TOT * 180. / PI
          PT = PHI_TOT * 180. / PI
        END IF
C
C-----      DETERMINING THE INTENSITIES AND THE FLUXES
C
        SUM = 0.0
        DO J = 1, NODES_Y
C
C-----      CALCULATION OF THE INPUT FLUX THROUGH THE GAUSSIAN CURVE FIT
C
         Y = (J-1) * DY
         FXFIT = A * EXP ( (Y-X0)**2 / B) / 100.**2
C
C-----      DETERMINING THE INTENSITY FIELD AT THE FRONT FACE FOR THE
C-----      DISCRETE ORDINATE DIRECTIONS.
C
         IF (MU(I_DIR) .LT. 0 .OR. THETA_TOT .LT. TC1 .OR.
     !       THETA_TOT .GT. TC2) THEN
          INTENSITY (1, J, I_DIR) = 0.0
         ELSE
          INTENSITY (1, J, I_DIR) = BETA(J,1) / COS (THETA_TOT)
     !      + BETA(J,2) / COS (THETA_TOT) / SIN(THETA_TOT)
     !      + BETA(J,3) / SIN(THETA_TOT)
          INTENSITY(1, J, I_DIR) = FXFIT * INTENSITY(1, J, I_DIR)
          INTENSITY(1, J, I_DIR) = INTENSITY(1, J, I_DIR)
C
         END IF
         END DO
C
C-----      PRINTING OUT THE BOUNDARY VALUES
C
         IF (MU(I_DIR) .GE. 0) THEN
          DO J = 1, NODES_Y
           WRITE(6,100)I_DIR, MU(I_DIR), XI(I_DIR), ETA(I_DIR), TT,
     !               INTENSITY(1,J,I_DIR)
 100       FORMAT(1X,I2,2X,F10.8,2X,F10.8,2X,F10.8, 3X,F6.1,3X, F15.3)
          END DO
         END IF
 25     END DO
C
C-----      RECALCULATING THE FRONT SURFACE FLUXES FOR COMPARISON
C-----      TO THE DATA USING GAUSSIAN QUADRATURE
C
       DO J = 1, NODES_Y
        SUM = 0.0
        DO I_DIR = 1, N_ORDS
         SUM = SUM + WEIGHT(I_DIR)
     !           * ( MU(I_DIR) ) * INTENSITY(1,J,I_DIR)
        END DO
        FX_CAL(J) = SUM
       END DO
C
C-----       CALCULATION OF THE MAXIMUM ESTIMATED FRONT SURFACE FLUX
```

```
C
      FX_CALMAX = FX_CAL(1)
      DO J = 2, NODES_Y
       IF (FX_INPUT(J) .GT. FX_CALMAX) FX_CALMAX = FX_INPUT(J)
      END DO
C
C-----     PRINTING OUT THE FLUX VALUES
C
      WRITE(6,120) (FX_INPUT(J), FX_CAL(J), FLUX_C(J), J = 1, NODES_Y)
 120  FORMAT(1( 5X, F13.4, 5X, F15.4, 5X, F15.4))
C
      RETURN
      END
C-------------------------------------------------------------------------C
C                                                                         C
C  THIS SUBROUTINE DETERMINES THE SPECTRAL COMPONENTS OF THE              C
C  INCIDENT INTENSITIES THAT WERE "READ IN" IN XOBOUND.  THIS IS          C
C  ACCOMPLISHED BY INTEGRATING AN EXPERIMENTALLY MEASURED SPECTRUM        C
C  OVER THE WAVELENGTH BANDS DEFINED BY THE USER.  THE INTEGRATION        C
C  IS CARRIED OUT USING THE TRAPEZOIDAL RULE DUE TO THE LARGE NUMBER      C
C  OF DATA POINTS.                                                        C
C                                                                         C
C-------------------------------------------------------------------------C
      SUBROUTINE SPECTRUM(INTENSITY, I_LAM_FLUX, IDIM_X, IDIM_Y,
     *                    IDIM_LAM, IDIM_M, N_LAM1, N_ORDS, NODES_Y)
      REAL LAMBDASPEC, LAMBDA, INTENSITY, I_LAM_FLUX
      DIMENSION Q1(500), LAMBDASPEC(500), LAMBDA(50), PERCENTINT(100)
      DIMENSION I_LAM_FLUX(IDIM_Y, IDIM_M, IDIM_LAM)
      DIMENSION INTENSITY(IDIM_X, IDIM_Y, IDIM_M)
C
C-----     READING IN THE SOLAR SPECTRUM FROM THE LYCOR DATA
C
      OPEN (UNIT=9, STATUS='UNKNOWN', FILE='LYCOR.DAT')
      DO I = 1, 401
       READ(9,*)LAMBDASPEC(I), Q1(I), Q2, Q3, Q4, Q5, Q6, Q7
      END DO
      CLOSE (UNIT=9)
C
C-----     SETTING UP THE SPECTRAL BANDS
C
      D_LAMBDABIG = (1.1 - 0.3) / FLOAT(N_LAM1)
      D_LAMBDASPEC = 0.002
      LAMBDA(1) = 0.3
      XMIN = LAMBDASPEC(1)
      XMAX = XMIN
      JBAND1 = 1
C
C-----     THE I LOOP WILL BE OVER N_LAM BANDS TO DETERMINE THE VALUE
C-----     OF THE INTEGRAL OVER EACH
C
      DO I = 1, N_LAM1
       LAMBDA(I+1) = LAMBDA(I) + D_LAMBDABIG
C
C-----     THIS SECTION DETERMINES THE WAVELENGTHS OF THE DATA POINTS
C-----     THAT LIE NEAREST THE BAND BOUNDARIES. THESE POINTS WILL BE
C-----     USED AS THE LIMITS ON THE INTEGRATION.  THE CONTRIBUTION OF
```

```
C-----      THE AREA BETWEEN THE LIMIT DATA POINT AND THE BAND BOUNDARY
C-----      IS ASSUMED NEGLIGIBLE.
C
       DO J = JBAND1, 401
        XMAX = XMAX + D_LAMBDASPEC
        IF(XMAX.GT.LAMBDA(I+1))THEN
         XMAX = XMAX - D_LAMBDASPEC
         JBAND2 = J - 1
         GO TO 10
        END IF
        IF(XMAX.EQ.LAMBDA(I+1))THEN
         JBAND2 = J
         GO TO 10
        END IF
       END DO
C
C-----      PERFORMING THE INTEGRATION USING THE TRAPEZOIDAL RULE
C
 10    SUM = 0.0
       DO J = JBAND1, JBAND2-1
        SUM = SUM + Q1(J)
       END DO
       PERCENTINT(I) = (D_LAMBDASPEC / 2.)
       PERCENTINT(I) = PERCENTINT(I) * (Q1(JBAND1)+2.*SUM+Q1(JBAND2))
C
C-----      RESETTING THE INTERVALS FOR THE NEW BAND
C
       JBAND1 = JBAND2 + 1
       XMIN = LAMBDASPEC(JBAND1)
       XMAX = XMIN
      END DO
C
C-----      CALCULATING THE TOTAL FLUX (OR INTENSITY) UNDER THE SPECTRUM
C
      SUMI = 0.0
      DO I = 1, N_LAM1
       SUMI = SUMI + PERCENTINT(I)
      END DO
      WRITE(*,100)SUMI
      WRITE(*,105)
C
C-----      CALCULATING THE PERCENTAGE OF THE TOTAL FLUX (OR INTENSITY)
C-----      THAT LIES IN EACH WAVELENGTH BAND AND MULTIPL_YING
C-----      THE INCIDENT INTENSITY BY THOSE VALUES TO DETERMINE
C-----      THE SPECTRAL DISTRIBUTION OF THE INCIDENT ENERGY.
C
      DO I = 1, N_LAM1
       PERCENTINT(I) = (PERCENTINT(I) / SUMI) * 100.0
       WRITE(*,110)LAMBDA(I), LAMBDA(I+1), PERCENT(I)
       DO J = 1,NODES_Y
        DO J_DIR = 1, N_ORDS
         I_LAM_FLUX(J,J_DIR,I) = INTENSITY(1,J,J_DIR) *
     *                           PERCENTINT(I) / 100.0
        END DO
       END DO
      END DO
```

```
C
C-----     FORMAT STATEMENTS
C
 100  FORMAT(//,5X,'THE TOTAL INTEGRATED FLUX UNDER THE CURVE IS...',
     *       F9.6,' W/M**2',//)
 105  FORMAT(5X,'LAMBDA(I)',5X,'LAMBDA(I+1)',6X,'PERCENTAGE IN BAND',//)
 110  FORMAT(7X,F5.3,10X,F5.3,17X,F7.3)
      RETURN
      END
C-------------------------------------------------------------------------C
C                                                                         C
C  THIS SUBROUTINE ITERATES THE EQUATION OF TRANSFER ACCORDING            C
C  TO THE DISCRETE ORDINATES FORMULATION.                                 C
C                                                                         C
C-------------------------------------------------------------------------C
      SUBROUTINE EOT(INTENSITY_LAM, N_LAM1, N_LAM2, NODES_X, NODES_Y,
     *               L_X, L_Y, IDIM_X, IDIM_Y, IDIM_M, IDIM_LAM,
     *               MU, XI, WEIGHT, N_ORDS, INTENSITY,
     *               FLUX, T, FLUX_LAM, PHI, DX, DY, SIGMA_S, T_INLET,
     *               I_LAM_FLUX, I_BLACK_YO, ALPHA, DELQ,
     *               E_POWER, BFLUX, FX_INPUT, FX_CAL, FXDATA,
     *               FX_CALMAX)
      REAL INTENSITY_LAM, INTENSITY, MU, I_BLACK, LAMBDA1, LAMBDA2
      REAL kappa, I_INNSCAT, I_LAM_FLUX, I_BLACK_YO
      DIMENSION INTENSITY_LAM(IDIM_X, IDIM_Y, IDIM_M, IDIM_LAM)
      DIMENSION INTENSITY(IDIM_X, IDIM_Y, IDIM_M), I_BLACK_YO(IDIM_LAM)
      DIMENSION I_LAM_FLUX(IDIM_Y, IDIM_M, IDIM_LAM)
      DIMENSION T(IDIM_X,IDIM_Y), MU(IDIM_M), XI(IDIM_M), WEIGHT(IDIM_M)
      DIMENSION DELQ(IDIM_X, IDIM_Y), BFLUX(IDIM_Y)
      DIMENSION FLUX(IDIM_X, IDIM_Y), E_POWER(IDIM_LAM)
      DIMENSION FX_INPUT(IDIM_Y), T_PR(10,20), FX_CAL(IDIM_Y)
      DIMENSION FXDATA(IDIM_Y)
C
C-----     INITIALIZATION AND BANDWIDTH SPECIFICATION
C
      D_LAM2 = (10.0 - 1.1) / FLOAT(N_LAM2)
      D_LAM1 = (1.1 - 0.3) / FLOAT(N_LAM1)
      N_LAMT = N_LAM1 + N_LAM2
      LAMBDA1 = 0.3
      C2 = 14388.0
      SIGMA = 5.729E-08
      PI = 4.0 * ATAN(1.0)
      RX = 1.0
C
C-----     SETTING THE TEMP FIELD TO 300 JUST TO GET THE CODE RUNNING
C-----     AND ADDING ON THE INLET EMISSION TERM TO THE FLUX TERM AT THE
C-----     CORNER (X=0, Y=0)
C
      KAPPA = ALPHA + SIGMA_S
      DO 1 I= 1, NODES_X
       DO 1 J = 1, NODES_Y
        T(I,J) = T_INLET
 1    CONTINUE
      DO 2 I_DIR = 1, N_ORDS
```

```
       DO 2 ILAM = 1, N_LAMT
        DO 2 J = 1, NODES_Y
         INTENSITY_LAM(1, J, I_DIR, ILAM) = I_LAM_FLUX(J, I_DIR, ILAM) +
     *                                      I_BLACK_YO(ILAM)
 2    CONTINUE
C
      I_ITER = 1
C
C-----     STARTING THE LOOP OVER THE WAVELENGTH BANDS CHOSEN
C
 10   DO ILAM = 1,N_LAMT
C
       IF (ILAM .LE. N_LAM1) THEN
        LAMBDA2 = LAMBDA1 + D_LAM1
       ELSE
        LAMBDA2 = LAMBDA1 + D_LAM2
       END IF
C
C-----    STARTING THE LOOPS OVER THE DIRECTIONS AND THE NODAL POINTS
C
       DO I = 2,NODES_X
        DO J = 2,NODES_Y
         DO I_DIR = 1,N_ORDS
C
C-----     CALCULATING THE EMISSION TERM USING THE F-FACTOR METHOD TO
C-----     INTEGRATE PLANCK'S EQUATION OVER WAVELENGTH
C
          V1 = C2 / LAMBDA1 / T(I, J)
          IF(V1.GE.2.0)THEN
           SUM = 0.0
           DO I_PLAN = 1,40
            SUM = SUM + (EXP(-I_PLAN*V1)/FLOAT(I_PLAN)**4)
     *                * (((I_PLAN*V1 + 3)*I_PLAN*V1 + 6)*I_PLAN*V1 + 6)
           END DO
           FOL1 = (15.0/PI**4) * SUM
          ELSE
           FOL1 = 1 - (15./PI**4) * V1**3 * (1./3. - V1/8. + V1**2/60.
     *         - V1**4/5040. + V1**6/272160. - V1**8/13305600.)
          END IF
C
C-----     FOR LAMBDA2
C
          V2 = C2 / LAMBDA2 / T(I, J)
          IF(V2.GE.2.0)THEN
           SUM = 0.0
           DO I_PLAN = 1,40
            SUM = SUM + (EXP(-I_PLAN*V2)/FLOAT(I_PLAN)**4)
     *                * (((I_PLAN*V2 + 3)*I_PLAN*V2 + 6)*I_PLAN*V2 + 6)
           END DO
           FOL2 = (15.0/PI**4) * SUM
          ELSE
           FOL2 = 1 - (15./PI**4) * V2**3 * (1./3. - V2/8. +
     *         V2**2/60. - V2**4/5040. + V2**6/272160.
     *         - V2**8/13305600.)
          END IF
```

```
C
C-----     THE EMISSIVE POWER IS JUST THE DIFFERENCE IN THE F FACTORS
C-----     MULTIPLIED BY THE LOCAL TEMPERATURE TO THE FIFTH POWER, THE
C-----     STEPHAN BOLTZMANN CONSTANT, AND THE EMITTANCE WHICH
C-----     IS EQUAL TO THE ABSORPTANCE
C
          E_POWER(ILAM) = (FOL2 - FOL1) * T(I, J)**5 * SIGMA/100.**2
C
C-----     DETERMINING THE BLACK-BODY INTENSITY BY DIVIDING BY PI DUE
C-----     TO THE DIFFUSE NATURE OF THE PARTICLE EMISSION
C
          I_BLACK = E_POWER(ILAM) / PI
C
C-----     CALCULATING THE IN-SCATTERING TERM USING GAUSS QUADRATURE
C-----     TO DETERMINE THE INTEGRAL
C
          DO I_IT_SCAT = 1, 3
           SUM_INNSCAT = 0.0
           DO I_SCAT = 1 , N_ORDS
            PHI = 1. + MU(I_SCAT) * MU(I_DIR) + XI(I_SCAT)*XI(I_DIR)
            SUM_INNSCAT = SUM_INNSCAT + WEIGHT(I_SCAT) * PHI
     *                  * INTENSITY_LAM (I, J, I_SCAT, ILAM)
           END DO
           I_INNSCAT = (SIGMA_S / 4.0 / PI) * SUM_INNSCAT
C
C-----     DETERMINING THE SPECTRAL INTENSITY AT NODE (I,J)
C-----     ACCORDING TO THE FINITE DIFFERENCE FORM OF THE
C-----     EQUATION OF TRANSFER
C
 100       BETA_M =ABS(MU(I_DIR))/DX+ABS(XI(I_DIR)) / DY + KAPPA
           INTENSITY_LAM(I, J, I_DIR, ILAM) = (1.0 / BETA_M) *
     *       ( ABS(MU(I_DIR)) * INTENSITY_LAM(I-1,J,I_DIR,ILAM) / DX
     *         + ABS(XI(I_DIR)) * INTENSITY_LAM(I,J-1,I_DIR,ILAM) / DY
     *         + ALPHA * I_BLACK + I_INNSCAT )
          END DO
C
C-----     SETTING ANY NEGATIVE INTENSITIES TO ZERO REMOVES
C-----     NON-REALISTIC VALUES THAT LARGE SCATTERING
C-----     CROSS-SECTIONS AND INADEQUATE SPATIAL RESOLUTION PRODUCE
C
          IF (INTENSITY_LAM(I,J,I_DIR,ILAM) .LT. 0.0) THEN
           INTENSITY_LAM(I,J,I_DIR,ILAM) = 0.0
          END IF
C
C-----     ENDING THE LOOPS ON X, Y, WAVELENGTH, AND DIRECTION
C
          I_ITER = I_ITER + 1
         END DO
        END DO
        LAMBDA1 = LAMBDA2
       END DO
C
C-----     CALCULATING THE DIVERGENCE OF THE RADIATIVE FLUX VECTOR
C-----     FROM THE SPECTRAL EMISSIVE POWER, THE MEAN
C-----     SPECTRAL INTENSITY AND THE SPECTRAL IN-SCATTERING
```

```
C-----      SOURCE TERM AT THE POINT (I,J)
C
      DO I = 1, NODES_X
       DO J = 2, NODES_Y
        SUMLAM = 0.0
        DO ILAM = 1, N_LAMT
         SUMINTEN = 0.0
         SUMSCAT = 0.0
         DO I_DIR = 1, N_ORDS
C
C-----      CALCULATION OF THE INTEGRATED PHASE FUNCTION ACCORDING TO
C-----      THE EQUATION BELOW EQ. 14.35 IN SEIGEL AND HOWELL
C
          SUMPHASE = 0.0
          DO I_PDIR = 1, N_ORDS
           PHI = 1.0 + (MU(I_PDIR) * MU(I_DIR) + XI(I_PDIR) * XI(I_DIR))
           SUMPHASE = SUMPHASE + WEIGHT(I_PDIR) * PHI
          END DO
          SUMPHASE = SUMPHASE / 4. / PI
C
C-----      CALCULATION OF THE MEAN INTENSITY AND THE SOLID
C-----      ANGLE INTEGRAL ON THE RHS OF EQ. 14-37 IN SEIGEL AND HOWELL
C
          SUMINTEN = SUMINTEN + WEIGHT(I_DIR) *
     *              INTENSITY_LAM(I,J,I_DIR,ILAM)
          SUMSCAT = SUMSCAT + WEIGHT(I_DIR) * SUMPHASE *
     *               INTENSITY_LAM( I, J, I_DIR, ILAM)
         END DO
C
C-----      CALCULATION OF THE INTEGRAL OVER WAVELENGTH OF EQ. 14-37
C
         IF (ILAM .LE. N_LAM1) THEN
          SUMLAM = SUMLAM + (ALPHA * (E_POWER(ILAM)-KAPPA*SUMINTEN/4.) +
     *                    SIGMA_S * SUMSCAT / 4.) * D_LAM1
         ELSE
          SUMLAM = SUMLAM + (ALPHA * (E_POWER(ILAM)-KAPPA*SUMINTEN/4.) +
     *                    SIGMA_S * SUMSCAT / 4.) * D_LAM2
         END IF
        END DO
C
C-----      CALCULATION OF THE DIVERGENCE OF THE RADIATIVE FLUX VECTOR
C
        DELQ(I,J) = 4. * SUMLAM
       END DO
      END DO
C
C-----      CALCULATING THE TEMPERATURE DISTRIBUTION FROM THE DIVERGENCE
C-----      OF THE RADIATIVE FLUX VECTOR, 'DELQ.'  THE THERMOPHYSICAL
C-----      PROPERTIES THAT ARE REQUIRED FOR THE ENERGY EQUATION
C-----      WERE DETERMINED BY WEIGHTING THE RESPECTIVE
C-----      PROPERTY VALUES FOR THE AIR AND THE PARTICLES USING
C-----      THE POROSITY AS THE WEIGHTING FACTOR.  THE VELOCITY
C-----      COMES FROM A CURVE FIT OF MEASURED DATA FOR THIS TYPE OF FLOW
C
      RHO_EFF = 2342.776 / 100.0**3
      CP_EFF = 864.220
```

```
      RHO_AIR = 1.16 / 100.0**3
      CP_AIR = 1007.
      PR_AIR = 0.709
      POR_AIR = 0.410
C
C-----     THE CURVE FIT COEFFICIENTS
C
      VA = 0.844137
      VB = 5.034810
      VC = -1.875972
      VD = 0.260033
C
      DO I = 1, NODES_X
       T_PR(I,1) = (T_INLET - 273.) * 9. / 5. + 32.
       DO J = 2, NODES_Y
C
C-----     CALCULATION OF THE VELOCITY
C
        Y = (J-1) * DY
        V = VA + VB * Y + VC * Y**2 + VD * Y**3
        V = V * 100.
C
C-----     CALCULATION OF THE CONVECTIVE LOSS TERM
C
        RE_D = .23242 * V
        H_EFF = 2.06 * RE_D**(-0.575) * PR_AIR**(-2./3.)
        H_EFF = H_EFF * RHO_AIR * CP_AIR * V
        H_EFF = H_EFF / POR_AIR
        QCONV = H_EFF * (T(I,J-1) - T_INLET)
C
C-----     CALCULATION OF THE TEMPERATURE FIELD
C
        T(I,J) = T(I,J-1) + (DY/RHO_EFF/CP_EFF/V) * (-DELQ(I,J) - QCONV)
        T_PR(I,J) = (T(I,J) - 273.) * 9. / 5. + 32.
C
       END DO
      END DO
C
C-----     CALCULATION OF THE AVERAGE EXIT TEMPERATURE
C
      SUMT = 0.0
      DO I = 1, NODES_X
       SUMT = SUMT + T(I, NODES_Y)
      END DO
      TAVG = ((SUMT / NODES_X) - 273.) * 9. / 5. + 32.
C
C-----     PRINTING OUT THE TEMPERATURE FIELD
C
      WRITE(6,155)
      DO J = 1, NODES_Y
       WRITE(6,160) (T_PR(I,J), I = 1, NODES_X,2)
      END DO
      WRITE(6,170) TAVG
      WRITE(6,171)
      READ(5,*)
C
```

```
C-----      CALCULATION AND PRINTING OF THE BACK SURFACE FLUX
C
      OPEN (UNIT = 1, STATUS='NEW', FILE='QMODEL.DAT')
      DO J = 1, NODES_Y
       SUMFLUXLAM = 0.0
       DO ILAM = 1, N_LAMT
        SUMBFLUX = 0.0
        DO I_DIR = 1, N_ORDS
         SUMBFLUX = SUMBFLUX + WEIGHT(I_DIR) *
     *        INTENSITY_LAM(NODES_X, J, I_DIR, ILAM) * (MU(I_DIR))
        END DO
        IF (ILAM .LE. N_LAM1) THEN
         SUMFLUXLAM = SUMFLUXLAM + SUMBFLUX * D_LAM1
        ELSE
         SUMFLUXLAM = SUMFLUXLAM + SUMBFLUX * D_LAM2
        END IF
       END DO
       FX_CALMAX = SIGMA * T_INLET ** 4. / 100.**2
       BFLUX(J) = SUMFLUXLAM / FX_CALMAX
       Y = DY * (J-1) / 13.97
       WRITE(6,180) Y, BFLUX(J), FX_CAL(J)/ FX_CALMAX
       WRITE(1,180) Y, BFLUX(J), FX_CAL(J)/ FX_CALMAX
      END DO
      CLOSE (UNIT=1)
C
C-----      ALLOWING FOR REITERATION
C
      WRITE(6,*)' '
      WRITE(6,*)'ENTER A ZERO TO PERFORM ANOTHER ITERATION'
      READ(5,*)I_ITERATION
      IF (I_ITERATION .EQ. 0) THEN
       GO TO 10
      END IF
C
C-----      THIS SECTION ALLOWS INTERACTIVE SCREEN PRINTING OF
C-----      THE INTENSITY DISTRIBUTIONS AS FUNCTIONS OF
C-----      BOTH WAVELENGTH AND VERTICAL HEIGHT. THE PRINTING
C-----      IS DONE FOR ALL X NODES AND ALL ORDINATE DIRECTIONS.
C
 99   WRITE(6,*)'INPUT A 1 FOR I(X,LAMBDA), A 2 FOR I(X,Y) OR '
      WRITE(6,*)'A 0 TO QUIT'
      READ(6,*)I_PRT
      IF (I_PRT .EQ. 0) GO TO 1000
      IF (I_PRT .EQ. 1) THEN
 101   WRITE(6,*)'INPUT j'
       READ(5,*)J
       IF(J.EQ.100) GO TO 999
       DO I_LAM = 1, N_LAMT
        WRITE(6,104)I_LAM
        DO I_DIR = 1, N_ORDS
         WRITE(6, 102) (INTENSITY_LAM (I, J, I_DIR, I_LAM),
     !                        I=1, NODES_X, 2)
        END DO
       END DO
```

```
       GO TO 101
      ELSE
 111   WRITE(6,*)'INPUT I_LAM'
       READ(5,*)I_LAM
       IF(I_LAM .EQ. 100) GO TO 999
       DO J = 1, NODES_Y
        WRITE(6,105)J
        DO I_DIR = 1, N_ORDS
         WRITE(6, 102) (INTENSITY_LAM (I, J, I_DIR, I_LAM),
     !                        I=1, NODES_X, 2)
        END DO
       END DO
       GO TO 111
      END IF
 999  GO TO 99
C
C-----     FORMAT STATEMENTS
C
 103  FORMAT( 8X, 'INTENSITY_LAM',/)
 102  FORMAT(1X, 5(F9.1,1X))
 104  FORMAT(/,4X,'FOR I_LAM = ',I2,/,4X,'--------------',/)
 105  FORMAT(/,4X,'FOR J = ',I2,/,4X,'---------',/)
 155  FORMAT(//,20X,'THE TEMP. DIST IS ...',/,20X,
     *'--------------------',//)
 160  FORMAT(1X,5(F15.1,1X))
 170  FORMAT(//,10X,'THE AVERAGE EXIT TEMPERATURE IS ...',
     *        F6.2,' DEG. F',//)
 171  FORMAT(//,3X,'HIT <RETURN> TO CONTINUE',//)
 180  FORMAT(10X,F7.4, 5X, F13.4, 5X, F13.4)
 1000 RETURN
      END
C-------------------------------------------------------------------------C
C                                                                         C
C  THIS SUBROUTINE DEFINES THE ORDINATES AND WEIGHTS FOR THE              C
C  DISCRETE ORDINATES FORMULATION OF THE EOT.  THE VALUES WERE            C
C  TAKEN FROM LEE.                                                        C
C                                                                         C
C-------------------------------------------------------------------------C
      SUBROUTINE ORDINATES(N_ORDS, MU, XI, ETA, WEIGHT, IDIM_M)
      REAL MU
      DIMENSION MU(IDIM_M), XI(IDIM_M), WEIGHT(IDIM_M), ETA(IDIM_M)
      PI = ATAN(1.0) * 4.0
C
      IF (N_ORDS.EQ.4)THEN
C
       MU(1) = -0.57735026
       MU(2) = 0.57735026
       MU(3) = -0.57735026
       MU(4) = 0.57735026
C
       XI(1) = -0.57735026
       XI(2) = -0.57735026
       XI(3) = 0.57735026
       XI(4) = 0.57735026
```

```
C
      DO I = 1, 4
       ETA(I) = 0.57735026
      END DO
      WEIGHT(1) = 1.0
      WEIGHT(2) = 1.0
      WEIGHT(3) = 1.0
      WEIGHT(4) = 1.0
C
     ELSE IF (N_ORDS.EQ.12)THEN
C
      MU(1) = -0.33333333
      MU(2) = 0.33333333
      MU(3) = -0.88191710
      MU(4) = -0.33333333
      MU(5) = 0.33333333
      MU(6) = 0.88191710
      MU(7) = -0.88191710
      MU(8) = -0.33333333
      MU(9) = 0.33333333
      MU(10) = 0.88191710
      MU(11) = -0.33333333
      MU(12) = 0.33333333
C
      XI(1) = -0.88191710
      XI(2) = -0.88191710
      XI(3) = -0.33333333
      XI(4) = -0.33333333
      XI(5) = -0.33333333
      XI(6) = -0.33333333
      XI(7) = 0.33333333
      XI(8) = 0.33333333
      XI(9) = 0.33333333
      XI(10) = 0.33333333
      XI(11) = 0.88191710
      XI(12) = 0.88191710
C
      ETA(1) = 0.33333333
      ETA(2) = 0.33333333
      ETA(3) = 0.33333333
      ETA(4) = 0.88191710
      ETA(5) = 0.88191710
      ETA(6) = 0.33333333
      ETA(7) = 0.33333333
      ETA(8) = 0.88191710
      ETA(9) = 0.88191710
      ETA(10) = 0.33333333
      ETA(11) = 0.33333333
      ETA(12) = 0.33333333
C
      WEIGHT(1) = 1./3.
      WEIGHT(2) = 1./3.
```

```
      WEIGHT(3) = 1./3.
      WEIGHT(4) = 1./3.
      WEIGHT(5) = 1./3.
      WEIGHT(6) = 1./3.
      WEIGHT(7) = 1./3.
      WEIGHT(8) = 1./3.
      WEIGHT(9) = 1./3.
      WEIGHT(10) = 1./3.
      WEIGHT(11) = 1./3.
      WEIGHT(12) = 1./3.
C
      ELSE
C
      MU(1) = -0.25819889
      MU(2) = 0.25819889
      MU(3) = -0.68313005
      MU(4) = -0.25819889
      MU(5) = 0.25819889
      MU(6) = 0.68313005
      MU(7) = -0.93094934
      MU(8) = -0.68313005
      MU(9) = -0.25819889
      MU(10) = 0.25819889
      MU(11) = 0.68313005
      MU(12) = 0.93094934
      MU(13) = -0.93094934
      MU(14) = -0.68313005
      MU(15) = -0.25819889
      MU(16) = 0.25819889
      MU(17) = 0.68313005
      MU(18) = 0.93094934
      MU(19) = -0.68313005
      MU(20) = -0.25819889
      MU(21) = 0.25819889
      MU(22) = 0.68313005
      MU(23) = -0.25819889
      MU(24) = 0.25819889
C
      XI(1) = -0.93094934
      XI(2) = -0.93094934
      XI(3) = -0.68313005
      XI(4) = -0.68313005
      XI(5) = -0.68313005
      XI(6) = -0.68313005
      XI(7) = -0.25819889
      XI(8) = -0.25819889
      XI(9) = -0.25819889
      XI(10) = -0.25819889
      XI(11) = -0.25819889
      XI(12) = -0.25819889
      XI(13) = 0.25819889
      XI(14) = 0.25819889
```

```
      XI(15) = 0.25819889
      XI(16) = 0.25819889
      XI(17) = 0.25819889
      XI(18) = 0.25819889
      XI(19) = 0.68313005
      XI(20) = 0.68313005
      XI(21) = 0.68313005
      XI(22) = 0.68313005
      XI(23) = 0.93094934
      XI(24) = 0.93094934
C
      ETA(1) = 0.25819889
      ETA(2) = 0.25819889
      ETA(3) = 0.25819889
      ETA(4) = 0.68313005
      ETA(5) = 0.68313005
      ETA(6) = 0.25819889
      ETA(7) = 0.25819889
      ETA(8) = 0.68313005
      ETA(9) = 0.93094934
      ETA(10) = 0.93094934
      ETA(11) = 0.68313005
      ETA(12) = 0.25819889
      ETA(13) = 0.25819889
      ETA(14) = 0.68313005
      ETA(15) = 0.93094934
      ETA(16) = 0.93094934
      ETA(17) = 0.68313005
      ETA(18) = 0.25819889
      ETA(19) = 0.25819889
      ETA(20) = 0.68313005
      ETA(21) = 0.68313005
      ETA(22) = 0.25819889
      ETA(23) = 0.25819889
      ETA(24) = 0.25819889
C
      WEIGHT(1) = 0.16086125
      WEIGHT(2) = 0.16086125
      WEIGHT(3) = 0.17247209
      WEIGHT(4) = 0.17247209
      WEIGHT(5) = 0.17247209
      WEIGHT(6) = 0.17247209
      WEIGHT(7) = 0.16086125
      WEIGHT(8) = 0.17247204
      WEIGHT(9) = 0.16086125
      WEIGHT(10) = 0.16086125
      WEIGHT(11) = 0.17247204
      WEIGHT(12) = 0.16086125
      WEIGHT(13) = 0.16086125
      WEIGHT(14) = 0.17247204
      WEIGHT(15) = 0.16086125
      WEIGHT(16) = 0.16086125
```

```
        WEIGHT(17) = 0.17247204
        WEIGHT(18) = 0.16086125
        WEIGHT(19) = 0.17247204
        WEIGHT(20) = 0.17247204
        WEIGHT(21) = 0.17247204
        WEIGHT(22) = 0.17247204
        WEIGHT(23) = 0.16086125
        WEIGHT(24) = 0.16086125
C
      END IF
      DO I = 1,N_ORDS
       WEIGHT(I) = WEIGHT(I) * PI
      END DO
C
      RETURN
      END
C-------------------------------------------------------------------------------C
```

Appendix 6

Model Predicted Temperature Distribution

The design of a direct absorption solar receiver is based on which type of receiver and heliostat field configuration optimizes the conversion efficiency of the system. To this end, any model of a certain receiver type should be able to predict the temperature distribution in the medium. If the medium is highly absorbing in nature, than a relatively small thickness for the receiver may be sufficient to completely attenuate the incident solar energy.

The spatial gradient of the temperature along the critical axis of the receiver (i.e. the direction into the medium along the path of the incident flux) will play an important role in the receiver design. The model discussed in this report is capable of providing information on this gradient.

Table A.6.1 illustrates the final temperature distribution for Test Run $Q4$ (obtained after total convergence is observed for the radiation problem) for the Masterbeads^{TM} according to the energy expression that was formulated for this problem. The inlet particle temperature was held at the constant value that was measured on the day of the particular test.

Notice that the spatial temperature gradient is fairly severe (i.e. the incident solar energy does not significantly change the temperatures at the rear of the curtain, $\hat{x} = 1.0$. This is expected due to the fact the Masterbeads^{TM} are highly absorbing with a low scattering albedo. For this reason, any receiver that utilizes these particles as the actively absorbing medium will either need to address the problem of significant temperature and flux non-uniformity within in the curtain, possibly by using a highly reflective rear wall, or accepting the situation as it stands.

Previous studies have shown[19] that significant non-uniformities in the absorbing medium can reduce the conversion efficiency of the receiver. However, since most direct absorption media that might be considered for this particular purpose are low scattering-high absorption materials, the problem of medium non-uniformity must eventually be addressed.

It should be stated, however, that a highly absorbing thermal media will

Table A.6.1: Interior Temperature Disrtibution

	Horizontal Position				
	0.0	0.25	0.50	0.75	1.0
Vertical Position	**Temperature (deg. F)**				
0.0	80.6	80.6	80.6	80.6	80.6
0.053	82.6	81.8	81.4	81.2	81.0
0.105	84.3	82.7	81.9	81.5	81.3
0.158	86.1	83.8	82.6	81.9	81.5
0.211	88.0	84.9	83.2	82.3	81.8
0.263	89.9	85.9	83.9	82.7	82.1
0.316	91.5	86.9	84.4	83.1	82.3
0.368	92.7	87.6	84.9	83.4	82.5
0.421	93.5	88.0	85.2	83.6	82.6
0.474	94.0	88.4	85.3	83.7	82.7
0.526	94.4	88.5	85.5	83.7	82.7
0.579	94.6	88.7	85.5	83.8	82.8
0.632	94.7	88.7	85.6	83.8	82.8
0.684	94.8	88.8	85.6	83.8	82.8
0.737	94.8	88.8	85.6	83.9	82.8
0.789	94.9	88.8	85.6	83.9	82.8
0.842	94.9	88.8	85.6	83.9	82.8
0.895	94.9	88.8	85.6	83.9	82.8
0.947	94.9	88.8	85.6	83.9	82.8
1.0	94.9	88.8	85.6	83.9	82.8

require relatively smaller curtain thicknesses to completely absorb the incident energy, thus reducing the total volume of material that needs to be delivered to the active area of the receiver.

Appendix 7

Users Manual for

Main Computer Program

To run the main program for this project involves determining the parameter values for the angular flux model in a separate program and reading in these values into this program through a data file. The main program is constructed with the specific form of the boundary intensity model built in. It does, however, allow for different sets of total flux data by reading in the parameter set for each run. The flux data, both the transmitted and the front face, may be separately inputted even though, for the plots in this report, the data from the NMSU Solar Furnace are already in the program.

The steps used in inputting the needed quantities and some explanation of the quantities that are not user defined follows.

Program *SPECTRA* is composed of seven segments including the main program. The main program simply calls the required subroutines and does not perform any clculations. Subroutine *INPUT* is initially called for obvious reasons. When the program is executed, *INPUT* will ask the user for the needed quantities.

Initially the code prompts the user for the curtain thickness in *mm*. The next prompt concerns the method of inputting the front face and transmitted flux data. If any number other than a zero is entered, the program will next prompt the user for the number of the data file that is requested. (Note that only those data files for which plots have been included in the body of this report are available.) The statement for this input is:

Enter the number of the data file... Q

and the cursor will stay at the end of this statement to read the desired file (i.e. *Q*4, etc.). If a zero is entered at the flag statement, the code will prompt the user for 5 values for the incident flux and 5 values for the transmitted flux. The "5" is because there were 5 flux gage locations used in the development of the data for this project. If there are more data points than 5, simply edit the code and change the value of *NPOINTS* to the appropriate value.

Next the input will prompt the user for the number of ordinate directions desired for the execution (the choices are 4, 12 or 24).

The last prompt is for the inlet particle temperature in $^{\circ}F$. Note that the subroutine defines the wavelength bands from statements that set the number of bands allowed. There are 5 bands in the solar region (i.e. 0.3 to 1.1 μm) and 2 bands in the IR (1.1 to 10. μm). Also, there are 20 nodes in the vertical direction for the curtain and 10 nodes in the thickness direction. These values were chosen because they represented the maximum active memory for the type of computer that was used. If the user wishes a finer grid for any of these three array dimensions, one need only change the values of *N_LAM1, N_LAM2, NODES_X* and *NODES_Y.*

After all of the desired information is inputted, the machine will move on to the next subroutine, *Y0BOUND.* This subroutine determines the intensity distribution at the top of the curtain, the particle inlet point. It accomplishes this task by assuming the particles are all at the inlet particle temperature and determines the emissive power in each wavelength band defined. The energy in each band is determined by integrating Planck's expression over each particular band. The logic in the subroutine is fairly straightforward and is simply based on the inlet temperature and the wavelength bands.

After *Y0BOUND* has set the intensity distribution along the top of the receiver, subroutine *ORDINATES* reads in the chosen ordinate values and their repsective weights.

Next, *X0BOUND* determines the intensity distribution along the front face of the curtain for the given incident flux values. The intensity distribution determined at this point is not spectral. The spectral values will be determined in the next routine. The critical section of this subroutine is the use of the boundary intensity model and the corresponding parameters. The model that was described in the main body of this report is used to determine the intensity field along each of the ordinate directions by breaking the ordinates down into

their respective angle values. These angular values are then translated to the required origin of the boundary model and used in the function to determine the intensity as a function of direction at the front face.

Notice that, if a different boundary model is used, this subroutine must be modified to allow for it. This should be done by changing the logic defining the 1) main intensity function, 2) the origin of the angular coordinate system, 3) the maximum cone angle for the concentrating system and 4) the reading in of the parameter vector for the given flux data.

The results of these calculations are printed to the screen in terms of each of the ordinate directions (all three ordinates are printed). The last visible column on the screen will be the total intensity for the given angles. There will be zeros for every ordinate direction that does not fall within the required cone angle of the concentrator.

Subroutine *SPECTRUM* is then called to determine, from the LYCOR solar spectrum data, the percent of the total soalr energy that exists inside each of the defined wavelength bands. This is accomplished by integrating the high resolution LYCOR data ($\Delta\lambda = 0.002\mu m$) over the chosen wavelength band. Then, the total energy under the entire spectrum is determined (through integration) and the ratio, for each band, represents the percent of the total energy that is present in that particular band. This percentage value is then multiplied by the total intensity determined above to yield the spectral front face intensity distribution.

Lastly, subroutine *EOT* is called to iterate the equation of transfer and the energy expression. For each iteration, the inn-scattering term is calculated three times and the total temperature distribution is printed to the screen. At this point, the machine allows the user to decide if another iteration is desired with a flag type prompt. If no new iteration is requested, the machine will print out the transmitted fluxes and the temperature distribution along with the average exit temperature. Note, any of these print statements may be

"commented" out or routed to a data file for plotting and hardcopy output if desired. Also, the code allows the user to actively inspect the intensity field for any wavelength, direction or node desired. This part of the output is the final section of this subroutine and ends when the user inputs the correct flag value to stop execution.

UNLIMITED RELEASE
INITIAL DISTRIBUTION

U.S. Department of Energy (5)
Forrestal Building
Code CE-314
1000 Independence Avenue, SW
Washington, DC 20585
Attn: H. Coleman
S. Gronich
M. Scheve
R. Shivers
T. Wilkins

U.S. Department of Energy
Forrestal Building
Code CE-33
1000 Independence Avenue, SW
Washington, DC 20585
Attn: C. Carwile

U. S. Department of Energy
CE-1, Forrestal
1000 Independence Avenue, Sw
Washington, DC 20585
Attn: D. Fitzpatrick

U.S. Department of Energy
San Francisco Operations Office
1333 Broadway
Oakland, CA 94612
Attn: R. Hughey

Analysis Review & Critique
6503 81st Street
Cabin John, MD 20818
Attn: C. LaPorta

Arizona Solar Energy Office
Dept. of Commerce
1700 W. Washington, 5th Floor
Phoenix, AZ 85007
Attn: Dr. Frank Mancini

Atlantis Energy Ltd.
Thunstrasse 43a
3005 Bern, Switzerland
Attn: Mario Posnansky

Battelle Pacific Northwest
Laboratory
P.O. Box 999
Richland, WA 99352
Attn: K. Drost

Bechtel National, Inc. (2)
50 Beale Street
50/15 D8
P. O. Box 3965
San Francisco, CA 94106
Attn: P. DeLaquil
R. Leslie

Black & Veatch Consulting
Engineers
P.O. Box 8405
Kansas City, MO 64114
Attn: J. E. Harder

Tom Brumleve
1512 Northgate Road
Walnut Creek, CA 94598

California Energy Commission
1516 Ninth Street, M-S 43
Sacramento, CA 95814
Attn: A. Jenkins

California Public Utilities Com.
Resource Branch, Room 5198
455 Golden Gate Avenue
San Francisco, CA 94102
Attn: T. Thompson

Centro Investigations Energetica
Medroansental Technologie (CIEMAT)
Avda. Complutense, 22
28040 Madrid
SPAIN
Attn: F. Sanchez

DFVLR, HA-ET (2)
Linder Hoehe
5000 Cologne 90
Federal Republic of Germany
Attn: M. Becker
M. Boehmer

EIR
CH-5303 Wurenlingen
Switzerland
Attn: W. Durish

Electric Power Research
Institute (2)
P.O. Box 10412
Palo Alto, CA 94303
Attn: J. Bigger
E. DeMeo

Flachglas Solar
Technikg G.M.B.
Sonnen Str. #25
8000-Munchen-1
Federal Republic of Germany

Foster Wheeler Solar Development
Corporation
12 Peach Tree Hill Road
Livingston, NJ 07039
Attn: S. F. Wu

Georgia Institute of Technology
GTRI/EMSL Solar Site
Atlanta, GA 30332
Attn: T. Brown

Leo Gutierrez
434 School Street
Livermore, CA 94550

HGH Enterprises, Inc.
23011 Moulton Parkway
Suite C-13
Laguna Hills, CA 92653
Attn: Dick Holl

Interatom GmbH
P. O. Box
D-5060 Bergisch-Gladbach
Fededral Republic of Germany
Attn: M. Kiera

Lawrence Berkeley Laboratory
MS 90-2024
One Cyclotron Road
Berkeley, CA 94720
Attn: Arlon Hunt

Los Angeles Department of Water
and Power
Alternate Energy Systems
Room 661A
111 North Hope Street
Los Angeles, CA 90012
Attn: Bill Engels

Luz International
924 Westwood Blvd.
Los Angeles, CA 90024
Attn: D. Kearney

New Mexico State University (2)
Mechanical Engineering Dept.
Las Cruces, NM 88003
Attn: G. Mullholand
M. J. Richtly

Platforma Solar de Almeria
Aptdo. 7
Tabernas (Almeria)
E-04200 Spain
Attn: M. Silva

Pacific Gas and Electric Company
3400 Crow Canyon Road
San Ramon, CA 94526
Attn: B. Norris

Ramada Energy Systems Ltd.
1421 S. McClintock Drive
Tempe, AZ 85281
Attn: R. Bingman

San Diego Gas and Electric Company
P.O. Box 1831
San Diego, CA 92112
Attn: R. Figueroa

Science Applications International
Corporation
2109 Airpark Road, SE
Albuquerque, NM 87106
Attn: D. Smith

Science Applications International
Corporation
10401 Roselle Street
San Diego, CA 92121
Attn: B. Butler

Solar Energy Research Institute (2)
1617 Cole Boulevard
Golden, CO 80401
Attn: M. Bohn
M. Carasso

Solar Kinetics, Inc.
P.O. Box 540636
Dallas, TX 75354-0636
Attn: J. A. Hutchison

Solar Power Engineering Company
P.O. Box 91
Morrison, CO 80465
Attn: H. C. Wroton

Sulzer Bros, Ltd.
New Technologies
CH-8401 Winterthur
Switzerland
Attn: Hans Fricker, Manager

Tom Tracey
6922 South Adams Way
Littleton, CO 80122

United Solar Tech, Inc.
3434 Martin Way
Olympia, WA 98506
Attn: R. J. Kelley

University of Utah
Mechanical and Industrial
Engineering
Salt Lake City, UT 84112
Attn: B. Boehm

400 J. A. Leonard
3141 S. A. Landenberger (5)
3151 W. I. Klein (3)
3154 C. L. Ward (8)
For DOE/OSTI
6010 D. E. Aruisu
6200 V. L. Dugan
6220 D. G. Schueler
6211 B. Granoff
6212 H. P. Stevens
6215 J. T. Holmes (10)
6215 C. P. Cameron
6216 C. E. Tyner
6217 P. C. Klimas
6217 J. M. Chavez
6217 G. J. Kolb
8024 P. W. Dean
8524 J. A. Wackerly
6517 M. J. Rightley